DEPARTMENT OF AEROSPACE ENGINEERING
INDIAN INSTITUTE OF TECHNOLOGY MADRAS
CHENNAI – 600036

Dynamics of interacting thermoacoustic systems

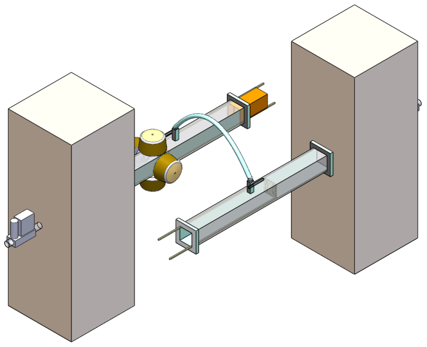

A Thesis

Submitted by

ANKIT SAHAY

For the award of the degree

Of

DOCTOR OF PHILOSOPHY

April 2024

DEPARTMENT OF AEROSPACE ENGINEERING
INDIAN INSTITUTE OF TECHNOLOGY MADRAS
CHENNAI – 600036

Dynamics of interacting thermoacoustic systems

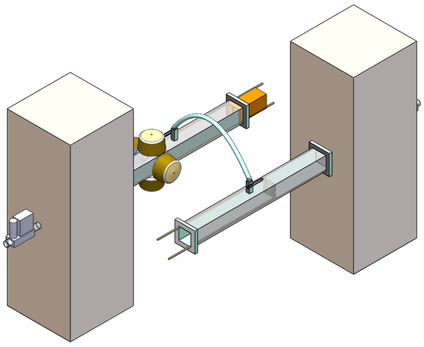

A Thesis

Submitted by

ANKIT SAHAY

For the award of the degree

Of

DOCTOR OF PHILOSOPHY

April 2024

© 2024 Indian Institute of Technology Madras

स॒ह ना॑ववतु॒ । सह नौ॑ भुनक्तु ।	sa̱ha nā̍vavatu | sa̱ha nau̍ bhunaktu |
स॒ह वी॒र्यं॑ करवावहे ।	sa̱ha vī̱rya̍ṁ karavāvahai |
ते॒ज॒स्विना॒वधी॑तमस्तु॒ मा वि॑द्विष॒वहै᳚ ॥	te̱ja̱svinā̱vadhī̍tamastu̱ mā vi̍dviṣa̱vahai᳚ ||
ॐ शान्ति॒ः शान्ति॒ः शान्ति॑ः ॥	om śānti̱ḥ śānti̱ḥ śānti̍ḥ ||

Let us together be protected and let us together be nourished by God.
Let us together join our mental forces in strength for the benefit of humanity.
Let our efforts at learning be luminous and filled with joy, and endowed with the force of purpose. Let us never be poisoned with the seeds of hatred for anyone.
Let there be peace and serenity in all the three universes.

– Taittiriya Upanishad , Chapter 2, Verse 1

To my family

For their unwavering patience and faith

Because they always understood

THESIS CERTIFICATE

This is to undertake that the Thesis titled **DYNAMICS OF INTERACTING THERMOACOUSTIC SYSTEMS**, submitted by me to the Indian Institute of Technology Madras, for the award of **Doctor of Philosophy**, is a bona fide record of the research work done by me under the supervision of **Dr. R. I. Sujith**. The contents of this Thesis, in full or in parts, have not been submitted to any other Institute or University for the award of any degree or diploma.

In order to effectively convey the idea presented in this Thesis, the following work of other authors or sources was reprinted in the Thesis with their permission:

1. Figure 1.1 is distributed under the the Creative Commons license (CC BY 3.0 IGO), and is free to use.

2. Figures 1.2 and 1.3 : Image from Smoot *et al.* (1998). Reproduced with permission from Elsevier Ltd.

3. Figure 1.4 : Image from Reichel and Paschereit (2017). Reproduced with permission from Elsevier Ltd.

4. Figure 1.5 : Image reproduced from Lieuwen *et al.* (1998). Reproduced with permission from Taylor & Francis.

5. Figure 1.6 : Image reproduced from Poinsot (2017). Reproduced with permission from Elsevier Ltd.

6. Figure 1.7 : Image reproduced from Ken *et al.* (1991). Reproduced with permission from Cambridge University Press.

7. Figures 1.8 and 1.9 : Image reproduced from Lieuwen and Yang (2005). Reproduced with permission from AIAA, Inc.

8. Figure 1.11 : Image reproduced from Moon *et al.* (2020*b*). Reproduced with permission from Elsevier Ltd.

9. Figure 1.12 : Image reproduced from Lang *et al.* (1987). Reproduced with permission from Elsevier Ltd.

10. Figure 1.13 : Image reproduced from Krishnan *et al.* (2021). Reproduced with

permission from Cambridge University Press.

11. Figure 1.14 : Image reproduced from Pawar *et al.* (2017). Reproduced with permission from Cambridge University Press.

Chennai 600036 **Ankit Sahay**

Date: April 2024

Prof. R. I. Sujith
Research advisor
D. Srinivasan Institute Chair Professor
Department of Aerospace Engineering
IIT Madras

© 2024 Indian Institute of Technology Madras

LIST OF PUBLICATIONS

I. REFEREED JOURNALS BASED ON THESIS

1. **Sahay, A.**, Roy, A., Pawar, S. A., and Sujith, R. I. (2021). Dynamics of coupled thermoacoustic oscillators under asymmetric forcing. *Physical Review Applied*, **15(4)**, 044011.

2. Srikanth, S., **Sahay, A.**, Pawar, S. A., Manoj, K., and Sujith, R. I. (2022). Self-coupling: An effective method to mitigate thermoacoustic instability. *Nonlinear Dynamics*, **1-15**.

3. **Sahay, A.**, Kushwaha, A., Pawar, S. A., Midhun, P. R., Dhadphale, J. M., and Sujith, R. I. (2023). Mitigation of limit cycle oscillations in a turbulent thermoacoustic system via delayed acoustic self-feedback. *Chaos: An Interdisciplinary Journal of Nonlinear Science*, **33(4)**, 043118.

4. **Sahay, A.**, Gopalakrishnan Meena, M., Taira K., and Sujith R. I., Insights into the interplay between hydrodynamic and acoustic fields in a turbulent combustor via community-based dimensionality reduction of vortical networks.
   The preprint is available at `https://arxiv.org/abs/2311.12541`, and is currently under review in the Journal of Fluid Mechanics.

II. PRESENTATIONS IN CONFERENCES

1. **Sahay, A.**, Roy, A., Pawar, S. A., and Sujith, R. I., Coupled behavior of oscillators under asymmetric forcing. *Dynamics Days Europe*, (2021).

2. Srikanth, S., **Sahay, A.**, Pawar, S. A., Manoj, K., and Sujith, R. I., Oscillation Quenching Through Self-Coupling: Experiments And Modeling. *13th Conference on Nonlinear Systems and Dynamics*, (2021).

3. **Sahay, A.**, Kushwaha, A., Pawar, S. A., Midhun, P. R., Dhadphale, J. M., and Sujith, R. I., Delayed acoustic self-feedback control of limit cycle oscillations in a turbulent combustor. *NODYCON*, (2023).

4. **Sahay, A.**, Gopalakrishnan Meena, M., and Sujith, R. I., Correlating hydrodynamic and acoustic fields in a turbulent combustor through community-based dimensionality reduction of vortical networks. *76th Annual Meeting of the APS Division of Fluid Dynamics*, (2023).

ACKNOWLEDGEMENTS

It's been a long journey since I stepped into RGD 11 on the evening of 31st January 2019 to discuss with **Prof. R. I. Sujith** about the prospects of completing the final year M.Tech. project in his lab and expecting to graduate in 2020. I did not know that I would spend the next five years working with him during an unforgettable chapter of my academic journey.

My greatest thanks are to Prof. Sujith, who has been a role model and a source of encouragement and guidance throughout the duration of my Ph. D.. He has provided a supportive environment that has allowed me to explore my interests, and I am grateful for his patience and optimism about my work. I hope that you might be as proud to be my mentor as I am to be your mentee. Your guidance has brought me to this place through false starts and hesitations. I would not be here without you.

I wish to thank the members of my Doctoral Committee - **Prof. Nandan Kumar Sinha**, **Prof. Sunetra Sarkar**, and **Prof. Arul Lakshminarayan** for their valuable suggestions and comments. I would also like to thank **Prof. P. Sriram** and **Prof. H. S. N. Murthy**, in their capacity as the Head of the Department, for their encouragement and support.

I express my sincere gratitude to the following funding agencies for their generous support during the course of my research: Office of Naval Research Global, J. C. Bose Fellowship (No. JCB/2018/000034/SSC) from the Department of Science and Technology (DST), the IoE initiative (SB/2021/0845/AE/MHRD/002696), and Oak Ridge Leadership Computing Facility (supported by the Office of Science of the US Department of Energy under Contract No. DE-AC05-00OR22725). Most of all, I am thankful to the citizens of my country for funding me through Half-Time Research Assistantship.

Working in Prof. Sujith's group has indeed been a pleasure. Every result described in this thesis was accomplished with the help and support of fellow labmates and collaborators. I am greatly indebted to my seniors - **Dr. Amitesh Roy**, **Dr. Samadhan Pawar**, and **Subham Banerjee** for guiding me through my first work. I am immensely thankful to **Dr. Manikandan Raghunathan** and **Midhun Raghunathan** for teaching me spatiotemporal analyses and about TARA, **Dr. Praveen Kasthuri** for his constant support in helping me understand complex networks, and Samadhan for his extensive talks on what it takes to be a good researcher. I will always cherish their enthusiastic approach toward answering my questions. I am grateful to **Sneha Srikanth**, **Krishna Manoj**, **Dr. Somnath De**, **Dr. Induja Pavithran**, **Dr. Ankan Banerjee** and **Dr. Gaurav Chopra** for the engaging discussions I have been a part of. I am indebted to **Dr. Abin Krishnan** for helping me in my multiple moments of self-doubts. I will always be thankful to **Thilaga Raj S.**, **Anand Selvam**, **Anaswara Bhaskaran**, **Reeja K. V.** and **Sudha Kans** for helping me with the experiments. Experiments form an essential part of my work, and I could not have done any of the experiments without their help. I also express my gratitude to **M. Shanmugapriya**, **Jabasteena Jabaseelan**, **Jegatha Balaji Regunath**, and **Richu George Philip**, who helped me with the administrative work.

A sound support system is vital to surviving and staying sane in grad school. I was lucky to have **Samarjeet**, **Abhishek**, and **Jayesh** with me through all these years. I could always ask them for advice and opinions on lab and research-related issues. I thank Samarjeet for our regular Cafe Coffee Day trips, especially when preparing for our Comprehensive Exam. Occasional visits to Purple Chameleon with Abhishek were a welcome diversion from the rigamarole of research. I will be forever grateful to Jayesh for spending umpteen days teaching me Python and Deep Learning.

I also thank the younger generation students, **Ramesh Bhavi**, **Siva Sudarsanan**, **Rohit**, **Sanket Ambedkar**, **Thonti Beeraiah**, and **Shruti Tandon**, for showing lots of enthusiasm and optimism while working in the lab. Their fresh perspectives and learning eagerness added a vibrant energy to my work. Their presence reminds me of the excitement and curiosity that come with new beginnings, and I genuinely appreciate the unique contributions all of them have brought to Prof. Sujith's group. I look forward to witnessing their growth and accomplishments as they continue to shape the future of this group. Thank you for being integral to my Ph. D. journey.

I am honoured to have collaborated with **Dr. Muralikrishnan Gopalakrishnan Meena**. Adding his varied perspectives on the topic of communities in complex networks helped me in taking this project to completion. His pilot research on communities in vortical networks provided a clear road map for my research on communities' interactions in a turbulent thermoacoustic system, particularly in the early stages. He patiently helped me through many hours of discussion on various aspects of complex networks and communities. Chapter 4 is a direct result of his help. I am grateful to **Prof. Kunihiko Taira** for introducing me to Dr. Gopalakrishnan Meena.

I also thank my friends from my M.Tech. days in IIT Madras: **Vishnu**, **Utkarsh**, **Venky**, **Prathamesh**, **Bhavya**, **Saurabh**, and **Waliya**, who helped me during my initial years at IIT Madras. It was an absolute delight to spend time with them in Chennai.

I must thank my teachers for showing me what it means to be dedicated to our work, each in their unique way. I will always be grateful to **Mrs. Sengupta**, who taught me English from Class 3rd to Class 7th, and **Mr. Sengupta**, who inculcated the scientific spirit essential for every young mind. During my early years in De Nobili School, I was fortunate to have been taught by three excellent teachers: my Hindi teacher **Mrs. Ila Prasad**, Geography teacher **Mrs. Mary Immaculate**, and English teacher **Mrs. Rita Bhattacharya**. As time passed, I could not forget how they truly loved teaching and cared for their students. This cherished memory became the driving force behind my decision to embrace teaching. Moving on to my undergraduate days, the tutelage of **Prof. Abhijit Nag**, **Prof. Apurba Kumar Roy**, and **Prof. Arun Dayal Udai** gave me the confidence and strength to switch to research. I extend my deepest appreciation to

Prof. Satadal Ghosh, whose approach in teaching AS5040 Flight Mechanics resonated profoundly with me during my first year in IIT Madras. Serving as a Teaching Assistant for four of Prof. Sujith's courses helped me with a significant insight into the art of balancing teaching and research. Each of you has given your time, energy, and expertise towards teaching me, and I am richer for it. Your love for teaching is contagious and is one of the primary reasons I decided to pursue a career in academia.

I particularly thank my most cherished friends, whom I have been extremely fortunate to have known. **Avinash**, my oldest and closest friend, whom I know I can unfailingly count on without any exception. He has been my "Fortress of Solitude" since the old days of yore. **Durgesh**, whom I have had countless interactions with about spirituality and philosophy, and who, as a grad student himself, somehow always knew what was on my mind during my Ph. D. His insights and opinions on non-academic issues have immensely helped me grow through the last ten years as a person. Thank you for introducing me to Advaita Vedanta. I am thankful to **Vipul** for supporting me during my longest period of crisis. I cannot forget **Asif**, **Ankit (Bhushan, not Sahay!)**, **Ankur**, and **Aniket** for their friendship and the warmth they have continued to extend to me through all these years. They continue to inspire me to be a better person. Thank you for your understanding and encouragement in my many, many moments of crisis. Your friendship makes my life a wonderful experience.

Finally, I am grateful beyond words to my dearest family, who kept the fires at the home burning, happily accommodated my mad schedules and dashed plans, and encouraged and inspired me, not just along this Ph. D. journey but always. The last word goes to my grandparents, who always had faith in me. This thesis is an ode to the memory of my late grandfather, whose unwavering support and encouragement propelled me towards this academic pursuit. Though he is no longer with us, his belief in my capabilities continues to inspire me as I navigate this journey, and his guiding presence remains an integral part of my accomplishments. This thesis is dedicated to him.

ABSTRACT

KEYWORDS Thermoacoustic instability; Intermittency; Limit cycle oscillations; Amplitude Death; Complex networks; Self-feedback; Coupling; Time delay

Thermoacoustic instability refers to large amplitude acoustic pressure and heat release rate oscillations of periodic nature that occur due to a positive feedback loop between the flame, the flow, and the acoustic fields in the reaction field of a combustor. All these subsystems directly or indirectly affect each other at different time-space scales during all the states of combustor operation. We can consider such systems as ‘complex systems’, as a thermoacoustic system involves a three-way interaction between the flame, the flow, and the acoustic fields. Emergence of large coherent structures in the reaction flow field of a turbulent combustor during the state of thermoacoustic instability is an indicator of complex systems.

In the first part of this thesis, we examine the interplay between acoustic field and interactions between regions of intense vorticity in the reactive field of a bluff-body stabilised turbulent combustor. We identify these regions of intense vortical interactions as vortical communities in the network space of weighted directed vortical networks constructed from two-dimensional velocity data. We condense the vortical interactions in the high-dimensional reactive flow into a low-dimensional network representation by leveraging inter-community strengths and weighted community centroids. Subsequently, we show that the mean and maximum of all inter-community interactions exhibit a strong delayed correlation with the acoustic pressure oscillations during the state of thermoacoustic instability. Spatiotemporal evolution of pairs of vortical communities with the maximum inter-community interactions provides insight into explaining the critical regions detected in the reaction field during the states of intermittency and thermoacoustic instability in previous studies. We further demonstrate that the high

correlations between network measures and acoustic pressure oscillations during the state of thermoacoustic instability weaken when steady air jets are introduced within the critical region to suppress the thermoacoustic oscillations.

The aforementioned thermoacoustic instability is a major source of concern in combustors used in gas turbine engines. A combustor in a gas turbine engine can acoustically interact with itself through downstream combustor-turbine transition gap. In the second part of the thesis, we use the concept of delayed acoustic self-feedback to examine the implications of a thermoacoustic system interacting with itself through acoustics. Through experiments conducted in the turbulent combustor mentioned in the previous paragraph, we report the occurrence of amplitude death (AD) by coupling the acoustic field of the combustor to itself through a single coupling tube attached near the anti-node position of the acoustic standing wave. Complete suppression (AD) of these oscillations is observed when the length of the coupling tube is nearly $3/8$ times the wavelength of the fundamental acoustic mode of the combustor. We show that the dynamical behavior of acoustic pressure changes from the state of limit cycle oscillations to low-amplitude chaotic oscillations via intermittency. We also study the change in the nature of the coupling between the unsteady flame dynamics and the acoustic field as the length of the coupling tube is increased. We find that the temporal synchrony between these oscillations changes from the state of synchronised periodicity to desynchronised aperiodicity through intermittent synchronisation. Furthermore, we reveal that the application of delayed acoustic self-feedback with optimum feedback parameters completely disrupts the positive feedback loop between the flame, the flow, and the acoustic fields present in the combustor during thermoacoustic instability, thus mitigating instability.

Given the inherent challenges of conducting intricate experiments within a turbulent combustor environment, we proceed by directing our focus towards a horizontal laminar Rijke tube to further study delayed acoustic self feedback in thermoacoustic systems. Rijke tube is a prototypical thermoacoustic oscillator consisting of a heat source placed at a certain location inside a duct. Rijke tube systems have simple designs, can be easily fabricated and operated, and enable precise execution of controlled experiments. We examine the effect of both system and coupling parameters on the occurrence of amplitude death. We thereby show that the parametric regions of amplitude death occur when the coupling tube length is close to an odd multiple of the length of the Rijke tube. Through experiments, we demonstrate that the optimal location to place the coupling tube for achieving amplitude death is near the antinode of the acoustic pressure standing wave in the Rijke tube. Furthermore, we find that self-coupling mitigates thermoacoustic instability in a Rijke tube more effectively than mutual coupling of two identical Rijke tubes.

In the third and final part of the present thesis, we address the dynamical behaviour arising as a result of two thermoacoustic systems interacting with each other. This scenario occurs when two adjacent combustors present in a can-annular configuration gas turbine engine acoustically interact with each other via cross-fire tubes. With an emphasis on the mitigation of thermoacoustic instability in mutually coupled thermoacoustic systems, we study the dynamics of two laminar horizontal Rijke tubes simultaneously subjected to mutual coupling and asymmetric external forcing through experiments and theoretical modelling. We investigate the forced response of both identical and nonidentical Rijke tubes for two different amplitudes of thermoacoustic instability. Under mutual coupling alone, identical Rijke tubes display the occurrence of partial amplitude death and amplitude death, whereas under forcing alone, asynchronous quenching of thermoacoustic instability is observed at nonresonant conditions. When the Rijke tubes are simultaneously subjected to mutual coupling and asymmetric forcing, we observe a larger parametric region of oscillation quenching than when the two mechanisms are utilised individually. This enhancement in the region of oscillation quenching is due to the complementary effect of amplitude death and asynchronous quenching. However, the forced response of coupled nonidentical Rijke tubes shows that the effect of forcing is insignificant on attaining synchronisation and quenching of oscillations in the Rijke tube that is not directly forced. Finally, we qualitatively capture the experimental results using a reduced-order theoretical model of two Rijke tubes that are coupled through dissipative and time-delay coupling and asymmetrically forced.

CONTENTS

Page

ACKNOWLEDGEMENTS i

ABSTRACT v

LIST OF TABLES xiii

LIST OF FIGURES xv

GLOSSARY xxix

ABBREVIATIONS xxxi

NOTATION xxxiii

CHAPTER 1 INTRODUCTION 1

1.1 Population explosion and environmental concerns . . . 1
1.2 NO_x emission problems in gas turbine engines . . . 3
1.3 NO_x emission mitigation techniques . . . 5
1.4 Lean premixed prevaporized combustion . . . 8
1.5 Challenges associated with lean, premixed combustion . . . 9
1.6 Thermoacoustic instability . . . 13
1.6.1 Driving mechanisms . . . 15
1.6.2 Damping mechanisms . . . 17
1.7 Thermoacoustic instability in gas turbines . . . 18
1.7.1 Thermoacoustic instability in can-annular combustors . . . 20
1.8 Control of thermoacoustic instability . . . 22
1.8.1 Active closed loop control . . . 23
1.8.2 Active open loop control . . . 26
1.8.3 Passive control . . . 28
1.9 Non-conventional approach of studying thermoacoustic instability . . . 29
1.9.1 Use of synchronisation to investigate interacting thermoacoustic systems through dynamical system theory . . . 31
1.9.2 Thermoacoustic instability through the perspective of complex systems theory . . . 34
1.9.3 Complex networks in thermoacoustic systems . . . 37
1.10 Motivation . . . 39
1.11 Objectives . . . 40
1.12 Overview of the thesis . . . 42

CHAPTER 2 COMPLEX NETWORKS AND COMMUNITY DETECTION 45

2.1 Complex network description of vortical interactions 47
2.2 Vortical network construction 50
2.3 Community detection 51
2.4 Community-based network reduction and interaction of vortical communities 53

CHAPTER 3 EXPERIMENTAL SETUPS AND DIAGNOSTICS 57

3.1 Bluff-body stabilised turbulent combustor 58
3.1.1 Measurements and data acquisition 60
3.2 Bluff-body stabilised turbulent combustor with delayed acoustic self-feedback 61
3.2.1 Measurements and data acquisition 63
3.3 Horizontal laminar Rijke tube with delayed acoustic self-feedback . . . 63
3.3.1 Measurements and data acquisition 65
3.4 Mutually coupled Rijke tubes with asymmetrical acoustic forcing . . . 65
3.4.1 Measurements and data acquisition 67

CHAPTER 4 INTERPLAY BETWEEN HYDRODYNAMIC AND ACOUSTIC FIELDS IN A TURBULENT COMBUSTOR 69

4.1 Spatial distribution of vortical communities during different dynamical states 77
4.2 Phase averaged analysis of strongest influential communities 79
4.3 Dimensionality reduction of vortical networks 83
4.4 Correlation of inter-community interactions with acoustic pressure oscillations 85
4.5 Interpretation of network measures through hydrodynamics 87
4.6 Spatiotemporal evolution of maximum interacting pairs of vortical communities 91
4.6.1 Combustion noise 91
4.6.2 Aperiodic epoch of intermittency 92
4.6.3 Periodic epoch of intermittency 93
4.6.4 Thermoacoustic instability 95
4.6.5 Interim summary of community interactions present during different dynamical states 98
4.7 Insights into critical region detected for smart passive control 99
4.7.1 Network measures during mitigation of thermoacoustic instability . . . 105
4.8 Interim summary 107

CHAPTER 5 DYNAMICS OF DELAYED ACOUSTIC SELF-FEEDBACK IN THERMOACOUSTIC SYSTEMS 111

5.1 Delayed acoustic self-feedback in a bluff-body stabilised turbulent combustor 115
5.1.1 Route from TAI to the state of suppression 116

5.1.2 Analysis of changes in the coupled p' and $\dot{q}'$ oscillations 121
5.1.3 Spatiotemporal analysis of thermoacoustic power production in the turbulent flow field during different states of self-delayed feedback . . . 125
5.1.4 Interim summary for effects of delayed acoustic self-feedback on a bluff-body stabilised turbulent combustor 127
5.2 Delayed acoustic self-feedback in a horizontal laminar Rijke tube . . . 129
5.2.1 Effect of system and coupling parameters on the oscillation quenching in the self-coupled Rijke tube 131
5.2.2 Comparison between self-coupled and mutually coupled Rijke tube oscillators 135
5.3 Interim summary 136

CHAPTER 6 ASYMMETRICALLY FORCED SYSTEM OF TWO MUTUALLY COUPLED RIJKE TUBES 139

6.1 Response of a thermoacoustic oscillator to external forcing 144
6.2 Response of thermoacoustic oscillators mutually coupled with each other 147
6.3 Response of coupled identical thermoacoustic oscillators under asymmetric forcing 149
6.4 Forced response of coupled non-identical limit cycle oscillators 155
6.5 Mathematical model 158
6.5.1 Model results for a single oscillator and mutually coupled oscillators . . 160
6.5.2 Model results for coupled behavior of thermoacoustic oscillators under asymmetric forcing 163
6.6 Interim summary 167

CHAPTER 7 CONCLUSION AND OUTLOOK 171

7.1 Interplay between hydrodynamic and acoustic fields 171
7.2 Delayed acoustic self-feedback 173
7.3 Asymmetrically forced system of coupled thermoacoustic systems . . . 174
7.4 Suggestions for future work 174

APPENDIX A VORTICAL COMMUNITIES 177

A.1 Vorticity thresholding 177
A.2 The Louvain algorithm and its non-deterministic nature 178
A.3 Spatial coherence of vortical communities 182

APPENDIX B KERNEL DENSITY ESTIMATION 185

B.1 Univariate kernel density estimation 187
B.2 Bivariate kernel density estimation 187

APPENDIX C MEASUREMENT OF ACOUSTIC DECAY RATE 189

APPENDIX D MATHEMATICAL MODEL OF COUPLED NON-IDENTICAL RIJKE TUBES WITH ASYMMETRIC EXTERNAL ACOUSTIC FORCING 191

APPENDIX E EXTERNAL FORCING AND MUTUAL COUPLING 197

E.1 R^2 values for synchronisation boundaries 197
E.2 Period-3 oscillations exhibit by a single Rijke tube oscillator under external forcing 198
E.3 Effect of varying coupling tube parameters on the amplitude dynamics of an identical Rijke tubes coupled system 200

REFERENCES 201

CURRICULUM VITAE 241

DOCTORAL COMMITTEE 243

LIST OF TABLES

Table **Caption** **Page**

6.1 Model parameters kept constant throughout the numerical analysis of the reduced-order model. 160

E.1 R^2 values of least-square-fitted boundaries of the Arnold tongue. The subscripts l, r denote the left and right boundaries, respectively. 197

LIST OF FIGURES

Figure **Caption** **Page**

1.1 Global population size, estimates (1950-2022) and medium scenario with 95 per cent prediction intervals, 2022-2100. Adapted from World Population Prospects 2022 published by Department of Economic and Social Affairs Population Division, United Nations. 2

1.2 Approaches for reducing NO_x emissions utilising collected data within a U-shaped furnace with a power output of 29 kW. Reproduced with permission from Smoot *et al.* (1998) published by Elsevier Ltd.. 6

1.3 Findings from three comprehensive, extended-duration projects funded by the Gas Research Institute, which aimed to assess the effectiveness of gas reburning in curbing NO_x emissions in coal-fired power plants. Reproduced with permission from Smoot *et al.* (1998) published by Elsevier Ltd. 7

1.4 Illustration of the burner, denoting distinct pathways of volume flow through either the swirl generator or axial injection. Reproduced with permission from Reichel and Paschereit (2017) published by Elsevier Ltd. 9

1.5 Empirically established relationship between the characteristic chemical time and the equivalence ratio for a hydrocarbon fuel, from Zukowski (1978). Reproduced with permission from Lieuwen *et al.* (1998) published by Taylor & Francis. 11

1.6 Rocket engine rendered inoperable due to instability issues in the initial stages of the US rocket program. Reproduced with permission from Poinsot (2017) published by Elsevier Ltd. 13

1.7 An illustration of Rayleigh's criterion for pulsating combustion modes. Reproduced with permission from Ken *et al.* (1991) published by Cambridge University Press. 14

1.8 Flame and flow processes that drive thermoacoustic instabilities in gas turbines. Reproduced with permission from Lieuwen and Yang (2005) published by American Institute of Aeronautics and Astronautics, Inc. . 16

1.9 Photographs of failed burner assembly and combustor damage caused by thermoacoustic instability. Reproduced with permission from Lieuwen and Yang (2005) published by American Institute of Aeronautics and Astronautics, Inc. 19

1.10 Arrangements of can, can-annular, and annular combustors used in gas turbine engines. The blue portion indicates cooling flow path, the red portion indicates the combustion products flow path, and the light yellow-red portion indicates the path through which the initial flame propagates to different combustors. 20

1.11 Diagram depicting a standard can-annular combustion system in a gas turbine, including stator vanes of the first stage turbine. Reproduced with permission from Moon *et al.* (2020*b*) published by Elsevier Ltd. 21

1.12 (a) Schematic of an active closed loop control setup used with a premixed propane-air combustor, and (b) stability margins in the phase-gain plane of active instability control for different configurations of the combustor. The combustor remains silent when the thermoacoustic system lies inside the closed curves. Reproduced with permission from Lang *et al.* (1987) published by Elsevier Ltd. 24

1.13 (a) Schematic of the cross-section of a combustion chamber with the spatial location of the secondary steady air-jet injection ports, and (b) variation of p'_{rms} of thermoacoustic instability due to microjet air injection through different ports with respect to the ratio of total momentum flux. The ratio of total momentum flux is equal to momentum of square of velocity of microjet air injection (v_a^2) divided by the square velocity of main air at the combustor inlet (v_j^2). Reproduced with permission from Krishnan *et al.* (2021) published by Cambridge University Press. . . . 27

1.14 Time series of p' and $\dot{q}'$ (heat release rate) oscillations acquired from a bluff-body stabilised turbulent combustor operating in the states of (a) combustion noise, (b) intermittency, (c) phase-synchronisation limit cycle state, and (d) generalised-synchronisation limit cycle state. Reproduced with permission from Pawar *et al.* (2017) published by Cambridge University Press. 32

1.15 Structure of this thesis. In Chapter 4, we analyse the interplay between acoustic pressure oscillations and interactions between regions of intense vorticity in the reactive field of a turbulent combustor. In Chapter 5, we introduce delayed acoustic self-feedback to mitigate thermoacoustic instability in laminar and turbulent thermoacoustic systems. Finally, in Chapter 6, we show the results obtained from experiments and reduced-order modelling of asymmetrically forced two mutually coupled thermoacoustic systems. 41

2.1 (a) Undirected and (b) directed networks. 48

2.2 (a) Interactions between two vortical elements in the vorticity field calculated from the experimental velocity field in the turbulent combustor. $u_{i\to j}$ denotes the velocity induced by the node i on node j, and vice-versa. The reactants enter the reaction field from the left side. During the states of periodic epochs of intermittency and thermoacoustic instability, vortices are shed at acoustic pressure minima from the backward facing step. The cross-hatched region indicates the bluff body and the shaft holding the bluff body. (b) The expression used to calculate the induced velocity from node j to node i takes into account the area of node j, i.e., S_j, and the distance between the two nodes given by $|\boldsymbol{r}_j - \boldsymbol{r}_i|$. This expression for a discretized flow domain is obtained from equation 2.2 that is valid for a continuous flow domain. 49

2.3 An overview of community-based reduction of a complex network. (a) A random modular graph having six communities layout according to the Fruchterman-Reingold algorithm (Fruchterman and Reingold, 1991), and the corresponding adjacency matrix in (b). The modular nature of the network manifests as a block structure in the adjacency matrix. The original network can be decomposed into two sub-networks: (c) an inter-community network comprising edges present only across different communities, and (f) an intra-community network comprising edges present only within the individual communities. Each community is now considered as a single node. All the edges between any pair of communities shown in (c) can be summed up to obtain (d) a reduced inter-community network, and (e) the corresponding adjacency matrix. Similarly, all the edges within each community, as shown in (f), can be summed up to obtain (g) a reduced inter-community network, and (h) the corresponding adjacency matrix. 54

3.1 (a) Schematic diagram of the experimental set-up. We simultaneously acquire the acoustic pressure measurement, high-speed flame images, and high-speed PIV for the current study. (b-d) The time series of acoustic pressure fluctuations during the states of combustion noise, intermittency, and thermoacoustic instability. (c) Schematic of the combustor cross-section indicating the PIV regions of investigation for different dynamical states. (a) adapted from Krishnan *et al.* (2019*b*) with permission from Cambridge University Press. 59

3.2 The schematic of a turbulent bluff body stabilised combustor subjected to delayed acoustic self-feedback using a single coupling tube. 62

3.3 Schematic of a horizontal Rijke tube self-coupled using a connecting tube. The axial location (normalised by the length of the Rijke tube, L_{duct}) of the heater mesh is denoted by x_f, while the normalised axial locations of the ends of the connecting tube are given by x_{c1} and x_{c2}. Ball-type coupling valves are manually opened to establish acoustic feedback in the system. 64

3.4 Experimental setup of two mutually coupled horizontal Rijke tubes A and B. Rijke tube A is acoustically forced with 4 acoustic drivers attached to its sides. An extension duct in Rijke tube A is used for implementing frequency detuning in the system. 66

4.1 Overview of vortical network community-based framework to understand the interplay between the acoustic pressure fluctuations p' and inter-community interactions. (a) Schematic of cross-section of bluff-body stabilised turbulent combustor used in the current chapter. (b) Vorticity field is used to construct temporal directed and weighted vortical networks through Biot-Savart law (Taira *et al.*, 2016). (c, d) Vorticity thresholding used to include fluid elements with sufficiently high vorticity in the detection of vortical communities through Louvain algorithm (Blondel *et al.*, 2008). (e, f) Community-based network reduction technique (Gopalakrishnan Meena *et al.*, 2018) utilised to condense each vortical community to a single node at the respective community centroid. The reduced network and the corresponding adjacency matrix are show in (e) and (f), respectively. The correlations between p' oscillations and vorticity network dynamics are analysed using two network metrics : (g-ii) mean $A_{\mathrm{r,mean}}$, and (g-iii) maximum $A_{\mathrm{r,max}}$, of all inter-community interactions. (h, i) The locations of pairs of communities with $A_{\mathrm{r,max}}$ are utilised to understand the critical regions detected in the same experimental setup in previous studies. (j) Cross-sectional representation of the combustion chamber illustrates the spatial positions of secondary steady air-jet injection ports, with an inset showcasing the distribution of maximum interacting vortical communities observed during thermoacoustic instability. 75

4.2 The instantaneous vorticity fields (second and fifth rows) and the detected vortical communities (3rd and 6th rows) at time instants (i), (ii), (iii), and (iv) marked on the time series of acoustic pressure fluctuations (1st and 4th rows) during the states of (a) combustion noise, (b) thermoacoustic instability, (c) aperiodic epoch, and (d) periodic epoch of intermittency. Different vorticity thresholds were used for detecting vortical communities during different dynamical states. The discussions related to the selection of vorticity thresholds during different dynamical states is present in Appendix A. 76

4.3 (a) Time instances denoting the phases in one acoustic cycle during the state of thermoacoustic instability. (b) Phase-averaged fields of participation coefficients P corresponding to the nodes in communities having the maximum P values at the indicated phases of the acoustic cycle during the state of thermoacoustic instability. The participation coefficient quantifies the influence of a single node on communities other than its own. We also plot the phase-averaged distribution of vorticity in (c). 81

4.4 An overview of dimensionality reduction of vortical networks using communities. (a) All the communities are considered individual nodes, and (b) the edge weights between the "community" nodes are weighted according to the sum of inter-community interactions between the corresponding pair of communities. The adjacency matrix of the reduced network is shown in (c), with the intra-community edge weights corresponding to diagonal elements set to zero. We do not study intra-community interactions in the present chapter. 84

4.5 Variation of the network measures: (i) mean ($A_{\mathrm{r,mean}}$) and, (ii) maximum ($A_{\mathrm{r,max}}$) of all inter-community interactions during the states of (a) combustion noise, (b) intermittency, and (c) thermoacoustic instability, respectively. The acoustic pressure time series is shown in blue, whereas the time series showing the mean and maximum of all inter-community interactions are shown in red and black, respectively. 86

4.6 Histograms showing the distributions of (a) magnitude of p' fluctuations, and (b) vorticity values present in the flow field during the three dynamical states (legend of the distributions is shown on top right of the figure). The mean values of all the inter-community interactions ($A_{\mathrm{r,mean}}$) are shown in (c). $A_{\mathrm{r,mean}}$ is calculated by considering all the detected vortical communities. The distributions of the area of all the detected vortical communities and the vorticity of the fluid elements matching with the vortical communities are shown in (d) and (e), respectively. The gaps in the distribution of the vorticity values shown in (e) correspond to the vorticity threshold used to detect vortical communities (ω = 456 s^{-1}, 380 s^{-1}, and 843 s^{-1} for the states of combustion noise, intermittency, and thermoacoustic instability, respectively). The maximum values of all the inter-community interactions ($A_{\mathrm{r,max}}$) present during the three dynamical states are shown in (f). $A_{\mathrm{r,max}}$ is calculated by extracting the pair of communities with the largest inter-community interaction at each time step. The distribution of the area of such communities (with the maximum inter-community interaction) and the vorticity of the fluid elements matching with these vortical communities are shown in (g) and (h), respectively. 88

4.7 Time series showing the variation of (a) mean ($A_{\mathrm{r,mean}}$), and (b) maximum ($A_{\mathrm{r,max}}$) of all inter-community interactions at three representative points marked (i-xii) during the state of combustion noise. The acoustic pressure fluctuations are marked in blue. The vorticity field and the corresponding spatial distribution of the inter-community in- and out-strengths between the pair of communities with the maximum inter-community interaction at each of the representative time instants marked in (a-b) are shown in (c). The grey regions represent other vortical communities that have lower inter-community interactions. The colorbars represent the inter-community in-strengths (k_{in}) and out-strengths (k_{out}), respectively. The direction of the maximum inter-community interaction is from the community marked with k_{out} values to the community marked with k_{in} values. k_{out} and k_{in} denote the sum of in- and out-edge weights present between communities with maximum inter-community interactions, respectively. The aperiodic nature of the network measures reflects the aperiodic nature of hydrodynamic interactions present in the reaction field. Due to the shedding of significant vortices from the upstream tip of the bluff-body, the pair of communities with the maximum inter-community interaction are always present above the bluff body. 90

4.8 Time series showing the variation of (a) mean ($A_{\mathrm{r,mean}}$), and (b) maximum ($A_{\mathrm{r,max}}$) of all inter-community interactions at three representative points marked (i-iii) during an aperiodic epoch of intermittency. The vorticity field and the corresponding spatial distribution of the inter-community in- and out-strengths between the pair of communities with the maximum inter-community interaction at each of the representative time instants marked in (a-b) are shown in (c). The aperiodic nature of vortical interactions present in the reaction field causes the network measures to be aperiodic. Correspondingly, there is no specific trend in the position of the pair of communities with maximum inter-community interaction, as seen in (c). 92

4.9 Time series showing the variation of (a) mean ($A_{\mathrm{r,mean}}$), and (b) maximum ($A_{\mathrm{r,max}}$) of all inter-community interactions at fifteen representative points marked (i-xv) during a periodic epoch of intermittency. The vorticity field and the corresponding spatial distribution of the inter-community in- and out-strengths between the pair of communities with the maximum inter-community interaction at each of the representative time instants marked in (a-b) are shown in (c). The red circles in (c) indicate the downstream convection of the coherent structure shed from the backward-facing step at the time instants (ii) and (xii). The location of the community with the maximum outward influence matches with the location of the downstream moving coherent structure indicated with red circles during time instants (ii-vii) and (xiii-xv). Subsequently, the coherent structure gets dissipated into the reaction field. The shedding and downstream convection of the coherent structure repeats during each acoustic cycle within the periodic epoch of intermittency, and is reflected in the periodic nature of $A_{\mathrm{r,max}}$ shown in (b). 94

4.10 Time series showing the variation of (a) mean ($A_{\text{r,mean}}$), and (b) maximum ($A_{\text{r,max}}$) of all inter-community interactions at fifteen representative points marked (i-xv during the state of thermoacoustic instability. The vorticity field and the corresponding spatial distribution of the inter-community in- and out-strengths between the pair of communities with the maximum inter-community interaction at each of the representative time instants marked in (a-b) are shown in (c). The red circles in (c) indicate the downstream convection of the coherent structure shed from the backward-facing step at the time instants (i) and (x). The location of the community with the maximum outward influence matches with the location of the downstream moving coherent structure indicated with red circles during the time instants (i-vii) and (xi-xv). Subsequently, the coherent structure gets dissipated into the reaction field. The shedding and downstream convection of the coherent structure repeats itself during each acoustic cycle present within the state of thermoacoustic instability, and is reflected in the periodic nature of $A_{\text{r,max}}$ shown in (b). 96

4.11 (i) The distribution of the spatial location of vortical communities with the maximum inter-community interactions during the states of (a) combustion noise, (b) intermittency, and (c) thermoacoustic instability. n($\text{Ci}_{\text{r,max}}$) denotes the number of overlapped vortical communities used to plot the distribution of the spatial location of vortical communities with the maximum inter-community interactions. (ii) Plot of kernel smoothed intensity function of the maximum inter-community interactions. Consistent with the results discussed in Fig. 4.8(c), most of the communities with maximum inter-community interactions are present above the bluff-body during the state of combustion noise. This is related to the significant shedding of coherent structures from the upstream tip of the bluff body during the state of combustion noise. The spatial region indicating the maximum probability of finding the most influential communities shifts upstream during the state of intermittency and thermoacoustic instability. These new regions observed in (b-c) are detected via community-based dimensionality reduction of vortical networks and are consistent with the critical regions detected in Roy *et al.* (2021). 101

4.12 (a) The cross-section of the combustion chamber showing the microjet injector locations. The coloured figure in the inset shows the region with maximum-interacting vortical communities detected during the state of thermoacoustic instability. (b-c) Variation of the network measures: mean ($A_{\mathrm{r,mean}}$) and, maximum ($A_{\mathrm{r,max}}$) of all inter-community interactions during the state of suppression of thermoacoustic instability with microjet injection through injector numbered 1. The time series of acoustic pressure fluctuations are shown in blue, whereas the time series showing the mean and maximum of all inter-community interactions are shown in red and black, respectively. The network measures exhibit aperiodicity during the state of suppression, indicating the aperiodic nature of hydrodynamic interactions present when air microjet is used to mitigate thermoacoustic instability. 106

5.1 A representative time series of acoustic pressure fluctuations p' illustrating the effect of delayed acoustic self-feedback on the limit cycle oscillations. The enlarged portions show the dynamics of p' during different stages of delayed acoustic self-feedback. The dimensions of the coupling tube are $L_c = 1400$ mm and $d_c = 25.4$ mm. 116

5.2 Effect of delayed acoustic self-feedback, induced by increasing the length of the coupling tube L_c, on the suppression of acoustic pressure fluctuations $\Delta\bar{p}$. The regions marked in I, II, and III denote the partial suppression, complete suppression, and no suppression, respectively, of LCO ($p'_{0,\mathrm{rms}} = 3200$ Pa). The values of d_c is fixed at 25.4 mm. 117

5.3 (i) Time series, (ii) power spectrum, and (iii) scalograms of p' as the system behavior transitions from a state of (a) TAI to (e) complete suppression of oscillations via (b-d) intermittency. A vertical dotted red line in (ii) indicates the natural frequency of TAI in the absence of delayed acoustic self-feedback. Zoomed regions of plots are shown in insets, where The green and red shaded regions in i-(d) highlight the aperiodic and periodic epochs of p' during the state of intermittency. . . 120

5.4 The percentage suppression of p' signals ($\Delta\bar{p}$) when delayed acoustic self-feedback is applied to (a) TAI of different amplitudes ($p'_{0,\mathrm{rms}}$) for constant values of $L_c = 1400$ mm and $d_c = 25.4$ mm, and (b) TAI of two amplitudes ($p'_{0,\mathrm{rms}} \approx 3400$ Pa and 4100 Pa) for different coupling tube diameters ($d_c = 6.35, 9.525, 12.7, 19.05$, and 25.4 mm) at a fixed value of $L_c = 1400$ mm. 121

5.5 CWT plots between $\dot{q}'$ & p' signals and the temporal variation of their phase difference $\Delta\phi$, calculated at the dominant frequency f_d (indicated by a horizontal red line and an arrow in each CWT plot), for (a) the state of TAI in the absence of delayed acoustic self-feedback and (b-d) in the presence of delayed acoustic self-feedback in the combustor with increasing values of L_c. The inset in (d) shows a magnified view of a phase jump. The value of d_c is kept constant at 25.4 mm. 122

5.6 The variation of PLV and Pearson's correlation coefficient ρ between the global heat release rate and acoustic pressure fluctuations under the influence of delayed acoustic self-feedback through connecting tubes of different lengths. The internal diameter of the coupling tube is kept constant at $d_c = 25.4$ mm, and p'_0 is kept constant at 3400 ± 150 Pa. . . 124

5.7 (i) Time instants of p' time series, and (ii - vii) instantaneous spatial distribution of local Rayleigh Index for the state of (a) TAI in the absence of delayed acoustic self-feedback, and for (b-e) different states of delayed acoustic self-feedback. The internal diameter of the coupling tube is kept constant at $d_c = 25.4$ mm, and p'_0 is kept constant around 3400 Pa. 126

5.8 Variation of the RMS value of acoustic pressure fluctuations with heater power in the forward and reverse paths for (a) the uncoupled Rijke tube ($p'_{0,\mathrm{rms}}$) and (b) the self-coupled Rijke tube (p'_{rms}). The normalised length of the coupling tube is $L/L_{\mathrm{duct}} = 1.17$ and its internal diameter is $d = 8$ mm in (b). The introduction of self-coupling shifts the Hopf point [marked as 'H' in (a)] and the fold point [marked as 'F' in (a)] to higher values of heater power. Air flow rate of 120 SLPM (or 0.002 m^3/s) is maintained in the Rijke tube for both the plots. 130

5.9 The amplitude response of the Rijke tube when self-coupling is induced for (a) $p'_{0,\mathrm{rms}} = 120$ Pa, and (b) $p'_{0,\mathrm{rms}} = 320$ Pa. The normalised change in the amplitude suppression $\Delta p'_{\mathrm{rms}}/p'_{0,\mathrm{rms}}$ is measured for different values of L_c/L_{duct} and d_c. A large parametric region of amplitude death (AD) is observed for lower value of $p'_{0,\mathrm{rms}}$ in (a); while for higher values of $p'_{0,\mathrm{rms}}$ in (b), the region of amplitude death shrink and is observed only for around $L/L_{\mathrm{duct}} \approx 1$ and $L/L_{\mathrm{duct}} \approx 3$. Air flow rate is maintained at 80 SLPM (or 0.00133 m^3/s) in the Rijke tube. 132

5.10 Amplitude response of the self-coupled Rijke tube for different values of the normalised length of coupling tube (L_c/L_{duct}) and the RMS value of the limit cycle oscillations in the uncoupled state ($p'_{0,\mathrm{rms}}$). The internal diameter of coupling tube (d_c) is fixed at (a) 4 mm, and (b) 8 mm. Air flow rate is maintained at 80 SLPM (or 0.00133 m^3/s) in the Rijke tube for both the plots. 133

5.11 Schematics of the Rijke tube and the experimentally obtained time series of the acoustic pressure fluctuations (p') depict the effect of coupling locations on the suppression of limit cycle oscillations (a) when the Rijke tube is uncoupled, (b, c) when the Rijke tube is coupled such that both ends of the coupling tube are fixed at the same distance (x_c) of 0.82 and 0.55 from the inlet, respectively, (d) when the ends of the coupling tube are at separate locations away from the centre of the Rijke tube ($x_{c1} = 0.12$ and $x_{c2} = 0.82$) and (e) when one end of the coupling tube is closer to the centre ($x_{c2} = 0.55$) while the other end is away from the centre of the Rijke tube ($x_{c1} = 0.12$). The red dashed line indicates the heater mesh located at $x_f = 0.26$. All distances are non-dimensionalised by the length of the Rijke tube, $L_{\mathrm{duct}} = 1.04$ m. Other parameters are maintained as $p'_{0,\mathrm{rms}} = 200$ Pa, $L_c = 95$ cm, and $d_c = 4$ mm in all of the plots. 134

5.12 Trends in the relative suppression of the acoustic pressure oscillations ($\Delta p'/p'_{0,\mathrm{rms}}$) in two mutually coupled identical Rijke tubes and in a self-coupled Rijke tube with change in the normalised length of the coupling tube (L_c/L_{duct}) in experiments (d_c = 8 mm and $p'_{0,\mathrm{rms}}$ = 320 Pa). The highlighted green region indicates the range of L_c/L_{duct} where the self-coupled Rijke tube exhibits greater amplitude suppression than the mutually coupled system. 136

6.1 Forced response of a single Rijke tube. (a,c) The phase response shown in terms of PLV and (b,d) amplitude response in terms of fractional change in the amplitude of LCO in the Rijke tube for (a,b) $p'_{0,\mathrm{rms}}$ = 120 Pa and (c,d) $p'_{0,\mathrm{rms}}$ = 200 Pa for different values of $\bar{A}_f$ and f_f. The synchronisation boundaries in (a-d) are obtained through least-square-fit of points where $PLV = 0.98$. The R^2 values for the least-square fitting are given in Section I of the Supplemental Material. The region of forced synchronisation decreases with increase in $p'_{0,\mathrm{rms}}$ (a,c), while quenching of LCO is observed only for $f_f < f_0$ (b,d). Green region around $f_f/f_0 = 1$ in (b,d) indicates the amplification of LCO above twice the value of unforced amplitude. 145

6.2 Coupled response of two Rijke tubes. Fractional change in the amplitude of LCO for Rijke tube A and B as functions of the frequency detuning ($\Delta f_0 = |f_0^A - f_0^B|$) and length of the connecting tube (L_c) for (a,b) $p'_{0,\mathrm{rms}}$ = 120 Pa and (c,d) $p'_{0,\mathrm{rms}}$ = 200 Pa in both the oscillators. The region of AD and PAD are indicated. At other regions in the plots, LCO is observed at reduced amplitude due to coupling. The parametric region exhibiting AD shrinks in size as $p'_{0,\mathrm{rms}}$ is increased from 120 Pa to 200 Pa. 148

6.3 (a)-(c) Time series of p' in Rijke tubes A (blue) and B (brown) sequentially illustrating the effect of coupling and forcing on the amplitude of LCO in both the Rijke tubes for different coupling and forcing parameters. In (a,c), the Rijke tubes are non-identical and have a frequency difference of 10 Hz. (i,ii) The enlarged portions of the desynchronised LCO and the state of PAD in (c), respectively. The coupling of oscillators always leads reduction in the amplitude of LCO, while forcing of oscillators can have both reduction or amplification effects, depending on the values of coupling and forcing parameters. The common parameters in all plots are: d_c = 10 mm, f_f = 140 Hz, and A_f = 30 mV. 150

6.4 Response of coupled, identical oscillators to asymmetric forcing. (a,b) Amplitude and (c,d) phase response as functions of the forcing amplitude (A_f) and length of the coupling tube (L_c). (e-g) Representative time series of p' for the points indicated in (a) depicting difference in the response of Rijke tube A and B. Complementary forcing and coupling enhances the region of L_c over which the suppression of LCO is observed in both the oscillators. Forcing is ineffective in synchronisation of LCO in Rijke tube B (the black region in (d) denotes the complete desynchrony of LCO in Rijke tube B with the forcing signal), while the region of quenching of LCO in Rijke tube A nearly coincides with the region of forced synchronisation ($PLV \approx 1$). The common parameters in all the plots are: $p'_{0,\text{rms}} = 200$ Pa, $f_f = 100$ Hz ($f_f/f_0 \approx 0.6$), $\Delta f_n = 0$ Hz, and $d_c = 1$ cm. 151
6.5 Amplitude and phase response (black lines) of Rijke tubes A and B when coupled identical oscillators are subjected to asymmetric forcing for (a,b) $p'_{0,\text{rms}} = 120$ Pa and (c,d) $p'_{0,\text{rms}} = 200$ Pa. The LCO in Rijke tube A is externally forced through the acoustic drivers. The region of forced synchronisation is wider for Rijke tube A than that observed for Rijke tube B, whereas a much larger magnitude of suppression of LCO is observed in Rijke tube B as compared to that in Rijke tube A. Green region around $f_f/f_0 = 1$ indicates the amplification of LCO above twice the value of LCO amplitude in the uncoupled-unforced Rijke tubes. Experimental conditions: $f^A_{n0} = f^B_{n0} \approx 160$ Hz, $L_c = 105$ cm, $d_c = 1$ cm. 154
6.6 The amplitude and phase response (black lines) of Rijke tubes A and B when coupled non-identical oscillators are subjected to asymmetric forcing for (a,b) $p'_{0,\text{rms}} = 120$ Pa and (c,d) $p'_{0,\text{rms}} = 200$ Pa. The effect of forcing is less effective in synchronizing and quenching of LCO in Rijke tube B, while it shows regions of forced synchronisation and quenching of LCO in Rijke tube A. The common parameters in all the plots are: $\Delta f_0 = 10$ Hz, $L_c = 105$ cm, $d_c = 1$ cm. 156
6.7 (a) The phase response and (b) the amplitude response obtained from the model of a single Rijke tube under external forcing. The synchronisation boundaries are obtained through a least-square-fit of points where $PLV = 0.98$. The Arnold tongue and extent of asynchronous quenching from the model show a qualitative match with the experimental results in Fig. 6.1. 161
6.8 Bifurcation plots between frequency mismatch between the two Rijke tube model oscillators and τ. K_d and K_τ are kept constant at 1.0 and 0.2, respectively. The dark red region in both the plots represent regions of AD observed in the model oscillators. At other places, LCO is observed at reduced amplitude due to coupling. 162

6.9 (a,b) Amplitude and (c,d) phase response of coupled, identical oscillators under asymmetric forcing for different values of τ and A_f. Amplitude response is indicated by the fractional change in the amplitude of LCO ($\Delta\bar{p}$) while phase response is quantified by the PLV between p' and forcing signal. For $\tau > 0.4$ and $A_f > 1.5$, large suppression in the amplitude of LCO is observed in the two Rijke tubes. 163
6.10 The amplitude response and overlapped Arnold tongue for identical, coupled Rijke tubes from the mathematical model. External forcing is applied to Rijke tube A. The synchronisation boundaries are obtained through least-square-fit of points where $PLV = 0.98$. The coupling parameters are: $K_d = 1.0$, $K_\tau = 0.2$ and $\tau = 0.4$. 164
6.11 The amplitude response and overlapped Arnold tongue for non-identical, coupled Rijke tubes from the mathematical model. External forcing is applied to Rijke tube A. The synchronisation boundaries in are obtained through least-square-fit of points where $PLV = 0.98$. The coupling parameters are: $K_d = 1.0$, $K_\tau = 0.2$ and $\tau = 0.4$. 166

A.1 (a) Variation of mean positive ($\overline{\omega}_+$) and mean negative ($\overline{\omega}_-$) vorticity threshold values with respect to the total circulation threshold (Γ_{th} in %) for the states of (i) combustion noise, (ii) intermittency, (iii) thermoacoustic instability, and (iv) suppression through air microjet injection. The fluid elements with vorticity $\omega \in [\overline{\omega}_-, \overline{\omega}_+]$ are disregarded to exclude the bottom Γ_{th} % of the total circulation present in the reaction field, thus capturing the influential regions of the flow. The $\overline{\omega}_+$ and $\overline{\omega}_-$ values present on the green band are subsequently used as thresholds while using the Louvain algorithm to detect vortical communities. (b) Variation of the mean of area percentage of the reaction field $\overline{A}_{\mathrm{th}}$ occupied by the vortical communities. We do not consider the area of the bluff-body mask while calculating the percentage w.r.t. the total area of the reaction field. (c) Variation of the average number of communities detected for each circulation threshold value. For all the cases, the resolution parameter γ used in the Louvain algorithm is kept consistent at 1 (Gopalakrishnan Meena *et al.*, 2018; Gopalakrishnan Meena and Taira, 2021). 179
A.2 (a) Plot of the standard deviation of modularity values, (b) coefficient of variation of the number of communities, and (c) maximum normalised variation of information calculated through 100 implementations of the Louvain algorithm at each time instant during the states of (i) combustion noise, (ii) intermittency, (iii) thermoacoustic instability, and (iv) suppression of thermoacoustic instability through air microjet injection. 180
A.3 Distributions of cohesion factor indicating the spatial coherence of (a) all vortical communities, and (b) vortical communities with maximum inter-community interactions during the three dynamical states. 183

B.1 Estimated kernel density for seven random data points selected from a normal distribution. The Gaussian kernels around each of the data points are shown with different colours. 187

B.2 (a) Two-dimensional histograms for fifty data points randomly selected from a bivariate normal distribution, and (b) the corresponding estimated kernel density distribution. 188

C.1 Acoustic pressure oscillations before and after the acoustic driver is switched off abruptly under no-flow conditions. The brown line denotes the upper envelope of the decaying acoustic pressure oscillations, and is used to calculate the decay rate. The exponential curve fitted to the decaying portion is shown in black. 190

E.1 Time series of (a) the acoustic pressure fluctuations and (b) instantaneous phase difference between the pressure and the forcing signal. (c) The power spectrum, (d) the reconstructed phase portrait, and (e) the first return map of the forced acoustic pressure oscillations in a single Rijke tube exhibiting LCO of amplitude $p'_{0,\mathrm{rms}} = 200$ Pa. The forcing is applied at $f_f/f_{n0} = 0.69$ and $\bar{A}_f = 0.65$. As a result, the acoustic pressure fluctuations show period-3 oscillations and, hence, remain desynchronised with the forcing signal, causing a lower value of PLV. The period-3 oscillations are confirmed from the presence of three-looped attractor in the phase space and three fixed points in the return map. . . 198

E.2 Experimental two-parameter bifurcation plots showing the variation of $\Delta p'_{\mathrm{rms}}/p'_0$ for different values of coupling tube length L and internal diameter d in identical Rijke tubes ($\Delta f_0 = 0$ Hz). The maximum suppression obtained is around 50% in Rijke tube A for $L_\mathrm{c} = 100$ cm and $d_\mathrm{c} = 10$ mm. 200

GLOSSARY

Amplitude Death	Phenomenon in which the oscillatory behavior of a state variable ceases completely as a consequence of coupling.
Asynchronous quenching	Type of asynchronous action that consists essentially in quenching a self-sustained oscillation by imposing an externally produced high-frequency perturbation on the oscillator.
Delayed acoustic self-feedback	Acoustic feedback, proportional to the deviation of the current state of an oscillator from its state τ time delay in the past, applied by the oscillator on itself.
Intermittency	Dynamical state consisting of apparently random epochs of periodic and aperiodic dynamics.
Limit Cycle Oscillations	Oscillations corresponding to a closed trajectory in phase space having the property that at least one other trajectory spirals into it either as time approaches infinity or as time approaches negative infinity.
Partial Amplitude Death	Situation when instead of all variables reaching a stationary state, only some of them do as a consequence of coupling.
Synchronance	Simultaneous occurrence of synchronisation and resonance in the frequency locking region causing shooting up of the response amplitude.
Thermoacoustic instability	Self-sustained, large amplitude oscillations of pressure and velocity arising primarily through an interaction of sound waves in a confined space with the unsteady heat release rate caused by combustion.

ABBREVIATIONS

AD	Amplitude Death.
CWT	Cross Wavelet Transform.
LCO	Limit Cycle Oscillations.
MFC	Mass Flow Controllers.
NO_x	Nitrogen Oxides.
PAD	Partial Amplitude Death.
PIV	Particle Image Velocimetry.
PLV	Phase Locking Value.
RMS	Root Mean Square.
TAI	Thermoacoustic Instability.
TARA	ThermoAcoustic Rig for Axial Instability.

NOTATION

$\Delta\phi$	phase difference
Δf	frequency detuning
$\dot{m}_a$	air flow rate
$\dot{m}_f$	fuel flow rate
$\dot{q}'(t)$	temporal variation of global heat release rate fluctuations
$\dot{q}'(x, y, t)$	spatiotemporal variation of heat release rate fluctuations
λ	wavelength of acoustic mode
ω	vorticity
$\overline{\omega}_\phi$	phase averaged vorticity
$\overline{A}_f$	A_f/p_0
$\overline{P}_\phi$	phase averaged participation coefficient
ϕ	equivalence ratio
ϕ	phase in an acoustic periodic cycle
ρ	covariance
τ	time delay due to coupling
A_f	forcing amplitude
f_0	natural frequency
f_f	forcing frequency
k_{in}	inter-community in-degree strength of nodes

k_{out}	inter-community out-degree strength of nodes
p', $p'(t)$	acoustic pressure fluctuations
$p'_{0,\mathrm{rms}}$	root mean square value of acoustic pressure fluctuations during the state of thermoacoustic instability
p'_{rms}	root mean square value of acoustic pressure fluctuations after coupling
p_0	reading obtained from piezoelectric transducer (in millivolts) corresponding to $p'_{0,\mathrm{rms}}$
P_i	participation coefficient of node i
T	time period of an acoustic periodic cycle
t	time
u', $u'(t)$	acoustic velocity fluctuations
$u_{i\rightarrow j}$	induced velocity from node i to node j
$\mathrm{A}_{\mathrm{r,max}}$	maximum of the reduced adjacency matrix values
$\mathrm{A}_{\mathrm{r,mean}}$	mean of the reduced adjacency matrix values
d_{c}	internal diameter of the coupling tube
L_{c}	length of the coupling tube
$\mathrm{L}_{\mathrm{duct}}$	length of the TARA combustor, or the horizontal Rijke tube
x_{c}	position of the coupling tube attachment

CHAPTER 1

INTRODUCTION

1.1 POPULATION EXPLOSION AND ENVIRONMENTAL CONCERNS

According to the United Nations population projections shown in Fig. 1.1, the current global population (about 7 billion people) will increase to 9.6 billion by 2050 and more than 10 billion by 2100 (Victor Gaigbe-Togbe *et al.*, 2022). The energy consumption is therefore anticipated to increase in line with the requirement for energy, from 13 terawatts (TW) presently to 28 TW in 2050 and 46 TW in 2100 (Lewis, 2007). Fossil fuels still produce 84.3% of the world's energy despite the emergence of other cleaner forms of energy (Ritchie *et al.*, 2020). However, fossil fuels are scarce and not distributed equally throughout the world, which causes issues with energy security and geopolitical unrest. Additionally, they are linked to pollution and global warming. Despite these disadvantages, it is nevertheless imperative to use fossil fuels efficiently in the context of emerging technologies.

A steadily increasing population and a growth in gross domestic product (GDP) across a wide variety of geographic, economic, and social settings correlate well with a rising demand for mobility. An essential aspect of this correlation is that, as the need for movement increases, travellers tend to choose quicker modes of transportation. As a result, high speed transportation, such as aviation, will continue to play an increasingly significant role and may account for slightly more than a third of the world's passenger traffic volume within the next thirty years (Lee *et al.*, 2004). According to the available data, the global aviation industry transported approximately 4.1 billion people in 2017. Fifty six million tonnes of goods were transported via 37 million commercial flights. Daily, aircrafts facilitate the transportation of more than 10 million passengers and around USD 18 billion worth of products (ICAO, 2022). The latest predictions project

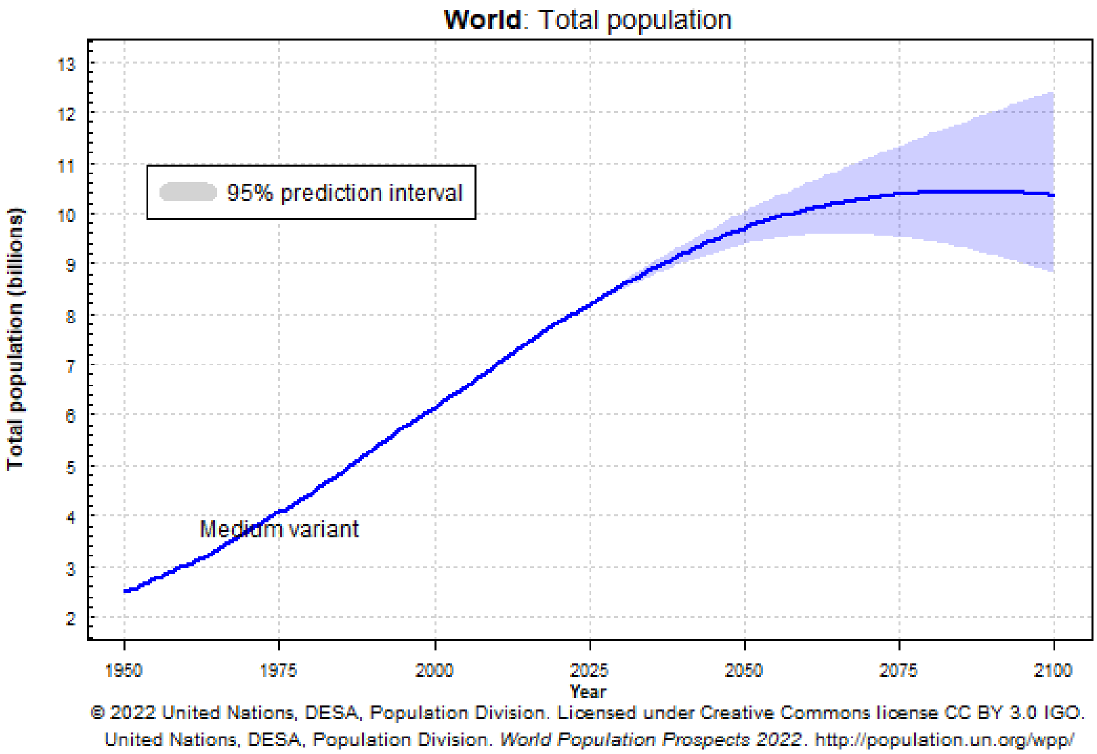

Figure 1.1: Global population size, estimates (1950-2022) and medium scenario with 95 per cent prediction intervals, 2022-2100. Adapted from World Population Prospects 2022 published by Department of Economic and Social Affairs Population Division, United Nations.

the demand for air transport to gradually rise to an average annual growth rate of 4.3% over the next two decades (ICAO, 2022).

The idea that man might someday be able to fly has long fascinated the humans. Ingenious minds have worked hard to convert the fantasy of flight into a reality, using everything from Icarus' wings to Da Vinci's flying inventions to lighter-than-air balloons. However, what was missing was a means of propulsion. With the invention of the internal combustion engine in the early 20th century, this was finally possible. This engine provided a source of compact and portable power, enabling man to triumph over the pull of gravity. When World War II ended, the aircraft piston engine was already a well-developed power plant starting to undergo incremental improvements. The invention of the gas turbine engine made significant improvements in aircraft performance possible. For the last many decades, gas turbine engines have been the workhorse for the billion-dollar aviation industry.

Gas turbines also play a preeminent role in stationary power generation. Gas turbines are the most viable alternative at power generation levels above 50 MW due to their comparatively low capital, operating, and maintenance costs.

1.2 NO_X EMISSION PROBLEMS IN GAS TURBINE ENGINES

The increase in the operation of gas turbines, both for land-based power generation and aviation, has significant repercussions for the environment worldwide, particularly in relation to climate change. Noise, poor air quality primarily due to ozone formation, particulate levels, and exhaust gas emissions are all acknowledged as severe impacts on a local to global scale. The combustion of hydrocarbons present in fossil fuels generates pollutant emissions, including greenhouse gases such as carbon dioxide (CO_2) and pollutants such as unburned hydrocarbons (UHC), nitrogen oxides (NO_x), and carbon monoxide (CO), as well as particles such as soot (Victor Gaigbe-Togbe *et al.*, 2022; Sawyer, 2009).

1. SO_2 emissions at the engine exhaust occur predominantly as gaseous SO_2, however, a minor amount of the fuel sulphur (estimated at 3.3% by Wayson *et al.* (2009)) is often expelled as a variety of heavier sulphur species classified as volatile particulate matter.

2. NO_x emissions consist mostly of NO and NO_2. At idle conditions, NO_x emissions have approximately 50% NO and 50% NO_2, whereas at high power, approximately 90% of NO_x is in the form of NO.

3. Unburned hydrocarbons contain a wide range of hydrocarbons, from huge fuel molecules to very light hydrocarbons, as well as numerous species classed as *hazardous air pollutants* (HAPs) due to their toxicity or carcinogenicity (Spicer *et al.*, 1994; Herndon *et al.*, 2009).

4. Particulate matter consists of both nonvolatile soot (small carbonaceous particles that comprise visible smoke) and volatile hydrocarbons and sulphur oxides that condense as the engine exhaust plume cools and mixes with ambient air.

A trade-off has to be maintained between the emissions and efficiency of a gas turbine engine. The operational temperature of a turbine is a crucial factor in determining its fuel-to-power efficiency. Elevated temperatures correspond to increased efficiency, potentially resulting in enhanced cost-effectiveness of operations. However, certain critical metals within the turbine exhibit a limited capacity to endure high temperatures, often ranging from 1300 to 1500°C. Manufacturers want to design machines with greater firing temperatures to improve the total thermodynamic efficiency. However, increased firing temperatures result in increased combustion temperatures, which produces more NO_x.

The significance of nitrogen oxides in tropospheric chemistry stems from their role as a precursor to ozone (O_3) generation (Crutzen, 1974). The impact of NO_x emissions on ozone production is particularly noteworthy in the high troposphere, where the background environment is very pristine. In this context, any additional NO_x emissions can have a substantial effect on O_3 generation. Commercial aircraft are a substantial contributor to the emission of NO_x in the upper troposphere. These emissions exhibit a greater efficiency, approximately four times higher, in the production of ozone compared to emissions originating from terrestrial sources (Hodnebrog *et al.*, 2011). Over four decades ago, concerns were raised on the emissions of O_3 originating from subsonic and supersonic aircraft of the then generation, while the aircraft operated inside the upper troposphere and lower stratosphere (Hidalgo and Crutzen, 1977). These emissions were deemed significant due to their potential to induce local alterations in O_3 levels, with the possibility of causing a percentage change of several percentages (Hidalgo and Crutzen, 1977). Multiple studies have later demonstrated that emissions of nitrogen oxides (NOx) from aviation have the propensity to enhance the development of ozone in the upper troposphere (Brasseur *et al.*, 1998; IPCC, 1999; Grewe *et al.*, 2002; Köhler *et al.*, 2008; Khodayari *et al.*, 2014).

Emissions of NO_x into the troposphere cause a short-term increase in photochemical ozone formation (resulting in a positive climate forcing or warming) and a long-term increase in atmospheric methane oxidation via interaction with the hydroxyl radical (OH) (resulting in a negative climate forcing or cooling) (Fuglestvedt *et al.*, 1999; Masson-Delmotte *et al.*, 2021). Additional research has demonstrated that the introduction of NO_x emissions at elevated elevations inside the stratosphere has the potential to contribute to the degradation of the ozone layer in the stratosphere (Wesocky and Prather, 1991). At lower altitudes, aviation exhaust products may contribute to acid rain and ground-level smog formation (Koo, 2011).

As a result of concerns regarding the impact of NO_x emissions on surface air quality, the International Civil Aviation Organization (ICAO) issued the first certification standard to restrict aircraft NO_x emissions in 1981.

1.3 NO_X EMISSION MITIGATION TECHNIQUES

The strategies for controlling and mitigating NO_x emissions (Fig. 1.2) can be roughly divided into two categories. The first category consists of techniques for eliminating NO_x emissions from combustion by-products. In contrast, the second category comprises techniques for minimising the formation of NO_x during combustion.

One of the ways to eliminate NO_x from combustion exhaust involves the elimination of NO_x via fuel reburning (Fig. 1.3), in which extra fuel is utilised to burn the byproducts of the initial combustion to transform NO_x into N_2 (Myerson, 1975; Smoot *et al.*, 1998; Hill and Smoot, 2000). Another post-flame technique for control of NO_x emissions is through selective catalytic reduction (SCR) and selective non-catalytic reduction (SNCR). SCR involves the injection of anhydrous ammonia (NH_3), aqueous ammonia (NH_4OH), or urea near the combustor exit, and reacted onto a catalyst. Commercial SCR systems have been proven to reduce NO_x emissions by 70-95% in big utility boilers, industrial boilers, and municipal solid waste boilers (Smoot, 1993). Active catalytic components are typically oxides of base metals (such as vanadium, molybdenum, and tungsten), zeolites,

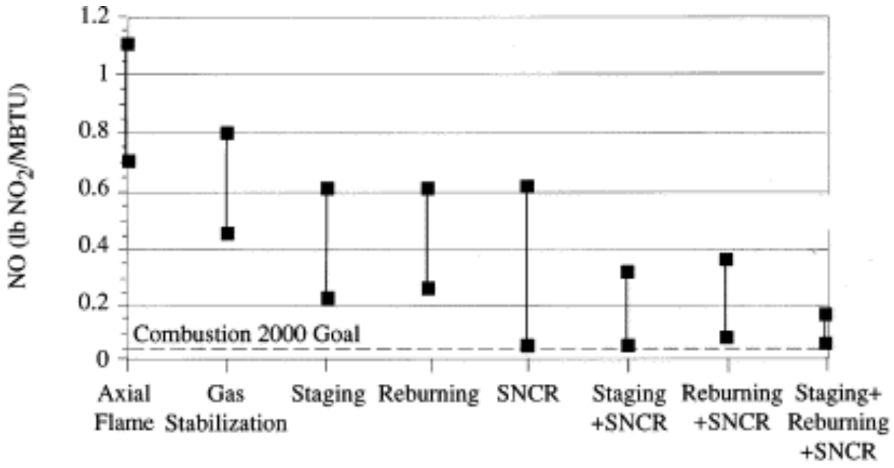

Figure 1.2: Approaches for reducing NO_x emissions utilising collected data within a U-shaped furnace with a power output of 29 kW. Reproduced with permission from Smoot *et al.* (1998) published by Elsevier Ltd..

or various precious metals (Gao *et al.*, 2010; Chen *et al.*, 2010). SCR catalysts can also be composed of various porous ceramic materials used as a support, such as titanium oxide. Another catalyst based on activated carbon that is effective for the elimination of NO_x at low temperatures was also developed (Marbán *et al.*, 2003; Samojeden and Grzybek, 2016; Li *et al.*, 2020). With SNCR, ammonia is injected in a higher temperature zone further upstream in the furnace (Lyon, 1987). Unfortunately, SNCR is only effective over a narrow temperature range, precluding its use in numerous applications. Other methods of post-flame NO_x control include oxidising NO_x into N_2O_5, which can be subsequently removed as dry deposition through scrubbing systems (Skalska *et al.*, 2010). However, this oxidisation requires ozone, which brings its own sets of problems in the aviation industry (Mok and Lee, 2006).

The second strategy is to limit the NO_x formation during the combustion itself. The principle is to minimise peak combustion temperatures and the residence time of the fuel-exhaust mixture at peak temperature. One of the methods to reduce peak temperature is to use exhaust gas recirculation (ElKady *et al.*, 2008; Evulet *et al.*, 2009; Li *et al.*, 2009) or water/steam injection (Hung, 1974; Daggett, 2004; Daggett *et al.*, 2010). However, the use of EGR or water injection reduces the O_2 concentration in exhaust gas, which

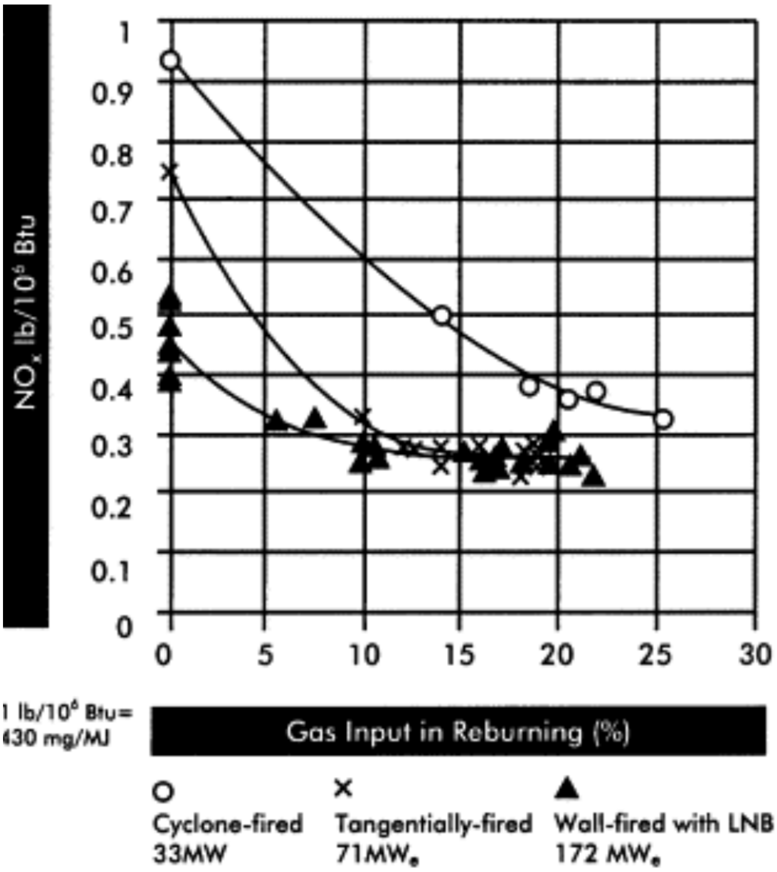

Figure 1.3: Findings from three comprehensive, extended-duration projects funded by the Gas Research Institute, which aimed to assess the effectiveness of gas reburning in curbing NO_x emissions in coal-fired power plants. Reproduced with permission from Smoot *et al.* (1998) published by Elsevier Ltd.

may cause adverse effects on combustion stability and complete combustion (Røkke and Hustad, 2005; ElKady *et al.*, 2009; Li *et al.*, 2011). The proportion of nitrogen in the outlet gases is also increased, along with CO_x, as the EGR ratio increases (Evulet *et al.*, 2009).

The third strategy is to use Rich Burn-Quick Quench-Lean Burn (RQL) combustion in gas turbine combustors (Rizk and Mongia, 1991). During RQL combustion, rich fuel-air mixture is burnt near the injector region. The rich mixture provides an oxygen-deficient environment, which limits the availability of oxygen for nitrogen to oxidise and form NO_x. Following the rich burn phase, the combustion products move into a quick quench zone. In this zone, the hot combustion gases are rapidly cooled, preventing further NO_x

formation. The rapid cooling helps quench the high-temperature combustion products, inhibiting the reaction pathways that lead to NO_x formation. Finally, the combustion gases then enter the lean burn phase, where additional air (oxygen) is introduced. This phase ensures that any remaining unburned fuel from the rich phase is oxidised, promoting more complete combustion. The lean conditions further limit the formation of NO_x due to lower peak temperatures and reduced availability of nitrogen and oxygen radicals, which are primary precursors of NO_x. RQL strategy is used in almost all aviation gas turbine engines. However, the potential of NO_x reduction is limited in practice due to the increased formation of soot (Bauer, 2004). Higher equivalence ratios, coupled with increased pressures and relatively high temperatures, facilitate the generation of soot particles (Kellerer *et al.*, 1995).

One of the alternatives that does not have the aforementioned drawbacks is the use of lean, premixed, and sometimes prevaporized combustion (Lefebvre, 1977; Becker *et al.*, 1986).

1.4 LEAN PREMIXED PREVAPORIZED COMBUSTION

In lean premixed prevaporized (LPP) combustion, excess oxidizer and fuel are thoroughly mixed prior to being delivered to the combustor. Figure 1.4 shows a schematic of a combustor with a mixing tube of 34 mm diameter present upstream of the combustor inlet. The process of premixing is effective in mitigating the occurrence of localised regions of high temperature within the combustor volume, which might result in significant reduction of nitrogen oxides generation. The lean premixed combustion process is known by different trade names, such as Rolls-Royce's Dry Low Emissions (DLE) process, General Electric's and Siemens-Westinghouse's Dry Low NO_x (DLN) process, and Solar Turbines' SoLo NO_x process. In lean premixed combustion, N_2 present in the ambient air acts as a diluent in the combustion process, especially in lean conditions. In general, it is common for the fuel-to-air ratio to be approximately one-half of the ideal

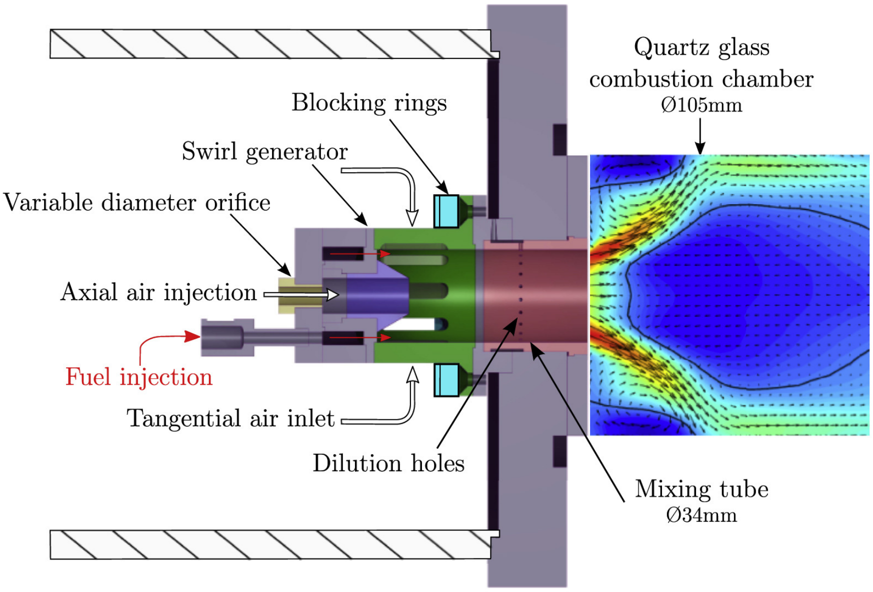
Quartz glass
combustion chamber
Ø105mm
Blocking rings
Swirl generator
Variable diameter orifice
Axial air injection
Fuel injection
Tangential air inlet
Dilution holes
Mixing tube
Ø34mm

Figure 1.4: Illustration of the burner, denoting distinct pathways of volume flow through either the swirl generator or axial injection. Reproduced with permission from Reichel and Paschereit (2017) published by Elsevier Ltd.

stoichiometric level, implying that approximately twice the amount of air necessary for fuel combustion is provided. The presence of an excessive amount of air plays a crucial role in the restriction of NO_x formation, as excessively lean circumstances are incapable of generating the elevated temperatures necessary for thermal NO_x production.

1.5 CHALLENGES ASSOCIATED WITH LEAN, PREMIXED COMBUSTION

Although the LPP combustor demonstrates enhanced pollution reduction capabilities, it is accompanied by significant limitations, including autoignition, flashback, thermoacoustic instability, and flame blowout. Fully and partially premixed combustion is almost exclusively used in land-based gas turbines. Absence of fully premixed combustion in aviation gas turbines can be primarily attributed to three reasons: (1) propensity toward autoignition, flashback, and flame blowout in aircraft engines, and (2) difficulty in premixing liquid fuels used in aviation gas turbine engines as the fuel and control system scale non-trivially with engine size, and (3) lower efficiency of premixed combustion under take-off, cruise, and landing stages (Ralph *et al.*, 2009; Hassa, 2013).

However, flame stabilisation in the combustor is the primary obstacle to implementing lean premixed combustion (Lieuwen and Yang, 2005). It is challenging to stabilise fully premixed flames as such flames are prone to lift off at the flame holder and flashbacks upstream of the flame holder along the fuel-air supply lines (Huang and Yang, 2009; Stöhr *et al.*, 2011; Benim and Syed, 2014). This increases the risk of autoignition of the fuel-air mixture before it reaches the combustion chamber. Moreover, premixed flames are prone to extinction and blowout, which may lead to a complete shutdown of the engine (Lieuwen *et al.*, 2008). Finally, lean conditions can result in a significant decrease of $\mathrm{NO_x}$ emissions due to decrease in combustion temperatures; however, this leads to conditions favourable for the emergence of thermoacoustic instability (Cohen and Anderson, 1996) (cf. figure 1-2 of Matveev (2003)). Thermoacoustic instability refers to the high-amplitude acoustic pressure oscillations (p') that occur as a result of a positive feedback loop between the flame, the flow, and the acoustic fields present in a confined combustor (Sujith and Pawar, 2021). Thermoacoustic instability can cause the engine to vibrate with a significant amplitude and lead to an increase in maintenance costs and an increase in thermal loading on turbine blades. It can result in structural failure immediately or due to fatigue and wear and tear (Lieuwen and McManus, 2003).

One possible explanation for the susceptibility of lean premixed combustion to thermoacoustic instability might be attributed to changes in the equivalence ratio of the inlet flow into a lean premixed prevaporized (LPP) combustor. Slight modifications in the equivalence ratio close to the lean flammability limit can potentially induce significant fluctuations in chemical time and flame attributes such as flame temperature and flame speed (Lieuwen *et al.*, 1998). The experimental data collected by Zukowski (1978), as depicted in Fig. 1.5, demonstrates that the rate of change of chemical time, $d\tau_{\mathrm{chem}}/d\phi$, exhibits a significant rise as the flame becomes more fuel-lean. The reaction rate in chemical systems is known to be inversely related to chemical time. Consequently, even a slight alteration in the equivalence ratio can lead to significant variations in the reaction rate under lean conditions compared to the stoichiometric

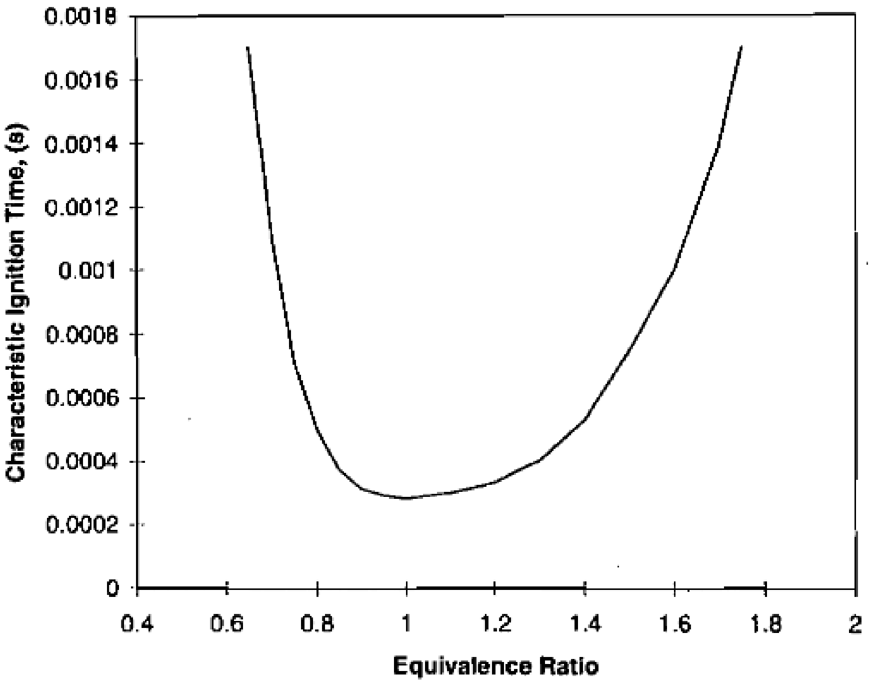

Figure 1.5: Empirically established relationship between the characteristic chemical time and the equivalence ratio for a hydrocarbon fuel, from Zukowski (1978). Reproduced with permission from Lieuwen *et al.* (1998) published by Taylor & Francis.

condition. Accordingly, the magnitude of p' oscillations exhibits a significant increase when the reaction rate oscillations interact with the acoustic field in the combustor system, thereby establishing a closed loop for the transfer of energy between the release of chemical energy and the driving of the acoustic pressure field.

The reason behind the tendency of low-emissions gas turbine engines to be prone to significant levels of unsteady and violent combustion dynamics can be attributed to their design, which is also, unfortunately, optimal to promote thermoacoustic instability. Consider the following points:

1. Low pressure loss contributes to low acoustic damping in the combustor. Combustors with low acoustic damping, in turn, are prone to thermoacoustic instability.

2. These LPP systems operate with lean, premixed conditions and at conditions very close to the point of blowout. As a result, the system is already on the stability line,

where even slight disturbances might result in disproportionately large responses.

3. As opposed to systems with diffusion flames, an LPP combustor is fed with limited dilution jets or film cooling air. In diffusion-flame systems, a portion of air (a typical value would be 30%) enters the combustor at the front, while the remainder enters through quench holes in the middle. The secondary air intakes serve as highly efficient acoustic dampers. In contrast, most air in an LPP system enters the combustion system at the front end, with downstream air input being governed by cooling needs. These combustion systems resemble pipes with solid walls and have considerably less acoustic dampening (O'Connor *et al.*, 2016).

4. Due to the physical structure of the combustor and the need for a high velocity fuel-air premixed to prevent flashback, the flame is typically positioned near the acoustic pressure anti-node position. This location (as opposed to an acoustic pressure node) is optimal for adding energy to the acoustic field via a heat release disturbance (Zinn and Lieuwen, 2005).

5. The length of the combustor is kept relatively long with respect to the length of the flame to enhance the oxidation of CO emissions. Thus, the flame is quite short relative to the wavelength of the acoustic mode inside the combustor, resulting in a concentrated heat release.

   All the aforementioned points provide us an understanding for the high tendency of a lean-premixed combustor to exhibit thermoacoustic instability.

Thermoacoustic instability is not limited to gas turbine engines; they have been seen in a variety of applications such as liquid rocket engines (Harrje and Reardon, 1972; Anderson and Yang, 2012), solid rocket motors (Summerfield *et al.*, 1992), ramjet and scramjet engines (Byrne, 1983; Crump *et al.*, 1986; Hegde *et al.*, 1987; Ken *et al.*, 1991; Ma *et al.*, 2005; Ouyang *et al.*, 2015, 2016, 2017; Li *et al.*, 2021), boilers and furnaces (Flynn *et al.*, 2017). There have been numerous reported cases of thermoacoustic instability in the Soviet space missions (Sutton, 2003; Dranovsky, 2007; Natanzon, 2008), missiles developed during the Cold War (Bloomfield, 2005), Apollo moon program (Biggs, 2009), and later gas turbines (Lieuwen and Yang, 2005). An instance of the damage caused due to thermoacoustic instability during the early US space program can be seen in Fig. 1.6. Engineers continue to struggle with thermoacoustic instability despite over 50 years of research.

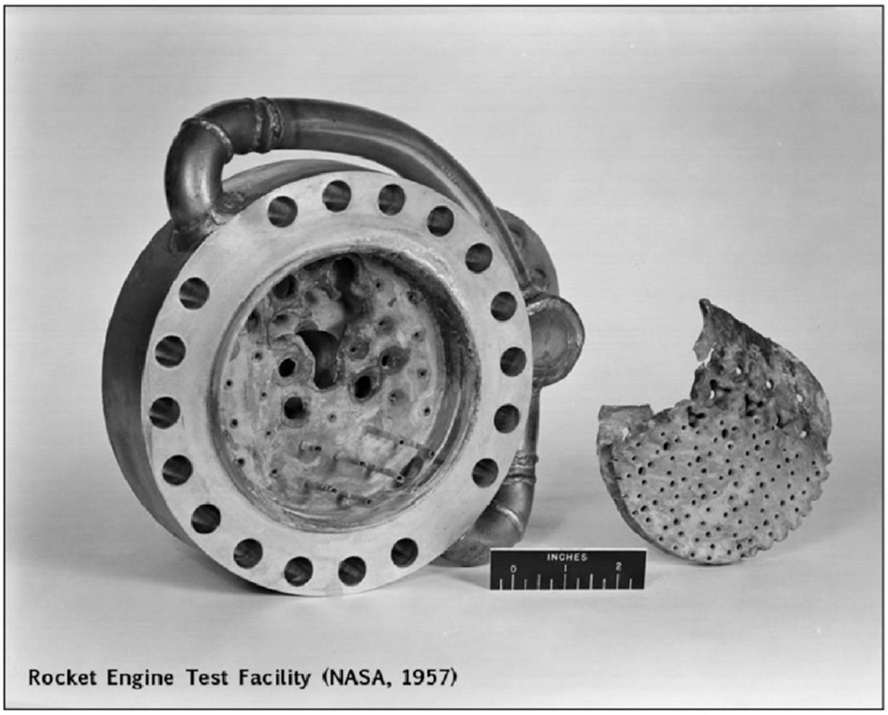

Figure 1.6: Rocket engine rendered inoperable due to instability issues in the initial stages of the US rocket program. Reproduced with permission from Poinsot (2017) published by Elsevier Ltd.

1.6 THERMOACOUSTIC INSTABILITY

As mentioned in the previous Section, thermoacoustic instability is characterised by undesirable high amplitude oscillations in acoustic and heat release rate fluctuations present in a combustion chamber. A positive feedback between combustor acoustics and heat release rate oscillations, coupled with the hydrodynamics of the system, leads to the emergence of thermoacoustic instability. Fluctuations in the heat release rate contribute energy to the acoustic field, causing pressure and velocity fluctuations that propagate throughout the combustor. These acoustic oscillations then excite flow oscillations or local equivalence ratio, which in turn leads to additional heat release rate fluctuations, closing the feedback loop. Combustion could operate as both a driving and a damping source, eliminating energy from the acoustic field. The phase mismatch between the unsteady heat release rate and p' oscillations determines whether combustion functions as a driving or damping source. Lord Rayleigh originally explained the physical mechanism

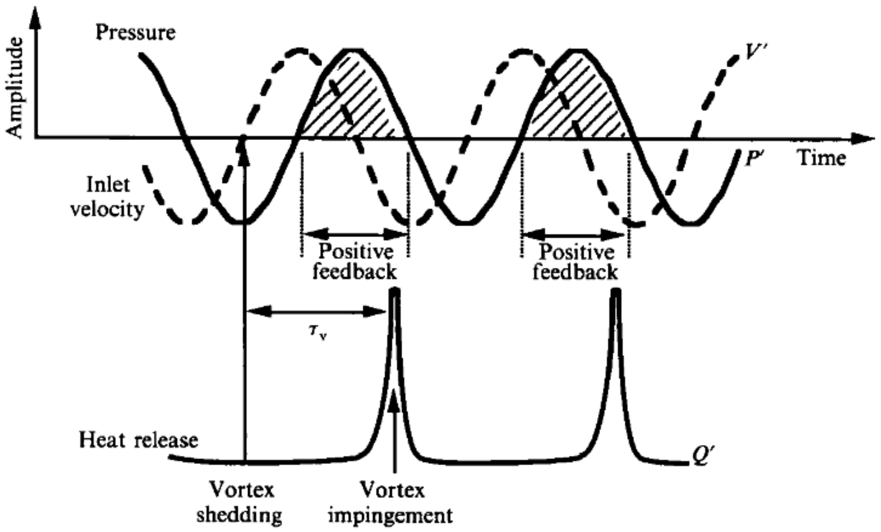
Amplitude
Pressure
V'
P'
Time
Inlet velocity
Positive feedback
Positive feedback
τ_v
Heat release
Q'
Vortex shedding
Vortex impingement

Figure 1.7: An illustration of Rayleigh's criterion for pulsating combustion modes. Reproduced with permission from Ken *et al.* (1991) published by Cambridge University Press.

by which energy is transmitted between a heat source and its surrounding acoustic field (Rayleigh, 1945):

> *If heat be given to the air at the moment of greatest condensation, or be taken from it at the moment of greatest rarefaction, the vibration is encouraged. On the other hand, if heat be given at the moment of greatest rarefaction, or abstracted at the moment of greatest condensation, the vibration is discouraged.*

This statement can be understood as follows. A heat source injects energy locally into the acoustic field when the phase difference between the p' and heat release rate $\dot{q}'$ oscillations, $\phi_{p'\dot{q}'}$, is in the range $0 < \phi_{p'\dot{q}'} < \pi/2$ (Fig. 1.7). In contrast, the heat source absorbs energy from the acoustic field when $\pi/2 < \phi_{p'\dot{q}'} < \pi$. Mathematically, the above statements can be expressed as:

$$\int_V \int_T p'(\vec{x},t)\dot{q}'(\vec{x},t)dtdV > 0 \tag{1.1}$$

This classical time-domain formulation implies that for positive feedback to occur, the product of the heat release rate and p' oscillations integrated over an acoustic cycle must be greater than zero.

While the Rayleigh criterion captures the energy transfer from the acoustic field due to the heat release, another crucial component is the intrinsic damping of combustion systems. All actual systems have damping; hence, the integral in Eq. 1.1 must be larger than the volume-integrated damping. Acoustic oscillations can only increase when the rate of energy given by the combustion process to its surrounding acoustic field exceeds the rate of acoustic energy dissipation within the combustor and/or transmission across its borders (Zinn and Lieuwen, 2005). Various factors elucidated below contribute to this tug-of-war between driving and damping.

1.6.1 Driving mechanisms

Depending on the specific system and its operating conditions, the driving mechanisms (Fig. 1.8) may be any of the following:

1. Fuel feed line-acoustic coupling - Pressure oscillations in the combustor modulate the pressure drop across unchoked fuel nozzles. The rate of fuel injection into the system is controlled by the pressure drop, which subsequently induces an oscillating heat-release mechanism, leading to the occurrence of acoustic oscillations (Crocco and Cheng, 1956; Kendrick *et al.*, 1999).

2. Equivalence ratio fluctuations - The value of the equivalence ratio is directly proportional to the fuel and oxidiser reacting in the combustor during combustion. The fluctuations in the fuel flow rate can directly cause fluctuations in the equivalence ratio, which can occur in two ways: (1) the improper mixing of the fuel and oxidiser due to the space and time constraints of practical combustors, and (2) the fluctuations in the injection mass flow rate of the unchoked fuel manifold, resulting from the interaction of the fluctuating chamber pressure with the injection pressure of the manifold. Fluctuations in the equivalence ratio cause fluctuations in the reaction rate and flame speed which, in turn, cause fluctuations in the heat release rate. The onset of thermoacoustic instability can occur when this oscillatory heat release rate is in phase with p' fluctuations in the combustor (Lieuwen *et al.*, 1998). Numerous studies have characterised the flame response to equivalence ratio fluctuations via experiments as well as simulations (Peracchio and Proscia, 1999; Lee *et al.*, 2000; Cho and Lieuwen, 2005; Shreekrishna and Lieuwen, 2010; Hermeth *et al.*, 2013).

3. Formation of large coherent structures : As the conditions favourable to intense acoustic excitation and strong feedback are approached, it is common to observe the presence of large-scale structures in the flow field. The emergence of these coherent structures are synchronised with the acoustic pressure oscillations (Schadow *et al.*, 1989; Schadow and Gutmark, 1992; Paschereit *et al.*, 1999). In bluff-body stabilised

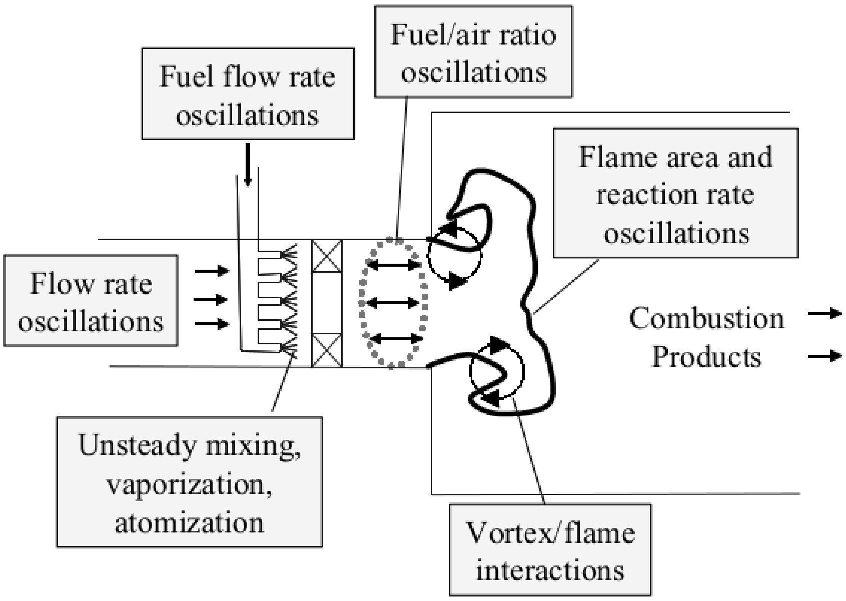
Fuel flow rate oscillations
Fuel/air ratio oscillations
Flame area and reaction rate oscillations
Flow rate oscillations
Combustion Products
Unsteady mixing, vaporization, atomization
Vortex/flame interactions

Figure 1.8: Flame and flow processes that drive thermoacoustic instabilities in gas turbines. Reproduced with permission from Lieuwen and Yang (2005) published by American Institute of Aeronautics and Astronautics, Inc.

turbulent combustors, large coherent vortices are shed from the dump plane and the bluff body tip. These vortices are subsequently convected downstream with the mean flow. These convecting vortices interact with their adjacent vortices or collide with obstacles in their path, such as bluff body or combustor walls. This, in turn, causes these vortices to break into fine-scale structures, resulting in a sudden heat release in the combustor due to the enhanced mixing. The presence of vortices also distorts the surface area of the flame, resulting in a fluctuating rate of heat release in the system (Renard *et al.*, 2000). The modulated rate of heat release adds energy to the acoustic field, which may stimulate the hydrodynamically unstable shear layers to shed another vortex. This shed vortex again influences the rate of heat release, creating a feedback loop. Thermoacoustic instability of solid rocket motors is significantly affected by this driving mechanism. Please refer to Flandro (1986) and Vuillot (1995) for further information.

4. Oscillations in atomisation, vaporisation and mixing of reactants - The perturbation of the flow field brought on by hydrodynamic instabilities may interact with spray and atomisation processes to induce thermoacoustic instability (Culick and Yang, 1995). The size of the droplets, the shape of the fuel spray, rates of evaporation and mixing with the gases in the surroundings can result in a periodic variation in the fuel flow rate and perturbations in the flame downstream of the injector. These factors can influence the flame heat release rate and its coupling to the acoustic field (Ducruix *et al.*, 2003; Chishty, 2005). According to mathematical models, the vaporisation of droplets is one of the primary driving factors in the emergence of thermoacoustic instabilities (Duvvur *et al.*, 1996; Anderson *et al.*, 1998; Lei

and Turan, 2009).

1.6.2 Damping mechanisms

Even if the Rayleigh criterion is satisfied, thermoacoustic instability will not occur if the acoustic driving is less than acoustic damping. The following processes can cause a thermoacoustic system to lose energy:

1. Radiation and convection of acoustic energy - The acoustic energy present within a duct can be dissipated by the mean flow of the medium via radiation and/or convection. In the case of an organ pipe, the sound produced is due to the acoustic energy (of the standing wave) escaping through the open end. Also, the fluid motion can induce acoustic convection, which can carry the energy of sound waves away from the system at a rate proportional to the Mach number of the mean flow (Ingard and Singhal, 1975).

2. Heat transfer damping and viscous damping - Boundary-layer losses arise when acoustic oscillations are present at surfaces where viscosity and thermal dissipation effects predominate (Zinn and Lieuwen, 2005). The presence of a no-slip boundary condition at the wall results in the conversion of a fraction of the energy in the acoustic mode into vortical velocity when an acoustic wave encounters a rigid wall at an oblique angle. In a similar manner, some acoustic energy is turned into entropy fluctuations due to boundary condition for the wall temperature (Zinn and Lieuwen, 2005). These two energy transfer processes convert acoustic energy into vortices and entropy fluctuations. Additionally, flow separation can dampen acoustic disturbances by transforming acoustic energy into vorticity (Zinn and Lieuwen, 2005).

3. Typically, oscillations occurring within an unstable combustor are characterised by one or more pure acoustic tones that manifest at specific frequencies. The occurrence of this phenomenon can be attributed to the fact that combustors typically exhibit characteristics of poorly damped acoustic resonators, which make them responsive to external disturbances within narrow frequency ranges. As a result, certain mechanisms exist that do not directly dissipate acoustic energy but instead facilitate the transfer of energy from the excited acoustic mode to other modes that either do not contribute to thermoacoustic instability or dissipate energy more effectively than the first excited mode.

4. The combustor liner itself generates substantial damping, typically incorporating a range of perforations of varying sizes to facilitate the provision of cooling and dilution air to the combustor (Putnam, 1971; Noiray *et al.*, 2007; Lořstad *et al.*, 2009; Lefebvre and Ballal, 2010; Gullaud and Nicoud, 2012). The phenomena of acoustic damping through orifices, namely the holes found in combustor liners, have been extensively studied in academic literature. These orifices are designed with different diameters to effectively attenuate a range of acoustic frequencies

(Howe, 1979, 1980; Cummings, 1984; Hughes and Dowling, 1990; Eldredge and Dowling, 2003; Bellucci *et al.*, 2004*a*). Furthermore, the boundary conditions at the intake of the combustor swirler and the nozzle output serve to dampen acoustic energy by facilitating the dissipation of such energy from the system (O'Connor *et al.*, 2015).

1.7 THERMOACOUSTIC INSTABILITY IN GAS TURBINES

The geometric configuration of combustors present in gas turbines often exhibit ideal characteristics for generating and sustaining thermoacoustic instability. The combustors are primarily characterised by their elongated and confined geometries. The elongated design of gas turbine combustors, necessitated by efficient heat transfer and combustion processes, inadvertently creates a lengthy combustion zone within a confined volume. This elongated zone, inadvertently, plays the role of an duct with a high tendency to support thermoacoustic instability in the presence of heat release rate in a narrow zone. Thermoacoustic instability can lead to flame flashback and blowout, mechanical fatigue, undesirable vibrations and structural damage (Fig. 1.9), increased noise emissions, reduced operational range, and increased safety concerns in gas turbine engines. Thus, the ultimate objective of scientists and engineers is to find cost-effective reliable ways to suppress thermoacoustic instability.

In the late 1940s and early 1950s, liners were developed through a predominantly empirical approach as passive control mechanisms to attenuate oscillations. Researchers at Lewis Laboratory, presently known as the NASA Glenn Research Centre, collated the predominant body of contemporary data and executed multiple tests in 1954 in order to establish fundamental design concepts (Harp *et al.*, 1954). Among the several solutions explored, including baffles, vanes, and altering the distribution of injectors, it was found that perforated liners proved to be the most productive choice. The utilisation of Helmholtz resonators had been previously explored by Pratt & Whitney Aircraft and the United Aircraft Research Laboratory. In 1953, they successfully showcased the initial practical implementation of perforated liners on a Pratt & Whitney J57 afterburner. A

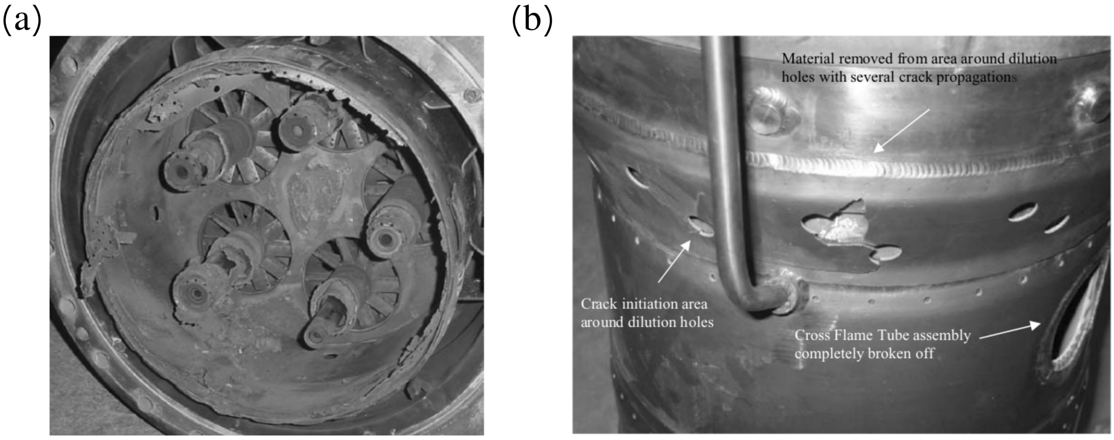
(a)
(b)
Material removed from area around dilution holes with several crack propagations
Crack initiation area around dilution holes
Cross Flame Tube assembly completely broken off

Figure 1.9: Photographs of failed burner assembly and combustor damage caused by thermoacoustic instability. Reproduced with permission from Lieuwen and Yang (2005) published by American Institute of Aeronautics and Astronautics, Inc.

lot of research related to the use of acoustic liners as a control strategy was done in 1960s-1970s (Blackman, 1960; Utvik *et al.*, 1966; Morgan and Phillips, 1967; Vincent, 1968; Phillips, 1969; Harrje and Reardon, 1972). Passive damping devices such as perforated liners (Lei *et al.*, 2010; Zhao *et al.*, 2011, 2019; Zhang *et al.*, 2020; Qin *et al.*, 2021), Helmholtz resonators (Duperé and Dowling, 2005), quarter-wave resonator (Park and Sohn, 2010; Laudien *et al.*, 1995*a*; Sohn and Park, 2011), half-wave resonators (Sohn *et al.*, 2007; Park and Sohn, 2009, 2010), and Herschel-Quincke tubes (Park *et al.*, 2008, 2009) have shown promising performance in suppressing the thermoacoustic instability in many lab-scale and practical combustors (Bellucci *et al.*, 2004*b*). An excellent review of acoustic dampers in the context of thermoacoustic instability can be found in Zhao and Li (2015).

There has been a notable increase in the availability of literature about the successful endeavours undertaken by diverse companies in controlling thermoacoustic instability inside their gas turbine engines (Lieuwen and Yang, 2005). Nevertheless, the gas turbine sector remains confronted with the issue of thermoacoustic instability. This predicament arises from the escalating emission regulations, heightened fuel efficiency and fuel

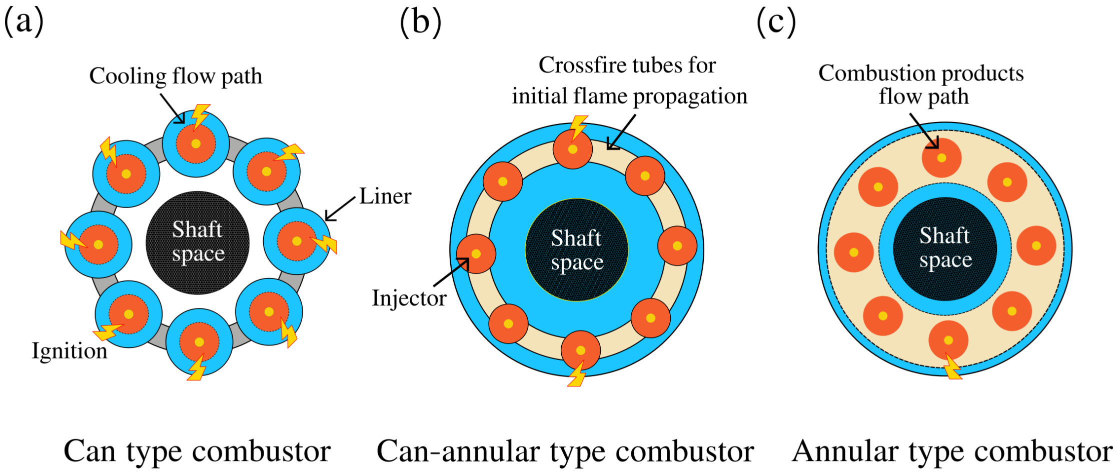
(a)
(b)
(c)
Cooling flow path
Liner
Shaft space
Ignition
Crossfire tubes for initial flame propagation
Injector
Shaft space
Combustion products flow path
Shaft space
Can type combustor
Can-annular type combustor
Annular type combustor

Figure 1.10: Arrangements of can, can-annular, and annular combustors used in gas turbine engines. The blue portion indicates cooling flow path, the red portion indicates the combustion products flow path, and the light yellow-red portion indicates the path through which the initial flame propagates to different combustors.

flexibility demands, and the continuous expansion of the aviation industry. Compounding the problem is the incomplete comprehension of the intricate coupling mechanisms that underlie thermoacoustic instability.

1.7.1 Thermoacoustic instability in can-annular combustors

Combustors in gas turbines have various configurations, each specifically engineered to enhance combustion efficiency, fuel-air blending, and emissions management. Three primary configurations exist and are shown in Fig. 1.10: annular, can, and can-annular. The annular configuration, which exhibits a circular geometry encompassing the central shaft of the turbine, has the benefit of being compact and facilitating streamlined airflow. This configuration promotes improved combustion stability and less pressure losses, and is primarily used in aviation gas turbine engines. On the other hand, the can layout entails the arrangement of separate combustion chambers. This configuration enables a modular design and facilitates easier maintenance. The configuration of this arrangement allows for effective cooling systems and convenient accessibility, rendering it appropriate for bigger gas turbines. The can-annular arrangement, shown in Fig. 1.11, is a hybrid

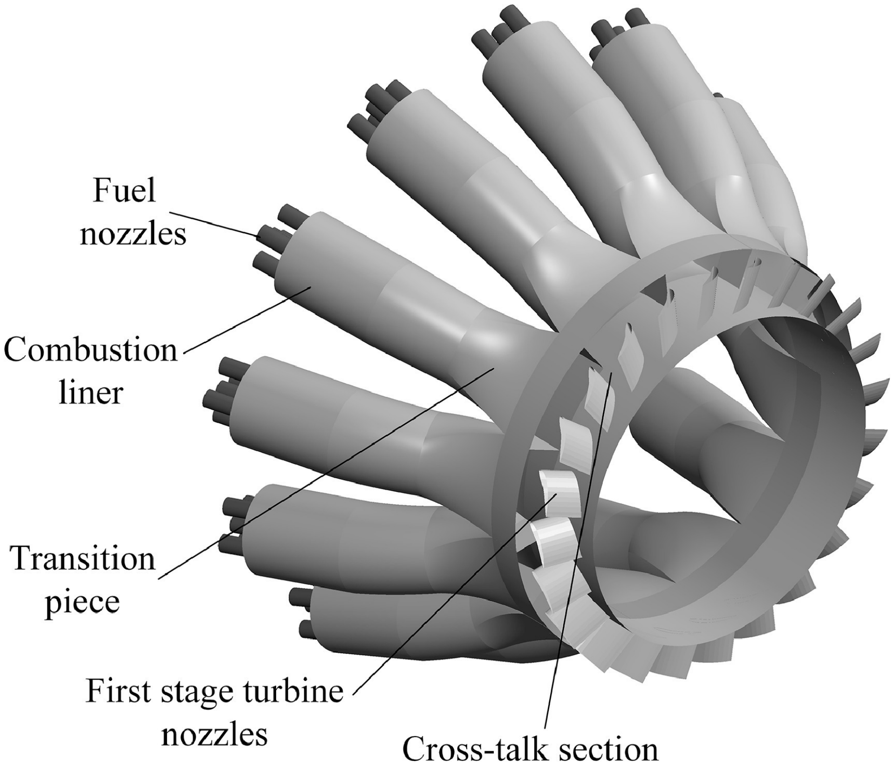

Figure 1.11: Diagram depicting a standard can-annular combustion system in a gas turbine, including stator vanes of the first stage turbine. Reproduced with permission from Moon *et al.* (2020*b*) published by Elsevier Ltd.

configuration that combines the features of the annular and can designs. It achieves this by integrating a circular arrangement of individual combustion cans around the central shaft, thus incorporating the benefits of both annular and can layouts. The design of this layout results in enhanced combustion dynamics and thermal efficiency. Each of these configurations offers distinct advantages and trade-offs, which are determined by several factors, including power production demands, environmental rules, and engineering limitations.

Can-annular gas turbine combustion systems are frequently utilised in the configuration of contemporary heavy-duty gas turbine engines (Davis, 1996; Mongia *et al.*, 2003). Figure 1.11 illustrates the structural design of a conventional can-annular gas turbine combustion system. This configuration consists of twelve can combustors arranged circumferentially, together with an annular open space located upstream of the stator vanes of the first stage turbine. Transition pieces connect the cylindrical combustors and the annular turbine section, bridging the gap between the individual combustors and the annular section (Luque *et al.*, 2015; Rosic *et al.*, 2011). The configuration described here results in a distinctive acoustic setting, which plays a crucial role in the excitation of longitudinal-mode combustion instabilities. An unobstructed region preceding the initial stage of the turbine allows for the unhindered transmission of acoustic waves between adjacent combustors. This phenomenon significantly impacts the interaction between combustion and acoustic fields in neighbouring combustors, ultimately dictating the overall dynamic properties of the entire system. In can-annular configurations, it is noteworthy that only a limited number of combustors are initially ignited. The rig combustors are interconnected with crossfire tubes, facilitating the propagation of the flame from the lighted cans to the cans that have not yet been ignited. Thus, aside from the transmission through upstream cross talk regions, the propagation of acoustic waves can also occur between cans through crossfire tubes. The intricacies associated with the interactions between multiple combustors produced by cross-talk significantly escalate as the number of constituent combustors rises. The growing interest in thermoacoustic instabilities in can-annular combustor architectures is evidenced by the extensive mathematical and experimental investigations conducted in both academic and industrial settings, such as Siemens (Bethke *et al.*, 2002; Krebs *et al.*, 2005; Kaufmann *et al.*, 2008; Farisco *et al.*, 2017), General Electric (Venkatesan *et al.*, 2019; Moon *et al.*, 2020*b*, 2021), and Ansaldo Energia Switzerland (Ghirardo *et al.*, 2019, 2020).

1.8 CONTROL OF THERMOACOUSTIC INSTABILITY

The ultimate objective of studying thermoacoustic instability is to acquire sufficient knowledge to control the amplitudes to acceptable levels. In gas turbine engines, various methodologies such as acoustic dampers, fuel staging, microjet injection, and redesigning different components such as nozzles, injectors, and flame stabilisation mechanisms have been used to suppress thermoacoustic instability (Lieuwen and Yang, 2005). All of these strategies require a large number of expensive experiments to determine the optimal design. Incorporating renewable energy technologies, which introduce power into the electrical grid irregularly, has prompted the need to operate gas turbine combustors that generate power throughout various output levels. This is essential for maintaining a balanced power capacity within the grid. Therefore, it is imperative to develop strategies to effectively suppress thermoacoustic instability across diverse operating situations in gas turbine engines. These engines are specifically engineered to function at different power levels and utilise various fuel sources. This necessitates the development of methods that are adaptable, intelligent, and economical. Thus, we next discuss the various aspects of controlling thermoacoustic instability.

1.8.1 Active closed loop control

Active closed loop control, also known as feedback control, involves modifying the output of the system based on the measurements of its output (Dorf and Bishop, 2008; Franklin *et al.*, 2002). As shown in Fig. 1.12, a feedback loop where a controller modifies the input of the system in response to the output is used to implement this closed loop control. The earliest concept of feedback control of thermoacoustic instabilities was derived with instabilities in rocket motors in mind (Tsien, 1952; Marble and Cox Jr, 1953); however, the earliest experiments of controlling thermoacoustic instability with closed loop control utilised Rijke tube with a laminar flame burning on a gauze (Ffowcs Williams, 1984). A novel method of controlling instability, known as antisound, was also conceptualised (Ffowcs Williams, 1984; Heckl, 1985). Antisound involves injecting acoustic energy with an appropriate combination of frequency and amplitude, such that destructive interference cancels out the unwanted thermoacoustic instability. Most active control applications that have been proven thus far are founded upon this particular principle of antisound.

Dines (1984) carried out the initial experimental demonstration of closed loop control of thermoacoustic instability in a Rijke tube. Using an optical fibre and photomultiplier,

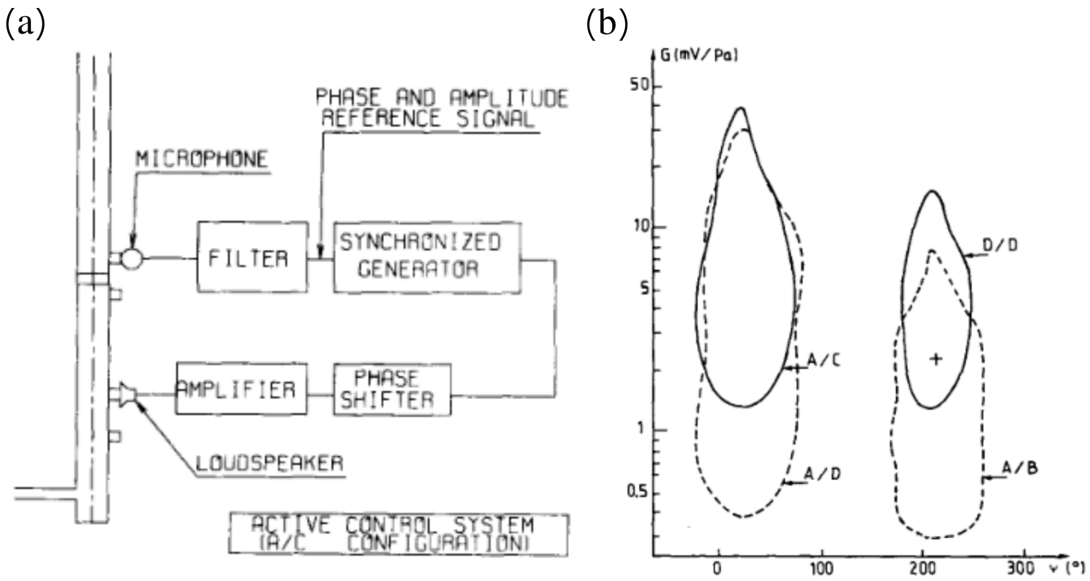
(a)
PHASE AND AMPLITUDE REFERENCE SIGNAL
MICROPHONE
FILTER
SYNCHRONIZED GENERATOR
AMPLIFIER
PHASE SHIFTER
LOUDSPEAKER
ACTIVE CONTROL SYSTEM (A/C CONFIGURATION)
(b)
G (mV/Pa)
50
10
5
1
0.5
0
100
200
300
v (°)
D/D
A/C
A/D
A/B
+

Figure 1.12: (a) Schematic of an active closed loop control setup used with a premixed propane-air combustor, and (b) stability margins in the phase-gain plane of active instability control for different configurations of the combustor. The combustor remains silent when the thermoacoustic system lies inside the closed curves. Reproduced with permission from Lang *et al.* (1987) published by Elsevier Ltd.

the signal acquired through the light generated by CH free radicals in a flame was phase-shifted, amplified, and used to drive an acoustic driver. The acoustic driver was placed on one end of the Rijke tube. The appropriate phase-shift and gain values were determined by trial and error. The experiments resulted in a 35 dB reduction of sound pressure level. Subsequently, Heckl (1988) used feedback control on a similar Rijke tube to reduce flame-driven oscillations by 40 dB, but with a microphone measuring the acoustic pressure at a position within the tube as the sensor signal.

After these initial successful experiments, a large number of studies used acoustic drivers to control thermoacoustic instability in Rijke tubes (Lang *et al.*, 1987), and in more complicated systems such as turbulent combustors (Poinsot *et al.*, 1989). Heckl (1988) developed the theory of feedback control, along with the implications of noise contamination toward the stability behaviour of a Rijke tube in 1990. Feedback control can also be implemented by other means, such as changing the area of the nozzle downstream of a choked plate (Bloxsidge *et al.*, 1988).

However, the power requirements of mechanical acoustic drives scale non-trivially at bigger scales, rendering them unsuitable to test or implement with larger combustors. Researchers have thus started focusing on methods that can alter the Rayleigh energy source term, $\int_V p'\dot{q}'dV$, via unsteady fuel injection. Langhorne *et al.* (1990) used a Nyquist-designed phase-shift controller to modulate the fuel supply to control thermoacoustic instability in a ducted premixed flame. An unsteady modulation of fuel with as little as 3% extra fuel reduced the spectral peak corresponding to the primary instability mode by 12 decibels.

A significant limitation of simple time-delay or phase-shift controllers is that these values are typically derived via experiments for a specific working condition. On the other hand, practical combustion systems exhibit several modes of instability. In such cases, a poor selection of controller parameters can enhance thermoacoustic instability (Seume *et al.*, 1998). Moreover, controllers with only a fixed time delay or phase shift can excite a new instability mode that may become unstable when the gain is increased (Cohen and Banaszuk, 2003; Fleifil *et al.*, 1998; Langhorne *et al.*, 1990).

Despite successful application of closed feedback control in laminar tube combustors (Tierno and Doyle, 1992; Isella *et al.*, 1997; Evesque and Dowling, 1998; Annaswamy *et al.*, 2000), premixed dump combustor (Kim *et al.*, 2000), swirl-stabilised dump combustor (Murugappan *et al.*, 2000, 2003), midscale rigs (liquid-fuel combustor (Yu and Wilson, 2002), bluff-body flame stabilised combustor (Langhorne *et al.*, 1990)), subscaled gas turbine combustors (Sattinger *et al.*, 2000; Banaszuk *et al.*, 2001), and large-scale rigs (Hermann *et al.*, 2001; Seume *et al.*, 1998), the field of active control has not achieved the prominence that was expected in 1980s-2000s. Ensuring rapid actuator response at frequencies where combustor dynamics are most sensitive is not easy. In addition, the durability of the actuators operating in harsh environment of the combustor is a significant factor that has prevented the widespread implementation of active control in practical gas turbines. Motivated by these limitations, active open loop control using secondary fuel/air injection has gained prominence in the last 20 years.

1.8.2 Active open loop control

In contrast to closed loop control, the control signal of an open loop controller is determined solely by the operator and is, therefore, independent of the state of the system. An open loop controller cannot adapt to changes in the system dynamics. However, open loop control is significantly simpler to implement in a combustor because neither a dynamic sensor signal nor a signal processor is necessary.

Open loop control can be accomplished through various means such as secondary air injection (Uhm and Acharya, 2004; Ghoniem *et al.*, 2005; Altay *et al.*, 2007; Murayama and Gotoda, 2019; Krishnan *et al.*, 2019*a*; Kurosaka *et al.*, 2021), fuel-flow modulation (Prasanth *et al.*, 2002; Lubarsky *et al.*, 2004; McManus *et al.*, 2004; Richards *et al.*, 2006; Paschereit and Gutmark, 2008), and external harmonic forcing (Lieuwen and Neumeier, 2002; Bellows *et al.*, 2008; Kashinath *et al.*, 2018; Guan *et al.*, 2019*a*; Mondal *et al.*, 2019). The location of secondary air injection is of primary importance during open loop control (Fig. 1.13). Secondary air injection at the flame anchoring position leads to the mitigation of thermoacoustic instability. However, it also affects flame stabilisation, which can, in turn, be controlled using H_2 injection (Ghoniem *et al.*, 2005; Altay *et al.*, 2010). Injection of H_2 can, however, lead to increase in flame temperature and thus, higher NO_x Consequently, studies have been performed to optimise the main flow after injection of secondary air and H_2 to lower the flame temperature, reduce NO_x emissions, and mitigate thermoacoustic instability at the same time (Ghoniem *et al.*, 2005).

Gopakumar *et al.* (2016) have recently demonstrated that in a swirl combustor, thermoacoustic instability can be suppressed by introducing a rotating swirler and selecting its rotational speed appropriately (Chaudhuri *et al.*, 2018; Mahesh *et al.*, 2018).

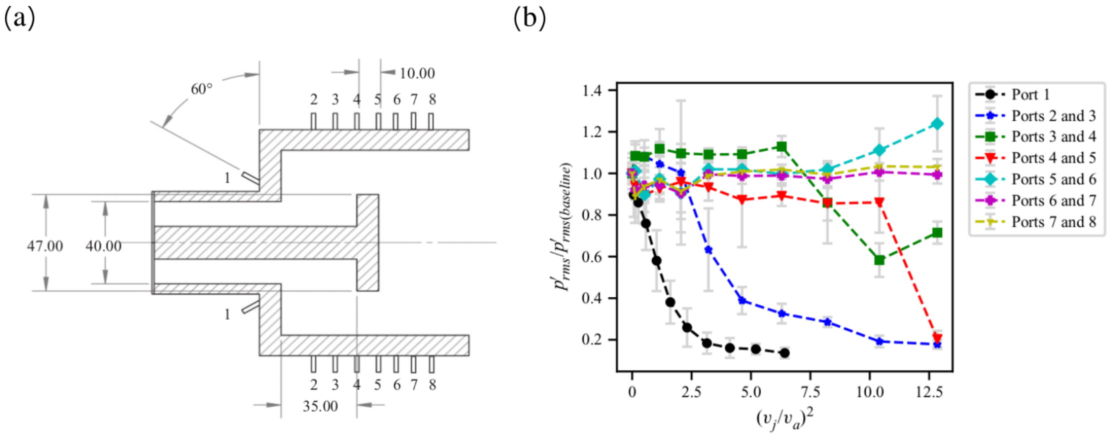

Figure 1.13: (a) Schematic of the cross-section of a combustion chamber with the spatial location of the secondary steady air-jet injection ports, and (b) variation of p'_{rms} of thermoacoustic instability due to microjet air injection through different ports with respect to the ratio of total momentum flux. The ratio of total momentum flux is equal to momentum of square of velocity of microjet air injection (v_a^2) divided by the square velocity of main air at the combustor inlet (v_j^2). Reproduced with permission from Krishnan *et al.* (2021) published by Cambridge University Press.

In addition, Gopakumar *et al.* (2017) demonstrated that the reduction of thermoacoustic instability caused by a rotating swirler occurs via an intermittency route. The authors successfully expanded upon a phenomenological model by including the synchronisation of Kuramoto oscillators, and accurately simulated the dynamic behaviour observed in experimental settings (Dutta *et al.*, 2019). Later, (Krishnan *et al.*, 2019*a*) used weighted spatial correlation networks constructed from velocity field to identify optimal location for implementing passive control strategies. They injected microjets at the optimal locations to suppress the amplitude of acoustic pressure oscillations observed during thermoacoustic instability by 86%. In the same experimental setup, (Roy *et al.*, 2021) used turbulent velocity amplitude and Hurst exponent to identify critical region for optimised passive control during thermoacoustic instability. Subsequently, researchers have used CO_2-Ar (Liu *et al.*, 2021), and helium (Liu *et al.*, 2022) to control thermoacoustic instability in ethanol and butane combustors, respectively. Recent studies have also investigated preheated CO_2-O_2 (Tao and Zhou, 2020; Zhou and Tao, 2020), superheated steam (Tao and Zhou, 2021*b*), N_2-O_2 (Zhou and Tao, 2020), CO_2

(Tao and Zhou, 2021*a*; Zhou and Hu, 2023), and plasma (Gomez del Campo, 2019; Zhou *et al.*, 2021; Deng *et al.*, 2022; Pavan *et al.*, 2022; Shanbogue *et al.*, 2022) to suppress thermoacoustic instability.

Thus, significant progress has been seen in the open loop control of thermoacoustic instability. However, implementing such strategies on complex turbulent combustors would be difficult and requires additional detailed study (Yi and Santavicca, 2009; Kopasakis *et al.*, 2009; Passarelli *et al.*, 2023).

1.8.3 Passive control

Passive control strategies are frequently preferred for controlling thermoacoustic instability due to their low cost and durability. In the early stages of combustor development, methods to mitigate thermoacoustic instabilities involved the design of passive controls (Putnam, 1971; Schadow and Gutmark, 1992). By incorporating geometrical modifications into the design of the combustor, the primary objective of the method is to change or shift the frequency of thermoacoustic instability to a non-resonant frequency (Richards and Janus, 1998; Steele *et al.*, 2000; Noiray *et al.*, 2007). This, in turn, alters the phase relationship between the acoustic field and heat release rate fluctuations, dampening the acoustic pressure oscillations in the combustor. This technique also aims to increase the acoustic damping of the system by installing static devices such as baffles, liners, porous inert media, and resonators (Gysling *et al.*, 2000; Eldredge and Dowling, 2003; Bellucci *et al.*, 2004*b*; Zhong and Zhao, 2012; Bothien *et al.*, 2014; Schuermans *et al.*, 2015; Dowd and Meadows, 2022). Installing dampers will remove the energy from the excited acoustic fluctuations in the combustor, thereby mitigating the thermoacoustic oscillations. Passive control techniques have been successfully used in rockets (Harrje and Reardon, 1972; Laudien *et al.*, 1995*b*) and gas turbines (Garrison, 1971; Rawlins, 1995; Pandalai and Mongia, 1998; Richards *et al.*, 2003; Williams *et al.*, 2016). Although this technique has the benefit of being simple, it is only effective for a few targeted frequencies and is primarily used to control high-frequency oscillations (Dowling and Morgans, 2005).

1.9 NON-CONVENTIONAL APPROACH OF STUDYING THERMOACOUSTIC INSTABILITY

The efficient design of control systems to mitigate thermoacoustic instability requires a nuanced approach to model the physical systems that participate in the phenomenon of thermoacoustic instability. Historically, thermoacoustic systems have been modelled as combustion-driven acoustic systems. The stability of a system susceptible to thermoacoustic instability is usually analysed through a linear stability analysis and eigenvalues of the thermoacoustic system. However, linear stability analysis is not suitable for examining the dynamics of the thermoacoustic system as the system undergoes transitions beyond the linearly stable regions. This is because the effect of nonlinearities in the acoustics is non-trivial outside the linearly stable regions. Acoustics, as well as the unsteady flame, can exhibit nonlinearities. However, since the p' fluctuations are lower in magnitude compared to the mean pressure of the medium, the propagation of acoustic waves can be considered as a linear phenomenon for further calculations. However, this assumption fails in the case of rockets. Nevertheless, the response of the flame to acoustic perturbations is still highly nonlinear.

Therefore, although the process of modelling sound waves is relatively simple to execute and is popular, the modelling of flame response to acoustic waves, especially in turbulent flows, is more complex and less straightforward. One of the approaches involves inducing acoustic perturbations in the flame and subsequently assessing the flame transfer function (FTF) or the flame describing function (FDF), which represents the ratio between the heat release rate and the acoustic velocity fluctuations, with appropriate normalisation. This evaluation can be conducted through experiments or computational fluid dynamics (CFD) simulations, such as large eddy simulations (LES).

The FDF technique takes into the flame into account as a nonlinear component that is connected with the linear acoustic system. In contrast to FTF, FDF has the capability to forecast the magnitude of limit cycle oscillation. Nevertheless, FDF relies on a quasi-linear assumption, meaning that the response of the flame is limited to the same frequency as the applied forcing. Specifically, the response of the flame to higher harmonic frequencies generated by the forcing is disregarded (Juniper and Sujith, 2018). Therefore, FDF may not be appropriate for accurately representing intricate phenomena that involve non-harmonic reactions, such as chaos and intermittency (Weng *et al.*, 2020). In the past, the conditions of a thermoacoustic system have been categorised as either operationally stable or unstable, specifically referring to the occurrence of limit cycle thermoacoustic oscillations. In a similar vein, the FTF/FDF methodologies primarily prioritise the identification of the unstable regime and the determination of the magnitude of periodic oscillation. Nevertheless, empirical evidence has demonstrated that thermoacoustic systems can manifest intricate dynamical phenomena beyond limit cycle oscillations (Keanini *et al.*, 1989; Sterling, 1993; Jahnke and Culick, 1994).

Several of these behaviours can be discerned even in laminar thermoacoustic systems. In addition to limit cycle oscillation, Kabiraj *et al.* (2012*a*) detected a route to chaos in a laminar Rijke tube through quasiperiodic oscillation, which aligns with the Ruelle-Takens scenario. Subsequent investigations delved into several bifurcations within the same system (Kabiraj *et al.*, 2012*b*), revealing a spectrum of complex phenomena, including the observation of strange non-chaotic attractors (Premraj *et al.*, 2020). These findings were additionally corroborated by other research teams (Kashinath *et al.*, 2014; Unni *et al.*, 2015; Guan *et al.*, 2018). In a separate investigation, Guan *et al.* (2020) also discovered a route to chaos through intermittency in a laminar Rijke tube. The compilation of these experiments demonstrates that a thermoacoustic system, despite its simplicity, may display complex dynamics. Thus, in recent years, a necessity has arisen to investigate thermoacoustic instability through other concepts such as dynamical system and complex system theories.

1.9.1 Use of synchronisation to investigate interacting thermoacoustic systems through dynamical system theory

Thermoacoustic instability is widely recognised as a result of the coupling between acoustic oscillations and heat release fluctuations within the combustor (Rayleigh, 1878). During the state of combustion noise, the acoustic pressure and heat release rate exhibit aperiodic low amplitude behaviour (Tony *et al.*, 2015). However, during the onset of thermoacoustic instability, we observe that both p' and heat release rate fluctuations exhibit large amplitude periodic behaviour and are *locked* with each other. This locking and unlocking behaviour of the two subsystems during the states of thermoacoustic instability and combustion noise has motivated many researchers to use synchronisation theory to study thermoacoustic instability (Fig. 1.14).

In simple terms, synchronisation is the matching of the rhythm of oscillating coupled objects. Synchronisation emerges in various nonlinear dynamical systems, such as brain impulses, cardiac rhythms, and firefly flashing. The history of synchronisation can be traced back to the 17th century when Christiaan Huygens observed synchronisation phenomenon in two pendulum clocks that were suspended from a shared wooden beam (Huygens, 1665). Huygens characterised the observed occurrences as the “sympathy of two timekeeping devices”. In the 19th century, Rayleigh (1945) provided a description of the phenomena of synchronisation observed between two distinct organ-pipes. This synchronisation occurs when the pipes are placed in close proximity and begin to produce sound in perfect harmony. Additionally, synchronisation has been observed in a substantial population of oscillating systems, such as the synchronised clapping in a sizeable audience.

Synchronisation theory provides a convenient framework to study two separate systems interacting with each other. This type of interaction is known as mutual coupling (Pikovsky *et al.*, 2003). The strength of mutual coupling and the time delay involved during the two oscillators interacting with each other play an important role in determining

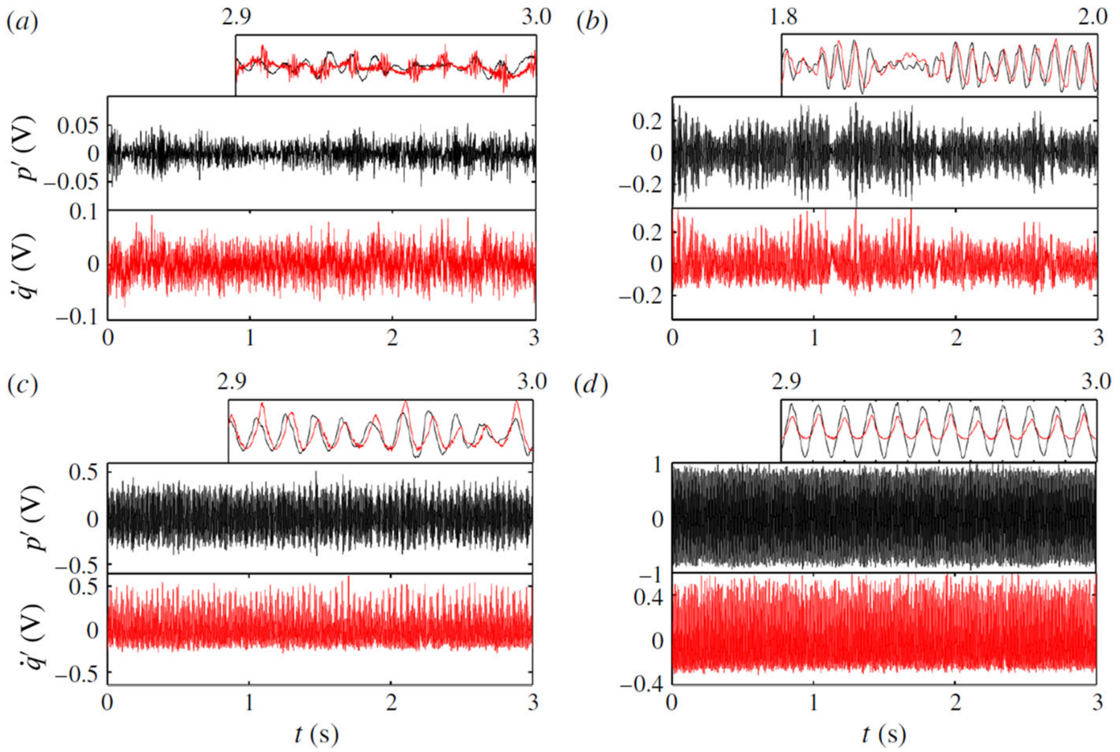

Figure 1.14: Time series of p' and $\dot{q}'$ (heat release rate) oscillations acquired from a bluff-body stabilised turbulent combustor operating in the states of (a) combustion noise, (b) intermittency, (c) phase-synchronisation limit cycle state, and (d) generalised-synchronisation limit cycle state. Reproduced with permission from Pawar *et al.* (2017) published by Cambridge University Press.

the synchronisation characteristics of the mutually coupled system. The investigation of synchronisation among oscillators often involves the analysis of the phase locking or frequency locking of their signals. Synchronisation of a system consisting of connected oscillators, starting in a desynchronised state, can be achieved by adjusting the coupling strength via periodic forcing or feedback mechanisms.

The phenomenon of mutual coupling between two self-sustained nonlinear oscillators can give rise to a range of phenomena, including phase-locking, phase-drifting, phase-flip bifurcation, and oscillation quenching (Lakshmanan and Senthilkumar, 2011; Dange *et al.*, 2019). In the context of weakly coupled oscillators, the extent of interaction between them is confined to their phases, resulting in phase-locking behaviour or synchronisation. Conversely, robust mutual coupling influences both the phase and amplitude of interconnected oscillations, and can result in the total cessation of oscillatory behaviour in all oscillators. The phenomenon in which a group of oscillators converge to a shared stable state due to coupling is known as amplitude death. In certain scenarios, mutual coupling may not invariably result in the suppression of oscillations in all interconnected oscillators. Instead, it can give rise to a coexistence of oscillatory and stable states, a phenomenon known as partial amplitude death (PAD).

The exploration of oscillation quenched states in thermoacoustic systems, resulting from the coupling of several oscillators, has been the subject of recent research (Manoj *et al.*, 2018; Dange *et al.*, 2019; Jegal *et al.*, 2019; Moon *et al.*, 2020*a*). The advancement of a reliable and efficient suppression method carries substantial practical importance in effectively mitigating or eliminating thermoacoustic instability. One possible method for reducing the large amplitude periodic oscillations in a network of interconnected thermoacoustic oscillators involves employing a strategy based on the amplitude death phenomenon. Applying dissipative and time-delayed couplings has been demonstrated to successfully reduce thermoacoustic instability in a system of mutually connected thermoacoustic oscillators (Manoj *et al.*, 2018; Dange *et al.*, 2019). Time-delayed coupling is implemented by utilising a hollow tube that functions as a conduit between the two ducts. A bidirectional interaction occurs in coupled oscillators, where an acoustic disturbance originating in one oscillator propagates via the gas medium within the interconnected hollow tubes to influence the behaviour of the other oscillator. Hence, the occurrence of a temporal delay emerges as an immediate outcome of the limited duration of the acoustic wave while it traverses the interconnecting tube. The temporal delay can be modified by manipulating the length of the tube.

Hyodo and Biwa (2018*c*) thoroughly investigated the stability analysis of amplitude death in a mathematical model of two mutually-coupled thermoacoustic oscillators. Their study encompassed the examination of both single-tube and double-tube couplings. The analysis was conducted using the linearised hydrodynamic equations. The experimental confirmation of suppressing self-sustained periodic oscillations of gas columns in two Rijke tube oscillators with time-delayed coupling was undertaken recently by Hyodo *et al.* (2020). The research presented in Hyodo and Biwa (2018*c*) and Hyodo *et al.* (2020) have shown that the minimal diameter of the connecting tube required to induce AD is significantly reduced when using double-tube coupling compared to single-tube coupling. Mutual coupling has proven to be a highly efficient method for mitigating undesired effects in combustion systems, showcasing a commendable level of dependability. The interaction between oscillators is confined solely to the connecting tube, making it a straightforward control technique. The practical implementation of the tube coupling technique to induce amplitude death has been successfully shown in a system including two lean-premixed swirl-stabilised combustors (Jegal *et al.*, 2019).

Around the same time, studies conducted by Dange *et al.* (2019) provides evidence that the coexistence of amplitude mismatch and frequency detuning amplifies AD in coupled thermoacoustic systems. The authors demonstrated that altering the length of the coupling tube results in a shift from antiphase to in-phase synchronisation, achieved through the state of AD. This phenomenon specifically occurs in cases of low amplitude limit cycle oscillations in identical thermoacoustic systems. In contrast, a sudden shift from antiphase to in-phase synchronisation, known as phase-flip bifurcation, is observed when high amplitude limit cycle oscillations are present in thermoacoustic systems. The comprehensive examination of amplitude death in thermoacoustic systems aims to identify potential avenues for utilising AD in effectively mitigating or suppressing detrimental oscillations in practical systems.

1.9.2 Thermoacoustic instability through the perspective of complex systems theory

In the previous paragraphs, we have mostly talked about thermoacoustic instability in laminar systems. However, the combustors present in gas turbine engines and rockets function in the turbulent regime. Due to turbulence, an extensive range of spatial and temporal scales exist in turbulent thermoacoustic systems. Furthermore, other intricate processes such as interaction among different acoustic modes, mixing of reactants at the molecular level, and chemical kinetics necessitate an approach to understand a thermoacoustic instability in turbulent systems with a non-conventional approach that usually involves Hopf bifurcations. The subsequent paragraphs delineate the qualities associated with a system that exhibits complexity.

1. Multifractality - Turbulent flows consist of a hierarchy of spatial and temporal scales (Richardson, 1922). Systems exhibiting multiple scales require a spectrum of fractal dimensions to characterise their complexity (Murcio *et al.*, 2015). Such a system is referred to as a multifractal system. Fractality is related to the self-similar nature of flow structures with multiple spatial scales present in turbulent flows (Sreenivasan and Meneveau, 1986; Benzi *et al.*, 1993). Fractal theory provides a geometrically simple interpretation of the complexity in the system.

   During a state of stable operation, thermoacoustic systems exhibit low amplitude aperiodic fluctuations, commonly known as "combustion noise". Research findings within the last fifteen years indicate that combustion noise exhibits a multifractal signature (Gotoda *et al.*, 2012; Nair and Sujith, 2014; Unni and Sujith, 2015; Raghunathan *et al.*, 2020). This validates a lack of a singular characteristic spatial or temporal scale in thermoacoustic systems under stable operating conditions (Nair and Sujith, 2014). The multifractality phenomenon indicates the intricate dynamics that arise from the nonlinear interplay between combustion, flow, and acoustics in a turbulent thermoacoustic system. In contrast, periodic oscillations observed during thermoacoustic instability are distinguished by prominent temporal and length scales. The occurrence of thermoacoustic instability leads to the loss of multifractality (Nair and Sujith, 2014; Unni and Sujith, 2015).

2. Combustion noise is high-dimensional chaos - Historically, the stable functioning of a thermoacoustic system has been regarded as a fixed point (Lieuwen, 2002, 2012). Nevertheless, a system characterised by turbulent reactive flow does not exhibit true "silence", and the fluctuations present in the thermoacoustic system are regarded as stochastic fluctuations (Clavin *et al.*, 1994; Burnley and Culick, 2000; Lieuwen and Banaszuk, 2005). In a study conducted by Tony *et al.* (2015), the authors showed that the low amplitude aperiodic pressure fluctuations that arise during the steady operation of a thermoacoustic system exhibit deterministic behaviour and are indicative of high dimensional chaos (Musielak and Musielak, 2009). Furthermore, the authors found that the chaotic dynamics are influenced by white and coloured noise. In contrast, thermoacoustic instability is distinguished by periodic fluctuations, specifically, a state of order. Thermoacoustic instability refers to the phenomenon when a system undergoes a shift from a state of chaos to a state of order. The transition from the state of combustion noise to the state of thermoacoustic instability occurs through the state of intermittency. Intermittency

is characterised by epochs of periodic oscillations that appear apparently randomly between epochs of low amplitude aperiodic fluctuations (Nair *et al.*, 2014).

3. Pattern formation - The interaction between different subsystems, namely the hydrodynamic field, the reactive field (flame), and the acoustic field, plays a significant role in shaping the spatiotemporal dynamics of a turbulent combustor. George *et al.* (2018) demonstrated that order arising from chaos during the emergence of thermoacoustic instability can be attributed to the interplay between patterns created in different subsystems. The observed patterns consist of the standing wave pattern in the auditory field, the large-scale coherent structures in the flow field, and the coherent patterns of the flame. The authors proposed that the interactions among the three subsystems are facilitated by the evolving spatiotemporal patterns, resulting in coherence in the combustion dynamics. For example, the small-scale vortices interact with each other, leading to self-organisation in the reaction field that causes the periodic formation of large-scale structures and coherent patterns during the periodic epochs of intermittency and during the state of thermoacoustic instability (Unni and Sujith, 2017).

Conventional methodologies address the phenomenon of thermoacoustic instability by characterising it as a transition from a fixed point to limit cycle oscillations while disregarding the intermediate state of intermittency as the thermoacoustic system transitions from chaos to limit cycle oscillations. Furthermore, the conventional framework places a significant emphasis on the dynamics of the unsteady flame while disregarding the phenomenon of self-organisation present in the reactive field of the thermoacoustic system. This conventional approach focuses on analysing the intricate dynamics of the flame while neglecting to look into the interplay between the constituent elements of flame, flow and acoustics and the self-organisation arising from an interplay among all these subsystems. This reductionist method involves focusing on the individual components and thoroughly analysing each part. Conversely, under the framework of a complex system approach, emphasis is placed on the interplay among the constituent pieces.

A complex system is characterised as a system with numerous interconnected components, where the behaviour of the system as a whole cannot be easily deduced from the behaviour of its components (Smith *et al.*, 2003). When employing a complex system method, the practice involves refraining from dissecting and examining individual components and their behaviours. Instead, emphasis is placed on exploring the phenomena that might arise from an interplay among all the constituent subsystems. The fundamental components of complex systems encompass (1) the presence of interdependent elements that interact with one another, (2) the existence of nonlinear feedback mechanisms that exert influence on the behaviour of these systems, and (3) the exchange of energy and mass with the surrounding environment (Johnson, 2009). Turbulent thermoacoustic systems that incorporate turbulent reacting flow have all the aforementioned three ingredients. Thus, techniques such as complex networks are being used to understand the dynamics of a turbulent thermoacoustic system and utilize the acquired knowledge to control the thermofluid systems.

1.9.3 Complex networks in thermoacoustic systems

The field of thermoacoustic instability has also witnessed notable advancements through the application of complex networks. Murugesan and Sujith (2015) employed the visibility method to construct networks from time series of acoustic pressure oscillations obtained from swirl and bluff body stabilised turbulent combustors. Their findings revealed that the network structure corresponding to the state of combustion noise exhibits scale-free characteristics. The power-law distribution of the node degrees of the scale-free network is related to the scale invariance during the state of combustion noise. This scale-free nature indicates an absence of any single characteristic scale in the dynamics of combustion noise. The absence of any single characteristic scale during the state of combustion noise is difficult to discern simply from the power spectrum of acoustic pressure oscillations, as the power spectrum is dominated by the acoustic modes of the combustor. The authors further showed that scale-free behaviour observed during the state of combustion noise is lost when the turbulent combustor exhibits an orderly spatiotemporal behavior during the state of thermoacoustic instability.

Existence of scale-free behaviour in combustion noise and the emergence of scale-dependent order at the onset of thermoacoustic instability strengthened the idea of spectral condensation in thermoacoustic systems, which was further explored in Pavithran *et al.* (2020). Meanwhile, Okuno *et al.* (2015) utilised phase space networks and cycle networks to illustrate the high-dimensional nature of thermoacoustic instability. In their exploration of diverse dynamical states observed during the operation of a turbulent combustor, Godavarthi *et al.* (2017) and Gotoda *et al.* (2017) utilised recurrence network analysis, revealing that the topology of the recurrence network retains the structure of the reconstructed phase space. In a turbulent thermoacoustic system, Godavarthi *et al.* (2018) detected synchronisation transitions using recurrence network metrics. A combination of principal component analysis and sequential horizontal visibility graph motifs was utilised by Murayama *et al.* (2018) to construct a precursor of thermoacoustic instability in a swirl-stabilised combustor. Later, the same group combined the concept of transfer entropy with complex networks to detect the directed flow of information entropy between acoustic pressure local heat release rate fluctuation (Hashimoto *et al.*, 2019). Murayama and Gotoda (2019) used synchronisation and complex networks to explain the attenuation behaviour of thermoacoustic instability in an axial swirl stabilised combustor. Moreover, Kasthuri *et al.* (2020) investigated the recurrence characteristics of slow-fast dynamics in heat release rate oscillations within a laboratory-scale gas turbine turbulent combustor and the acoustic pressure oscillations in a model liquid rocket combustor during the state of thermoacoustic instability. Complex networks have also been used to explain the spatiotemporal dynamics of turbulent coaxial jet (Kobayashi *et al.*, 2019), and the presence of high-frequency thermoacoustic instability in model rocket engine combustor (Shima *et al.*, 2021; Kawano *et al.*, 2023). The application of complex networks and machine learning, along with an explosion in the research related to complex networks, presents an exciting future where networks will be utilised in understanding a wide variety of physical systems.

1.10 MOTIVATION

Thermoacoustic instability continues to pose substantial challenges across the aerospace and power generation sectors. Advancing our understanding of thermoacoustic instability necessitates using complex systems theory to investigate the connection among different subsystems constituting a turbulent thermoacoustic system: flame, flow, and acoustics.

An additional level of complexity arises due to the intricate dynamics induced by coupling a thermoacoustic system with itself and other thermoacoustic systems. In practice, this interaction occurs in can-annular and annular combustors in gas turbine engines. A combustor present in a can-annular configuration can interact with itself and with adjacent combustors through acoustic waves. On the other hand, a combustor in the annular configuration interacts with the adjacent combustors through acoustic waves, and hydrodynamics. During the last few years, the diverse dynamics arising from the interaction between adjacent can combustors within gas turbine engines have become a focal point for investigation. The prevalence of can-annular systems underscores the urgency of comprehending the underlying dynamics to address this issue effectively.

Beyond the confines of gas turbine engines, the implications of understanding the coupling of combustors in can-annular configuration extend far and wide. This understanding is pivotal in deciphering quenching dynamics within interconnected dynamical networks spanning a diverse array of nonlinear systems. These systems encompass a variety of fields, including biology (Roongthumskul *et al.*, 2021; Jiménez *et al.*, 2022), and ecological networks (Fan *et al.*, 2021), as well as engineering domains such as permanent-magnet synchronous motors (Zhang *et al.*, 2022) and multi-module floating airports (Xu *et al.*, 2018).

The present thesis is, therefore, motivated directly by the requirement of developing an understanding of the dynamics of coupled thermoacoustic systems.

1.11 OBJECTIVES

The present thesis attempts to shed light on the interaction between the acoustic and hydrodynamic fields present in the reaction field of a turbulent thermoacoustic system and establish a correlation between the local and global behaviour exhibited by the thermoacoustic system. More precisely, local dynamics are related to the spatiotemporal dynamics of the hydrodynamic and local heat release rate fields present in the reaction field of the combustor. In contrast, global dynamics refer to the global behaviour exhibited by the thermoacoustic systems and can be assessed through p' and the global heat release rate oscillations. Consequently, the dynamics of the local hydrodynamic and heat release rate fields are expected to play a dominant role in the acoustic pressure and global heat release rate oscillations exhibited by a thermoacoustic system.

Furthermore, a combustor present in can-annular configurations can interact with itself through acoustic waves that reflect from the upstream face of first turbine stage. In this case, the length of the combustor-turbine gap plays a crucial role in determining the time delay with which the acoustic field of a single combustor will interact with itself. An appropriate choice of this time delay can have significant implications on the passive control of thermoacoustic instability. Finally, the mitigation of thermoacoustic instability in combustors depends significantly on the acoustic interaction a combustor has with the adjacent combustors. Thus, there is a need to further our understanding of the dynamics of two mutually coupled thermoacoustic systems, emphasising the mitigation of thermoacoustic instability. In cognisance of the above, the objectives of the thesis are:

1. To characterise and quantify the interplay between hydrodynamic and acoustic fields in a thermoacoustic system.

2. To understand the dynamics of the thermoacoustic system subjected to delayed acoustic self-feedback and its implications on the control of thermoacoustic instability.

3. To utilise a combination of asynchronous quenching and mutual coupling to increase the parametric region of amplitude death in a system of two coupled thermoacoustic systems.

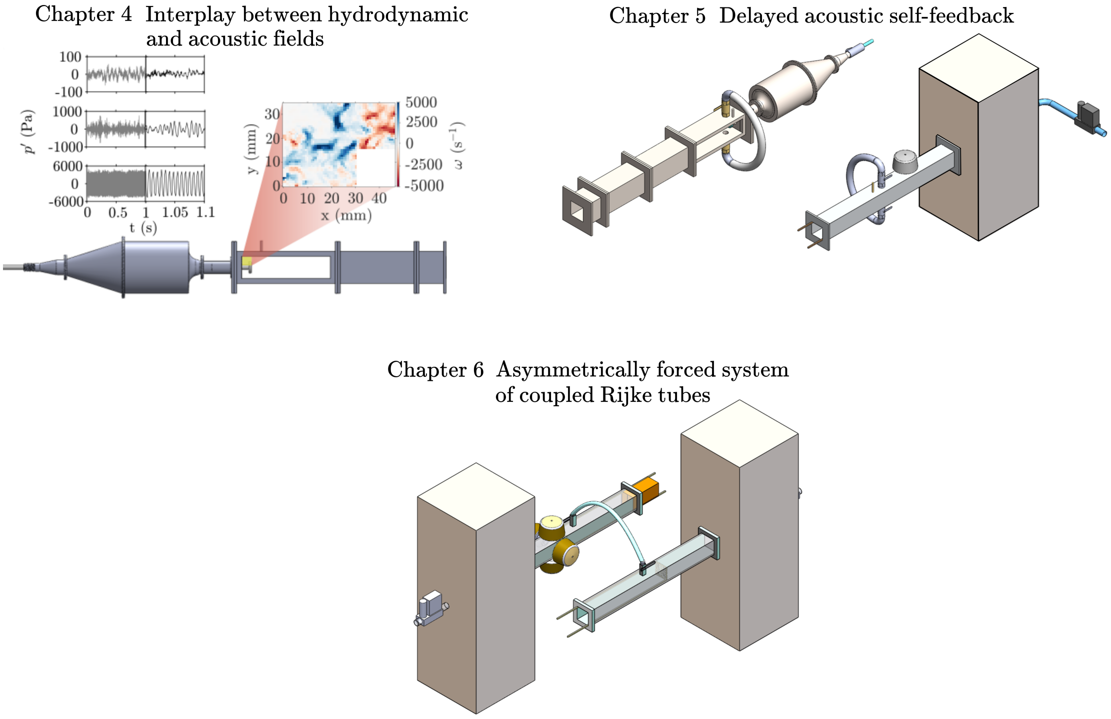
Chapter 4 Interplay between hydrodynamic and acoustic fields
100
0
-100
1000
0
-1000
6000
0
-6000
p′ (Pa)
0
0.5
1
1.05
1.1
t (s)
30
20
10
0
y (mm)
0
10
20
30
40
x (mm)
5000
2500
0
-2500
-5000
ω (s⁻¹)
Chapter 5 Delayed acoustic self-feedback
Chapter 6 Asymmetrically forced system of coupled Rijke tubes

Figure 1.15: Structure of this thesis. In Chapter 4, we analyse the interplay between acoustic pressure oscillations and interactions between regions of intense vorticity in the reactive field of a turbulent combustor. In Chapter 5, we introduce delayed acoustic self-feedback to mitigate thermoacoustic instability in laminar and turbulent thermoacoustic systems. Finally, in Chapter 6, we show the results obtained from experiments and reduced-order modelling of asymmetrically forced two mutually coupled thermoacoustic systems.

1.12 OVERVIEW OF THE THESIS

The thesis is organised as follows. In **Chapter 2**, we[1] give an overview of the complex networks and community detection used to study the interplay between the hydrodynamics and acoustic fields in a single thermoacoustic system. We discuss the methodologies of constructing temporal weighted directed vortical networks and the Louvain algorithm we use to detect vortical communities. Subsequently, we expound on the role of complex networks in improving our understanding of thermofluid systems.

Chapter 3 summarises the description of experimental setups where the experiments reported in this thesis were conducted. We explain the experimental procedure and the diagnostic techniques for obtaining the flame, flow, acoustic pressure, and global heat release rate data.

In **Chapter 4**, we analyse the interplay between acoustic field and interactions between regions of intense vorticity in the reactive field of a turbulent combustor. We show that the mean and maximum of all inter-community interactions exhibit a strong delayed correlation with the acoustic pressure oscillations during the state of thermoacoustic instability. In contrast, during the state of combustion noise (stable operation), the correlation between the acoustic pressure oscillations and the inter-community interactions is lost due to incoherent spatiotemporal behaviour.

In **Chapter 5**, we introduce delayed acoustic self-feedback to mitigate thermoacoustic instability in laminar and turbulent thermoacoustic systems effectively. The response of the thermoacoustic systems to different coupling parameters is characterised using temporal and spatiotemporal analysis techniques.

Chapter 6 summarises the results obtained from experiments and reduced-order modelling of asymmetrically forced two mutually coupled thermoacoustic systems. We analyse the forced response of a laminar Rijke tube and study the idea of unidirectional external acoustic forcing to mitigate thermoacoustic instability through asynchronous quenching. Subsequently, we investigate the role of coupling and system parameters toward achieving amplitude death in a system of two mutually coupled laminar Rijke tubes. In the final part of this chapter, we discuss the results obtained from experiments and mathematical model of an asymmetrically forced system of mutually coupled Rijke tubes. We show the enhancement of the region of oscillation quenching of thermoacoustic instability in the system of coupled identical Rijke tubes by compounding the effect of asynchronous quenching and mutual synchronisation.

---

[1] I use the pronoun “we” throughout this dissertation, as the successful completion of my research would not have been possible without the collaboration with others.

We conclude our discussions in **Chapter 7**, where we highlight the key findings of the present thesis, discuss the context of these findings, and their practical implications. We finally discuss the future direction of the current work.

CHAPTER 2

COMPLEX NETWORKS AND COMMUNITY DETECTION

The term “network” is commonly employed in everyday discourse to denote a complex interconnection of individuals or a conglomerate of tangible entities. Airline networks, power grid networks, social networks, neural networks, communication networks, and food chain networks are among the prominent networks widely recognised. In the last thirty years, network science has gained prominence as an interdisciplinary academic discipline that integrates several fields such as graph theory, dynamical systems, statistical physics, data science, control theory, climatology, and biology (Newman, 2008; Barabási, 2009; Newman, 2018; Barabási, 2013; Latora *et al.*, 2017; Cohen and Havlin, 2010). The effects of network science research extend beyond the realm of basic research and are observed by a broader audience encompassing the general population (Costa *et al.*, 2011).

The field of network science has its foundations in graph theory, which may be traced back to Leonhard Euler’s resolution of the Königsberg bridge problem (Euler, 1741). Examining a collection of interrelated components through mathematical analysis has resulted in the development of graph theory, which incorporates methods from algebra and geometry (Bollobás, 1998; Diestel, 2000). Recently, there has been a resurgence of interest, spearheaded by scholars with a background in statistical physics, in establishing the fundamental principles for examining contemporary networks of significant scale (Newman, 2003; Barabási, 2013). The industry and government have provided extensive support for their endeavours in researching communication networks (Faloutsos *et al.*, 1999), information networks (Sun and Han, 2013), and social networks (Otte and Rousseau, 2002). These studies have significant implications for resource management

(Prell *et al.*, 2009) and national security (Ressler, 2006). In a broader context, the utilisation of applications has been observed in several domains, such as semantic networks within the field of linguistics (Sowa *et al.*, 1992), ecological networks (Montoya *et al.*, 2006), biological networks (Junker and Schreiber, 2008), and knot theory within the realm of algebraic topology (Crowell and Fox, 2012). Mapping structural and functional connections in the human brain is considered a successful application of network science (Bassett and Bullmore, 2006; Lynn and Bassett, 2019). These studies support medical research focused on treating various medical diseases, such as Alzheimer's disease and schizophrenia (Lynn and Bassett, 2019). Furthermore, the utilisation of network-based transmission models has enhanced the formulation of approaches for allocating a constrained quantity of vaccines to a substantial populace in the era of the global health crisis (Tetteh *et al.*, 2021).

The field of fluid mechanics investigates the intricate dynamics and multiscale spatiotemporal characteristics that emerge from the interactions between vortices and flow structures (Taira *et al.*, 2016). Historically, scholars have examined these connections through rigorous theoretical pursuits. The availability of substantial computational resources and recent advancements in large-scale network algorithms have rendered network science-inspired analysis an appealing approach for examining fluid dynamics from a contemporary complex dynamics standpoint. The field of network science offers a theoretical framework for discerning the fundamental structure of relationships, enabling the analysis of complicated interactions by breaking down their structural and dynamic features. Readers can read through Iacobello *et al.* (2021) and Taira and Nair (2022) to understand the state-of-the-art network-inspired analysis of vortical flows.

In this chapter, we briefly explore the use of complex networks in fluid mechanics through vortical networks and the application of community detection in vortical networks.

2.1 COMPLEX NETWORK DESCRIPTION OF VORTICAL INTERACTIONS

Complex networks are fundamental in various fields, encompassing diverse systems such as social interactions, neural connections, and the internet. They are characterised by nodes and edges, representing entities and their relationships, respectively.

In a network, nodes are the entities or elements of interest. These can represent anything from individuals in a social network to routers in a computer network. Edges, on the other hand, denote the connections or relationships between these nodes. Edges define how nodes are linked and interact, forming the foundation of the network's structure (Barabási, 2013).

Edges in a network can have weights associated with them. Edge weights represent the strength, intensity, or significance of the relationship between connected nodes. Edge weights can be binary or non-binary. In the case of binary edge weights, the connections are considered either present (1) or absent (0). In contrast, non-binary edge weights imply weighted networks, where numerical values represent connections with varying strengths.

Networks can be categorised as directed or undirected, as shown in Fig. 2.1. In directed networks, the edges have a specific direction, indicating a one-way relationship between nodes. For example, in a social network, directed edges can represent followers and followees. In undirected networks, edges lack direction, representing a bidirectional or symmetric relationship between nodes. These networks capture mutual interactions.

The information of a network can often be encoded using an adjacency matrix. This square matrix is where rows and columns correspond to nodes. The elements of the matrix represent the connections between nodes. In the case of unweighted networks, the elements are typically 0 or 1, denoting the absence or presence of connections. For weighted networks, the elements can take on various numerical values, indicating the strength of the connections.

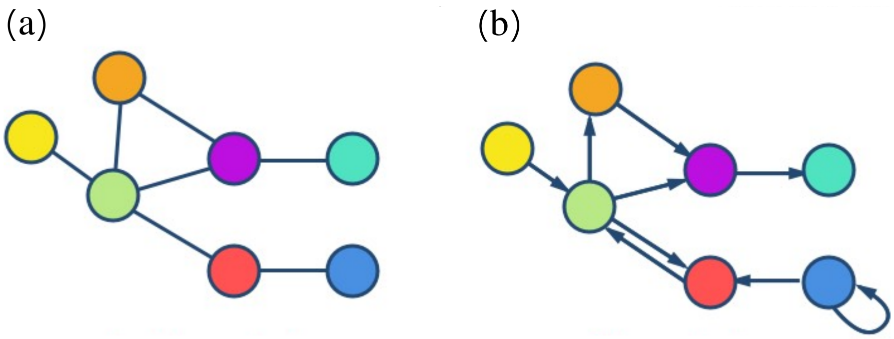

Figure 2.1: (a) Undirected and (b) directed networks.

In directed networks, the adjacency matrix is typically asymmetrical. This means that the presence or absence of connections can differ depending on the direction of the edge. On the other hand, undirected networks have symmetrical adjacency matrices. In these matrices, the element in row i and column j is the same as the element in row j and column i, reflecting the mutual nature of relationships between nodes.

Taira *et al.* (2016) introduced weighted network analysis as a method to characterise the vorticity interactions in a two-dimensional decaying isotropic turbulent flow field obtained from direct numerical simulations. The nodes of the network were the cells in the computational grid representing the vortical elements in the flow field, and the weight of the link was the average velocity induced by the vortical elements. The induced velocities were calculated using the Biot–Savart law (Taira *et al.*, 2017). Gopalakrishnan Meena *et al.* (2018) used this *vortical network* to formulate reduced-order models for laminar wake flows on a circular cylinder and an airfoil with a Gurney flap. The authors used the model to predict lift and drag forces on bluff bodies in wake flows. Gopalakrishnan Meena and Taira (2021) used this framework to identify groups of closely connected vortical nodes, called communities, in a network constructed from two- and three-dimensional isotropic turbulence. Through the interactions between different communities, they found the most influential community that has the potential to alter the system dynamics dramatically. By utilising inter-community connections, they demonstrated that local turbulent mixing

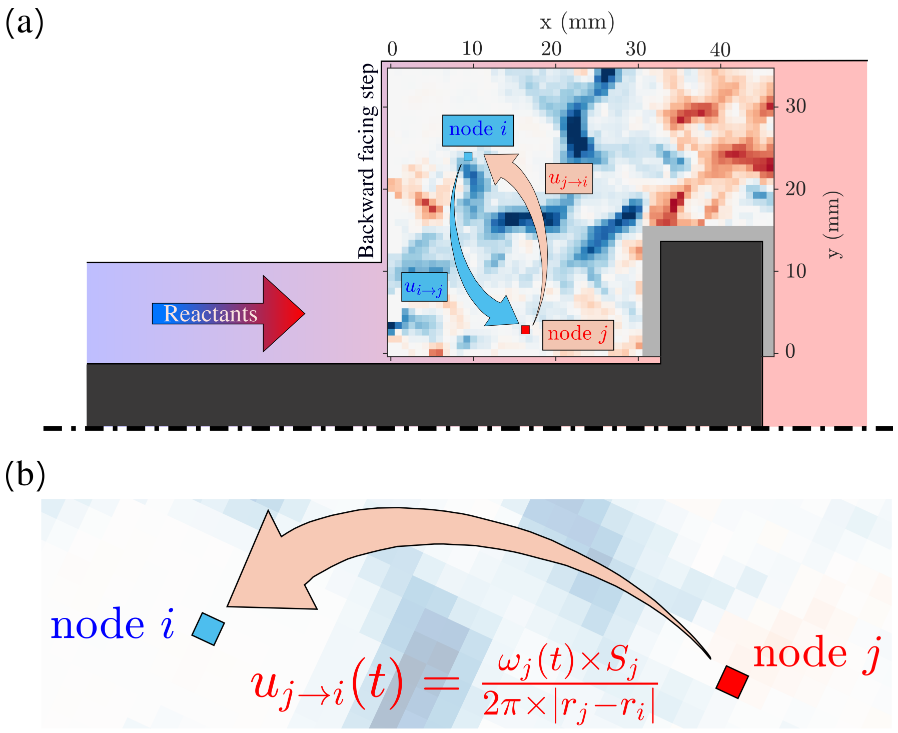
(a)
x (mm)
0
10
20
30
40
Backward facing step
node i
$u_{j\to i}$
$u_{i\to j}$
node j
Reactants
30
20
10
0
y (mm)
(b)
node i
node j
$u_{j\to i}(t) = \frac{\omega_j(t)\times S_j}{2\pi\times|r_j - r_i|}$

Figure 2.2: (a) Interactions between two vortical elements in the vorticity field calculated from the experimental velocity field in the turbulent combustor. $u_{i\to j}$ denotes the velocity induced by the node i on node j, and vice-versa. The reactants enter the reaction field from the left side. During the states of periodic epochs of intermittency and thermoacoustic instability, vortices are shed at acoustic pressure minima from the backward facing step. The cross-hatched region indicates the bluff body and the shaft holding the bluff body. (b) The expression used to calculate the induced velocity from node j to node i takes into account the area of node j, i.e., S_j, and the distance between the two nodes given by $|\boldsymbol{r}_j - \boldsymbol{r}_i|$. This expression for a discretized flow domain is obtained from equation 2.2 that is valid for a continuous flow domain.

could be improved using vortical structures associated with low circulation.

In the ensuing section, we discuss the methodologies of network construction, community detection, and community-based dimensionality reduction of complex networks. These concepts are used in Chapter 4 of this thesis.

2.2 VORTICAL NETWORK CONSTRUCTION

We adopt the framework used in Gopalakrishnan Meena and Taira (2021) to construct vortical networks from the vorticity data obtained through particle image velocimetry (PIV) measurements. The details of the experimental setup and data acquisition techniques are discussed in the next chapter. Velocity data is acquired from a two-dimensional plane illuminated with a laser sheet inside the reaction field of a turbulent combustor. Thus, the vorticity used in this study is out-of-plane vorticity with the velocity components in the horizontal (x) and vertical (y) directions (Raffel *et al.*, 1998). We discretise the out-of-plane vorticity field and refer to the discrete fluid elements as nodes, which we call vortical nodes. We consider the induced velocity imposed by any vortical node on others to characterise the interactions between them (figure 2.2). The Biot–Savart law (Taira *et al.*, 2017) provides the following expression to calculate the induced velocity from a vortical element as a function of circulation and distance between the vortical elements:

$$\boldsymbol{u}(\boldsymbol{r},t) = \frac{1}{2(n_d-1)\pi}\int_S \frac{\boldsymbol{\omega}(\boldsymbol{r}',t)\times(\boldsymbol{r}-\boldsymbol{r}')}{\|\boldsymbol{r}-\boldsymbol{r}'\|_2^{n_d}}\,\mathrm{d}S, \tag{2.1}$$

where $\boldsymbol{u}(\boldsymbol{r},t)$ is the induced velocity at a time instant t at location $\boldsymbol{r}$ in the spatial domain from a group of vortical elements enclosed in area S with a vorticity distribution of $\boldsymbol{\omega}(\boldsymbol{r}',t)$ at positions $\boldsymbol{r}'$. Here, $n_d = 2$ is the spatial dimension of the vorticity field in the present study. The Euclidean norm is denoted by $\|\cdot\|_2$. From the perspective of point vortices, the velocity induced by a vortical node (element) i on a vortical node j is evaluated as

$$u_{i\to j} = \frac{1}{2(n_d-1)\pi}\int_{S_i} \frac{\omega_i(\boldsymbol{r}',t)\times\left(\boldsymbol{r}_j-\boldsymbol{r}_i'\right)}{\left\|\boldsymbol{r}_j-\boldsymbol{r}_i'\right\|_2^2}\,\mathrm{d}S_i, \tag{2.2}$$

where $u_{i\to j}$ denotes the magnitude of velocity induced by vortical node i on a vortical node j. S_i denotes the area of the fluid element that corresponds to the vortical node i. The corresponding equation for a discretized flow domain can be expressed as

$$u_{i\to j} = \frac{\omega_i(t)\times S_i}{2\pi|\boldsymbol{r}_j-\boldsymbol{r}_i|}, \tag{2.3}$$

where S_i denotes the area of the flow domain node i. A structured grid with all the cells in the flow domain having equal area is used in the analysis of the PIV data acquired for this study. For a vortical flow network consisting of n nodes, the weighted adjacency matrix $A \in \mathbb{R}^{n\times n}$ for this network is defined as

$$A_{ij} = \begin{cases} w_{ij}, & i \neq j \\ 0, & i = j, \end{cases} \tag{2.4}$$

where w_{ij} is the edge weight given by

$$w_{ij} = \alpha u_{i\to j} + (1-\alpha)u_{j\to i}, \tag{2.5}$$

with $\alpha \in [0, 1]$ being a parameter to capture the induced velocity direction to construct the vortical network. $\alpha = 0$ or 1 gives a directed adjacency matrix, whereas $\alpha = 1/2$ yields a symmetric adjacency matrix corresponding to an undirected network. In the present study, we use $\alpha = 0$ to define the weighted directed vortical network as

$$A_{ij} = u_{j\to i}. \tag{2.6}$$

The above formulation gives an asymmetric adjacency matrix with non-binary entries, representing a weighted directed network. Adding directions to the edges helps to differentiate between the influential and influenced vortical nodes (Barabási, 2013). The adjacency matrix contains zero values on its diagonal due to the absence of velocity influence between vortical nodes onto themselves. As every vortical node is interconnected with all others, the vortical network is a complete graph.

2.3 COMMUNITY DETECTION

For large networks, the identification of clusters or communities of interconnected nodes proves to be a valuable undertaking. Community detection is a highly effective technique in the field of network research, which aims to cluster nodes that exhibit significant interconnections into cohesive communities. The nodes of a recognised community exhibit strong interconnections while minimising the presence of edges connecting distinct communities.

The method of community detection comes under the more general topic of graph partitioning. Graph partitioning can be accomplished using local search techniques, such as the Kernighan-Lin algorithm (Kernighan and Lin, 1970), which depend on an arbitrary initial partition, as well as global strategies, such as spectral partitioning (McSherry, 2001), which rely on overall network features. Spectral partitions are obtained by utilising the approximate eigenvectors of the adjacency matrix. This particular approach exhibits resemblances to grid partitioning, a widely utilised technique in parallel fluid dynamics simulations, aiming to minimise interprocessor connections (Xiong *et al.*, 2018). In numerous instances, the pre-existing knowledge on the number of communities within a network may be lacking. One often employed approach in the exploration of networked systems for the identification of naturally occurring clusters involves the maximisation of network modularity (Newman, 2006).

Modularity maximisation is a technique for community detection that is frequently used to identify communities (Newman and Girvan, 2004). This technique seeks to optimise the modularity quality function, M, by dividing the nodes of a network into K nonoverlapping communities, $C_1, C_2, ..., C_K$. To receive a higher M score, the communities that a partition defines should be internally more dense than what can be predicted by chance. The community structure of a network is therefore assumed to be best represented by the division that gets the highest value of M. Modularity M is given by

$$M = \frac{1}{2n_e} \sum_{ij} \left[A_{ij} - \gamma_M \frac{s_i^{in} s_j^{\text{out}}}{2n_e} \right] \delta\left(c_i, c_j\right), \tag{2.7}$$

where

$$s_i^{\text{out}} = \sum_j A_{ji} \quad \text{and} \quad s_i^{in} = \sum_j A_{ij}. \tag{2.8a, b}$$

s_i^{out} and s_i^{in} denote the out- and in-strengths of a node, respectively. In (2.7), γ_M is the resolution parameter to detect the presence of large or small communities in the network (Reichardt and Bornholdt, 2006; Fortunato and Barthelemy, 2007), n_e is the total number of edges in the network, $\delta\left(c_i, c_j\right)$ is the Kronecker delta, $c_i \in \hat{C}_k$ is the label of the community to which node i is assigned, and $\hat{C}_k$ is the set of k community in the network. Here, $k = 1, 2, ..., K$, with K being the total number of communities. K is not a user-defined variable and is determined by the community detection algorithm used. Various algorithms are available to detect the communities in a network (Fortunato, 2010). In the present study, we use the method introduced by Blondel *et al.* (2008) to detect communities. We refer to these detected communities on vortical networks as vortical communities (Gopalakrishnan Meena *et al.*, 2018). In this study, we use $\gamma_M = 1$ for detecting vortical communities during all three dynamical states. Furthermore, the fluid elements with high vorticity play an important role in the dynamics exhibited by the turbulent combustor. Thus, we neglect the effects of fluid elements with low vorticity. We consider only those spatial locations for nodes in vortical communities that exhibit vorticity magnitude above $\omega = 456\ s^{-1}$, $380\ s^{-1}$, and $843\ s^{-1}$ during the states of combustion noise, intermittency, and thermoacoustic instability, respectively. Further details on calculations for these threshold values are provided in Appendix A.

2.4 COMMUNITY-BASED NETWORK REDUCTION AND INTERACTION OF VORTICAL COMMUNITIES

It is not easy to characterise the interactions between the vortical components since the spatiotemporal dynamics exhibited by the turbulent combustor are high-dimensional in nature. Analysis, simulation, and modelling of dynamics on such large networks demand massive amounts of processing power and necessitate decreasing the problem's

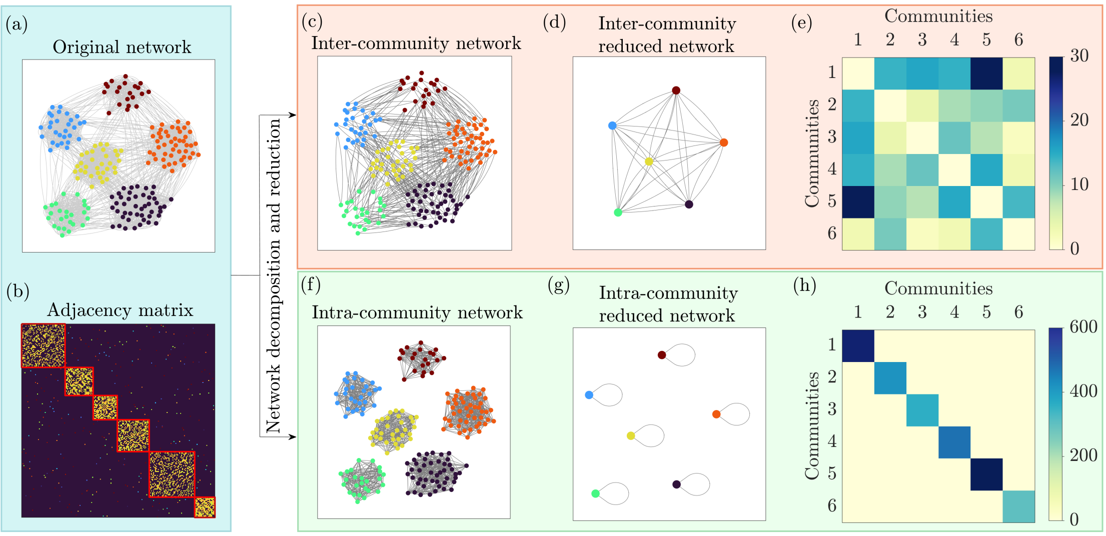
(a)
Original network
(b)
Adjacency matrix
Network decomposition and reduction
(c)
Inter-community network
(d)
Inter-community reduced network
(e)
Communities
1 2 3 4 5 6
Communities
1 2 3 4 5 6
30
20
10
0
(f)
Intra-community network
(g)
Intra-community reduced network
(h)
Communities
1 2 3 4 5 6
Communities
1 2 3 4 5 6
600
400
200
0

Figure 2.3: An overview of community-based reduction of a complex network. (a) A random modular graph having six communities layout according to the Fruchterman-Reingold algorithm (Fruchterman and Reingold, 1991), and the corresponding adjacency matrix in (b). The modular nature of the network manifests as a block structure in the adjacency matrix. The original network can be decomposed into two sub-networks: (c) an inter-community network comprising edges present only across different communities, and (f) an intra-community network comprising edges present only within the individual communities. Each community is now considered as a single node. All the edges between any pair of communities shown in (c) can be summed up to obtain (d) a reduced inter-community network, and (e) the corresponding adjacency matrix. Similarly, all the edges within each community, as shown in (f), can be summed up to obtain (g) a reduced inter-community network, and (h) the corresponding adjacency matrix.

computational complexity while preserving the fundamental physics of the system. We use a sample model problem as shown in Fig. 2.3 to demonstrate our dimensionality reduction method in the current study. In Fig.2.3, we consider a sample random modular graph constructed using methods discussed in Lancichinetti *et al.* (2008). Each node i has a scalar weight, γ_i, associated with it. This scalar weight is analogous to the vorticity value of each fluid element in a flow system. In Fig. 2.3(b), we cluster the nodes into network communities using the Louvain algorithm (Blondel *et al.*, 2008). We decompose the original network into inter-community and intra-community networks in Figs. 2.3(c) and 2.3(f), respectively. The inter-community network is further condensed to a weighted-centroid-based network (Gopalakrishnan Meena *et al.*, 2018) in Fig. 2.3(d). The weighted centroids of each community are calculated using

$$\boldsymbol{\xi}_k = \frac{\sum_{i \in C_k} \gamma_i \boldsymbol{r}_i}{\sum_{i \in C_k} \gamma_i}, \quad k = 1, 2, \ldots, m \tag{2.9}$$

and the sum of all the scalar weights belonging to nodes of each community

$$\Gamma_k = \sum_{i \in C_k} \gamma_i \tag{2.10}$$

is concentrated at the community centroid, reducing the community to a single node at the respective community centroid. Here, $\boldsymbol{r}_i$ denotes the position vector of each node i. Γ_k is the node attribute of each node in the community-based reduced network, where k refers to the k^{th} community present in the original network. By employing this framework for the vortical network, we use the weight of each community centroid and the position vector to reconfigure the vortical network and reduce the dimensions of the system.

We use the aforementioned techniques on the two-dimensional velocity data acquired from a bluff-body stabilised turbulent combustor through PIV measurements. In the next chapter, we discuss the details of the turbulent combustor and other experimental setups and data acquisition techniques related to the results presented in the present thesis.

CHAPTER 3

EXPERIMENTAL SETUPS AND DIAGNOSTICS

In this chapter, we discuss the experimental facilities and diagnostics used for conducting experiments and acquiring data related to the results presented in this thesis. Four studies were performed on primarily two different setups:

1. Data set for a bluff body stabilised turbulent combustor was used to study the interplay between hydrodynamic and acoustic fields present in the reaction field of the combustor. **The data set was acquired by a team consisting of Dr. Nitin Babu George, Dr. Manikandan Raghunathan, Mr. Midhun P. R. and Prof. R. I. Sujith in February 2018.**

2. A steel-braided flexible tube is attached to the aforementioned bluff body stabilised turbulent combustor to study the effects of delayed acoustic self-feedback in a turbulent thermoacoustic system.

3. A system of two mutually coupled Rijke tubes is utilised for studying the dynamics of coupled thermoacoustic oscillators, with an emphasis on the mitigation of thermoacoustic instability. The same setup is subsequently used to analyze the combined effects of asynchronous quenching and mutual coupling through an asymmetrically forced system of mutually coupled Rijke tubes.

4. One of the aforementioned Rijke tubes is used to conduct detailed investigations of

---

The content of this chapter is present in the following articles:

1. Sahay, A., Meena, M. G., & Sujith, R. I. (2023), Insights into the interplay between hydrodynamic and acoustic fields in a turbulent combustor via community-based dimensionality reduction of vortical networks, arXiv. `https://arxiv.org/abs/2311.12541`

2. Sahay, A., Roy, A., Pawar, S. A., & Sujith, R. I. (2021), Dynamics of coupled thermoacoustic oscillators under asymmetric forcing, *Physical Review Applied*, 15(4), 044011. `https://doi.org/10.1103/PhysRevApplied.15.044011`

3. Srikanth, S., Sahay, A., Pawar, S. A., Manoj, K., & Sujith, R. I. (2022). Self-coupling: An effective method to mitigate thermoacoustic instability. *Nonlinear Dynamics*, 110(3), 2247-2261. `https://doi.org/10.1007/s11071-022-07750-7`

4. Sahay, A., Kushwaha, A., Pawar, S. A., Dhadphale, J. M., & Sujith, R. I. (2023). Mitigation of limit cycle oscillations in a turbulent thermoacoustic system via delayed acoustic self-feedback. *Chaos: An Interdisciplinary Journal of Nonlinear Science*, 33(4), 043118. `https://doi.org/10.1063/5.0129512`

delayed acoustic self-feedback in a thermoacoustic system. Additionally, the same setup is used to analyze the forced response of a laminar thermoacoustic system toward external acoustic forcing.

3.1 BLUFF-BODY STABILISED TURBULENT COMBUSTOR

A schematic of a bluff-body stabilised combustor with a rectangular cross-section, possessing dimensions of $1100 \times 90 \times 90$ mm^3, is shown in Fig. 3.1. The combustor comprises a settling chamber, a burner section, and a rectangular duct. In order to protect the flow entering the combustor from upstream disturbances, compressed air first enters the settling chamber. The fuel (liquefied petroleum gas - 60% butane + 40% propane) is injected upstream of the backward-facing step (59 mm upstream of the bluff-body) through four 1 mm diameter holes bored symmetrically around the circular shaft holding the bluff-body in the combustor. Thus, the fuel gets partially mixed in the air stream as it enters the combustor. An 11 kV ignition transformer is used to spark ignite the partially premixed air fuel mixture at the backward-facing step. The flame stabilisation device is a bluff-body in the shape of a circular disc with a diameter of 47 mm and a thickness of 10 mm, and is positioned 35 mm downstream of the backward-facing step. The combustion products are exhausted through a long duct into the atmosphere via a decoupler. The decoupler is a large chamber used to keep the combustor exit at an acoustically open boundary state ($p' \approx 0$) and decouple the combustor from external perturbations.

In the experiments, the fuel flow rate $\dot{m}_f$ is maintained at a constant value ($\dot{m}_f = 30 \pm 0.44$ standard litre per minute (SLPM)), and the air flow rate $\dot{m}_a$ is varied ($480 \pm 7.84 \leq \dot{m}_a \leq 780 \pm 10.24$ SLPM) which changes the global equivalence ratio ($\phi = (\dot{m}_f/\dot{m}_a)_{\text{actual}}/(\dot{m}_f/\dot{m}_a)_{\text{stochiometric}}$), of the reactant mixture from 0.97 to 0.57. The maximum uncertainty in the calculation of ϕ is ± 0.02. Digital mass flow controllers (Alicat Scientific - MCR Series, 100 SLPM model for fuel flow, 4000 SLPM for the main air flow) are used to control the flow rates of air and fuel. The mass flow controllers have an uncertainty of ± (0.8 % of reading + 0.2 % of full scale). The Reynolds number

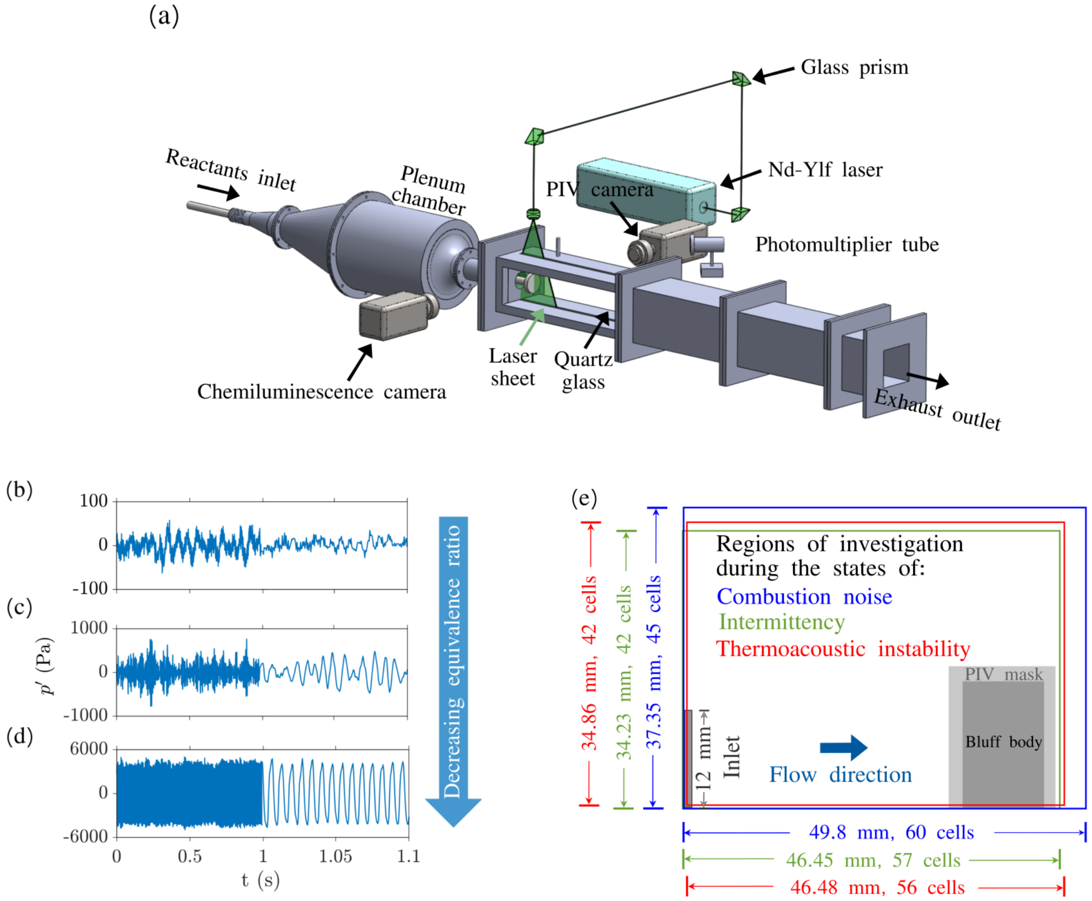
(a)
Glass prism
Reactants inlet
Plenum chamber
PIV camera
Nd-Ylf laser
Photomultiplier tube
Chemiluminescence camera
Laser sheet
Quartz glass
Exhaust outlet
(b)
100
0
-100
(c)
1000
0
-1000
(d)
6000
0
-6000
p' (Pa)
0
0.5
1
1.05
1.1
t (s)
Decreasing equivalence ratio
(e)
Regions of investigation during the states of:
Combustion noise
Intermittency
Thermoacoustic instability
PIV mask
Bluff body
Flow direction
Inlet
12 mm
34.86 mm, 42 cells
34.23 mm, 42 cells
37.35 mm, 45 cells
49.8 mm, 60 cells
46.45 mm, 57 cells
46.48 mm, 56 cells

Figure 3.1: (a) Schematic diagram of the experimental set-up. We simultaneously acquire the acoustic pressure measurement, high-speed flame images, and high-speed PIV for the current study. (b-d) The time series of acoustic pressure fluctuations during the states of combustion noise, intermittency, and thermoacoustic instability. (c) Schematic of the combustor cross-section indicating the PIV regions of investigation for different dynamical states. (a) adapted from Krishnan *et al.* (2019*b*) with permission from Cambridge University Press.

(calculation based on the flow conditions of the air at the inlet of the combustor) is the control parameter, and is varied from 19300 to 31300, with a maximum uncertainty of ±400 (1.28 %).

3.1.1 Measurements and data acquisition

The acoustic pressure fluctuations $p'(t)$ are measured using a PCB103B02 piezoelectric transducer (sensitivity: 217.5 mV/kPa and uncertainty: ±0.15 Pa) mounted on the combustor wall, at 20 mm downstream of the backward facing step. A photomultiplier tube (PMT, Hamamatsu H10722-01) equipped with a CH* filter (wavelength of 430 nm and 12 nm FWHM) is used to capture the global heat release rate fluctuations $\dot{q}'(t)$ in the flame. Both p' and $\dot{q}'$ signals are simultaneously acquired for 3 s at a sampling rate of 10 kHz using an A/D card (NI-6143, 16 bit). The frequency bin size in the power spectrum is 0.3 Hz. High-speed OH* chemiluminescence images of the flame are simultaneously captured with p' and $\dot{q}'$ signals at 2000 fps for 2 s using a CMOS camera (Phantom - V12.1 with a ZEISS 50 mm camera lens). The OH* chemiluminescence represents the local heat release rate ($\dot{q}'(x, y, t)$) as the intensity of light emitted by OH* radicals is proportional to the chemical reaction rate (Hardalupas and Orain, 2004).

High-speed two component particle image velocimetry is performed to acquire the two components of velocity (V_x: streamwise parallel to the flow direction and V_y: perpendicular (cross-stream) to the flow direction). The reactive flow field is seeded with ≈ 1 mm sized TiO_2 particles (Kronos make product - 1071). The Stokes number (St) of the seeded flow is 7×10^{-4}. For such low values of St ($St << 1$), the seeded particles faithfully follow the streamlines (Raffel *et al.*, 1998). A single cavity double pulsed Nd:YLF laser (with 527 nm and a pulse width of 250 ns) is used to illuminate the flow through a narrow quartz window ($400 \times 20 \times 10$ mm^3) on the top wall of the combustion chamber.

To capture the Mie scattering light from the seeding particles, a high-speed CMOS camera (Photron FASTCAM SA4) is synchronised with the laser pulses. A short band pass optical filter (centred at 527 nm with 12 nm FWHM) is mounted in front of the lens to capture the Mie scattered light. A total of 3797 Mie Scattering image pairs are recorded for approximately 2 seconds. The physical dimension of the region of interest used for the analysis of PIV is 50 mm × 36 mm, located just downstream of the backward facing step and slightly above the bluff-body shaft. The Mie scattered images are processed using PIVview2C software (PIVTEC GmbH). We use the cross-correlation algorithm to calculate the velocity fields (Raffel *et al.*, 1998). After further processing of the raw velocity data, the final velocity data corresponding to the region of interest at each time instant during the three dynamical states has the following dimensions:

1. Combustion noise - 37.35 mm × 49.8 mm, corresponding to 45 × 60 pixels.
2. Intermittency - 34.23 mm × 46.45 mm, corresponding to 42 × 57 pixels.
3. Thermoacoustic instability - 34.86 mm × 46.48 mm, corresponding to 42 × 56 pixels.

A detailed explanation of the high-speed chemiluminescence imaging technique and the preprocessing and post-processing algorithms employed for the analysis of Particle Image Velocimetry (PIV) data, as well as a comprehensive discussion concerning velocity uncertainties, can be found in George *et al.* (2018). Additional details are available in the supplementary material provided by Krishnan *et al.* (2019*a*).

3.2 BLUFF-BODY STABILISED TURBULENT COMBUSTOR WITH DELAYED ACOUSTIC SELF-FEEDBACK

We experimentally demonstrate the application of delayed acoustic self-feedback of the acoustic field to mitigate thermoacoustic instability in the bluff-body stabilised turbulent combustor discussed in the previous section. In this study, the bluff body is positioned 30 mm downstream of the dump plane. The global equivalence ratio is varied from 1.00 to approximately 0.6, with an uncertainty of ±0.02. The air flow rate varies from 527 to 900 SLPM (standard litre per minute), with a maximum uncertainty in the flow rate of air

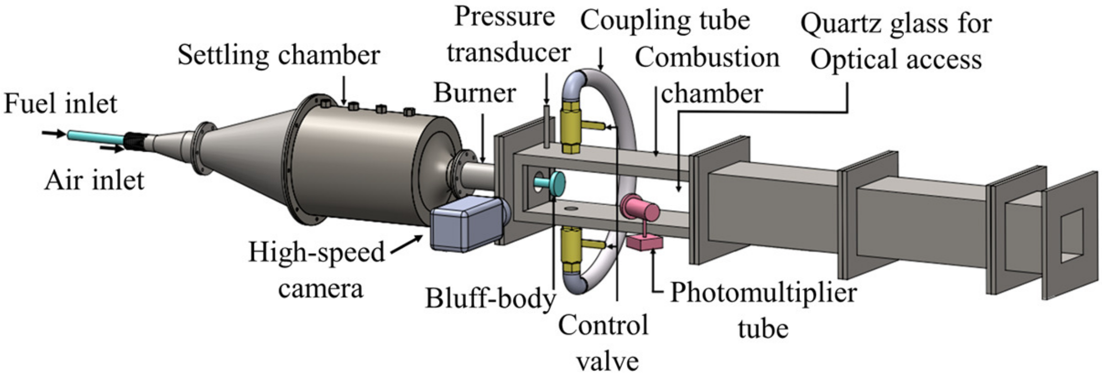
Fuel inlet
Air inlet
Settling chamber
Pressure transducer
Burner
Coupling tube
Combustion chamber
Quartz glass for Optical access
High-speed camera
Bluff-body
Control valve
Photomultiplier tube

Figure 3.2: The schematic of a turbulent bluff body stabilised combustor subjected to delayed acoustic self-feedback using a single coupling tube.

being ±10.24 SLPM. The fuel flow rate is kept constant at 34 SLPM, and the maximum uncertainty in the fuel flow rate is ±0.44 SLPM. The Reynolds number of the air flow increases in the range of 14,500 to 25,000, with a maximum uncertainty of ±400. The diameter of the combustor inlet is used as a length scale to calculate Reynolds number.

Delayed acoustic self-feedback is established in the combustor using a single coupling tube made of flexible stainless steel braided hose of length L_c and internal diameter d_c (refer to Fig. 3.2). The value of L_c is varied from 1000 to 2000 mm in steps of 100 mm, while the value of d_c is varied from 6.35 to 25.4 mm (d_c = 6.35, 9.525, 12.7, 19.05, and 25.4 mm). The coupling tube is attached at an axial distance of 70 mm from the dump plane on two opposite faces of the combustor walls. This position is near the anti-node of the acoustic pressure standing wave that, in turn, induces stronger acoustic feedback in the coupled system. Previous studies have shown that the optimal location for pressure actuation is near the pressure maxima of the acoustic standing wave (Magri and Juniper, 2013; Skene and Taira, 2022). We have not used any other position on the combustor duct to attach the coupling tube. Ball-type valves are manually operated to switch on and off the delayed self-feedback. We first establish thermoacoustic instability in the system and then switch on the delayed feedback by opening the valves of a coupling tube of length L_c and internal diameter d_c.

3.2.1 Measurements and data acquisition

The acoustic pressure fluctuations p' are measured using a PCB103B02 piezoelectric transducer (sensitivity: 217.5 mV/kPa and uncertainty: ±0.15 Pa) mounted on the combustor wall at 20 mm from the dump plane. A photomultiplier tube (PMT, Hamamatsu H10722-01) equipped with a CH* filter (wavelength of 430 nm and 12 nm FWHM) is used to capture the global heat release rate fluctuations in the flame $\dot{q}'$. We simultaneously acquired both p' and $\dot{q}'$ signals for 3 s at a sampling rate of 10 kHz using an A/D card (NI-6143, 16 bit). The frequency bin size in the power spectrum is 0.3 Hz. High-speed CH* chemiluminescence images of the flame are simultaneously captured with p' and $\dot{q}'$ signals at 2000 fps for 3 s using a CMOS camera (Phantom - V12.1 with a ZEISS 50 mm camera lens). The image of the flow-field from the dump plane spans 90 mm × 120 mm with a resolution of 574 × 764 pixels. To ensure consistency in experimental conditions for different trials, the experiments were performed only when the decay rate of periodic perturbations in the acoustic pressure field, measured in the absence of flow, remained in the range 11 ± 1.5 s^{-1}. This decay rate is ensured in the combustor irrespective of the presence of the coupling tube. Details about the calculation of the decay rate are presented in Appendix C.

3.3 HORIZONTAL LAMINAR RIJKE TUBE WITH DELAYED ACOUSTIC SELF-FEEDBACK

Given the inherent challenges of conducting intricate experiments within a turbulent combustor environment, we conducted further experiments related to delayed acoustic self-feedback with a laminar horizontal Rijke tube. In Fig. 3.3, we show a schematic representation of the Rijke tube used for these experiments. The Rijke tube is a long duct with a rectangular cross section of 9.3 cm × 9.4 cm and a length (L_{duct}) of 104 cm, similar to the ones used in Gopalakrishnan and Sujith (2014) and in Dange *et al.* (2019). An electrically heated wire mesh powered by an external DC power supply acts as a compact heat source. The heated wire mesh is located 27 cm downstream of the inlet in

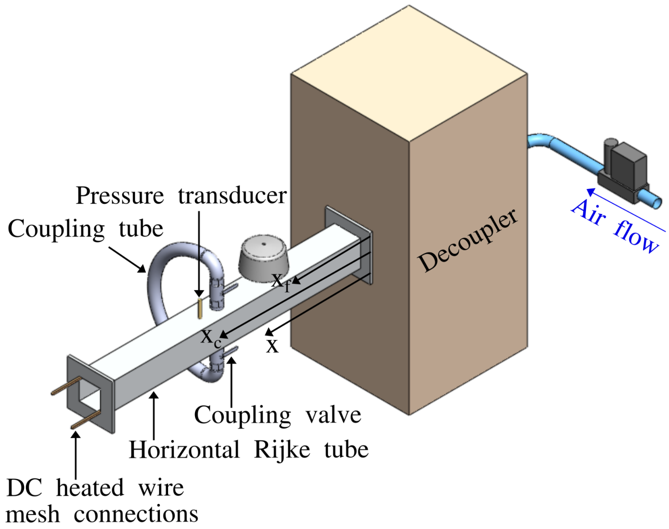

Figure 3.3: Schematic of a horizontal Rijke tube self-coupled using a connecting tube. The axial location (normalised by the length of the Rijke tube, L_{duct}) of the heater mesh is denoted by x_f, while the normalised axial locations of the ends of the connecting tube are given by x_{c1} and x_{c2}. Ball-type coupling valves are manually opened to establish acoustic feedback in the system.

the duct. Air flow is supplied to the Rijke tube through a mass flow controller (MFC, Alicat Scientific) of uncertainty ±(0.8% of the measured reading + 0.2% of the full scale reading). A decoupler of dimensions 102 cm × 45 cm × 45 cm is attached to the inlet of the Rijke tube. In this setup, the decoupler is used to dampen out the fluctuations in the incoming air flow so that a steady air flow enters the Rijke tube. During experiments, the heater power supplied to the wire mesh is increased so that the system behavior transitions from steady state to limit cycle oscillations via subcritical Hopf bifurcation for the given air flow rate (Etikyala and Sujith, 2017).

In order to quench the limit cycle oscillations, we implement self-coupling to acoustically couple the Rijke tube to itself using a single vinyl tube of length L_c and internal diameter d_c. The axial location of the ends of the coupling tube on the Rijke tube, normalised by L_{duct}, are given by x_{c1} and x_{c2}. We refer to x_{c1} and x_{c2} as the coupling locations. Unless otherwise specified, both the ends of the coupling tube are connected to the Rijke tube at an axial distance of 57 cm from the inlet of the Rijke tube (i.e., the coupling location is

$x_{c1} = x_{c2} = x_c = 0.55$). The length of the coupling tube (L_c) is varied from 92 cm to 362 cm in steps of 5 cm. Coupling tubes of diameters (d_c) 4 mm to 12 mm in steps of 2 mm are considered in this study.

3.3.1 Measurements and data acquisition

To measure the acoustic pressure fluctuations in the system, a piezoelectric pressure transducer (PCB 103B02, sensitivity 217.5 mV/kPa, uncertainty ±0.15 Pa) is mounted along the length of the duct at 57 cm from the inlet. The pressure data is acquired from the Rijke tube at a sampling rate of 10 kHz for a duration of 3 s for each parametric condition using a data acquisition system (NI USB 6343). The resolution of frequency in the power spectrum of the signal is 0.3 Hz. To measure the acoustic damping in the Rijke tube, we send an acoustic pulse into the Rijke tube using a loudspeaker in the absence of air flow and heating and calculate its decay rate. We observe the decay rate for the Rijke tube to be 15.8 ± 2 s^{-1}. To ensure consistency of the experimental conditions and repeatability of the results, the experiments are conducted only when the measured acoustic decay rates lie in the aforementioned range. Before starting any experiment, the Rijke tube is preheated for 10 minutes in the steady state regime of operation by supplying DC power at 1 V to the wire mesh. The preheating ensures a steady temperature profile inside the Rijke tube.

3.4 MUTUALLY COUPLED RIJKE TUBES WITH ASYMMETRICAL ACOUSTIC FORCING

The experimental setup for the mutually coupled Rijke tubes is similar to the above description, except that we couple two Rijke tubes with a connecting tube (Fig. 3.4). Rijke tube A has a cross-section of 9.3×9.4 cm^2 with a length of 102 cm. Rijke tube B has a cross-section of 9.3×9.5 cm^2 and a length of 104 cm. For asymmetrical external acoustic forcing, four wall mounted acoustic drivers (Minsound TD-200A) are attached on each side of Rijke tube A, 41 cm downstream of the inlet. The acoustic drivers are

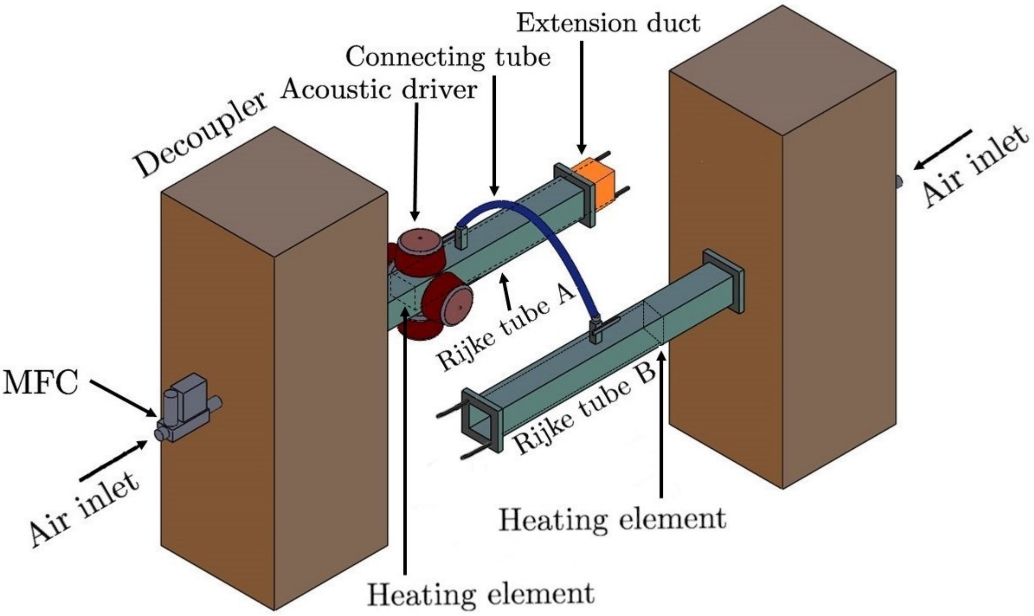

Figure 3.4: Experimental setup of two mutually coupled horizontal Rijke tubes A and B. Rijke tube A is acoustically forced with 4 acoustic drivers attached to its sides. An extension duct in Rijke tube A is used for implementing frequency detuning in the system.

connected in parallel to a power amplifier (Ahuja UBA-500M). Sinusoidal forcing signal with mean-to-peak amplitude (A_f, in mV) and frequency (f_f, in Hz), generated using a Tektronix function generator (Model No. AFG1022), is input to the power amplifier to drive the coupled system of Rijke tubes.

Both the Rijke tubes are coupled using a single connecting tube of internal diameter d_c and length L_c (see Fig. 3.1). The ports for the connecting tube for both the Rijke tubes are located x_c = 57 cm downstream of the inlet. Ball-type valves are manually opened to establish coupling between the two oscillators. For experiments used to study the effect of asymmetrical forcing, four wall mounted acoustic drivers are attached on each side of the duct. Further details are mentioned in the previous section.

A telescopic slide mechanism of 12 cm length is used to vary the length of Rijke tube A. The natural frequency of Rijke tube A can be varied between f_{n0} = 162 Hz to f_{n0} = 148 Hz with an uncertainty of ±2 Hz due to the uncertainty in measuring the length of the

Rijke tube. After preheating both the Rijke tubes, the heater power is increased such that the system undergoes subcritical Hopf bifurcation. Subsequently, the heater power is maintained away from the bistable region in all experiments such that the Rijke tubes exhibit LCO before coupling is induced. LCO is maintained in each of the Rijke tubes before coupling is induced. The amplitude of the LCO is controlled by varying the heater power and the air flow rate. All the experiments are reported for two different amplitudes (root-mean-square) of the LCO in both the Rijke tubes in the uncoupled state: (a) lower amplitude $p'_{0,\mathrm{rms}} = 120$ Pa maintained by supplying a constant air flow rate of 40 ± 0.08 SLPM (Re = 1370) in each Rijke tube, and (b) higher amplitude $p'_{0,\mathrm{rms}} = 200$ Pa maintained by supplying a constant air flow rate of 65 ± 0.13 SLPM (Re = 2284) in each Rijke tube.

3.4.1 Measurements and data acquisition

The hardware used to measure acoustic pressure oscillations is also the same as that mentioned in the previous section. The rate of decay of an acoustic pulse generated from loudspeakers in the absence of flow is used to measure the damping in the two Rijke tubes. The acoustic decay rate values for Rijke tubes A and B are measured to be 16.5 ± 2 s^{-1} and 12.9 ± 1.8 s^{-1}, respectively. During each experiment, both the Rijke tubes are preheated for 10 minutes with 1 V to ensure a steady temperature profile inside the acoustic ducts.

CHAPTER 4

INTERPLAY BETWEEN HYDRODYNAMIC AND ACOUSTIC FIELDS IN A TURBULENT COMBUSTOR

The ubiquitous nature of turbulence around us warrants enduring efforts to understand the dynamics of turbulence. Turbulent flows contain definable flow configurations, known as coherent structures, that retain their identity over a considerable distance downstream (Hussain, 1986). Among various research avenues, the investigation of large-scale coherent structures has garnered substantial attention for several decades (Fiedler, 1988). Coherent structures, as defined by Hussain (1983), represent a connected, large-scale turbulent fluid mass with phase-correlated vorticity over its spatial extent. Consistent arguments have been made that coherent structures control the dominant aspects of transport (Zilitinkevich, 1970), mixing (Eckart, 1948; Yu and Schadow, 1997), entrainment (Govindarajan, 2002; Neamtu-Halic *et al.*, 2019), and noise generation in turbulent shear flows (Armstrong *et al.*, 1977; Mankbadi and Liu, 1984). Insights into these structures motivates the development of novel strategies for targeted control of turbulent flows to achieve specific objectives, including airfoil lift enhancement (Steinfurth and Haucke, 2018), noise mitigation (Coderoni *et al.*, 2019; Prasad and Morris, 2019), drag reduction (Sirovich and Karlsson, 1997; Farsiani *et al.*, 2020), and mixing augmentation (Fröhlich *et al.*, 2008; Hitimana *et al.*, 2021).

Large-scale coherent structures play a pivotal role in various thermofluid systems, including combustion systems exhibiting thermoacoustic instability (Poinsot *et al.*, 1987;

---

1. The data set used to obtain results presented in this chapter was acquired by a team consisting of Dr. Nitin Babu George, Dr. Manikandan Raghunathan, Mr. Midhun P. R. and Prof. R. I. Sujith in February 2018.

2. The manuscript corresponding to this chapter is available at `https://arxiv.org/abs/2311.12541`, and is currently under review in the Journal of Fluid Mechanics.

Paschereit *et al.*, 1999). The emergence of large-scale coherent structures is one of the key mechanisms, along with periodic inhomogeneities in the mixture fraction and pressure sensitivity of the flame speed, that drive thermoacoustic instability in combustion systems (Poinsot *et al.*, 1987; Schadow *et al.*, 1989; Schadow and Gutmark, 1992). In such combustors prone to vortex-driven thermoacoustic instability, the roll-up of a coherent structure near the backward-facing step entrains a quantity of unburned fresh gases that burns rapidly in a very short period of time. This sudden combustion leads to an abrupt heat release that generates an acoustic wave, which produces an acoustic disturbance with a certain time lag (Pierce, 1983; Ducruix *et al.*, 2003; Candel *et al.*, 2004). The acoustic perturbation causes the formation of the next coherent structure in the shear layer formed close to the edge of the reactant inlet (Crow and Champagne, 1971; Ho and Huang, 1982; Ho and Huerre, 1984).

Most early research on spatiotemporal dynamics in combustion systems exhibiting thermoacoustic instability centred on examining the periodic shedding of large-scale vortical structures (Rogers and Marble, 1956; Zukoski, 1985; Poinsot *et al.*, 1987; Schadow and Gutmark, 1992; Coats, 1996; Renard *et al.*, 2000). Yu *et al.* (1991) demonstrated that both the vortex and acoustic modes coexist in a backward-facing step configuration with a choked exit. Similar characteristics were also observed in the context of thermoacoustic instability in partially premixed flames within a one-sided backward-facing step combustor (Desai *et al.*, 2010) and a bluff-body combustor (Sivakumar and Chakravarthy, 2008). Hong *et al.* (2013) demonstrated the emergence and growth of large-scale structures across various phases of acoustic pressure oscillations in a laboratory scale backward-facing step combustor. Numerous researchers have also observed the existence of such large-scale structures during thermoacoustic instability in swirl geometry through the use of time-resolved measurements (Steinberg *et al.*, 2010; Boxx *et al.*, 2012). A recent study by George *et al.* (2018) examined vortex size variations during different states of combustor operation using a vortex identification algorithm (Varun *et al.*, 2008) applied to two-component particle image velocimetry (PIV) fields within a bluff-body stabilised turbulent combustor. Their findings indicated that the vortex size was the smallest during the state of combustion noise, and the largest during the state of thermoacoustic instability. In addition, the frequency of vortex shedding recorded during the periodic epoch of intermittency is greater than those during the aperiodic epoch of intermittency. The occurrence of these large-scale vortices during periodic intervals of intermittency and thermoacoustic instability was ascribed to the collective interplay of smaller-scale vortices (Ho and Nosseir, 1981). Furthermore, Raghunathan *et al.* (2020) categorised vortex sizes as small-scale, medium-scale, and large-scale during combustion noise, intermittency, and thermoacoustic instability, respectively, based on Mie-scattering images obtained from the same experimental configuration employed in the current chapter.

The vortices shed into the reaction field of a turbulent combustor can induce a positive feedback between the heat release rate and the acoustic field of the combustor, leading to thermoacoustic instability in the combustor (Ducruix *et al.*, 2003). During the state of thermoacoustic instability, the emergence of large coherent structures within the turbulent flow serves as a clear indicator of complex system behavior. As mentioned in Chapter 1, a complex system is defined as a system with *multiple interacting components whose behavior cannot be simply inferred from the behavior of its components* (Smith *et al.*, 2003). The study of unsteady reactive fluid flows present in turbulent combustors often involves complex systems with high-dimensionality, necessitating advanced experimental and computational techniques to capture the intricate spatiotemporal dynamics and interplay of various physical processes. For such high-dimensional systems, graph theory offers a concrete mathematical framework for quantifying interactions between elements of a system (Barabási, 2012; Gross *et al.*, 2018). Graph-theoretic formulations have yielded important insights and models for high-dimensional systems such as brain (Sporns, 2016), transport systems (Lin and Ban, 2013), economics (Kenett and Havlin, 2015), and climatology (Donges *et al.*, 2009). Furthermore, the extensive repertoire of network science tools allows for the characterisation, modelling, and control of interaction-based processes.

In recent years, the adoption of complex networks has expanded to encompass the analysis and representation of fluid flows. The framework of complex networks has been harnessed to investigate induced velocity interactions among vortical elements (Nair and Taira, 2015), Lagrangian motion of fluid elements (Ser-Giacomi *et al.*, 2015; Hadjighasem *et al.*, 2016), oscillator-based representation of the energy fluctuations (Nair *et al.*, 2018), time series of fluid-flow properties (Zou *et al.*, 2019), triadic interactions in turbulence (Gürcan, 2017, 2018), and the effects of perturbations on time-varying vortical flows (Yeh *et al.*, 2021). The application of complex network methodologies has expanded to investigate a wide array of turbulent flows, including two-dimensional isotropic turbulence (Taira *et al.*, 2016), thermoacoustic oscillations in turbulent combustors (Godavarthi *et al.*, 2017; Singh *et al.*, 2017; Krishnan *et al.*, 2019*b*), wall turbulence (Iacobello *et al.*, 2018*b*), mixing in turbulent channel flow (Iacobello *et al.*, 2018*a*, 2019*a*,*b*), and isotropic magnetohydrodynamic turbulence (Gürcan, 2018). Iacobello *et al.* (2021) and Taira and Nair (2022) provide a comprehensive overview of the advancements in network-inspired analysis, modelling, and control for a variety of unsteady fluid flows such as turbulent and vortical flows.

Although numerous investigations have explored the characteristics of coherent structures in turbulent flows and their relevance to phenomena such as aerodynamics, aeroacoustics, and thermoacoustics, limited attention has been given to the quantification and analysis of vortical interactions. Vortical interactions refer to the interactions from one fluid element having a non-zero vorticity on another fluid element, and is calculated using Biot-Savart law. Krishnan *et al.* (2021) used vortical interactions present in a turbulent thermoacoustic system to show that the fluid elements with high vorticity have significantly stronger influence over the time-varying undirected weighted vortical networks than the fluid elements with moderately high vorticity. The authors termed the two groups of nodes as primary and secondary hubs, respectively. Furthermore, the authors were able to suppress thermoacoustic instability by targeting the primary hubs present downstream of the backward-facing step and above the bluff body. Such flow fields consist of a spatially discretised field comprising n distinct cells. In such cases, an exhaustive consideration of direction-wise interactions necessitates evaluating $2 \times n \times (n - 1)$ interactions. A tractable way of studying such interactions is by using clustering methods to reduce the dimensionality of the system. This line of thought assumes further importance when experimental data is involved, as no analytical techniques exist to work with datasets with such large dimensionality.

The application of clustering techniques for identifying and analysing coherent structures in turbulent flows has gained significant traction in recent years. In the Lagrangian-based paradigm for fluid-flow networks, spectral clustering techniques have been employed to identify vortices (Hadjighasem *et al.*, 2016; Schneide *et al.*, 2018). Furthermore, a coherent structure colouring technique based on a Lagrangian framework has been utiliued to detect coherence in fluid flows where only sparse velocity data is available (Schlueter-Kuck and Dabiri, 2017). In addition, Gabriel graphs have been leveraged to analyze and classify vortical flows based on their topological similarities (Krueger *et al.*, 2019). Recent advances have also witnessed the use of community detection methods to identify vortical structures within turbulent flow fields (Murayama *et al.*, 2018) and develop reduced-order models for laminar wake flows (Gopalakrishnan Meena *et al.*, 2018; Gopalakrishnan Meena, 2020).

Gopalakrishnan Meena and Taira (2021) developed a community-based network formulation to extract flow-modifying vortical structures in two- and three-dimensional isotropic turbulence. The induced velocity, ascribed to the weighted network edges, was used to quantify the web of interactions between vortical elements. This interaction-based paradigm was utilised to find communities of vortical nodes with dense connections. The inter- and intra-community interactions between groups of vortical nodes were used to determine the connector and periphery nodes that exert the most and least effect on other communities, respectively. In a separate study, Murayama *et al.* (2018) leveraged the spatial distribution of vortex strengths in the turbulence network and the community structure of the vorticity field to investigate the relationship between the local pressure fluctuations and the presence of a primary hub near the injector rim in a turbulent combustor. The authors established that the location of local minima in pressure fluctuations corresponded to the proximity of the primary hub to the injector rim of the combustor. This finding provided insight into the interplay between the network properties and pressure variations within the combustor. Later, Kawano *et al.* (2023) extended the concept of clustering of complex networks in thermofluid systems to analyze the spatiotemporal dynamics of a model single-element rocket combustor using a spatial network constructed from flux balance of acoustic energy. The authors demonstrated that the development of spatially large communities exhibiting strong connections plays a crucial role in driving thermoacoustic instability. The cumulative body of research conducted thus far has progressively deepened our comprehension of the intricate spatiotemporal dynamics of thermoacoustic systems.

In the realm of spatial network analyses discussed thus far, the spatiotemporal understanding of interactions among different regions of intense vortical activity from a quantitative perspective has remained largely unexplored. However, the significance of coherent structures in the onset of thermoacoustic instability in combustors has been well-established (Poinsot *et al.*, 1987). Therefore, the primary objective of this study is to quantitatively analyze the interactions among regions of high vortical activity present in a turbulent combustor through the lens of complex networks, and gain valuable insights into the interplay between such vortical interactions and the global acoustic dynamics exhibited by the turbulent combustor. This objective is met by employing community detection and community-based network reduction techniques on vortical networks constructed from spatial vorticity data (Fig. 4.1a-d). Following the methodology formulated by Taira *et al.* (2016) and explained in Chapter 2, we construct time-varying vortical networks, and use the Louvain community detection algorithm

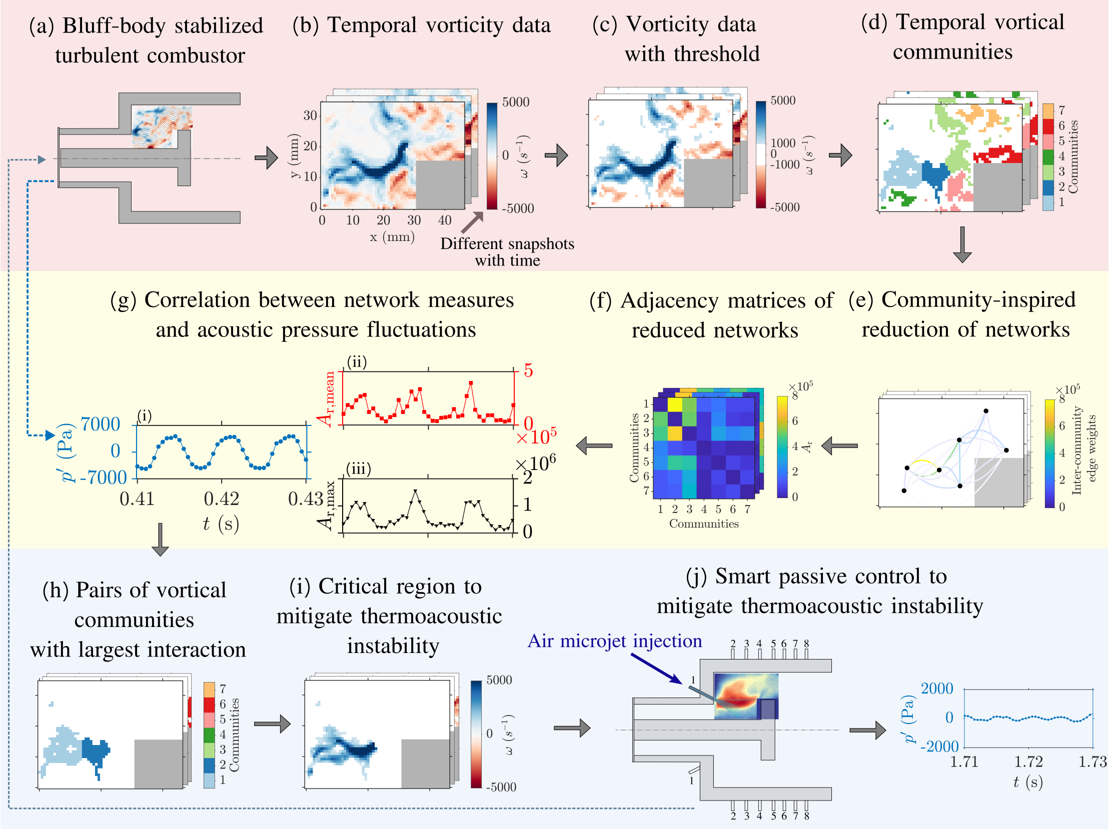
(a) Bluff-body stabilized turbulent combustor
(b) Temporal vorticity data
y (mm)
x (mm)
0 10 20 30 40
5000
0
-5000
ω (s⁻¹)
Different snapshots with time
(c) Vorticity data with threshold
1000
-1000
(d) Temporal vortical communities
Communities
(g) Correlation between network measures and acoustic pressure fluctuations
(i)
p′ (Pa)
7000
-7000
0.41
0.42
0.43
t (s)
(ii)
A_r,mean
×10⁵
(iii)
A_r,max
×10⁶
(f) Adjacency matrices of reduced networks
Communities
A_r
(e) Community-inspired reduction of networks
Inter-community edge weights
(h) Pairs of vortical communities with largest interaction
(i) Critical region to mitigate thermoacoustic instability
(j) Smart passive control to mitigate thermoacoustic instability
Air microjet injection
2000
-2000
1.71
1.72
1.73

Figure 4.1: Overview of vortical network community-based framework to understand the interplay between the acoustic pressure fluctuations p' and inter-community interactions. (a) Schematic of cross-section of bluff-body stabilised turbulent combustor used in the current chapter. (b) Vorticity field is used to construct temporal directed and weighted vortical networks through Biot-Savart law (Taira *et al.*, 2016). (c, d) Vorticity thresholding used to include fluid elements with sufficiently high vorticity in the detection of vortical communities through Louvain algorithm (Blondel *et al.*, 2008). (e, f) Community-based network reduction technique (Gopalakrishnan Meena *et al.*, 2018) utilised to condense each vortical community to a single node at the respective community centroid. The reduced network and the corresponding adjacency matrix are show in (e) and (f), respectively. The correlations between p' oscillations and vorticity network dynamics are analysed using two network metrics : (g-ii) mean $A_{\mathrm{r,mean}}$, and (g-iii) maximum $A_{\mathrm{r,max}}$, of all inter-community interactions. (h, i) The locations of pairs of communities with $A_{\mathrm{r,max}}$ are utilised to understand the critical regions detected in the same experimental setup in previous studies. (j) Cross-sectional representation of the combustion chamber illustrates the spatial positions of secondary steady air-jet injection ports, with an inset showcasing the distribution of maximum interacting vortical communities observed during thermoacoustic instability.

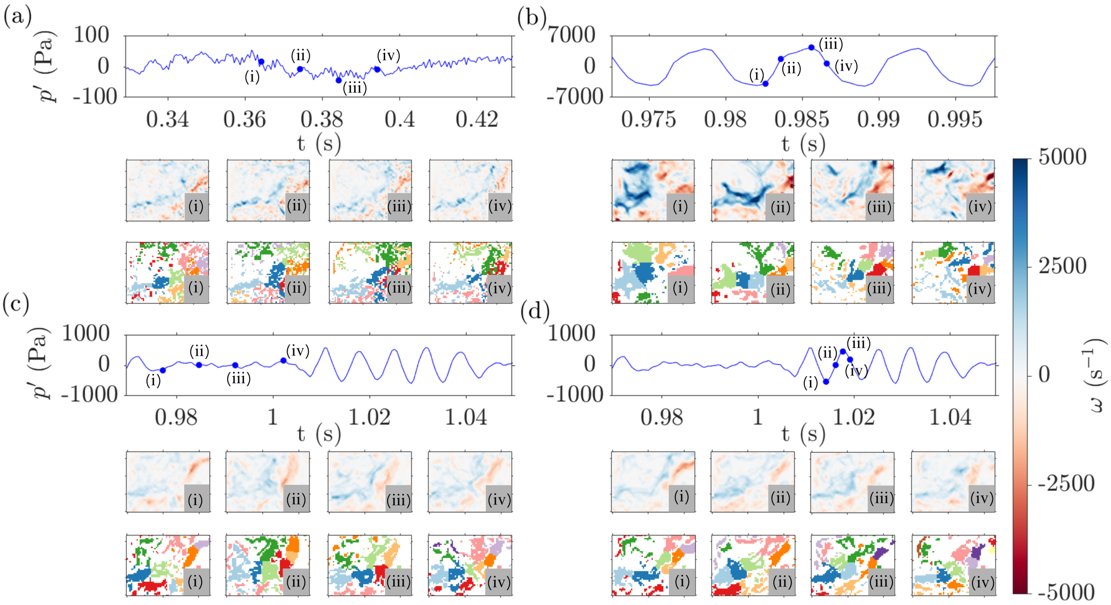

Figure 4.2: The instantaneous vorticity fields (second and fifth rows) and the detected vortical communities (3rd and 6th rows) at time instants (i), (ii), (iii), and (iv) marked on the time series of acoustic pressure fluctuations (1st and 4th rows) during the states of (a) combustion noise, (b) thermoacoustic instability, (c) aperiodic epoch, and (d) periodic epoch of intermittency. Different vorticity thresholds were used for detecting vortical communities during different dynamical states. The discussions related to the selection of vorticity thresholds during different dynamical states is present in Appendix A.

(Blondel *et al.*, 2008) to identify vortical communities. These communities are then utilised to reduce the dimensions of the time-varying vortical networks using the community-based network reduction approach proposed by Gopalakrishnan Meena *et al.* (2018) (Fig. 4.1e-f). The findings demonstrate a strong delayed correlation between the vortical community interactions and the acoustic pressure fluctuations during the state of thermoacoustic instability (Fig. 4.1g), thus unveiling the strong interplay that exists between hydrodynamic and acoustic fields present in the turbulent combustor. Additionally, by employing the maximum vortical community interactions as shown in Fig. 4.1(h-j), the present work offers insights into the occurrence of critical regions detected through different methods during the states of intermittency and thermoacoustic instability in previous studies by Unni and Sujith (2017), Krishnan *et al.* (2019*a*), and Roy *et al.* (2021).

4.1 SPATIAL DISTRIBUTION OF VORTICAL COMMUNITIES DURING DIFFERENT DYNAMICAL STATES

In the present chapter, time-varying weighted directed vorticity networks are constructed at each time instant during the three dynamical states. We subsequently use modularity maximisation algorithm to detect vortical communities at each time instant. We first visually analyze the vortical communities present during the different dynamical states before using statistical measures to quantify the dynamics of inter-community interactions.

In Fig. 4.2(a), we examine the vorticity field and the vortical communities at four representative time instants (i-iv) marked on the time series of p' fluctuations during the state of combustion noise. The grey color rectangles in the spatial distribution of vorticity and vortical communities represent the mask used to account for the presence of the bluff-body in the analysis of PIV data. Counterclockwise vorticity is represented by positive values of ω, while negative values of ω indicate clockwise vorticity. We notice small vortices along the inner and outer shear layers (cf. Fig. 10 of George *et al.* (2018)). During this state of combustion noise, we observe spatially fragmented communities predominantly located along the shear layer and above the bluff-body. The high spatial density of the communities above the bluff-body is associated with the vortices shed from the tip of the bluff-body. The incoherent distribution of the individual communities at different instants of time during the occurrence of combustion noise is related to the presence of a few small vortices with high interaction strengths scattered throughout the spatial domain.

In Fig. 4.2(b), we present the vorticity flow field and the vortical communities present at different time instants during a periodic cycle of thermoacoustic instability. Unlike the results observed during the state of combustion noise, we notice large regions of spatially coherent vortical communities downstream of the backward-facing step during the state of thermoacoustic instability. The magnitude of vorticity in the flow field is one order higher compared to that observed during the occurrence of combustion noise. The formation of large coherent structures in the reaction field of the combustor during the state of thermoacoustic instability has been reported in earlier studies (Zukoski, 1985; Poinsot *et al.*, 1987; Schadow and Gutmark, 1992; Coats, 1996). The implementation of community detection on vortical networks constructed from vorticity data clusters the fluid elements according to their spatial proximity and magnitude of vorticity. Thus, the vortical communities during the state of thermoacoustic instability are highly organized in the spatial domain, similar to the large coherent structures observed in the reaction field. Also, the vortical communities during the state of thermoacoustic instability are significantly less fragmented in the spatial domain compared to that observed during the state of combustion noise, as seen in Fig. 4.2(a). Spatial fragmentation of communities present in different dynamical states are discussed and compared in Appendix A.3.

As previously stated, the state of intermittency is characterized by the presence of randomly embedded bursts of periodic oscillations amidst low-amplitude aperiodic oscillations in the acoustic pressure oscillations (Nair *et al.*, 2014). In Fig. 4.2(c), we examine the vortical communities present during an aperiodic epoch of intermittency. We observe that spatial regions of coherent vortical communities with low vorticity magnitude begin to emerge in the hydrodynamic field. The amplitude of vorticity present during the aperiodic epoch of intermittency is comparable to that observed during the state of combustion noise (Fig. 4.2a). The difference between the spatial distribution of vortical communities present during combustion noise and the aperiodic epoch of intermittency is attributed to the presence of large regions of low vorticity magnitude present during the state of intermittency.

Finally, in Fig. 4.2(d), we examine the vorticity flow field and the vortical communities present during the periodic epoch of intermittency. We observe spatially coherent vortical communities downstream of the backward-facing step, similar to that seen during the state of thermoacoustic instability in Fig. 4.2(b). However, the size and node strength of the vortical communities are not as large as that observed during thermoacoustic instability (node strength can be approximately inferred from the values of vorticity in the corresponding locations). This difference can be attributed to the smaller size of the vortices shed from the backward-facing step during the state of periodic epochs of intermittency than the vortices present during the state of thermoacoustic instability. Furthermore, the values of vorticity present during the state of thermoacoustic instability are larger than those observed during the state of intermittency. The aforementioned differences in the size and strength of vortices shed during the states of periodic epoch of intermittency and thermoacoustic instability causes the corresponding differences in the size and node strength of the vortical communities during these dynamical states.

4.2 PHASE AVERAGED ANALYSIS OF STRONGEST INFLUENTIAL COMMUNITIES

A significant feature of the shedding of coherent structures in unsteady fluid flows is the presence of periodic fluctuating dynamics. The resulting periodic forces can inflict destructive unsteady loading on the structure of the physical systems and may lead to catastrophic incidents. Since coherent structures are related to the regions of high vorticity in the hydrodynamic field, an important step in understanding the role of interaction among regions of high vorticity toward such periodic dynamics is to use complex networks to analyze the *outward* influence of vortical communities on other fluid elements. To this end, we use phase-averaged analysis during the state of thermoacoustic instability to understand the variation in the location and strength of the communities with maximum *outward* influence, as shown in Fig. 4.3.

We use participation coefficient P to quantify the *outward* influence of nodes present in vortical communities (Guimera and Amaral, 2005). Participation coefficient is a relative measure of inter-community strength of a node, and provides an indication of how well-distributed the edges of a node are amongst all other communities other than its own. The participation coefficient P_i of node i is given by:

$$P_i = 1 - \left[\left(\frac{s_i^{\text{intra}}}{s_i} \right)^2 + \sum_{k, k \neq c_i} \left(\frac{s_{i,k}}{s_i} \right)^2 \right], \tag{4.1}$$

where, s_i^{intra} is the intra-community strength of node i, s_i is the total strength of node i, $s_{i,k}$ is the strength of node i to influence all nodes in community k, and c_i represents the community that node i belongs to. $s_{i,k}$ and P_i can be evaluated for both in- and out-edges. Since we are interested to understand the influence of a vortical community on other fluid elements, we evaluate the out-edge based measures in the current chapter to understand the outward influencing properties of the fluid elements.

We plot the phase-averaged distribution of P_i of all the nodes belonging to the community with the maximum outward inter-community interaction in Fig. 4.3(b). Around 50 realizations for each phase of the cycle were averaged, resulting in an ensemble averaged quantity of interest at each of the 8 phases ($\phi = 0°$ to $315°$ in interval of $45°$). The phase angle $\phi = 0°$ corresponds to the local minima of acoustic pressure fluctuations, p', and is shown in Fig. 4.3(a). During the state of thermoacoustic instability, the vortex shedding from the backward-facing step starts near the time instant corresponding to local minima of p', denoted by $\phi = 0°$ here. We also plot the phase-averaged distribution of vorticity $\overline{\omega}_\phi$ in Fig. 4.3(c), to interpret the phase-averaged distribution of the participation coefficient $\overline{P}_\phi$ from the perspective of hydrodynamics present in the flow field during the state of thermoacoustic instability.

We observe a region of high phase-averaged participation coefficient $\overline{P}_\phi$ at the phase value of 0° in Fig. 4.3(b). This region lies in the region of high positive phase-averaged vorticity $\overline{\omega}_\phi$. At this phase, the coherent structures are shed from the backward-facing step when the acoustic pressure is at minima. Thus, we observe a region of high vorticity immediately adjacent to the backward-facing step.

At the subsequent phase angles of 45° to 135°, we observe a gradual stretching of the

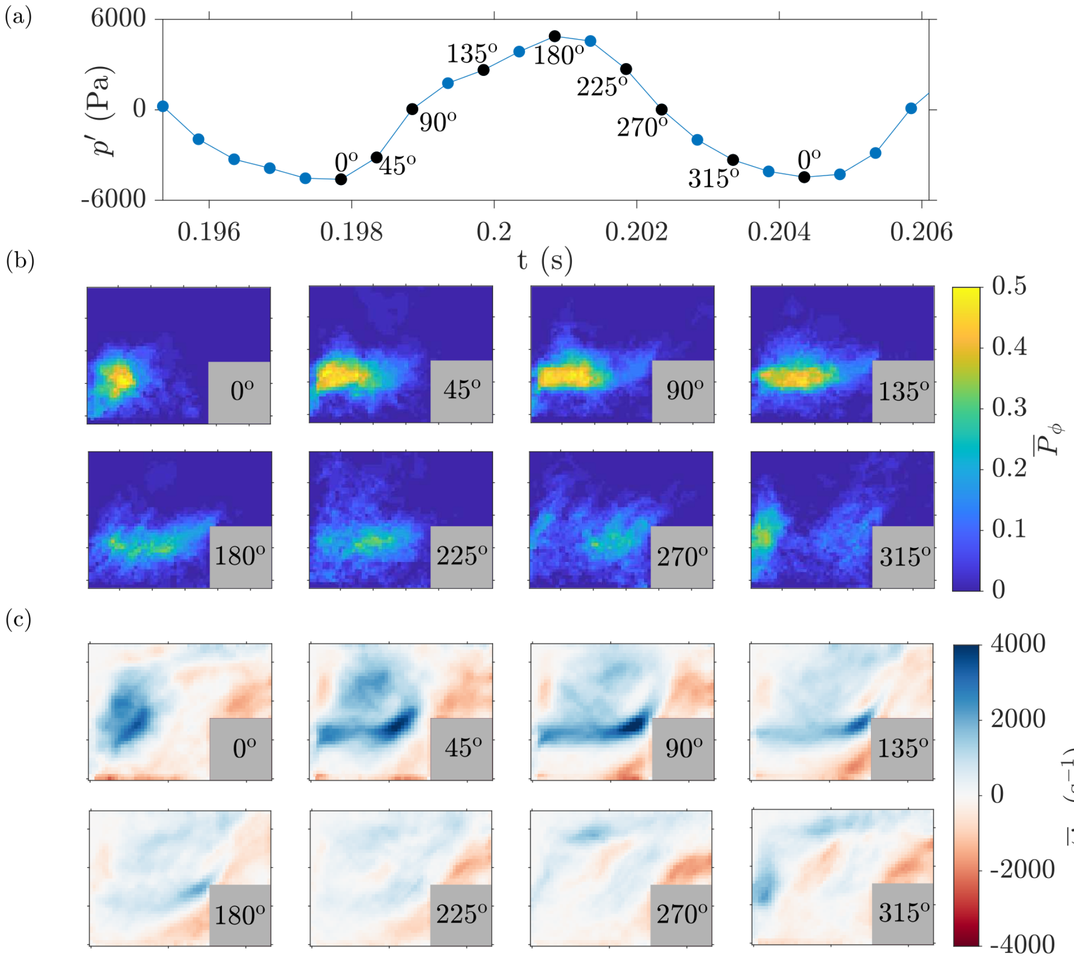

Figure 4.3: (a) Time instances denoting the phases in one acoustic cycle during the state of thermoacoustic instability. (b) Phase-averaged fields of participation coefficients P corresponding to the nodes in communities having the maximum P values at the indicated phases of the acoustic cycle during the state of thermoacoustic instability. The participation coefficient quantifies the influence of a single node on communities other than its own. We also plot the phase-averaged distribution of vorticity in (c).

regions of high $\overline{P}_\phi$ in the downstream direction. These regions of high $\overline{P}_\phi$ values do not spatially align with the regions of highest phase-averaged vorticity $\overline{\omega}_\phi$. We attribute this difference to the interpretation of participation coefficient P_i and vorticity ω from the network and hydrodynamics points of view. P_i reflects the combined influence of the strength and position of the vortical elements present around node i in the network space. However, ω is an attribute of the node i only, and does not depend on the other vortical elements. Thus, although the regions of high vorticity continue to move downstream as the phase angle increases from 0° to 135°, the regions of highest $\overline{P}_\phi$ values do not spatially match with the regions of highest $\overline{\omega}_\phi$ values. This spatial mismatch between regions of highest $\overline{\omega}_\phi$ and highest $\overline{P}_\phi$ between the phases 45° to 135° indicates that in addition to tracking the downstream convection of the coherent structure shed from the backward-facing step, spatial proximity of other regions of high vorticity must also be taken into account to understand the spatiotemporal behaviour of vortical interactions present during the state of thermoacoustic instability.

At further phase angles of 180° to 270°, the values of participation coefficients in regions of high $\overline{P}_\phi$ decrease significantly. The decrease in $\overline{P}_\phi$ is due to the decrease in the vorticity values present in the flow domain, which in turn, decreases the strength of the nodes present in the vortical communities detected at these phase values. Finally, at the phase value of 315°, we observe the emergence of a region of high $\overline{P}_\phi$ values near the backward-facing step, along with an increase in the values of vorticity $\overline{\omega}_\phi$ in the same region. The increases in the values of $\overline{P}_\phi$ and ω at $\phi = 315°$ occur for a short time before the coherent structures are again shed at the acoustic pressure minima ($\phi = 0°$). The spatiotemporal dynamics of $\overline{P}_\phi$ and ω is subsequently repeated in all acoustic cycles during the state of thermoacoustic instability.

Values of $\overline{P}_\phi$ can be interpreted as an indicator of the combined influence of strength and position of the vortical elements present in the spatial field under consideration. A fluid element with a significantly high vorticity magnitude but located at the periphery of the spatial domain can exert a comparatively less influence on other fluid elements, as compared to a fluid element with a lower magnitude of vorticity but located towards the centre of the spatial domain. Although this information is embedded in the formulation of Biot-Savart law, and thus, in the edge weights of the adjacency matrix; $\overline{P}_\phi$ brings out the combined influence of strength and position of the vortical elements more clearly.

4.3 DIMENSIONALITY REDUCTION OF VORTICAL NETWORKS

In the previous section, we focused on understanding the spatial phase-averaged dynamics of the maximum outward influencing vortical communities present in the reaction field of a turbulent combustor during the state of thermoacoustic instability. The phase-averaged analyses discussed the outward influence of most influential communities during different phases in an acoustic cycle during the state of thermoacoustic instability. Such vortical communities with maximum outward inter-community interactions exist for all the three dynamical states. A nontrivial divergence between regions of high phase-averaged participation coefficient and regions of high phase-averaged vorticity, as seen in Fig. 4.3, provides us the motivation to explore this nontriviality as we proceed forward. Related to this, a critical question lies in understanding how these vortical communities with maximum outward interactions affect other vortical communities and whether such inter-community interactions are correlated with the temporal variations in the macroscopic dynamics exhibited by the combustor, viz., the acoustic pressure oscillations. To answer the aforementioned questions, we must look at the temporal networks present at each time instant during the three dynamical states.

The characterisation of interactions among the vortical elements is challenging due to the high-dimensional nature of the turbulent system. Thus, there is a need to reduce the dimension of the system while preserving the overall interaction structure. One way to reduce the dimensionality of complex dynamical systems considers discretising the phase space through clustering. In the current study, we adopt a more specific route of

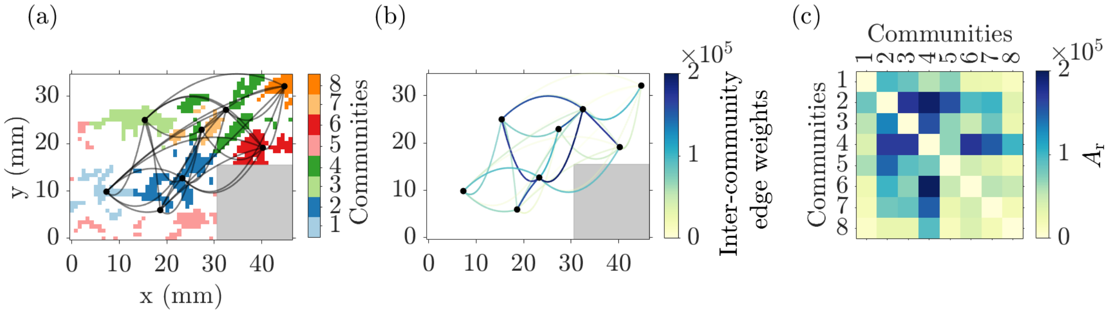

Figure 4.4: An overview of dimensionality reduction of vortical networks using communities. (a) All the communities are considered individual nodes, and (b) the edge weights between the "community" nodes are weighted according to the sum of inter-community interactions between the corresponding pair of communities. The adjacency matrix of the reduced network is shown in (c), with the intra-community edge weights corresponding to diagonal elements set to zero. We do not study intra-community interactions in the present chapter.

reducing the dimensionality of complex interactions between different vortical elements by employing community detection on vortical networks. Following our discussions in section 2.4, we perform clustering of vortical networks through the community detection method as described in Fig. 2.3. Subsequently, we reduce the dimensionality of the temporal networks by distilling the vortical community into a point vortex at the community centroid (Fig. 4.4b). The vortical network is redefined using the position vector (Eq. 2.9) and the circulation (Eq. 2.10) of each community centroid, thus reducing the dimension of the system significantly. With the formulation for dimensionality reduction established for vortical flows, we proceed with understanding the interplay between the temporal dynamics of such community-inspired reduced networks with acoustic pressure oscillations.

In the subsequent sections, we discuss various network measures used to correlate the vortical community interactions with the acoustic pressure oscillations. Furthermore, we explain the variation in network measures from a fluid dynamics perspective, and leverage the information gained to provide insights into the occurrence of critical regions during the three dynamical states in previous studies.

4.4 CORRELATION OF INTER-COMMUNITY INTERACTIONS WITH ACOUSTIC PRESSURE OSCILLATIONS

In Fig. 4.5(a), we compare the temporal evolution of p' fluctuations with the average and maximum of all the inter-community interactions during the state of combustion noise. Since the acoustic pressure remains approximately constant throughout the reaction field of the combustor (George *et al.*, 2018), tracking the temporal evolution of the average of all inter-community interactions allows us to correlate the dynamics of the entire reaction field with the acoustic pressure fluctuations. On the other hand, tracking the maximum of all the inter-community interactions will help us to analyse the spatiotemporal evolution of the pair of communities with maximum inter-community interaction. Subsequently, this spatiotemporal evolution can be correlated with different phases of a cycle of acoustic pressure oscillations. We quantify the spatiotemporal evolution of the pair of communities with maximum inter-community interaction using the average and maximum of all inter-community interactions present at any given instant of time, denoted by $A_{\mathrm{r,mean}}$ and $A_{\mathrm{r,max}}$, respectively.The time series of acoustic pressure oscillations is shown in blue. We observe that the time series of network measures is aperiodic during the state of combustion noise. The aperiodic nature of the inter-community interactions results from the incoherent spatiotemporal distribution of the vortical communities present during the state of combustion noise, as shown previously in Fig. 4.2(a).

We observe similar aperiodicity during the aperiodic epoch of intermittency (the interval of aperiodic epoch during intermittency is highlighted with a yellow background in Fig. 4.5b). We also notice that the mean of inter-community interactions $A_{\mathrm{r,mean}}$ shows an aperiodic behaviour during the periodic epoch on intermittency (interval highlighted with green background in Fig. 4.5b-i). Taking the mean of all inter-community interactions possibly smears the ability of the network measure $A_{\mathrm{r,mean}}$ to reflect the periodic spatiotemporal dynamics present in the reaction field during the periodic epoch of intermittency. However, we observe a significant correlation between the maximum of all

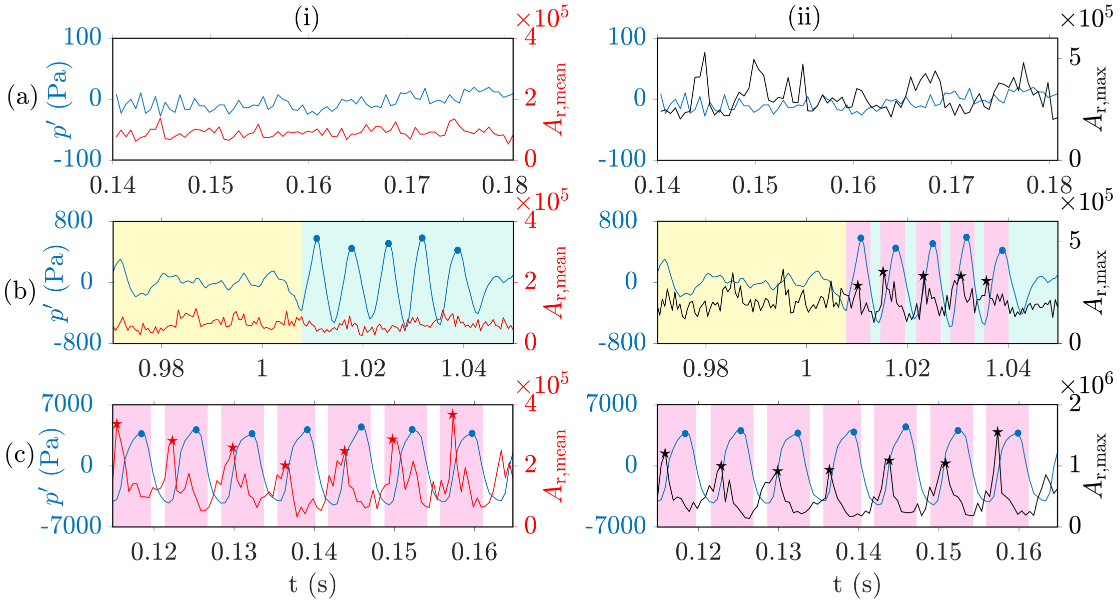

Figure 4.5: Variation of the network measures: (i) mean ($A_{\mathrm{r,mean}}$) and, (ii) maximum ($A_{\mathrm{r,max}}$) of all inter-community interactions during the states of (a) combustion noise, (b) intermittency, and (c) thermoacoustic instability, respectively. The acoustic pressure time series is shown in blue, whereas the time series showing the mean and maximum of all inter-community interactions are shown in red and black, respectively.

inter-community interactions $A_{\mathrm{r,max}}$ and the acoustic pressure fluctuations p' during the periodic epoch of intermittency. We denote the local maxima of $A_{\mathrm{r,max}}$ and p' through star and circle-shaped markers in Fig. 4.5(b-ii), respectively. A pair of local maxima of $A_{\mathrm{r,max}}$ and p' is present in each acoustic cycle during the periodic epoch of intermittency, as shown in each of the pink highlighted bands in Fig. 4.5(b-ii).

The evolution of the $A_{\mathrm{r,mean}}$ and $A_{\mathrm{r,max}}$ exhibits a significant periodic behaviour during the state of thermoacoustic instability. A consistent time lag is visible between the local maxima of the network measures (shown as red stars for $A_{\mathrm{r,mean}}$, and black stars for $A_{\mathrm{r,max}}$ in Fig. 4.5c) and time series of p' oscillations (shown as blue circles). Thus, the time series of inter-community interactions exhibit a strong delayed correlation with the time series of acoustic pressure fluctuations. The periodic behaviour of the network measures results from the periodic shedding of vortices from the backward-facing step and the ordered dynamics present in the combustor during thermoacoustic instability.

Interestingly, we also observe that the network measures $A_{\mathrm{r,mean}}$ and $A_{\mathrm{r,max}}$ calculated during the state of combustion noise are greater than that calculated during the periodic epoch of intermittency. This seems counter-intuitive at first, as the magnitude of p' fluctuations during the periodic epoch of intermittency is 6-7 times greater than that present during the state of combustion noise. To explain this, in the next section, we examine the distributions of vorticity, the magnitude of acoustic pressure fluctuations, and the network measures during all the three dynamical states exhibited by the combustor.

4.5 INTERPRETATION OF NETWORK MEASURES THROUGH HYDRODYNAMICS

The magnitude of acoustic pressure fluctuations present during the state of combustion noise is lower than that present during the state of intermittency (see Fig. 4.6a). However, we observe that the network measures $A_{\mathrm{r,mean}}$ (Fig. 4.6(c)) and $A_{\mathrm{r,max}}$ (Fig. 4.6f) present during the state of combustion noise are significantly higher than that present during the state of intermittency. This counter-intuitive behaviour of network measures with respect to the magnitude of acoustic pressure oscillations is due to a combination of two factors: the spatial distribution (Fig. 4.6d, g) and magnitude of vorticity (Fig. 4.6e, h) of the fluid elements that correspond to the nodes present in the vortical communities during the states of combustion noise and intermittency.

Calculating the mean of all the inter-community interactions $A_{\mathrm{r,mean}}$ involves taking into account the spatial positions and the vorticity of the fluid elements corresponding to the nodes present in all the vortical communities. We notice that the magnitude of vorticity present in all the vortical communities during the state of combustion noise (blue coloured distribution in Fig. 4.6e) is significantly greater than that during the state of intermittency (yellow coloured distribution in Fig. 4.6e). The higher values of the vorticity present in the vortical communities cause the network measures to be higher for the state of combustion noise, compared to that observed during the state of intermittency.

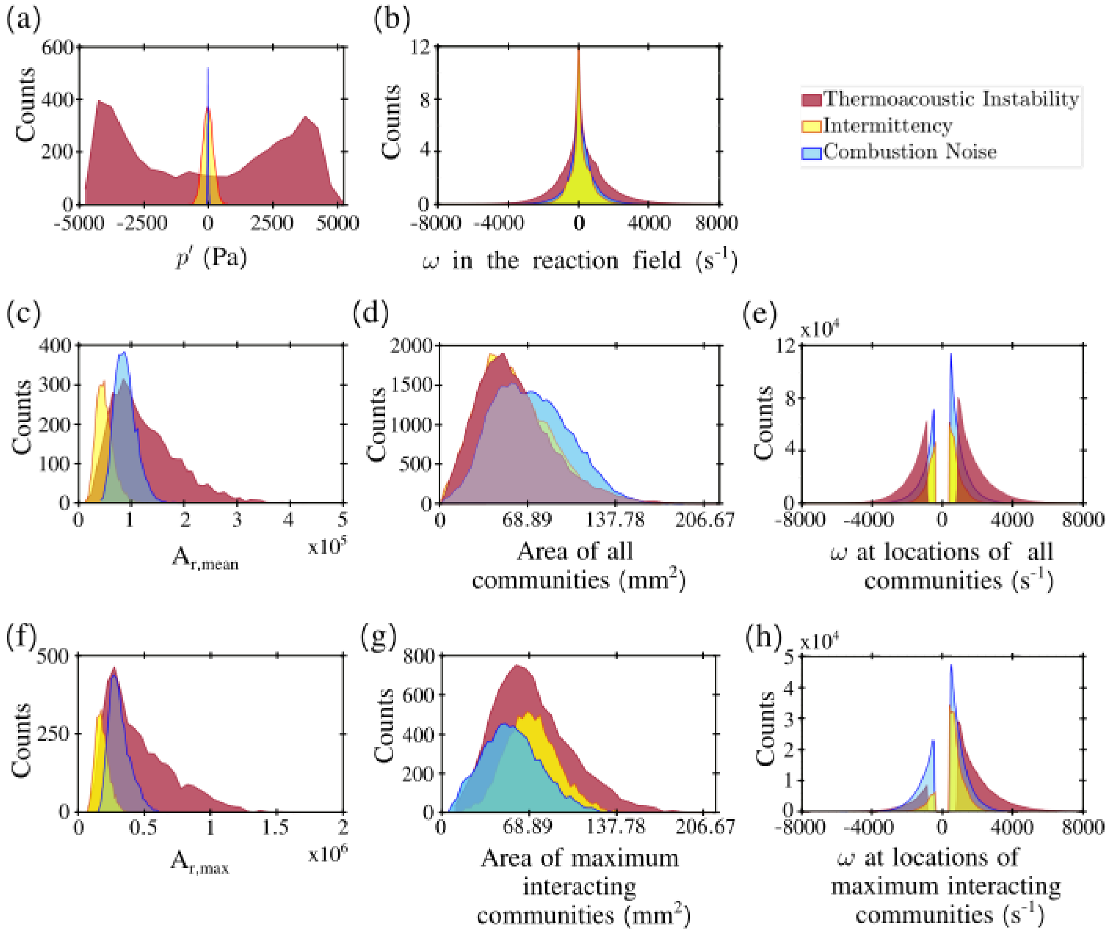

Figure 4.6: Histograms showing the distributions of (a) magnitude of p' fluctuations, and (b) vorticity values present in the flow field during the three dynamical states (legend of the distributions is shown on top right of the figure). The mean values of all the inter-community interactions ($A_{\mathrm{r,mean}}$) are shown in (c). $A_{\mathrm{r,mean}}$ is calculated by considering all the detected vortical communities. The distributions of the area of all the detected vortical communities and the vorticity of the fluid elements matching with the vortical communities are shown in (d) and (e), respectively. The gaps in the distribution of the vorticity values shown in (e) correspond to the vorticity threshold used to detect vortical communities (ω = 456 s^{-1}, 380 s^{-1}, and 843 s^{-1} for the states of combustion noise, intermittency, and thermoacoustic instability, respectively). The maximum values of all the inter-community interactions ($A_{\mathrm{r,max}}$) present during the three dynamical states are shown in (f). $A_{\mathrm{r,max}}$ is calculated by extracting the pair of communities with the largest inter-community interaction at each time step. The distribution of the area of such communities (with the maximum inter-community interaction) and the vorticity of the fluid elements matching with these vortical communities are shown in (g) and (h), respectively.

Furthermore, in Fig. 4.6(f), we observe a similar trend in the maximum of all the inter-community interactions $A_{\mathrm{r,max}}$ calculated during the states of combustion noise and intermittency, i.e., the distribution of $A_{\mathrm{r,max}}$ corresponding to combustion noise (blue coloured distribution in Fig. 4.6f) has larger values than that corresponding to the state of intermittency (yellow coloured distribution in Fig. 4.6f). We notice that the area of the vortical communities with maximum inter-community interactions is smaller during the state of combustion noise (blue coloured distribution in Fig. 4.6g), as compared to that present during the state of intermittency (yellow coloured distribution in Fig. 4.6g). Also, the magnitude of vorticity present in maximum interacting vortical communities during the state of combustion noise (blue coloured distribution in Fig. 4.6h) is substantially greater than that present during the state of intermittency (yellow coloured distribution in Fig. 4.6h). A lower area of maximum interacting vortical communities, combined with higher values of vorticity present in such communities, leads to higher values of $A_{\mathrm{r,max}}$ during the state of combustion noise compared to that observed during the state of intermittency.

It would be useful at this stage to delve deeply into interpreting the correlations observed between acoustic pressure fluctuations and the network measures. We are now in a position to discuss the spatiotemporal evolution of the vortical communities with maximum inter-community interactions. In the following section, we will analyze the connection between the network measures, the spatiotemporal evolution of maximum interacting vortical communities, and the corresponding hydrodynamics present in the reactive flow field.

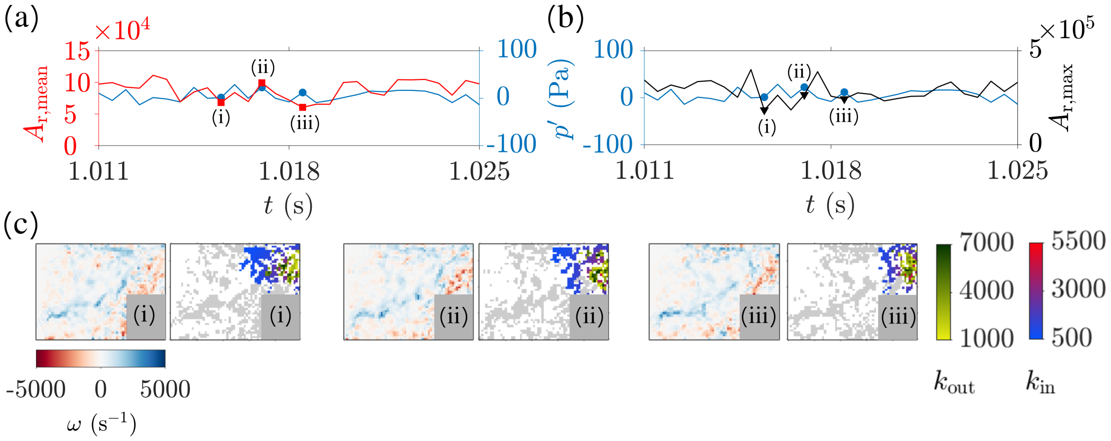

Figure 4.7: Time series showing the variation of (a) mean ($A_{\mathrm{r,mean}}$), and (b) maximum ($A_{\mathrm{r,max}}$) of all inter-community interactions at three representative points marked (i-xii) during the state of combustion noise. The acoustic pressure fluctuations are marked in blue. The vorticity field and the corresponding spatial distribution of the inter-community in- and out-strengths between the pair of communities with the maximum inter-community interaction at each of the representative time instants marked in (a-b) are shown in (c). The grey regions represent other vortical communities that have lower inter-community interactions. The colorbars represent the inter-community in-strengths (k_{in}) and out-strengths (k_{out}), respectively. The direction of the maximum inter-community interaction is from the community marked with k_{out} values to the community marked with k_{in} values. k_{out} and k_{in} denote the sum of in- and out-edge weights present between communities with maximum inter-community interactions, respectively. The aperiodic nature of the network measures reflects the aperiodic nature of hydrodynamic interactions present in the reaction field. Due to the shedding of significant vortices from the upstream tip of the bluff-body, the pair of communities with the maximum inter-community interaction are always present above the bluff body.

4.6 SPATIOTEMPORAL EVOLUTION OF MAXIMUM INTERACTING PAIRS OF VORTICAL COMMUNITIES

4.6.1 Combustion noise

In Fig. 4.7, we show the spatiotemporal evolution of the vortical communities with the maximum inter-community interactions across 3 representative points during the state of combustion noise. Fig. 4.7(a,b) shows the time series of acoustic pressure fluctuations and network measures. Fig. 4.7(c) shows the vorticity field and the corresponding pair of maximum interacting communities in the spatial domain. At each time instant, the pair of vortical communities consists of two different communities with one inter-community edge directed from, say, community 1 to community 2. Community 1 will exhibit outward inter-community strength distribution with k_{out} values, whereas, community 2 will exhibit inward inter-community strength with k_{in} values. Thus, in Fig. 4.7, the direction of the maximum inter-community interaction is from the community marked with k_{out} values to the community marked with k_{in} values. k_{out} and k_{in} indicate the sum of inter-community outward and inward edge weights present between the pair of communities with maximum inter-community interactions, respectively. The range of k_{out} and k_{in} are indicated in the colorbars. The aperiodic nature of the network measures shown in Fig. 4.7(a,b) reflect the aperiodicity in the spatiotemporal evolution of vortical interactions present during the state of combustion noise. The spatial distribution of the pair of communities in Fig. 4.7(c) shows that most of the vortical communities with maximum inter-community interactions are located above the bluff-body. This is due to a large concentration of coherent structures shed from the upstream tip of the bluff-body during the state of combustion noise, that can be seen in the corresponding vorticity fields in Fig. 4.7(c). Furthermore, the vortical communities shown are quite fragmented in space due to the presence of small regions of high vorticity present in the spatial domain. This is in contrast to the large spatially coherent vortical communities present during the aperiodic epochs of intermittency, as discussed in the next subsection.

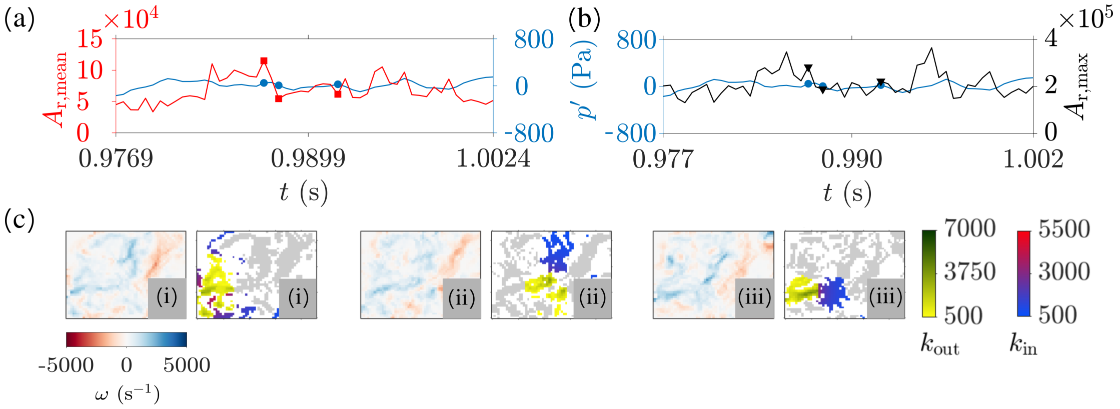

Figure 4.8: Time series showing the variation of (a) mean ($A_{\mathrm{r,mean}}$), and (b) maximum ($A_{\mathrm{r,max}}$) of all inter-community interactions at three representative points marked (i-iii) during an aperiodic epoch of intermittency. The vorticity field and the corresponding spatial distribution of the inter-community in- and out-strengths between the pair of communities with the maximum inter-community interaction at each of the representative time instants marked in (a-b) are shown in (c). The aperiodic nature of vortical interactions present in the reaction field causes the network measures to be aperiodic. Correspondingly, there is no specific trend in the position of the pair of communities with maximum inter-community interaction, as seen in (c).

4.6.2 Aperiodic epoch of intermittency

In this subsection, we look at the spatiotemporal evolution of maximum interacting vortical communities during the aperiodic epoch of intermittency. Fig. 4.8(a,b) shows the time series of acoustic pressure fluctuations and network measures during an aperiodic epoch of intermittency. Fig. 4.8(c) shows the vorticity field and the corresponding pair of maximum interacting communities in the spatial domain. The aperiodic nature of the network measures shown in Fig. 4.8(a,b) reflect the aperiodicity in the spatiotemporal evolution of vortical interactions present during the aperiodic epoch of intermittency. In Fig. 4.8(c), we observe large regions of low vorticity present in the reaction field, unlike the small localised regions of high vorticity present during the state of combustion noise. Thus, in comparison to the fragmented nature of vortical communities present during the state of combustion noise, we observe large spatially coherent vortical communities during the aperiodic epoch of intermittency. Moreover, the average of the inter-community node strengths is slightly lower than that observed during combustion noise (refer to the variation of $A_{\mathrm{r,mean}}$ in Fig. 4.7a-i and b-i). The lower values of $A_{\mathrm{r,mean}}$ observed during the aperiodic epoch of intermittency is due to the large spatial extent of low vorticity regions present during the aperiodic epoch of intermittency, in contrast with the small spatial extent of high vorticity regions present during combustion noise. The difference in the values of $A_{\mathrm{r,mean}}$ observed during the states of combustion noise and the aperiodic epoch of intermittency is an artefact of different spatiotemporal reaction fields present during the two dynamical states, even though the acoustic pressure fluctuations are of similar magnitude during these two dynamical states.

4.6.3 Periodic epoch of intermittency

During the periodic epoch of intermittency, we observe that spatially coherent regions with large magnitudes of vorticity begin to emerge in the reaction field (Fig. 4.9). Fig. 4.9(a,b) shows the time series of acoustic pressure fluctuations and network measures during a periodic epoch of intermittency. Fig. 4.9(c) shows the vorticity field and the corresponding pair of maximum interacting communities in the spatial domain. One can observe the emergence of coherent structures shed from the backward-facing step during acoustic pressure minima (at time instant (ii) in Fig. 4.9c). This emergence of localised coherent spatial structures is suggestive of self-organisation in the reaction field (Mondal *et al.*, 2017; George *et al.*, 2018). The downstream convection of the coherent structure shed from the backward-facing step is indicated through red circles in Fig. 4.9(c). At the instant of the coherent structure shedding from the backward-facing step (shown at time instant (ii)), the regions of vortical communities with the maximum inter-community interaction do not overlap with the locations of the coherent structure shed from the backward-facing step. This is due to the coherent structure being present near the periphery of the spatial domain (adjacent to the backward-facing step), which results in low inter-community strength of the nodes belonging to the vortical communities that overlap with the recently shed coherent structure. Subsequently, as the coherent structure that was shed from the backward-facing step convects downstream (time instants ii-vii in Fig. 4.9c), the inter-community interactions start to increase. Thus, the regions

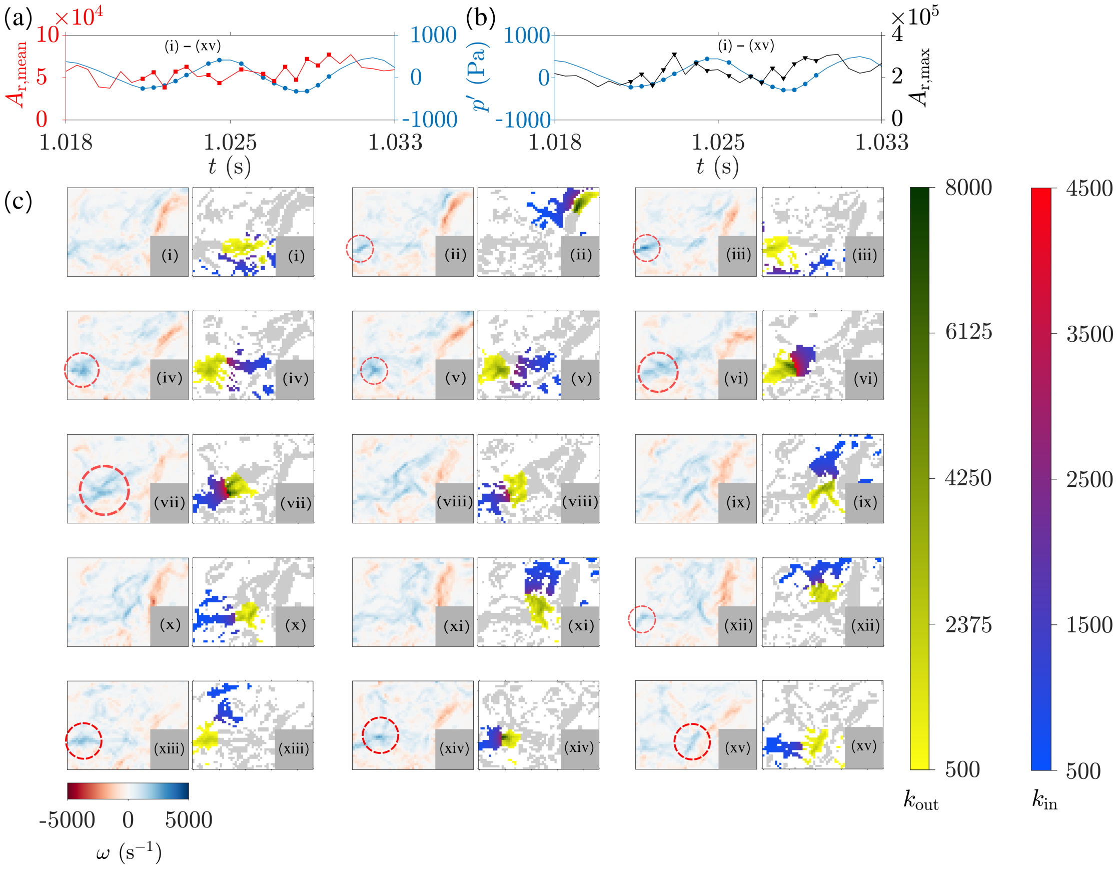

Figure 4.9: Time series showing the variation of (a) mean ($A_{\rm r,mean}$), and (b) maximum ($A_{\rm r,max}$) of all inter-community interactions at fifteen representative points marked (i-xv) during a periodic epoch of intermittency. The vorticity field and the corresponding spatial distribution of the inter-community in- and out-strengths between the pair of communities with the maximum inter-community interaction at each of the representative time instants marked in (a-b) are shown in (c). The red circles in (c) indicate the downstream convection of the coherent structure shed from the backward-facing step at the time instants (ii) and (xii). The location of the community with the maximum outward influence matches with the location of the downstream moving coherent structure indicated with red circles during time instants (ii-vii) and (xiii-xv). Subsequently, the coherent structure gets dissipated into the reaction field. The shedding and downstream convection of the coherent structure repeats during each acoustic cycle within the periodic epoch of intermittency, and is reflected in the periodic nature of $A_{\rm r,max}$ shown in (b).

with vortical communities with maximum inter-community interactions match with the regions of downstream convecting coherent structure till the acoustic pressure reaches the local maxima at the time instant (vii). Later, the coherent structure dissipates into the reactive flow field during the time instants marked (viii-xi). We again observe the shedding of a new coherent structure near the acoustic pressure minima at time instant (xii), and the above discussed spatiotemporal dynamics continues for the next acoustic cycle during the periodic epoch of intermittency. This periodicity in vortical interactions that occur due to a periodic shedding and downstream convection of coherent structures during the periodic epoch of intermittency is reflected in the periodic time series of the network measure $A_{\mathrm{r,max}}$, as seen in Fig. 4.9(b).

4.6.4 Thermoacoustic instability

Finally, in Fig. 4.10, we take a look at the spatiotemporal dynamics of maximum interacting vortical communities over an acoustic pressure cycle during the state of thermoacoustic instability. Fig. 4.10(a,b) shows the time series of acoustic pressure fluctuations and network measures during a periodic epoch of intermittency. Fig. 4.10(c) shows the vorticity field and the corresponding pair of maximum interacting communities in the spatial domain. The periodicity in the network measures seen in Fig. 4.10(a,b) reflects the periodic nature of vortical interactions present in the reaction flow field during the state of thermoacoustic instability. Similar to our discussion of coherent structures shedding from the backward-facing step during the periodic epoch of intermittency, we can observe the shedding of the coherent structure from the backward-facing step during the acoustic pressure minima (at time instant (i)) during the state of thermoacoustic instability. The downstream convection of the coherent structure shed from the backward-facing step at the minima of p' oscillations is indicated through red circles in Fig. 4.10(c). The regions of vortical communities with the maximum inter-community interaction match with the regions of coherent structure shed from the backward-facing step during the time instants (ii-vii). This matching of spatial regions of coherent structure shed from the backward-facing step and the community with maximum outward-interaction

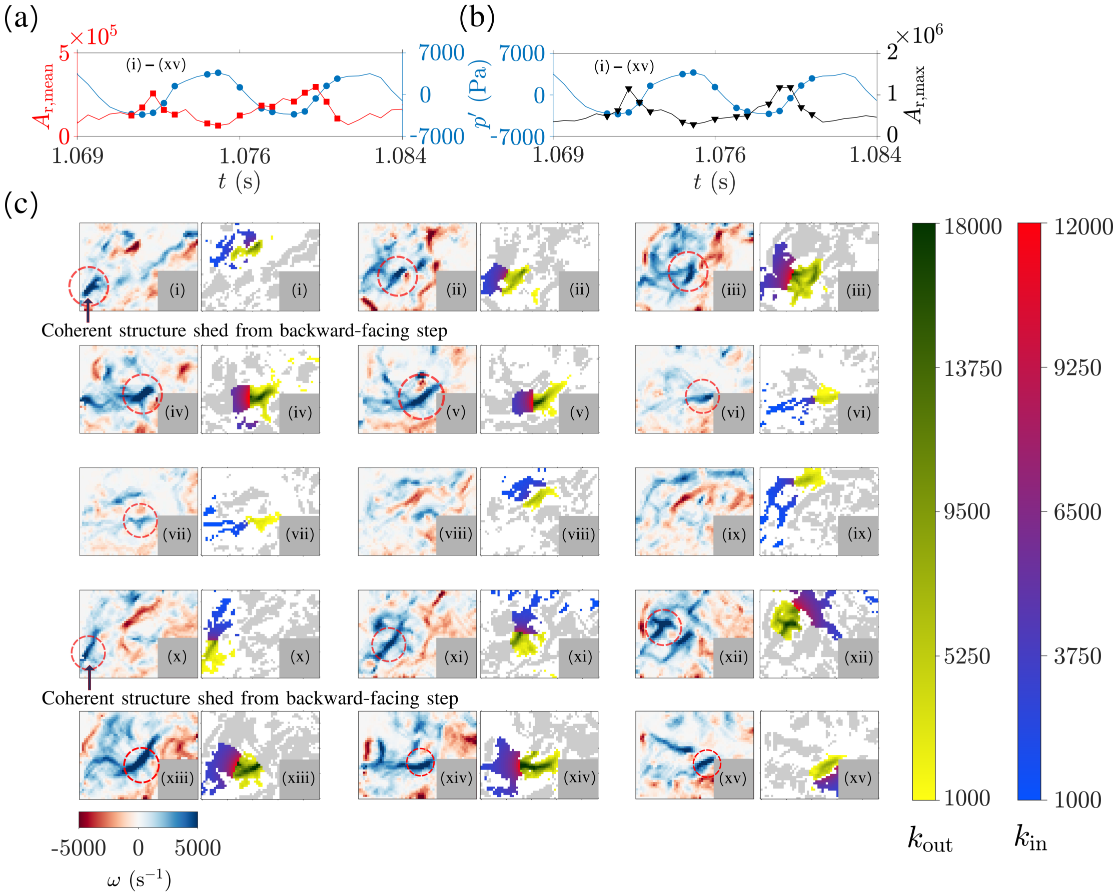

Figure 4.10: Time series showing the variation of (a) mean ($A_{\text{r,mean}}$), and (b) maximum ($A_{\text{r,max}}$) of all inter-community interactions at fifteen representative points marked (i-xv during the state of thermoacoustic instability. The vorticity field and the corresponding spatial distribution of the inter-community in- and out-strengths between the pair of communities with the maximum inter-community interaction at each of the representative time instants marked in (a-b) are shown in (c). The red circles in (c) indicate the downstream convection of the coherent structure shed from the backward-facing step at the time instants (i) and (x). The location of the community with the maximum outward influence matches with the location of the downstream moving coherent structure indicated with red circles during the time instants (i-vii) and (xi-xv). Subsequently, the coherent structure gets dissipated into the reaction field. The shedding and downstream convection of the coherent structure repeats itself during each acoustic cycle present within the state of thermoacoustic instability, and is reflected in the periodic nature of $A_{\text{r,max}}$ shown in (b).

is clearly visible till the acoustic pressure reaches the local maxima at the time instant (vii). Subsequently, as the coherent structure dissipates into the reactive flow field and the magnitude of vorticity present in the reactive field decreases during the time instants marked (viii-ix), it is difficult to discern the downstream movement of the coherent structure being discussed. We again observe the shedding of a new coherent structure near the acoustic pressure minima at time instant (x), and the above discussed spatiotemporal dynamics continues for the next acoustic cycle.

The locations of the two highest interacting communities being next to each other is expected, since lower distances between the two communities lead to larger edge weights, indicating larger vortical interactions. We have also seen that during the periodic epochs of intermittency and the state of thermoacoustic instability, the location of community with highest outward inter-community interaction matches with the location of the coherent structure shed from the backward-facing step. Poinsot *et al.* (1987) have showed that in a dump combustor that exhibits vortex-driven thermoacoustic instability, the time lag between the maximum of p' oscillations and the instant of vortex formation instant is one-fourth of the acoustic period T. However, in our study, we observe that the instant of vortex formation lags behind the maximum of p' oscillations with $T/2$ interval. Also, the time lag between the instant of maximum inter-community interactions and the maximum of p' oscillations is slightly less than $T/2$, as the inter-community interactions increase to a maximum at the time instant when the coherent structure shed from the backward-facing step has moved slightly downstream into the reaction field. Furthermore, a consistent time lag exists between the mean of all inter-community interactions and the p' oscillations. This indicates that in addition to the crucial role coherent structures play in combustion systems, the interaction of vortical elements is also necessary to comprehensively understand the flow physics in combustion systems.

4.6.5 Interim summary of community interactions present during different dynamical states

To summarize the findings we have discussed so far, we observe incoherent or fragmented vortical communities during the state of combustion noise. The pairs of communities with maximum inter-community interactions are predominantly located in the region above the bluff-body. The locations of these highly interacting communities overlap with the regions of the coherent structures that are shed from the tip of the bluff-body and convect downstream during the state of combustion noise. The time series of network measures show aperiodic behaviour similar to that present in the time series of acoustic pressure fluctuations.

During the state of intermittency, we observe large spatially coherent vortical communities located upstream of the bluff-body. It is interesting that, although the magnitude of p' fluctuations present during the periodic epoch of intermittency is 7-8 times larger than that present during the state of combustion noise or the aperiodic epochs of intermittency (Fig. 4.6c), the network measures calculated during the state of intermittency are smaller compared to that observed during the state of combustion noise (Fig. 4.5a-b). We attribute this behaviour to the presence of small clusters of large vorticity present in a narrow region above the bluff-body during the state of combustion noise (Figs. 4.2(a) and 4.7(c)), in contrast to the presence of large regions of low vorticity present downstream of the backward-facing step during the state of intermittency (Figs. 4.2(c-d), 4.8(c), and 4.9(c)). The combination of highly localised coherent structures of high vorticity present in a narrow region leads to higher network measures during the state of combustion noise, as compared to that observed during the state of intermittency.

Finally, during the state of thermoacoustic instability, we observe sustained periodic emergence of vortical communities from the backward-facing step. The vortical communities with the maximum outward inter-community interactions overlap with the regions of coherent structures shed from the backward-facing step till the acoustic pressure reaches its local maxima. Subsequently, the spatial correlation of the highest outward interacting community with the strongest coherent structure is lost as the coherent structure weakens and dissipates into the reaction field. We again observe the shedding of a new coherent structure near the acoustic pressure minima, and the above discussed spatiotemporal dynamics continues for the next acoustic cycle during the state of thermoacoustic instability.

4.7 INSIGHTS INTO CRITICAL REGION DETECTED FOR SMART PASSIVE CONTROL

Having analyzed the spatiotemporal evolution of maximum interacting pairs of communities during different dynamical states exhibited by the turbulent combustor, we now turn our attention to the relevance of maximum inter-community interactions toward the mitigation of thermoacoustic instability. The turbulent combustor being discussed in the current study exhibits vortex-driven thermoacoustic instability. Thus, the mitigation of thermoacoustic instability in this type of combustor is intricately related to leveraging our understanding of the spatiotemporal dynamics of the combustor. The control of thermoacoustic instability in practical systems continues to be a challenging problem. Open-loop control strategies are widely used in practical combustion systems due to their minimal maintenance requirements and high durability. One of the open-loop control methods is to target certain *critical* regions using secondary fuel or air to perturb the flow regions responsible for controlling the overall dynamics of the system. Ghoniem *et al.* (2005) and co-workers (Altay *et al.*, 2007, 2010) determined the optimum region as the region of flame anchoring and considered a steady injection of secondary air for achieving control in a dump combustor. Uhm and Acharya (2005) considered the region of local maxima in the heat release rate field to be the critical region. In a similar study, Tachibana *et al.* (2007) optimised the secondary fuel injector parameters using Rayleigh Index distribution to actively control thermoacoustic instability in a swirl-stabilised lean premixed combustor.

In the experimental setup used in the current chapter, Unni *et al.* (2018), Krishnan *et al.* (2019*a*), and Roy *et al.* (2021) have detected the presence of such critical regions using different methods. Unni *et al.* (2018) used the spatial distribution of various network measures such as degree, local clustering coefficient, betweenness, and closeness centrality obtained from spatial Pearson correlation coefficient and dot product networks. They found that the bluff body wake region controls the dynamics during the state of combustion noise. As the equivalence ratio of the reactant mixture is decreased and the combustor starts to exhibit the state of intermittency, other regions of the flow field such as the region between the outer and inner shear layer and the wake behind the backward-facing step start to display higher network measures. With further decrease in the equivalence ratio of the reactant mixture, the combustor starts to exhibit the state of thermoacoustic instability. During this state, the bluff body wake loses its significance and the shear layer region emerges as the most critical region.

Subsequently, Krishnan *et al.* (2019*a*) generated weighted spatial correlation networks based on the velocity field. They applied network measures, including strength, weighted local clustering coefficient, and weighted closeness centrality, to determine the most suitable implementation site for open-loop control strategies. The authors were able to lower the amplitude of the pressure oscillations to a value comparable to that seen during the state of combustion noise by injecting microjets at these optimal locations. Subsequently, Roy *et al.* (2021) used several measures, such as the Fourier amplitude of turbulent velocity fluctuations, Hurst exponent, time-averaged vorticity, averaged heat release rate (HRR), and Rayleigh index to quantify the spatiotemporal dynamics of the turbulent combustor during the three dynamical states. The authors observed that the Fourier amplitude of turbulent velocity fluctuations provides the most optimal locations for application of open-loop control to mitigate themroacoustic instability. The authors also showed that Hurst exponent can predict the critical region during the state of intermittency, in contrast to the other physical measures discussed above.

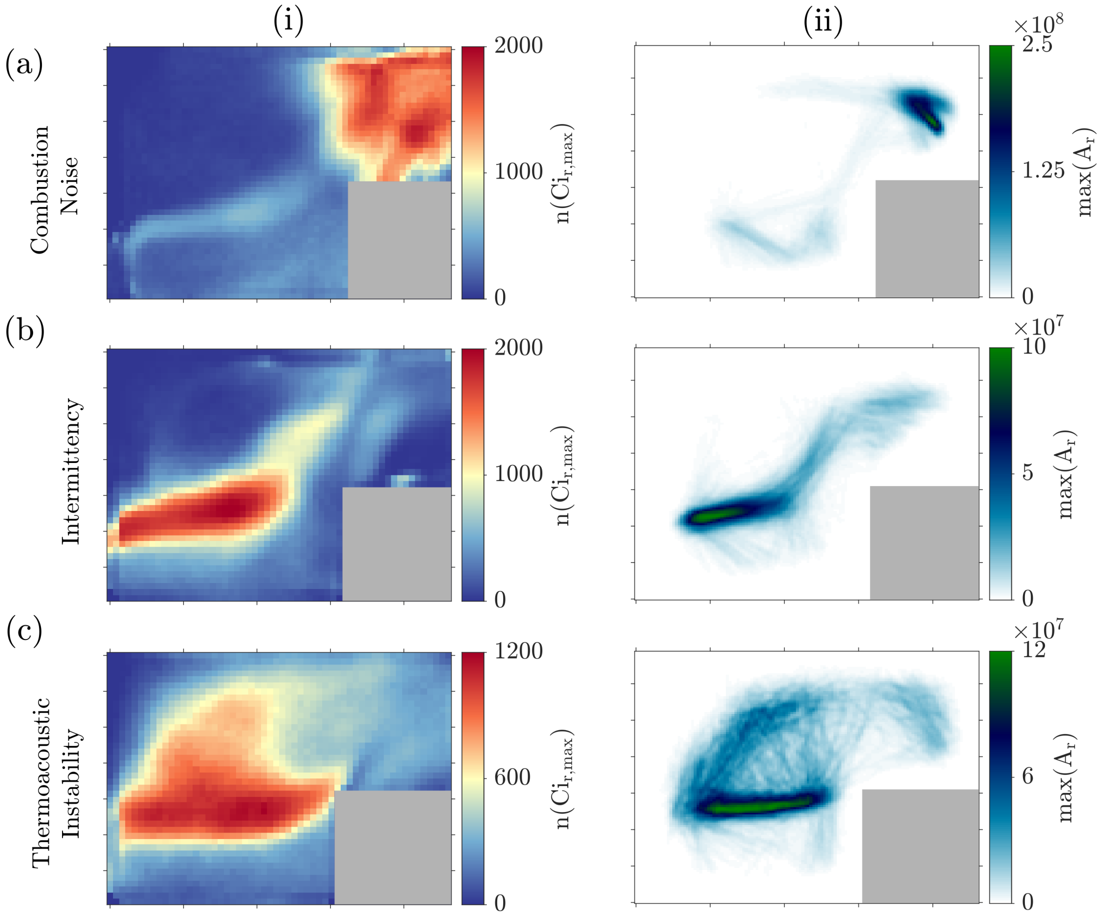

Figure 4.11: (i) The distribution of the spatial location of vortical communities with the maximum inter-community interactions during the states of (a) combustion noise, (b) intermittency, and (c) thermoacoustic instability. $n(\mathrm{Ci}_{r,\max})$ denotes the number of overlapped vortical communities used to plot the distribution of the spatial location of vortical communities with the maximum inter-community interactions. (ii) Plot of kernel smoothed intensity function of the maximum inter-community interactions. Consistent with the results discussed in Fig. 4.8(c), most of the communities with maximum inter-community interactions are present above the bluff-body during the state of combustion noise. This is related to the significant shedding of coherent structures from the upstream tip of the bluff body during the state of combustion noise. The spatial region indicating the maximum probability of finding the most influential communities shifts upstream during the state of intermittency and thermoacoustic instability. These new regions observed in (b-c) are detected via community-based dimensionality reduction of vortical networks and are consistent with the critical regions detected in Roy *et al.* (2021).

The high correlation between network measures and acoustic pressure fluctuations during the state of thermoacoustic instability, as seen in Fig. 4.5(c), motivates us to conjecture that communities with maximum inter-community interactions play a critical role towards the macroscopic dynamics exhibited by the combustor. Disrupting the interactions between the communities having the maximum interaction during thermoacoustic instability can help us to break the positive coupling between the vortical interactions and acoustics in the combustor, thus suppressing the high amplitude acoustic pressure fluctuations. This would, in turn, correspond to perturbing the closely positioned regions of high vorticity that are detected as largest interacting pair of communities in the network space.

Thus, our current objective is to understand the occurrence of the critical regions in the reaction flow field through the lens of vortical interactions analysed via complex networks. To this end, we plot the spatial distribution of vortical communities having the maximum interaction (at all time instants) during the states of combustion noise, intermittency, and thermoacoustic instability, in Fig. 4.11(i). For each dynamical state, a total of 3796 snapshots (equivalent to 300 acoustic cycles present during the state of thermoacoustic instability) are utilised for this analysis. The spatial distribution of the communities having maximum interaction is plotted by first detecting the pair of such communities at each time instant during a dynamical state. All the pairs of communities having the maximum inter-community interactions at all the time instants are subsequently overlapped in the spatial domain to identify the region where such influential communities are most likely to be found. The colourbar for Fig. 4.11(i) represents the number of vortical communities with maximum inter-community interactions detected during the three different dynamical states.

We observe the influential communities present primarily above the bluff-body during the state of combustion noise (Fig. 4.11i-a). These vortical communities correspond to the small-sized clockwise vortices shed from the tip of the bluff-body due to the flow turning at the corner of the bluff-body. The red region above the bluff-body matches with the region where the vortices that have been predominantly shed from the tip of the bluff-body during the state of combustion noise are present.

The methodology presented in this work also detects a distinct region with maximum-interacting vortical communities downstream of the backward-facing step in Fig. 4.11(i)-(b) during the state of intermittency. Both the periodic as well as aperiodic epochs were considered while calculating the region of maximum interacting pair of interactions during the state of intermittency. The vortices are shed almost periodically at the backward-facing step for short epochs of time during the periodic epoch of intermittency, after which they may break down into smaller vortices or impinge on the walls of the combustor or bluff-body. This region is consistent with the critical regions detected during the state of intermittency in Roy *et al.* (2021) and Tandon and Sujith (2023). Other physical measures such as Fourier amplitude of turbulent velocity fluctuations and the weighted closeness centrality in a weighted spatial correlation network obtained from the velocity field in Krishnan *et al.* (2019*a*) can identify critical region only during the state of thermoacoustic instability, not during intermittency.

Finally, during thermoacoustic instability (Fig. 4.11i-c), the region with maximum-interacting vortical communities increases in size and extends from the backward-facing step to the upstream boundary of the bluff-body. A significant part of this region, calculated through the present methodology during the state of thermoacoustic instability, is consistent with the corresponding critical regions detected through the spatial distribution of Hurst exponent (Roy *et al.*, 2021) and weighted closeness centrality of weighted spatial correlation networks constructed from velocity field (Krishnan *et al.*, 2019*a*). The consistency of the region having maximum-interacting vortical communities detected in the current study with that of critical regions detected in previous studies corroborates the applicability of the methodology proposed in this chapter.

We also examine the spatial distribution of weights of the maximum inter-community interactions in Fig. 4.11(b), where we plot the corresponding kernel smoothed intensity function of $A_{\mathrm{r,max}}$. $A_{\mathrm{r,max}}$ is the magnitude of largest inter-community interaction, and is equal to the largest value of the reduced adjacency matrix. The inter-community edge weights cannot be discerned on a discretised spatial domain, unlike the nodes that can be accurately identified on the discretised spatial domain. Thus, we use the kernel smoothed intensity function to plot the embedding of maximum inter-community edge weights in the spatial domain. We use the inter-community edge weights to estimate the number of points corresponding to the weights per unit area in the spatial domain. The expected number of points per unit area corresponding to the edge weights are termed as *intensity*, and is a function of spatial location. A kernel smoothed intensity function is an estimate of this *intensity* function of the maximum inter-community edge weights that generate a point pattern data embedded in the spatial domain (Diggle, 1985; Baddeley *et al.*, 2015). We use an isotropic Gaussian kernel with a standard deviation $\sigma = 0.3$ for both directions to calculate the intensity function. Details on the method of kernel density estimation are presented in Appendix B.

The regions with kernel density estimates of $A_{\mathrm{r,max}}$ indicate the spatial embedding of weights between vortical communities with maximum inter-community interaction. During the state of combustion noise, the most significant coherent structures are shed from the tip of the bluff-body. Thus, we observe that most of the maximum inter-community interactions occur above the bluff-body (Fig. 4.11ii-a). The region of maximum inter-community interactions shifts upstream during the state of intermittency as seen in Fig. (4.11ii-b). Finally, this region of maximum inter-community interactions increases in size along with an increase in the values of $A_{\mathrm{r,max}}$ during the state of thermoacoustic instability. The values of the kernel smoothed intensity function of $A_{\mathrm{r,max}}$ obtained during the state of combustion noise (Fig. 4.11ii-a) are in between the values corresponding to intermittency (Fig. 4.11ii-b) and thermoacoustic instability (Fig. 4.11ii-c). This is consistent with the distribution of $A_{\mathrm{r,max}}$ shown in Fig. 4.6(f). Thus, the present framework proves to be a reliable method for understanding the spatiotemporal dynamics of thermoacoustic systems through the complex network perspective.

4.7.1 Network measures during mitigation of thermoacoustic instability

Two primary strategies for mitigating thermoacoustic instability are active control, involving the deployment of actuators such as loudspeakers or solenoid valves and oscillatory air/fuel injection, and passive control, encompassing geometric alterations such as acoustic liners, baffles, resonators, or injector adjustments. Active control comprises of closed-loop and open-loop active control. In contrast to closed-loop active control methods that exhibit reliability issues such as the use of electro-mechanical components in the harsh environment present inside a combustor, open-loop control methods are significantly simpler to implement in a combustor because neither a dynamic sensor signal nor a signal processor is necessary.

Open-loop control requires knowledge about the relative importance of different regions in the flow field. In the experimental setup used in the present study, Krishnan *et al.* (2019*a*) used node strengths of a weighted spatial correlation network constructed from velocity fields to identify a critical region in the reaction zone of the combustor. Subsequently, the authors introduced microjets of air into the critical region to suppress thermoacoustic instability. Microjets of air steadily injected through the injector numbered 1 (cf. Fig. 4.12a) resulted in the most efficient mitigation of thermoacoustic instability, compared to injection via other ports. We conjecture that this targeted control disrupted the key vortical communities with the maximum inter-community interactions present during the state of thermoacoustic instability, thus leading to the mitigation of instability. The disruption of interactions between the key vortical communities would have also perturbed the region of interaction between the hydrodynamic and the heat release rate subsystems, as conjectured by Tandon and Sujith (2023). Results derived from community-based network reduction in the current study complement and help us explain the observations from earlier studies about identifying a critical region and the subsequent targeting of the critical region to mitigate thermoacoustic instability. The strong interplay between

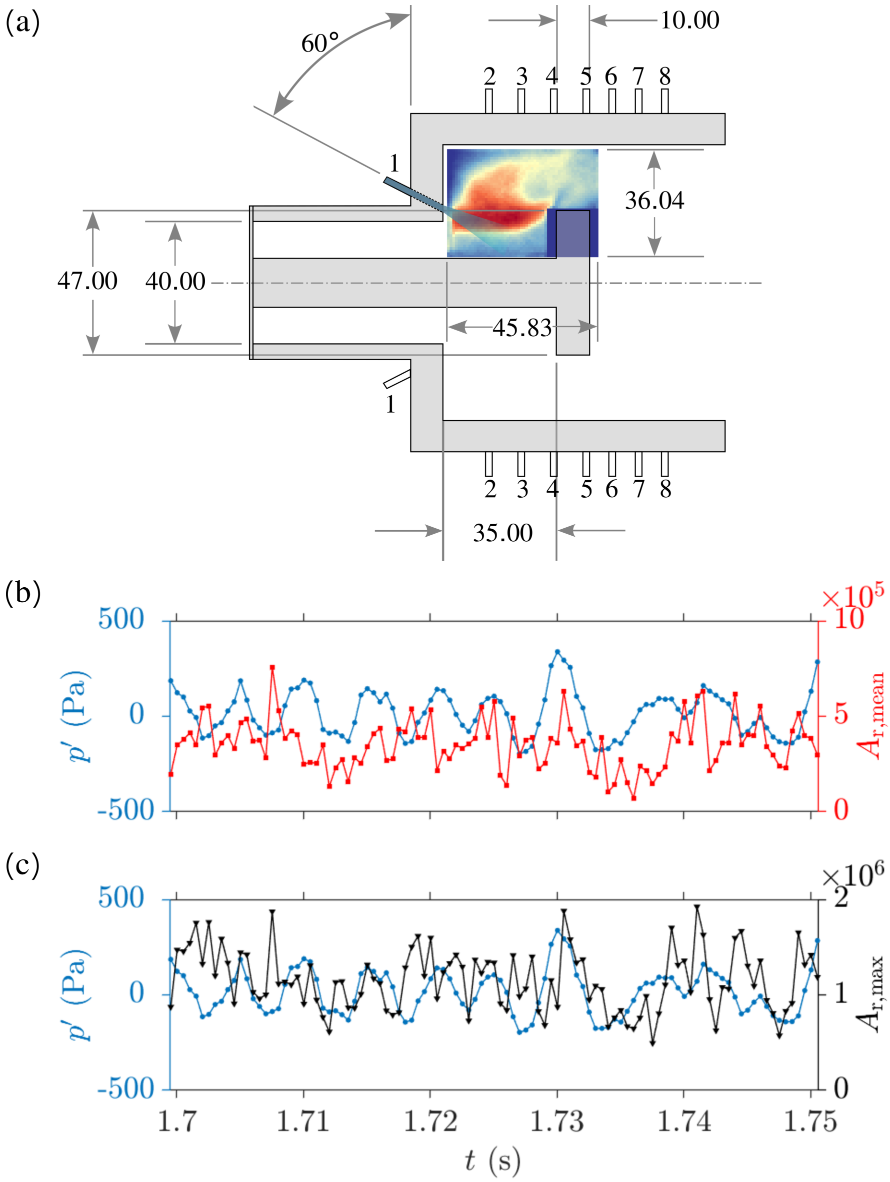

Figure 4.12: (a) The cross-section of the combustion chamber showing the microjet injector locations. The coloured figure in the inset shows the region with maximum-interacting vortical communities detected during the state of thermoacoustic instability. (b-c) Variation of the network measures: mean ($A_{\mathrm{r,mean}}$) and, maximum ($A_{\mathrm{r,max}}$) of all inter-community interactions during the state of suppression of thermoacoustic instability with microjet injection through injector numbered 1. The time series of acoustic pressure fluctuations are shown in blue, whereas the time series showing the mean and maximum of all inter-community interactions are shown in red and black, respectively. The network measures exhibit aperiodicity during the state of suppression, indicating the aperiodic nature of hydrodynamic interactions present when air microjet is used to mitigate thermoacoustic instability.

hydrodynamic and acoustic fields during the state of thermoacoustic instability (Fig. 4.5c), quantitatively investigated using correlation between time series of vortical network measures and acoustic pressure oscillations, emboldens us to hypothesise that these strongly interacting vortical communities play a critical role towards the generation of thermoacoustic instability. Perturbations through targeted attacks via secondary air injections disrupt the inter-community interactions or the most influential communities themselves that are detected during the state of thermoacoustic instability.

During the state of suppression of thermoacoustic instability through microjet injection via injector 1, we observe that the time series of the mean ($A_{\mathrm{r,mean}}$) and maximum ($A_{\mathrm{r,max}}$) of all inter-community interactions exhibit aperiodic dynamics, similar to that present in the time series of acoustic pressure fluctuations. The aperiodic dynamics exhibited by the network measures is similar to that observed during the state of combustion noise shown in Fig. 4.5(a). However, the magnitude of network measures present during the state of suppression is comparable to that observed during the state of thermoacoustic instability. We believe that the increased magnitude of network measures is due to the presence of additional shear layer regions introduced in the flow region through microjet injection.

4.8 INTERIM SUMMARY

A great deal of previous research into thermoacoustic instability has focused on the role of coherent structures toward driving the instability in turbulent combustors. Rogers and Marble (1956) provided the earliest description of the role of vortices in thermoacoustic instability. They showed that a transverse acoustic mode excited in an acoustic duct triggered the shedding of vortices in the reaction field. The heat release pulse from the combustion of reactants inside the vortices feeds energy into the transverse acoustic mode and leads to themroacoustic instability. Subsequently, a significant portion of the work done since the 1980s have extended our knowledge of understanding how coherent structures contribute to thermoacoustic instability (Parker *et al.*, 1979; Pitz and Daily, 1981; Keller *et al.*, 1982; Zukoski, 1985; Poinsot *et al.*, 1987; Schadow *et al.*, 1989; Schadow and Gutmark, 1992; Wu and Kung, 2000; Matveev and Culick, 2003; Speth *et al.*, 2008; Hussain *et al.*, 2022).

The current chapter sets out to shine new light on the connection between thermoacoustic instability and the interactions between regions of high vorticity present in a turbulent combustor. We compute the key interactions between regions of intense vorticity through induced velocities calculated using Biot-Savart Law. These induced velocities are used to construct time-varying weighted directed networks, which we term as vortical networks. The vortical networks are used to identify the communities or modular structures in the unsteady flows through the modularity maximisation algorithm. We then collapse the complete vortical network through the centroid of each community, considerably reducing the dimension of the fluid flow. Subsequently, we investigate the correlation of the maximum and mean of all the vortical community interactions with the global dynamics exhibited by the combustor during different dynamical states. The correlations help us to understand the interplay between hydrodynamic and acoustic fields present in the reaction field of the combustor. This allows us to understand the occurrence of critical regions detected during the states of intermittency and thermoacoustic instability in previous studies.

The methodology mentioned above is applied to the vorticity data obtained from experiments in a bluff-body stabilised turbulent combustor operating during the states of combustion noise, intermittency, and thermoacoustic instability. We explain the occurrence of vortical communities with maximum outward influencing capability (quantified using out-strength of inter-community edges) from the perspective of vorticity field. Furthermore, we observe strong correlations between the statistics of the vortical community interactions and the acoustic pressure fluctuations during thermoacoustic instability. The correlations decrease significantly when the combustor exhibited disordered dynamics during the state of combustion noise.

As mentioned above, the strong delayed correlations observed between the statistics of vortical community interactions and the acoustic pressure fluctuations during the state of thermoacoustic instability emboldens us to hypothesise that the key vortical community interactions play a critical role toward the behavior exhibited by the combustor. Taking a cue from this hypothesis, we use the locations and edge weights of maximum interacting vortical communities to explain the occurrence of critical region detected during different dynamical states in previous studies. Our results complement the findings in earlier works by Krishnan *et al.* (2019*a*), Roy *et al.* (2021), Tandon and Sujith (2023), and Premchand *et al.* (2023) on the same experimental setup, thus validating our approach.

In closing of this chapter, we note that the current method has the potential for widespread application in combustion and other fluid-mechanical systems. First, it enables us to recognise and quantify how the interactions between different vortical communities correlate with the macroscopic dynamics exhibited by the fluid-mechanical systems. Thus, we show that in addition to the already well-established role of coherent structures in combustion systems, an analysis of the interaction between different vortical elements is essential to understand the spatiotemporal dynamics of combustion systems. Secondly, for combustion systems susceptible to thermoacoustic instability, the distribution of vital vortical communities during the state of intermittency can be used to explain the occurrence of critical regions that have been shown to drive thermoacoustic instability. Thirdly, the present work provides a way forward to develop low-order models for a turbulent thermoacoustic system using statistical behaviour of communities, the inter- and intra-community strengths, and the locations of communities in the reactive field of the combustor. Finally, we believe that the present methodology provides a path for future model development and advanced flow control efforts to alter the dynamics of vortical structures in turbulent fluid-mechanical systems. We believe that the present methodology is generalisable to arbitrary thermofluid systems where instability control is a crucial requirement.

CHAPTER 5

DYNAMICS OF DELAYED ACOUSTIC SELF-FEEDBACK IN THERMOACOUSTIC SYSTEMS

In the previous chapter, we highlighted the interplay between hydrodynamic interactions and acoustic field in a thermoacoustic system. We also discussed the implications of this interplay toward the control of thermoacoustic instability by injecting air microjets in the critical region. This type of control strategy belongs to the category of open loop control, where no feedback is involved in the control action. In this chapter, we discuss a novel strategy of delayed acoustic self-feedback to understand how a thermoacoustic system can influence itself via its own acoustic field, and the role of such interactions toward mitigating thermoacoustic instability.

Traditionally, different mechanisms of closed-loop and open-loop active controls have been developed for suppressing thermoacoustic instability (Dowling and Morgans, 2005). In these methods, the dynamics of a thermoacoustic system is forced using external perturbations of specific amplitudes and frequencies. However, these methods suffer from several limitations, such as the use of complex electromechanical components, lack of reliability of sensors while working in the hostile conditions of practical combustors, and high maintenance and replacement costs. Another way to mitigate thermoacoustic instability is to use passive damping devices such as perforated liners, quarter and

---

The results presented in this chapter are published in the following two papers:

1. Srikanth, S., Sahay, A., Pawar, S. A., Manoj, K., & Sujith, R. I. (2022). Self-coupling: An effective method to mitigate thermoacoustic instability. *Nonlinear Dynamics*, 110(3), 2247-2261. `https://doi.org/10.1007/s11071-022-07750-7`

2. Sahay, A., Kushwaha, A., Pawar, S. A., Dhadphale, J. M., & Sujith, R. I. (2023). Mitigation of limit cycle oscillations in a turbulent thermoacoustic system via delayed acoustic self-feedback. *Chaos: An Interdisciplinary Journal of Nonlinear Science*, 33(4), 043118. `https://doi.org/10.1063/5.0129512`

half-wave resonators, Helmholtz resonators (Zhao and Li, 2015), Herschel-Quincke tubes (Rajaram and Ritland, 2012), modification of the fuel injector geometry/location (Steele *et al.*, 2000; Smith, 2005), and secondary air/fuel injections (Schadow and Gutmark, 1992; Huang and Yang, 2009). Engine manufacturers have used such passive damping devices to suppress thermoacoustic instability in practical combustors (Lieuwen and Yang, 2005; Bellucci *et al.*, 2004*b*).

The aforementioned disadvantages of traditional passive and active control methodologies point to the need for a control strategy that is cheap, simple to implement on practical combustion systems, and is effective in mitigating thermoacoustic instability. Recent studies have demonstrated that the method of mutual coupling, i.e., connecting two thermoacoustic systems with a tube, can mitigate thermoacoustic instability in the connected systems (Dange *et al.*, 2019; Jegal *et al.*, 2019). Such a phenomenon wherein coupling one or more oscillators quenches all oscillations in the coupled system to a common fixed point is referred to as ‘amplitude death’ (AD) (Mirollo and Strogatz, 1990; Reddy *et al.*, 2000).

Recently, a concept from synchronisation theory (Lakshmanan and Murali, 1996; Pikovsky *et al.*, 2003), called mutual coupling of oscillators, has been adopted to suppress limit cycle oscillations (LCO) in two or more thermoacoustic systems (Sujith and Pawar, 2021). At appropriate values of coupling parameters, the coupled systems approach the same steady state of oscillation quenching, known as amplitude death (Zou *et al.*, 2021). Through rigorous experimental and numerical analysis, amplitude death (Thomas *et al.*, 2018*b*; Hyodo *et al.*, 2020; Ghosh *et al.*, 2022) and partial amplitude death (Dange *et al.*, 2019; Srikanth *et al.*, 2022) have been studied in coupled laminar thermoacoustic systems (Doranehgard *et al.*, 2022). Here, partial amplitude death is a phenomenon in which some of the oscillators are in the suppressed state, but the others continue their oscillations (Atay, 2003). In addition, a few studies have investigated the dynamics of coupled turbulent combustors (Thomas *et al.*, 2018*b*; Jegal *et al.*, 2019; Moon *et al.*, 2020*a*; Guan *et al.*, 2021; Pedergnana and Noiray, 2022*a*; Fournier *et al.*, 2021; Moon *et al.*, 2020*b*; Pedergnana and Noiray, 2022*b*), and have reported the presence of amplitude death (Jegal *et al.*, 2019). Here, the mutual coupling between the systems is achieved by using one (or more than one) connecting tube of a fixed length and diameter. In all the studies, it is often assumed that an increase in the length of the coupling tube correspondingly increases the delay time in the coupling of the acoustic fields in the systems (Dange *et al.*, 2019).

Till now, the concept of amplitude death has been proposed to mitigate thermoacoustic instability in multiple coupled thermoacoustic systems. A majority of these studies have extensively focused on suppressing thermoacoustic instability in Rijke tubes. Rijke tubes are mostly laminar thermoacoustic systems and are relatively simpler when compared to practical turbulent thermoacoustic systems (Manoj *et al.*, 2022). In a Rijke tube, the system behavior loses the stability of the steady state and starts exhibiting LCO via a Hopf bifurcation due to a change in the control parameter (Manoj *et al.*, 2022). In contrast, in a typical turbulent combustion system, the system behavior transitions from high-dimensional chaos to LCO (thermoacoustic instability) via intermittency (Nair *et al.*, 2014). Intermittency is characterised by epochs of low-amplitude chaotic oscillations interspersed with seemingly random bursts of high-amplitude periodic oscillations. Due to the turbulent flow field, the interactions between the flame, flow, and the acoustic fields are significantly complex when compared to the dynamics present in laminar systems (Sujith and Pawar, 2021). The nonlinear interplay of such different subsystems at local scales in a turbulent system can lead to the emergence of collective behavior at the global scale. The process of larger entities, patterns, and regularities emerging through interactions between constituent entities that are unable to exhibit these features on their own is known as "emergence," and it is a key component of complex systems. Large coherent vortices and an ordered acoustic field are developed from the background of turbulent combustion during the onset of thermoacoustic instability in a turbulent combustion system.

In the present chapter, we propose the method of self-coupling in which we provide acoustic self-feedback using a tube. In self-coupling, the acoustic wave takes a finite time to propagate through the coupling tube and affect the acoustic field of the Rijke tube (Biwa *et al.*, 2016). This leads to a delay in the self-feedback of acoustic oscillations of the system. Such delayed self-feedback has generally been implemented in the past to stabilise steady states in several systems, including the Van der Pol oscillator (Suchorsky *et al.*, 2010), the Rössler oscillator (Ahlborn and Parlitz, 2005), and in electrochemical and optomechanical (Parmananda *et al.*, 1999; Naumann *et al.*, 2014) systems. However, the practical implementation of these self-feedback techniques involve electronic components to capture the delayed signal and to amplify and feed it back to the system. This is resolved in the method of self-coupling used in the current chapter where the acoustic pressure signal from a thermoacoustic system is directly fed to itself, without any explicit signal processing or modifying the inlet flow conditions. Thus, this method completely removes the requirement for any electro-mechanical components such as signal processors, sensors, and actuators used in traditional active and self-feedback controls. Additionally, the connecting tube is easier to design and implement as compared to traditional passive controls. Though methods similar to self-coupling, such as the Herschel-Quincke tube and the infinity tube have been used in the past to suppress electrically driven acoustic pressure oscillations (Biwa *et al.*, 2016; Lato *et al.*, 2019), their application in thermoacoustic systems is yet to be examined.

In the first section of this chapter, we demonstrate the effectiveness of coupling the acoustic field of a single turbulent combustor with itself to break the closed-loop interaction between the heat release rate and the acoustic pressure fluctuations and, thus, mitigating thermoacoustic instability. This method of coupling the acoustic field with itself after a particular duration is referred to as delayed acoustic self-feedback (Biwa *et al.*, 2016). As compared to the traditional closed-loop active controls (Dowling and Morgans, 2005) where the acoustic field in the combustor is subjected to its own feedback after processing it via digital delay lines and power amplifiers to alter the inlet conditions of the combustor (Annaswamy and Ghoniem, 2002), the method of self-feedback is realised by continuously making the acoustic field in the system interact with itself through a connecting tube. The connecting tube induces a time delay in the feedback, where the time delay is proportional to the length of the tube (Biwa *et al.*, 2015; Dange *et al.*, 2019). Time delayed feedback introduced electronically, has been successfully used in diverse experimental systems, such as lasers (Basso *et al.*, 1998), gas-discharge (Pierre *et al.*, 1996), hydrodynamic (Lüthje *et al.*, 2001), electrochemical (Parmananda *et al.*, 1999), and ferromagnetic (Benner and Just, 2002) systems. Recently, time delayed feedback through the use of a connecting tube has also been used to suppress LCO in the acoustic field of different systems, such as electroacoustic system (Biwa *et al.*, 2016), and acoustic pipeline (Lato *et al.*, 2019). These studies have shown that the suppression of LCO is realised only when a tube of a length close to the odd multiple of the half-wavelength of the anticipated acoustic standing wave is used (Biwa *et al.*, 2016; Lato *et al.*, 2019). We here discuss the application of this method to suppress LCO in a single turbulent combustion system. Toward this purpose, we systematically address the following questions in this section - (i) how effective is delayed acoustic self-feedback in disrupting the complex interactions between the acoustic pressure and the heat release rate fluctuations and consequently mitigating thermoacoustic instability in a turbulent combustor? (ii) What is the nature of the transition of acoustic pressure fluctuations during the suppression of thermoacoustic instability? Moreover, (iii) how do the temporal and spatiotemporal couplings affect the heat release rate and acoustic pressure oscillations due to delayed acoustic self-feedback?

5.1 DELAYED ACOUSTIC SELF-FEEDBACK IN A BLUFF-BODY STABILISED TURBULENT COMBUSTOR

In this section, we characterise the effect of delayed acoustic self-feedback on the suppression of thermoacoustic instability in the turbulent combustor. We first discuss the dynamical behavior of the acoustic pressure signal (p') alone and then present the

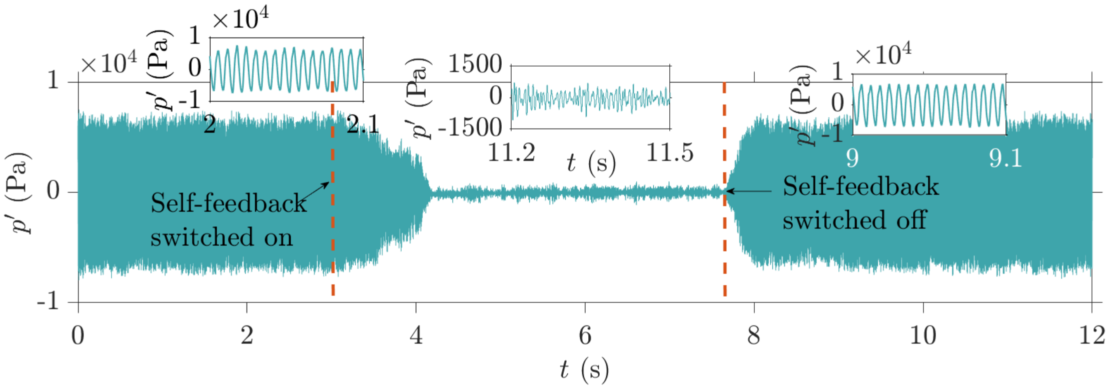

Figure 5.1: A representative time series of acoustic pressure fluctuations p' illustrating the effect of delayed acoustic self-feedback on the limit cycle oscillations. The enlarged portions show the dynamics of p' during different stages of delayed acoustic self-feedback. The dimensions of the coupling tube are L_c = 1400 mm and d_c = 25.4 mm.

change in the coupled behavior of both global heat release rate ($\dot{q}'$) and acoustic pressure (p') fluctuations during the suppression of thermoacoustic instability.

5.1.1 Route from TAI to the state of suppression

In Fig. 5.1, we show a representative time series of the acoustic pressure fluctuations under the influence of an optimal delayed acoustic self-feedback induced using a coupling tube of length L_c = 1400 mm and an internal diameter of d_c = 25.4 mm. Prior to the initiation of feedback, we observe LCO with a root-mean-square (RMS) value of $p'_{0,\mathrm{rms}}$ = 4390 Pa and a frequency of 164 Hz in the combustor. The subscript 0 in $p'_{0,\mathrm{rms}}$ indicates the state of thermoacoustic instability in the absence of delayed acoustic self-feedback. The application of delayed acoustic self-feedback causes a maximum reduction in the RMS value of the LCO to about p'_{rms} = 230 Pa, where the acoustic pressure fluctuations exhibit chaotic oscillations. We refer to this state of complete suppression of thermoacoustic instability in a turbulent combustor as amplitude death (Reddy *et al.*, 2000). We emphasise that the turbulent combustor is not perfectly silent during its stable state of operation, where we notice $p'_{0,\mathrm{rms}}$ = 120 ± 50 Pa. The removal of delayed acoustic self-feedback at around t = 7.6 s revives the LCO, and the combustor returns to the original state of thermoacoustic instability.

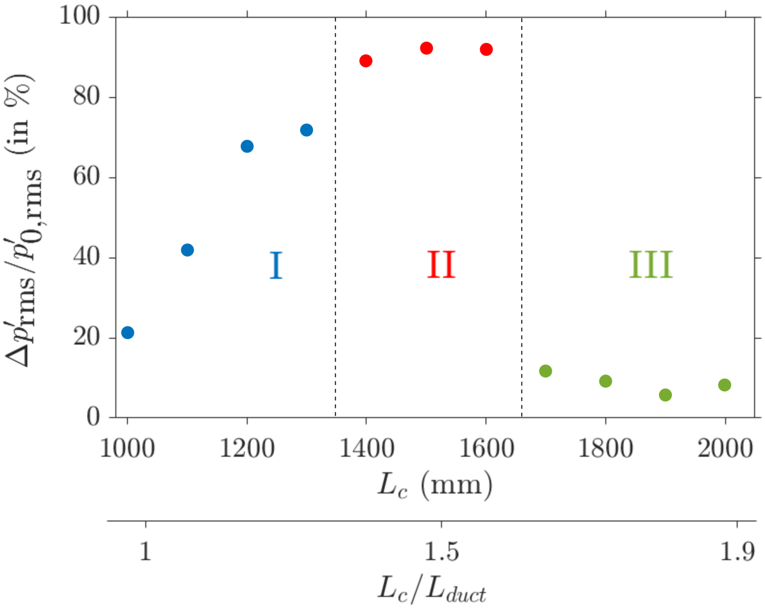

Figure 5.2: Effect of delayed acoustic self-feedback, induced by increasing the length of the coupling tube L_c, on the suppression of acoustic pressure fluctuations $\Delta\bar{p}$. The regions marked in I, II, and III denote the partial suppression, complete suppression, and no suppression, respectively, of LCO ($p'_{0,\mathrm{rms}} = 3200$ Pa). The values of d_c is fixed at 25.4 mm.

In Fig. 5.2, we show the percentage change in the RMS value of p' signals, i.e., $\Delta p'_{\mathrm{rms}}/p'_{0,\mathrm{rms}} \times 100$, as a function of the length of the coupling tube (L_c) when its internal diameter is kept constant at 25.4 mm. Here, $p'_{0,\mathrm{rms}}$ indicates the RMS values of the p' signal during the state of thermoacoustic instability when the delayed acoustic self-feedback is off, p'_{rms} denotes the RMS value of p' oscillations after delayed acoustic self-feedback is switched on. We define the partial suppressed state as the state where the suppression of limit cycle oscillations is greater than 20% but less than 80% (region *I* in Fig. 5.2). The states exhibiting suppression less than 20% and greater than 80% are defined as the states with no suppression and complete suppression (amplitude death), respectively. These states are illustrated as regions II and III in Fig. 5.2, respectively. We notice that as the length of the coupling tube is increased, the amplitude suppression of thermoacoustic instability also correspondingly increases (region I in Fig. 5.2). Once L_c is above a critical value, we observed amplitude death in the system. If L_c is increased post the region of amplitude death (i.e., in region III of Fig. 5.2), $\Delta p'_{\mathrm{rms}}/p'_{0,\mathrm{rms}}$ dips suddenly below 20% as thermoacoustic instabilities are nearly unaffected by the presence of the coupling tube. This further indicates that there exists a critical length of the coupling tube for a given value of the tube diameter (d_c), where amplitude death is observed due to delayed self-feedback. Also, we note that the variation of $\Delta p'_\mathrm{rms}/p'_\mathrm{0,rms}$ is asymmetric across the region of amplitude death (in regions I and III in Fig. 5.2). Furthermore, we find that the optimum value of L_c corresponding to the amplitude death of thermoacoustic instability is around 1.5 times the length of the combustor (i.e., $L_\mathrm{c}/L_\mathrm{duct} \approx 1.5$). Since the combustor geometry can be modelled as an open-closed acoustic duct (Seshadri and Sujith, 2016), and as the combustor exhibits the first acoustic mode during the state of thermoacoustic instability (i.e., $L_\mathrm{duct} = \lambda/4$), the optimum value of L_c corresponding to the state of amplitude death is approximately equal to $\frac{3}{2} \times L_\mathrm{duct} = \frac{3}{2} \times \frac{\lambda}{4} = \frac{3\lambda}{8}$, where λ is the wavelength of the acoustic standing wave developed in the combustor duct during the state of thermoacoustic instability.

Figure 5.3 shows the change in the characteristics of p' signal in the absence of coupling (Fig. 5.3a) and when the combustor is subjected to delayed acoustic self-feedback for different lengths of the coupling tube (Figs. 5.3b-e). In the absence of such feedback, during thermoacoustic instability (Fig. 5.3a), we observe large amplitude LCO in the p' signal (Fig. 5.3a-i) with a sharp spectral peak at 163.9 Hz corresponding to the fundamental mode of the combustor (Fig. 5.3a-ii). The scalogram of the p' signal shows a continuous distribution of the spectral power throughout the time in a narrow frequency band around 163.9 Hz (Fig. 5.3a-iii). The introduction of delayed acoustic self-feedback leads to a significant change in the dynamical behavior of the p' signal. As the suppression of thermoacoustic instability is approached on increasing L_c, the dynamics of p' signal changes from the state of large amplitude LCO (Fig. 5.3b) to low amplitude chaotic oscillations (Fig. 5.3e) via a regime of intermittent oscillations (Figs. 5.3c and 5.3d). During the occurrence of intermittent oscillations, epochs of low amplitude aperiodic fluctuations appear amidst epochs of large amplitude periodic oscillations in an apparently random manner (see inset in Fig. 5.3d-iii). With an increase in L_c, we also notice that the dominant frequency (f_d) of p' signal shifts gradually towards lower values (compare Fig. 5.3a-ii to Fig. 5.3e-ii). Similar observation has been observed in a variety of systems subjected to self-delayed feedback (Flunkert and Schöll, 2007; Schöll *et al.*, 2009; Dai *et al.*, 2015), where a change of the natural frequency of an oscillator is reported with an increase in the coupling time delay. As the change in L_c corresponds to a change in the acoustic feedback delay in our system, we attribute the change in the peak spectral frequency (f_d) of p' signals to the change in the length of the coupling tube. Furthermore, we notice that the spectral magnitude of the f_d decreases continuously such that the power spectrum appears broadband during the state of amplitude death. The scalogram plots during this transition show an increase in discontinuities in the variation of the dominant spectral amplitude of the signal (Fig. 5.3b-iii to Fig. 5.3d-iii), where these discontinuities increase as we approach the state of amplitude death (Fig. 5.3e-iii).

Since the amplitude of LCO observed in the practical turbulent systems during the state of thermoacoustic instability could be different, we next examine the effectiveness of delayed acoustic self-feedback on the suppression of such instabilities of different amplitudes ($p'_{0,\mathrm{rms}}$) in the system (Fig. 5.4a). The values of $L_\mathrm{c} = 1400$ mm and $d_\mathrm{c} = 25.4$ mm are fixed during these experiments, as they correspond to the regime of amplitude death of LCO ($p'_{0,\mathrm{rms}} \approx 3200$ Pa) in Fig. 5.2. Here, the amplitude of LCO before initiating the feedback is increased by increasing the fuel flow rate in the reactant mixture while keeping the equivalence ratio constant at the same time. In Fig. 5.4(a), we observe that LCO of amplitudes $p'_{0,\mathrm{rms}} \leq 5000$ Pa can be completely suppressed with an optimum size of the coupling tube. In contrast, quenching of larger amplitude LCO (i.e., $p'_{0,\mathrm{rms}} > 5000$ Pa) is not observed with this coupling tube. By "optimum size", we imply the dimensions (length and minimum internal diameter) of the connecting tube that are sufficient to achieve amplitude death in the system. The brown-coloured data points on the right side of Fig. 5.4(a) indicate no suppression of LCO due to delayed acoustic self-feedback. Thus, we infer that a coupling tube with optimal values of L_c and d_c can mitigate thermoacoustic instability lesser than a certain critical value of $p'_{0,\mathrm{rms}}$.

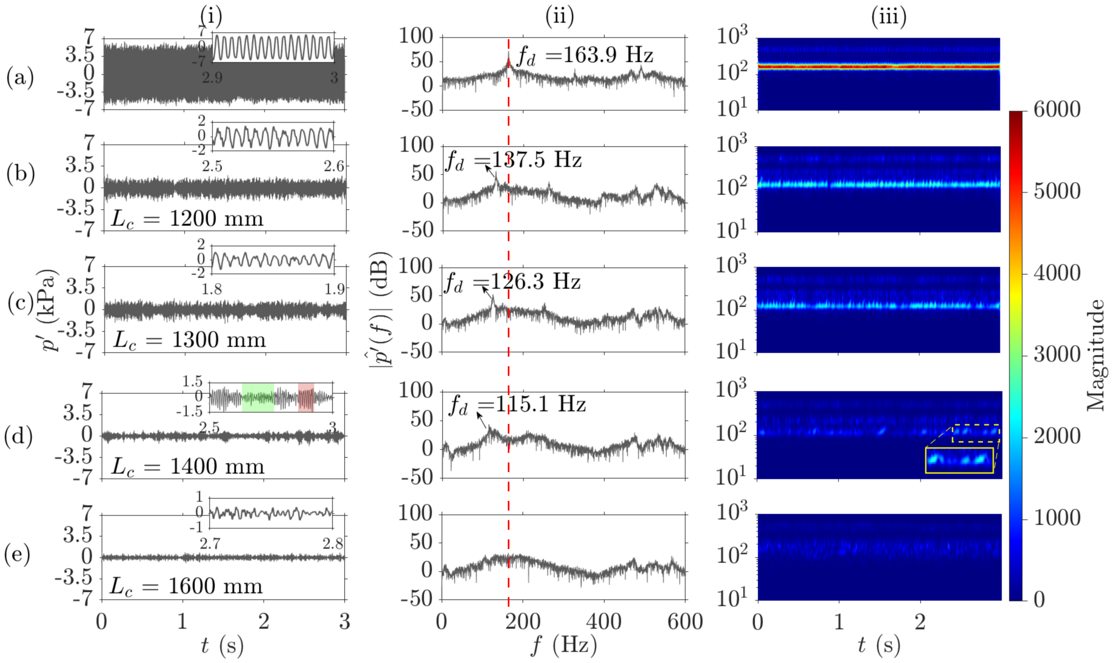

Figure 5.3: (i) Time series, (ii) power spectrum, and (iii) scalograms of p' as the system behavior transitions from a state of (a) TAI to (e) complete suppression of oscillations via (b-d) intermittency. A vertical dotted red line in (ii) indicates the natural frequency of TAI in the absence of delayed acoustic self-feedback. Zoomed regions of plots are shown in insets, where The green and red shaded regions in i-(d) highlight the aperiodic and periodic epochs of p' during the state of intermittency.

Furthermore, we investigate the effects of the internal diameter of the coupling tube on the suppression of thermoacoustic instability (refer to Fig. 5.4b). For two amplitudes of LCO (i.e., $p'_{0,\mathrm{rms}}$ = 3400 ± 150 and 4100 ± 150 Pa), we perform experiments with coupling tubes having five different internal diameters ranging from d_c = 6.3 to 25.4 mm, keeping the length of the coupling tube constant at L_c = 1400 mm. We observe that the occurrence of amplitude death depends on d_c, where a larger diameter coupling tube can quench such oscillations easily for the optimum value of L_c. Furthermore, LCO with higher amplitude ($p'_{0,\mathrm{rms}} \approx 4100$ Pa) undergoes lower suppression than those with lower amplitudes ($p'_{0,\mathrm{rms}} \approx 3400$ Pa) for the same coupling parameters.

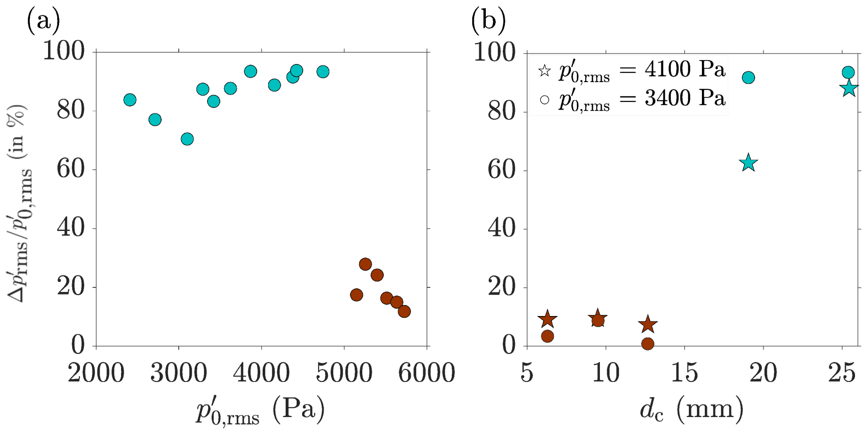

Figure 5.4: The percentage suppression of p' signals ($\Delta\bar{p}$) when delayed acoustic self-feedback is applied to (a) TAI of different amplitudes ($p'_{0,\mathrm{rms}}$) for constant values of L_c = 1400 mm and d_c = 25.4 mm, and (b) TAI of two amplitudes ($p'_{0,\mathrm{rms}} \approx$ 3400 Pa and 4100 Pa) for different coupling tube diameters (d_c = 6.35, 9.525, 12.7, 19.05, and 25.4 mm) at a fixed value of L_c = 1400 mm.

5.1.2 Analysis of changes in the coupled p' and $\dot{q}'$ oscillations

As discussed in Chapter 1, thermoacoustic instability occurs due to a closed-loop interaction between the global heat release rate ($\dot{q}'$) and acoustic pressure (p') fluctuations. Several studies have recently shown that the onset of such instability in turbulent combustors is a consequence of mutual synchronisation between these p' and global $\dot{q}'$ fluctuations (Pawar *et al.*, 2017; Godavarthi *et al.*, 2018; Kasthuri *et al.*, 2022; Murayama and Gotoda, 2019; Guan *et al.*, 2019c; Dutta *et al.*, 2019; Guan *et al.*, 2022). Therefore, quenching of thermoacoustic instability can be achieved by breaking the synchrony between these two oscillations. Thus, in this section, we investigate the effect of delayed acoustic self-feedback on the coupled behavior of the global $\dot{q}'$ and p' fluctuations during the occurrence of amplitude death. We use different tools from synchronisation theory to study the coupled behavior of these oscillations.

In Fig. 5.5, we examine the locking of the instantaneous phases and frequencies of p' and global $\dot{q}'$ signals using a cross-wavelet transform (CWT) (Grinsted *et al.*, 2004; Pawar *et al.*, 2019). In this plot, the regions of common spectral power for both signals are

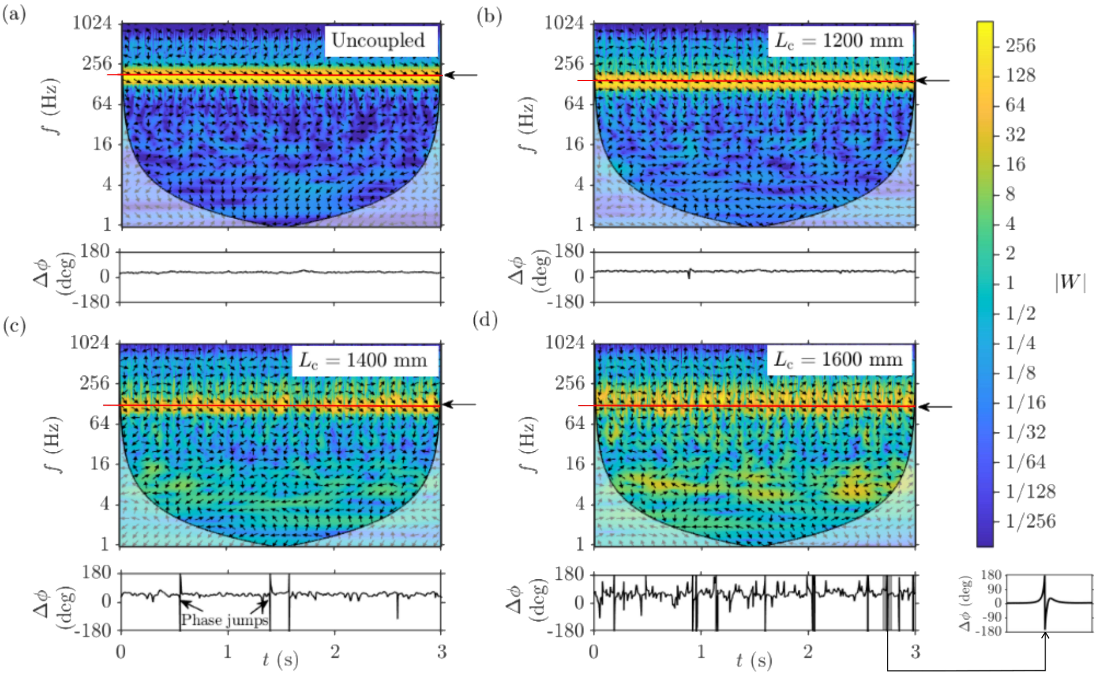

Figure 5.5: CWT plots between $\dot{q}'$ & p' signals and the temporal variation of their phase difference $\Delta\phi$, calculated at the dominant frequency f_d (indicated by a horizontal red line and an arrow in each CWT plot), for (a) the state of TAI in the absence of delayed acoustic self-feedback and (b-d) in the presence of delayed acoustic self-feedback in the combustor with increasing values of L_c. The inset in (d) shows a magnified view of a phase jump. The value of d_c is kept constant at 25.4 mm.

highlighted by the bright color, and the corresponding wrapped instantaneous relative phases between them are indicated by arrows. When the signals are synchronised, their CWT shows a larger magnitude of the spectral power throughout the time and a constant alignment of arrows at a particular phase difference. In contrast, the desynchronisation of signals is indicated in the CWT by a near random distribution of the common spectral power and an arbitrary alignment of arrows in time.

In Fig. 5.5(a), we notice that, in the absence of delayed acoustic self-feedback in the system, a common frequency band occurs around the dominant frequency of 163.9 Hz in the CWT for the entire duration of the p' and global $\dot{q}'$ signals, and the relative phase ($\Delta\phi$) between them is observed to stay constant around a mean value of 35.3°. Here, the instantaneous phase of the signals is calculated using the analytic signal method with the Hilbert transform (Pikovsky *et al.*, 2003). These behaviours of the frequency and phase indicate the existence of phase synchronisation between the global heat release rate and acoustic pressure oscillations (Pawar *et al.*, 2019; Kasthuri *et al.*, 2022). When the system is subjected to delayed acoustic self-feedback for lower values of L_c (see for $L_c = 1200$ mm in Fig. 5.5b), i.e., in regime I of partial suppression of Fig. 5.2, we observe similar properties of phase synchronisation between p' and global $\dot{q}'$ signals as that witnessed in the absence of delayed acoustic self-feedback (Fig. 5.5a). Just prior to the amplitude death of thermoacoustic instability (i.e., for $L_c = 1400$ mm in Fig. 5.5c), we notice the presence of discontinuities in the common frequency bands of CWT of p' and global $\dot{q}'$ signals. These discontinuities can be easily seen in the plot of $\Delta\phi$, where we notice the number of phase jumps about a mean phase difference of these signals. During each phase jump, the value of $\Delta\phi$ shows a sudden change of 2π rad, and the phase jump happens due to the desynchronisation of the signals (Pikovsky *et al.*, 2003). Furthermore, we find that these instances of desynchronised oscillations coincide with low amplitude aperiodic oscillations observed in p' and global $\dot{q}'$ signals (Fig. 5.3d). Thus, in this condition of delayed acoustic self-feedback, the p' and global $\dot{q}'$ exhibit a property of intermittent phase synchronisation.

During the state of amplitude death of thermoacoustic instability (i.e., for $L_c = 1600$ mm in Fig. 5.5d), we notice an increase in the discontinuities in the common frequency bands of CWT of p' and global $\dot{q}'$ signals as compared to that seen in Fig. 5.5(c). This can also be confirmed from the $\Delta\phi$ plot, where we notice an increase in the number of phase jumps about a mean phase difference, which indicates desynchronisation of p' and global $\dot{q}'$ signals in the system.

In addition to CWT, we also use two other measures, called phase locking value (PLV) and Pearson's correlation coefficient (ρ), to detect the synchronisation behavior of p' and global $\dot{q}'$ signals for different values of L_c shown in Fig. 5.2. PLV helps us to detect

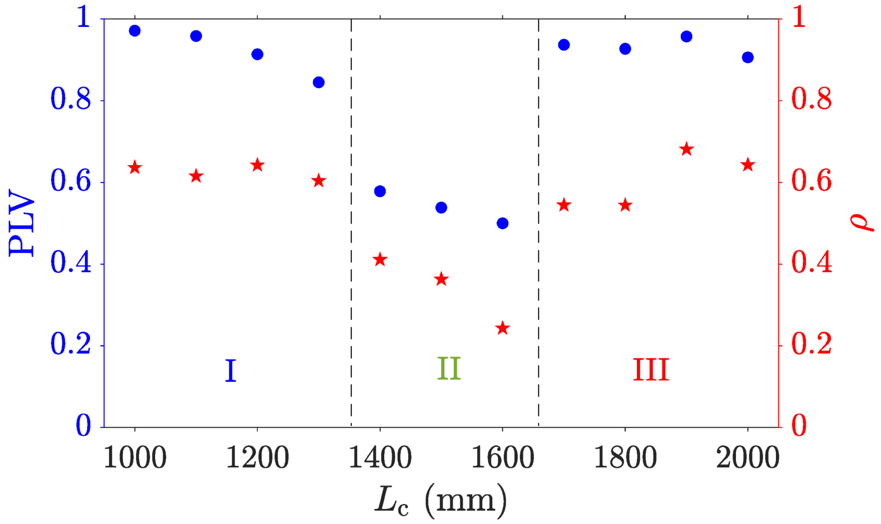

Figure 5.6: The variation of PLV and Pearson's correlation coefficient ρ between the global heat release rate and acoustic pressure fluctuations under the influence of delayed acoustic self-feedback through connecting tubes of different lengths. The internal diameter of the coupling tube is kept constant at $d_c = 25.4$ mm, and p'_0 is kept constant at 3400 ± 150 Pa.

phase synchronisation between two signals and is calculated as:

$$\mathrm{PLV} = \frac{1}{N}\left|\sum_{n=1}^{N} \exp(i\Delta\phi)\right|, \tag{5.1}$$

where N is the number of data points in the two signals, and $\Delta\phi$ is the instantaneous phase difference between the p' and global $\dot{q}'$ signals. On the other hand, Pearson's correlation coefficient ρ aids in finding the amplitude correlation between the signals (Gonzalez-Miranda, 2002), and is calculated as:

$$\rho = \frac{\mathrm{Cov}(p', \dot{q}')}{\sigma_{p'}\sigma_{\dot{q}'}}, \tag{5.2}$$

where Cov represents the covariance between two signals, and σ denotes the standard deviation of a signal. We present the values of these measures in Fig. 5.6. We find that in the regime of partial suppression of thermoacoustic instability, both p' and global $\dot{q}'$ signals are phase synchronised, confirmed from a value of PLV near 1. The presence of a high correlation between p' and global $\dot{q}'$ signals in the regimes of oscillatory states is confirmed by the high positive value (between 0.55 and 0.7) of ρ. The value of ρ drops to 0.25 in the regime of suppression of thermoacoustic instability (region II in Fig. 5.6), which happens due to the lack of correlation between desynchronised p' and global $\dot{q}'$ signals (Pawar *et al.*, 2017).

Thus, we observe that the extent of synchronisation between the coupled p' and global $\dot{q}'$ signals decreases during the mitigation of thermoacoustic instability in a turbulent combustor, where the signals change their behavior from the state of phase synchronised periodicity to desynchronised aperiodicity via intermittent synchronised oscillations. Next, we look at the effectiveness of delayed acoustic self-feedback to disrupt the complex closed-loop interactions between the flame, flow, and the acoustic fields that exist inside the turbulent combustor during the state of thermoacoustic instability.

5.1.3 Spatiotemporal analysis of thermoacoustic power production in the turbulent flow field during different states of self-delayed feedback

In this section, we compare the spatiotemporal changes in the reaction field of the combustor as thermoacoustic instability is suppressed through delayed acoustic self-feedback. The local heat release rate fluctuations $\dot{q}'(x, y, t)$ in the combustor are obtained by the high-speed CH* chemiluminescence imaging on the flame. In Fig. 5.7, we examine the local thermoacoustic power $p'(t)\dot{q}'(x, y, t)$ field (see panels ii-vii) at some representative time instances marked on p' signal (see panel i). Regions with $p'(t)\dot{q}'(x, y, t) > 0$ represent thermoacoustic power sources, and regions with $p'(t)\dot{q}'(x, y, t) < 0$ represent thermoacoustic power sinks (Krishnan *et al.*, 2019*b*). Due to the periodic formation of large-scale vortical structures at the dump plane and the tip of the bluff body, we observe the coherent production of thermoacoustic power sources over large clusters in the reaction field during thermoacoustic instability (Fig. 5.7a). In these coherent regions of thermoacoustic power, the magnitude of the thermoacoustic power sources is significantly greater than their negative counterparts in regions of thermoacoustic power sink. The regions of thermoacoustic power sources grow in size when the acoustic pressure fluctuations approach local extrema (Figs. 5.7a-iii and

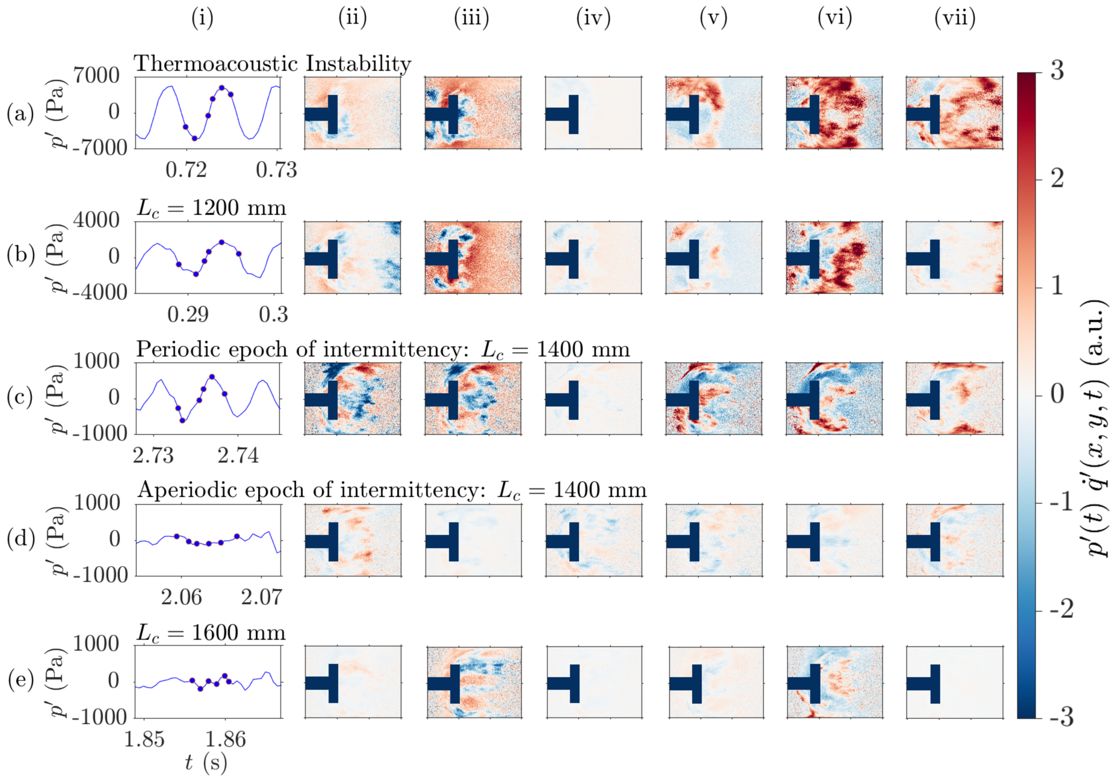

Figure 5.7: (i) Time instants of p' time series, and (ii - vii) instantaneous spatial distribution of local Rayleigh Index for the state of (a) TAI in the absence of delayed acoustic self-feedback, and for (b-e) different states of delayed acoustic self-feedback. The internal diameter of the coupling tube is kept constant at $d_c = 25.4$ mm, and p'_0 is kept constant around 3400 Pa.

5.7a-vii), and they decrease in their spatial size when the acoustic pressure fluctuations p' approach the mean value of zero (Figs. 5.7a-ii and 5.7a-iv).

A similar trend of change in the size of thermoacoustic power sources over time is observed when the turbulent combustor is subjected to delayed acoustic self-feedback by coupling it with a connecting tube of length $L_c = 1200$ mm (Figs. 5.7b-ii and 5.7b-vii)), and also during a periodic epoch of intermittency observed in Fig. 5.7(c) for $L_c = 1400$ mm. High spatial coherence of thermoacoustic power sources is observed at a large scale in Fig. 5.7(b)-(vi) downstream of the bluff body. However, the magnitude and spatial coherence of thermoacoustic power sources observed in Fig. 5.7(b) and Fig. 5.7(c) are low compared to that observed during the state of thermoacoustic instability. This is accompanied with an increase in the suppression of thermoacoustic instability from Fig. 5.7(b) to Fig. 5.7(c). During the aperiodic epoch of intermittency, we do not observe any large coherent regions of thermoacoustic power in Fig. 5.7(d), similar to that observed during the periodic epochs of intermittency. However, we observe small scale patches of thermoacoustic power sources downstream (Figs. 5.7d-i and 5.7d-vii) and upstream (Fig. 5.7d-iv) of the bluff body. We believe these small scale thermoacoustic power sources result from small scale vortices shed from the dump plane and the tip of the bluff body that do not grow in size and combust shortly after they are formed.

Finally, when the length of the connecting tube is increased to $L_c = 1600$ mm, we notice the occurrence of amplitude death of thermoacoustic instability, where the acoustic pressure exhibits low amplitude chaotic oscillations as seen in Fig. 5.7(e)-(i). During this state, the spatial distribution of $p'(t)\dot{q}'(x, y, t)$ seems granular and devoid of a discernible pattern for different instants of time. These grainy structures can be considered as disordered patterns (or incoherent) patterns in the spatial dynamics of the turbulent reacting field. We hypothesise that the presence of several small scale vortices in the flow field results in incoherent thermoacoustic power production. As discussed in Chapter 1, the occurrence of thermoacoustic instability in a turbulent combustion system is a complex process and happens due to nonlinear interaction between the flame, the flow, and the acoustic field of a combustor. The application of optimal delayed acoustic self-feedback disrupts this complex interaction in the turbulent combustor, thus mitigating thermoacoustic instability.

5.1.4 Interim summary for effects of delayed acoustic self-feedback on a bluff-body stabilised turbulent combustor

In summary, we demonstrate the mitigation of thermoacoustic instability (i.e., limit cycle oscillations) in a bluff body stabilised turbulent combustor by inducing a delayed acoustic self-feedback in the system. The complex closed-loop coupling between flame, flow, and the acoustic fields developed during thermoacoustic instability is disrupted when optimal delayed acoustic self-feedback is introduced in the system. This delayed self-feedback is achieved by coupling the acoustic field of the combustor to itself, using a connecting tube attached near the pressure anti-node position of the acoustic standing wave. We observe a significant suppression of thermoacoustic instability when the length of the coupling tube is approximately 3/8 times the wavelength of the fundamental acoustic mode established during the state of thermoacoustic instability in the combustor. The amplitude of the acoustic pressure fluctuations during the state of suppression is comparable to that observed for the state of stable operation (combustion noise). As the length of the coupling tube is increased, we find that the mitigation of thermoacoustic instability is associated with a gradual decrease in the amplitude of acoustic pressure oscillations and a shift in their dominant frequency toward lower values. Furthermore, we notice that the dynamical behavior of acoustic pressure fluctuations changes from the state of limit cycle oscillations to low amplitude chaotic oscillations via intermittent oscillations during the suppression of thermoacoustic instability. The synchronisation of the global heat release rate and acoustic pressure fluctuations, observed during the uncoupled state of thermoacoustic instability, breaks down gradually and the oscillations become desynchronised as the system approaches the state of amplitude death. During this state, we do not observe any coherent structures of thermoacoustic power production in the reaction field as witnessed during thermoacoustic instability. We also notice the disintegration of thermoacoustic power sources in the flow field during the state of suppression of oscillations, which happens due to the destruction of the local coupling between acoustic pressure and heat release rate fluctuations in the spatial field of the combustor.

Thus, we show that delayed acoustic self-feedback achieved through a single connecting tube provides a promising control mechanism to suppress TAI in turbulent combustors. Unlike in traditional active closed-loop controls used in thermoacoustic studies, we do not need to preprocess the acoustic pressure signal acquired from the combustor prior to feedback using any electromechanical devices in the method of delayed acoustic self-feedback. Therefore, we believe this methodology based on delayed acoustic self-feedback opens up novel, cost-effective ways to mitigate TAI in turbulent combustion systems used in practical propulsion and gas turbine engines.

5.2 DELAYED ACOUSTIC SELF-FEEDBACK IN A HORIZONTAL LAMINAR RIJKE TUBE

Given the inherent challenges of conducting intricate experiments within a turbulent combustor environment, we proceed by directing our focus towards a horizontal laminar Rijke tube to further study delayed acoustic self feedback in thermoacoustic systems. This shift enables us to conduct detailed experiments and meticulously address the following inquiries: (i) What are the optimal values of coupling parameters (length, diameter, and location of the coupling tube) for attaining amplitude death in a thermoacoustic system? (ii) How does the amplitude of the limit cycle oscillations prior to introducing self-coupling affect its quenching?

The Rijke tube is a convenient prototype of a thermoacoustic oscillator traditionally used to study the occurrence and mitigation of thermoacoustic instability (Rijke, 1859; Raun *et al.*, 1993; Matveev, 2003; Mariappan and Sujith, 2011; Gopalakrishnan and Sujith, 2014; Manoj *et al.*, 2022). It consists of a duct with a heat source (e.g., an electrically heated wire mesh) present inside. The interaction between the heat released by the heat source and the acoustic field of the Rijke tube can lead to thermoacoustic instability.

In this section, we first discuss the effect of self-coupling on the bifurcation characteristics of the Rijke tube as observed in our experiments. In Fig. 5.8a, we show the variation in the root-mean-square (RMS) value of acoustic pressure fluctuations (in Pa) as a function of the heater power (in W) in the absence of self-coupling in the system. We denote the RMS value using $p'_{0,\mathrm{rms}}$ for the uncoupled case and p'_{rms} for the coupled case. In the forward path (increasing heater power in Fig. 5.8b), we observe that the transition from fixed point to limit cycle oscillations of RMS value around 290 Pa happens via

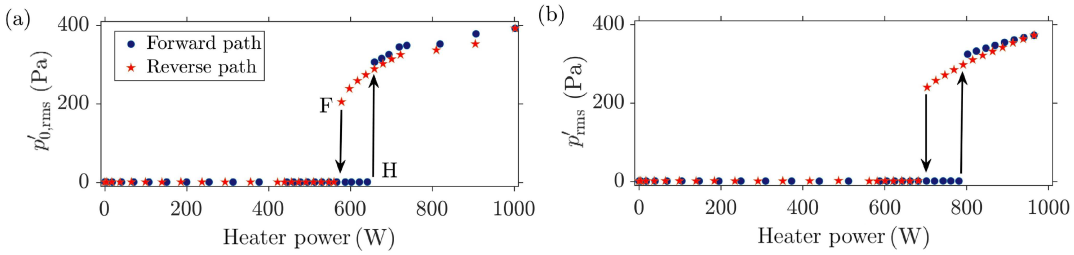

Figure 5.8: Variation of the RMS value of acoustic pressure fluctuations with heater power in the forward and reverse paths for (a) the uncoupled Rijke tube ($p'_{0,\mathrm{rms}}$) and (b) the self-coupled Rijke tube (p'_{rms}). The normalised length of the coupling tube is $L/L_{\mathrm{duct}} = 1.17$ and its internal diameter is $d = 8$ mm in (b). The introduction of self-coupling shifts the Hopf point [marked as 'H' in (a)] and the fold point [marked as 'F' in (a)] to higher values of heater power. Air flow rate of 120 SLPM (or 0.002 m^3/s) is maintained in the Rijke tube for both the plots.

subcritical Hopf bifurcation; while in the reverse path (decreasing heater power) shown in Fig. 5.8(b), the system attains fixed point via fold bifurcation when $p'_{0,\mathrm{rms}}$ is around 200 Pa. Thus, the transition between the steady state and the state of limit cycle oscillations is explosive (subcritical) and hysteretic. In Fig. 5.8a, 'H' denotes the Hopf bifurcation point and 'F' denotes the fold bifurcation point. We notice a bistable region in between the two bifurcation points.

When the Rijke tube is self-coupled with a coupling tube of dimensions $L_c/L_{\mathrm{duct}} = 1.17$ and $d_c = 8$ mm in Fig. 5.8b, we observe that the system undergoes the same type of bifurcations as we observed in the uncoupled case (see Fig. 5.8a). However, we notice that the introduction of self-coupling shifts the Hopf and the fold bifurcation points to higher values of the heater power than those values observed for the uncoupled oscillator. This, in turn, indicates that self-coupling enhances the parameter space of steady state in the system; in other words, it delays the transition to limit cycle oscillations in the system.

Next, we study the effect of variation in the parameters of the coupling tube (i.e., length L_c and diameter d_c) and the RMS value of limit cycle oscillations in the uncoupled state ($p'_{0,\mathrm{rms}}$) on the suppression characteristics in the self-coupled Rijke tube oscillator. We note that prior to implementing self-coupling, we establish limit cycle oscillations in the system. As seen in Fig. 5.8a, the value of $p'_{0,\mathrm{rms}}$ can be increased by increasing the heater power. To study the behavior of the self-coupled Rijke tube over a larger range of $p'_{0,\mathrm{rms}}$ than that shown in Fig. 5.8a, we maintain the air flow rate at a value of 80 SLPM (or 0.00133 m^3/s) in our subsequent experiments. Lowering the air flow rate reduces the value of $p'_{0,\mathrm{rms}}$ that the Rijke tube exhibits after the subcritical Hopf bifurcation (Etikyala and Sujith, 2017). At this air flow rate, we vary the value of $p'_{0,\mathrm{rms}}$ for a larger range of 120 Pa to 320 Pa by varying the heater power. We refer to the dimensions of the coupling tube (i.e., L_c and d_c) as coupling parameters and the RMS value ($p'_{0,\mathrm{rms}}$) and frequency (f_0) of limit cycle oscillations prior to coupling as system parameters in the subsequent discussion of the paper.

5.2.1 Effect of system and coupling parameters on the oscillation quenching in the self-coupled Rijke tube

Figure 5.9 illustrates the amplitude response of the self-coupled Rijke tube for different coupling parameters. Here, we show the amplitude response in terms of the normalised change in the RMS value of limit cycle oscillations in the Rijke tube due to self-coupling, $\Delta p'_{\mathrm{rms}}/p'_{0,\mathrm{rms}} = (p'_{0,\mathrm{rms}} - p'_{\mathrm{rms}})/p'_{0,\mathrm{rms}}$, as a function of L_c/L_{duct} and d_c. The color bar illustrates values of $\Delta p'_{\mathrm{rms}}/p'_{0,\mathrm{rms}}$ ranging from 0 to 1, where $\Delta p'_{\mathrm{rms}}/p'_{0,\mathrm{rms}} \approx 1$ corresponds to complete suppression of limit cycle oscillations (i.e., amplitude death) and $\Delta p'_{\mathrm{rms}}/p'_{0,\mathrm{rms}} \approx 0$ indicates the absence of any suppression of limit cycle oscillations in the Rijke tube due to self-coupling. We study the response of the self-coupled Rijke tube oscillator for two different RMS values of limit cycle oscillations in the uncoupled state: $p'_{0,\mathrm{rms}} = 120$ Pa (see Fig. 5.9a), and $p'_{0,\mathrm{rms}} = 320$ Pa (see Fig. 5.9b).

In Fig. 5.9a, we note that when the RMS value of the limit cycle oscillations is low ($p'_{0,\mathrm{rms}} = 120$ Pa), self-coupling of the Rijke tube causes a significant reduction in the amplitude of acoustic pressure oscillations for a vast parametric region of coupling parameters. However, as the value of $p'_{0,\mathrm{rms}}$ is increased to a higher value of 320 Pa in

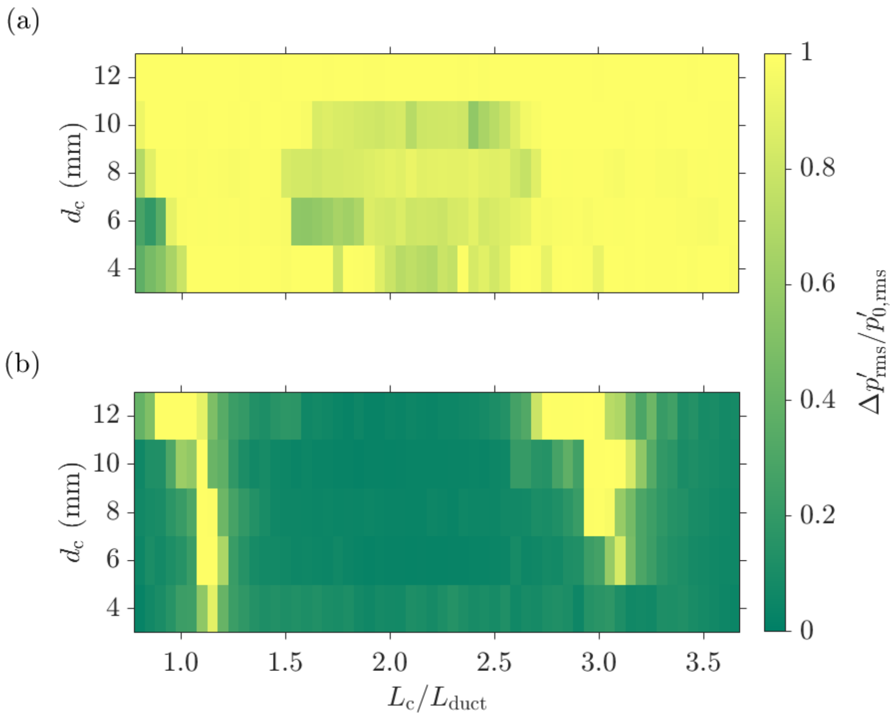

Figure 5.9: The amplitude response of the Rijke tube when self-coupling is induced for (a) $p'_{0,\mathrm{rms}}$ = 120 Pa, and (b) $p'_{0,\mathrm{rms}}$ = 320 Pa. The normalised change in the amplitude suppression $\Delta p'_{\mathrm{rms}}/p'_{0,\mathrm{rms}}$ is measured for different values of L_c/L_{duct} and d_c. A large parametric region of amplitude death (AD) is observed for lower value of $p'_{0,\mathrm{rms}}$ in (a); while for higher values of $p'_{0,\mathrm{rms}}$ in (b), the region of amplitude death shrink and is observed only for around $L/L_{\mathrm{duct}} \approx 1$ and $L/L_{\mathrm{duct}} \approx 3$. Air flow rate is maintained at 80 SLPM (or 0.00133 m^3/s) in the Rijke tube.

Fig. 5.9b, we observe the region of amplitude death only around odd values of L_c/L_{duct} (i.e., $L_c/L_{\mathrm{duct}} \approx 1$ and 3). We also notice that the range of L_c/L_{duct} for which the Rijke tube exhibits amplitude death increases as the internal diameter of the coupling tube (d_c) is increased.

Next, we examine in detail the amplitude response of the self-coupled Rijke tube on variation of the RMS value of the limit cycle oscillations in the uncoupled state ($p'_{0,\mathrm{rms}}$) and the normalised length of the coupling tube (L_c/L_{duct}). The internal diameter of the coupling tube is kept constant at 4 mm and 8 mm in Fig. 5.10a and 5.10b, respectively. Note that the ordinate representing the $p'_{0,\mathrm{rms}}$ values is unevenly distributed. In Fig. 5.10, we observe that limit cycle oscillations of low RMS values (i.e., for $p'_{0,\mathrm{rms}} \leq 140$ Pa), and

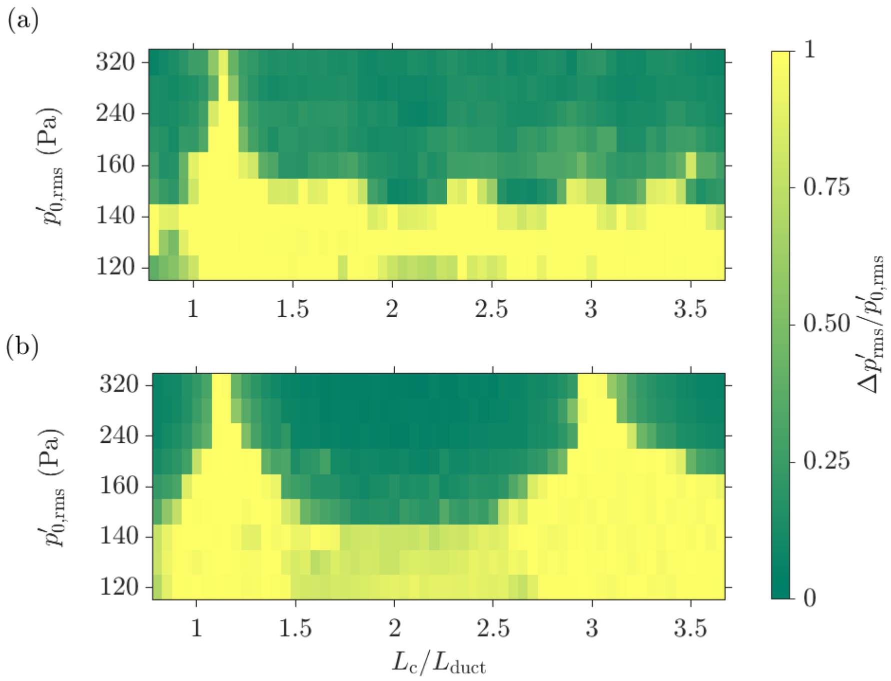

Figure 5.10: Amplitude response of the self-coupled Rijke tube for different values of the normalised length of coupling tube (L_c/L_duct) and the RMS value of the limit cycle oscillations in the uncoupled state ($p'_{0,\mathrm{rms}}$). The internal diameter of coupling tube (d_c) is fixed at (a) 4 mm, and (b) 8 mm. Air flow rate is maintained at 80 SLPM (or 0.00133 m^3/s) in the Rijke tube for both the plots.

thus low amplitudes, can be easily suppressed for a large range of L_c/L_duct. As $p'_{0,\mathrm{rms}}$ is increased above 140 Pa, we notice that the region of amplitude death shrinks. The amplitude death now occurs only in a narrow range of L_c/L_duct. For a low value of d_c in Fig. 5.10a, we observe amplitude death to occur near $L_c/L_\mathrm{duct} = 1$ when $p'_{0,\mathrm{rms}}$ is greater than 140 Pa. In contrast, we notice two distinct regions of amplitude death in Fig. 5.10b when the value of d_c is increased to 8 mm. Here, the two regions of amplitude death occur at around $L_c/L_\mathrm{duct} = 1$ and 3, respectively, which is similar to what we observe in Fig. 5.2b. Thus, from Fig. 5.9 and 5.10, we infer that self-coupling can quench small amplitude limit cycle oscillations for a large range of coupling parameters. On the other hand, the quenching of large amplitude limit cycle oscillations is possible only for a critical range of the length of the coupling tube and it is comparatively easy when the diameter of the coupling tube is bigger.

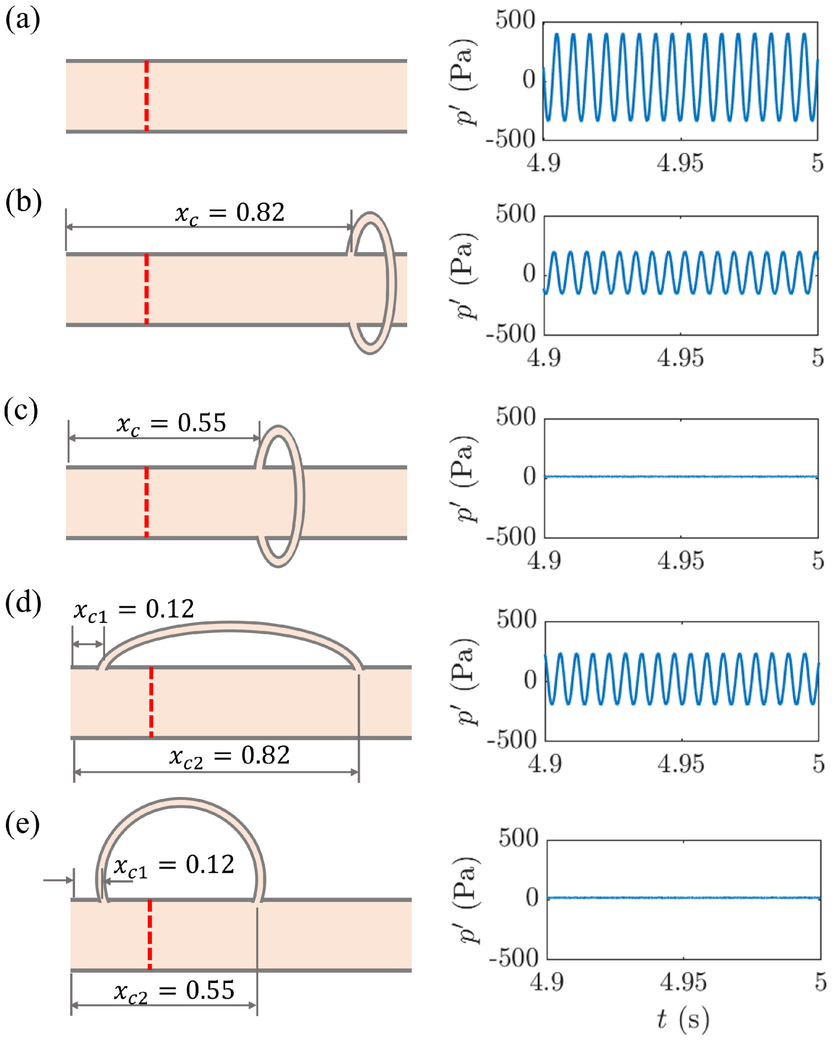

Figure 5.11: Schematics of the Rijke tube and the experimentally obtained time series of the acoustic pressure fluctuations (p') depict the effect of coupling locations on the suppression of limit cycle oscillations (a) when the Rijke tube is uncoupled, (b, c) when the Rijke tube is coupled such that both ends of the coupling tube are fixed at the same distance (x_c) of 0.82 and 0.55 from the inlet, respectively, (d) when the ends of the coupling tube are at separate locations away from the centre of the Rijke tube ($x_{c1} = 0.12$ and $x_{c2} = 0.82$) and (e) when one end of the coupling tube is closer to the centre ($x_{c2} = 0.55$) while the other end is away from the centre of the Rijke tube ($x_{c1} = 0.12$). The red dashed line indicates the heater mesh located at $x_f = 0.26$. All distances are non-dimensionalised by the length of the Rijke tube, $L_{\text{duct}} = 1.04$ m. Other parameters are maintained as $p'_{0,\text{rms}} = 200$ Pa, $L_c = 95$ cm, and $d_c = 4$ mm in all of the plots.

So far, we have discussed the behavior of the self-coupled Rijke tube when both ends of the Rijke tube are at a particular coupling location ($x_c = 0.55$). In Fig. 5.11, we examine how varying the coupling locations affect the quenching of limit cycle oscillations by tracking the temporal variation of acoustic pressure oscillations in the system. Due to limitations in the experimental setup, we are able to connect the coupling tube only for a few values of coupling locations. In Fig. 5.11b and 5.11c, we maintain $x_{c1} = x_{c2} = x_c$ and vary the value of x_c. We observe that as compared to the uncoupled state (depicted in Fig. 5.11a), coupling the Rijke tube at a location towards the end of the duct does not cause significant suppression of limit cycle oscillations (Fig. 5.11b). On the other hand, when the axial location of the coupling tube is closer to the centre of the Rijke tube (i.e., x_c is closer to 0.5, see Fig. 5.11c), the limit cycle oscillations are quenched and AD is achieved.

In Fig. 5.11d and 5.11e, we present the case when the two ends of the coupling tube are at separate axial locations, i.e., $x_{c1} \neq x_{c2}$. In this scenario, we observe that AD is achieved only when at least one end of the coupling tube is close to the centre of the Rijke tube. Thus, our experimental observations suggest that to quench limit cycle oscillations, the optimal coupling location is around the centre of the Rijke tube. We also discuss this behavior of the self-coupled Rijke tube through modelling in the next section.

5.2.2 Comparison between self-coupled and mutually coupled Rijke tube oscillators

In order to compare the amplitude suppression characteristics of limit cycle oscillations in a mutually coupled system of identical Rijke tubes and a single self-coupled Rijke tube, we fix the same system and coupling parameters and measure the fractional change in the RMS value of limit cycle oscillations after coupling is induced in the system ($\Delta p'_{\mathrm{rms}}/p'_{0,\mathrm{rms}}$). We repeat this for different values of the normalised coupling tube length (L_c/L_{duct}) in experiments or the coupling delay (τ) in the model. In the experiments (Fig. 5.12), we observe that in the green regions present around odd values of L_c/L_{duct} or τ, the self-coupled system suppresses limit cycle oscillations to a greater extent than the

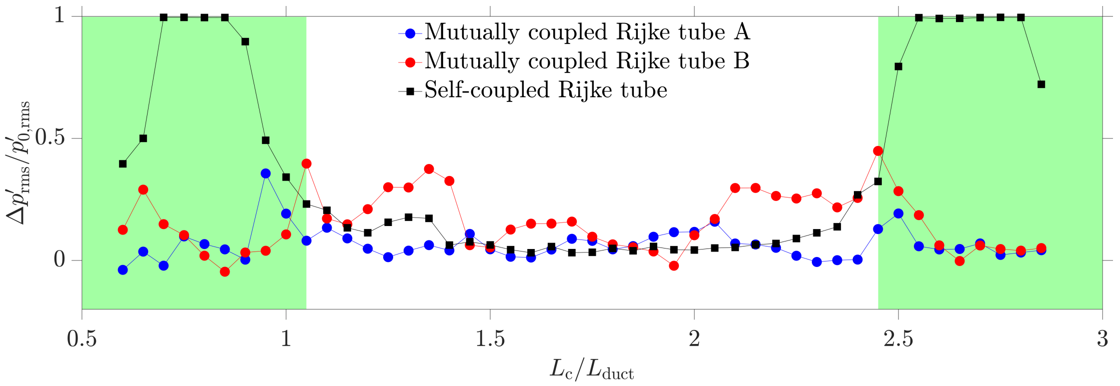

Figure 5.12: Trends in the relative suppression of the acoustic pressure oscillations ($\Delta p'/p'_{0,\mathrm{rms}}$) in two mutually coupled identical Rijke tubes and in a self-coupled Rijke tube with change in the normalised length of the coupling tube (L_c/L_duct) in experiments (d_c = 8 mm and $p'_{0,\mathrm{rms}}$ = 320 Pa). The highlighted green region indicates the range of L_c/L_duct where the self-coupled Rijke tube exhibits greater amplitude suppression than the mutually coupled system.

mutually coupled system and even induces amplitude death. Away from these optimal values of L_c/L_duct or τ, the magnitude of amplitude suppression is nearly the same for both self and mutual couplings. Here, we note that previous studies have introduced frequency mismatch to quench high amplitude limit cycle oscillations in mutually coupled Rijke tubes (Dange *et al.*, 2019; Doranehgard *et al.*, 2022). We do not consider such mismatch in the current chapter. Thus, we emphasise that a self-coupled system performs significantly better in suppressing the oscillations in a nonlinear system, compared to the amplitude suppression in a mutually coupled system of identical oscillators.

5.3 INTERIM SUMMARY

In this chapter, we demonstrated the mitigation of thermoacoustic instability in a laminar and a turbulent thermoacoustic system. In the first part of this chapter, we induced delayed acoustic self-feedback in a bluff body stabilised turbulent combustor. The complex closed-loop coupling between the flame, flow, and the acoustic fields developed during thermoacoustic instability is disrupted when optimal delayed acoustic self-feedback is introduced in the system. This delayed self-feedback is achieved by coupling the acoustic field of the combustor to itself, using a connecting tube attached near the pressure anti-node position of the acoustic standing wave. We observe a significant suppression of thermoacoustic instability when the length of the coupling tube is approximately 3/8 times the wavelength of the fundamental acoustic mode established during the state of thermoacoustic instability in the combustor. The amplitude of the acoustic pressure fluctuations during the state of suppression is comparable to that observed for the state of stable operation (combustion noise). As the length of the coupling tube is increased, we find that the mitigation of thermoacoustic instability is associated with a gradual decrease in the amplitude of acoustic pressure oscillations and a shift in their dominant frequency toward lower values. Furthermore, we notice that the dynamical behavior of acoustic pressure fluctuations changes from the state of limit cycle oscillations to low amplitude chaotic oscillations via intermittent oscillations during the suppression of thermoacoustic instability. The synchronisation of the global heat release rate and acoustic pressure fluctuations, observed during the uncoupled state of thermoacoustic instability, breaks down gradually and the oscillations become desynchronised as the system approaches the state of amplitude death. During this state, we do not observe any coherent structures of thermoacoustic power production in the reaction field as witnessed during thermoacoustic instability. We also notice the disintegration of thermoacoustic power sources in the flow field during the state of suppression of oscillations, which happens due to the destruction of the local coupling between acoustic pressure and heat release rate fluctuations in the spatial field of the combustor.

Given the experimental constraints involved in conducting detailed experiments in a turbulent combustor, we proceeded to further investigate the effects of delayed acoustic self-feedback in a thermoacoustic system by focusing our efforts toward a laminar horizontal Rijke tube. The Rijke tube is a convenient prototype of a thermoacoustic oscillator traditionally used to study the occurrence and mitigation of thermoacoustic instability (Rijke, 1859; Raun *et al.*, 1993; Matveev, 2003; Manoj *et al.*, 2022). Through experiments, we found that the optimal lengths of the coupling tube to achieve amplitude death are around odd integral multiples of the length of the Rijke tube. Increasing the diameter of the coupling tube increases the ranges of the coupling tube length over which amplitude death can be achieved. Additionally, we observed that limit cycle oscillations of low amplitude are more easily quenched as compared to those of high amplitude. Furthermore, our experiments indicate that the optimal axial locations of the ends of the coupling tube for mitigating thermoacoustic instability is around the antinode of the acoustic pressure standing wave in the uncoupled Rijke tube. Furthermore, we demonstrated that self-coupling is more effective in achieving amplitude death in a Rijke tube as compared to mutual coupling of two such identical Rijke tubes. The corresponding analytical and numerical results from a reduced-order mathematical model were obtained by my lab colleague Sneha Srikanth, and can be found in Srikanth (2022). Thus, we anticipate self-coupling to be a simple, cost-effective alternative to traditional feedback controls for mitigating thermoacoustic instability in single and multiple thermoacoustic systems, such as those practical gas turbine and rocket combustors. It would be interesting to explore the mitigation of thermoacoustic instability through the combined application of self and mutual couplings in multiple combustion systems. Quenching transverse thermoacoustic instabilities in a combustor through self-coupling is also a scope for future studies.

CHAPTER 6

ASYMMETRICALLY FORCED SYSTEM OF TWO MUTUALLY COUPLED RIJKE TUBES

In our discussion regarding delayed acoustic self-feedback applied to a thermoacoustic system in Chapter 5, we highlighted the role of acoustic waves in controlling the thermoacoustic instability. The interaction of different thermoacoustic systems through acoustic waves is of primary importance while analysing the dynamics of coupled thermoacoustic systems. Such acoustically-coupled systems are present in combustors with can-annular arrangements, where the independent combustors are arranged in a ring layout, and the adjacent combustors interact through the acoustic field. Coupled nonlinear oscillator systems can be used to model such combustors (Farisco *et al.*, 2017; Ghirardo *et al.*, 2019; Orchini *et al.*, 2022; Buschmann *et al.*, 2023).

Coupled interacting nonlinear oscillators appear extensively in physical systems around us (Jenkins, 2013). Depending upon the nature of coupling, a population of interacting oscillators can synchronise starting from an initially incoherent or desynchronised state. Such synchronised oscillators can exhibit an emergence of ordered patterns as observed in several examples in nature, such as flocking of bird or flashing of light by fireflies (Strogatz, 2004). However, synchronisation of oscillations may be detrimental sometimes, and may need to be desynchronised (Strogatz *et al.*, 2005) or quenched (Biwa *et al.*, 2015). In this chapter, we study the practical application of synchronisation theory in attaining control of self-excited oscillations in a system of coupled Rijke tubes. As discussed in Chapter 5, Rijke tube is a prototypical thermoacoustic oscillator used for studying thermoacoustic oscillations (Manoj *et al.*, 2022).

The results presented in this chapter are published in Sahay, A., Roy, A., Pawar, S. A., & Sujith, R. I. (2021), Dynamics of coupled thermoacoustic oscillators under asymmetric forcing, *Physical Review Applied*, 15(4), 044011. `https://doi.org/10.1103/PhysRevApplied.15.044011`

In general, there are two types of interactions leading to synchronisation of oscillators: forced & mutual (Pikovsky *et al.*, 2003). In the former, oscillators mutually interact through bidirectional coupling, leading to the adjustment of phases and frequencies of both the oscillators to a common state of mutual synchronisation. Oscillation quenching attained through the phenomenon of amplitude death (AD) in mutually coupled systems is an exciting prospect that has been shown to work for various systems (Pyragas *et al.*, 2000; Kumar *et al.*, 2011; Huddy and Skufca, 2012; Mirollo and Strogatz, 1990). Amplitude death in a population of strongly coupled oscillators refers to a situation where all the oscillators pull each other off of their oscillatory state into the same stable fixed point, leading to complete cessation of oscillations. If the mutual coupling is not strong enough, the situation of partial amplitude death (PAD) may arise, where some oscillators retain their oscillatory behavior while oscillations are ceased in others (Atay, 2003). On the other hand, in the case of forced synchronisation, an independent master system (an external force) drives a slave system (driven oscillator); thus, forming a unidirectional master-slave system (Balanov *et al.*, 2008). In this type of coupling, the driven system adjusts its phase and frequency to that of the external forcing during the state of synchronisation. The purpose of this thesis is to obtain the degree of doctor for its author. Depending upon the frequency and the amplitude of forcing, the natural oscillations can be phase-locked to forcing, and in some cases, the self-excited oscillations can be completely suppressed through the phenomenon of asynchronous quenching (Keen and Fletcher, 1970; Hyodo and Biwa, 2018*b*; Mondal *et al.*, 2019).

Quite a few numerical studies have been conducted to investigate the simultaneous effect of forcing in a system of coupled oscillators. In a system of two weakly coupled Van der Pol oscillators, Battelino (Battelino, 1988) observed that when each oscillator is externally forced, and a constant phase difference is present between the forcing signals applied to each of the oscillators, the system exhibits three-frequency quasiperiodicity. As the coupling strength and forcing amplitude are increased, three-frequency quasiperiodicity is first replaced by a two-frequency quasiperiodic regime, and subsequently by phase-locked periodic and chaotic regimes. The transition between the phase-locked region and the two- and three-frequency quasiperiodic regions takes place through saddle-node bifurcations (Anishchenko *et al.*, 2009*a*,*b*). The external force first destroys the regime of mutual synchronisation of oscillators. As the forcing amplitude is increased, the oscillator which is subjected to external forcing synchronises with the forcing signal first, followed by the forced synchronisation of the entire system (Anishchenko *et al.*, 2008). Similar observations were made in a system of coupled Van der Pol and Duffing oscillators (Wei *et al.*, 2011). Such an approach was utilised for modelling the effect of a pacemaker on the dynamics of the human heart (Honerkamp, 1983). On the flip side, to the best of our knowledge, only one experimental study has been conducted to understand the effect of forcing on mutually coupled electronic circuits with the aim of verifying the phase dynamics associated during regimes of desynchronised, mutually synchronised, two-frequency quasiperiodic, three-frequency quasiperiodic, and forced synchronised oscillations (Anishchenko *et al.*, 2009*b*). Further, all the aforementioned studies focus on the phase dynamics of the system with particular attention afforded to the dynamics of bifurcations among quasiperiodic, periodic, and chaotic regimes. In light of the above discussed limitations of past studies, there is a need to experimentally quantify the effect of mutual coupling and external forcing on the amplitude of the limit cycle oscillations (LCO) observed in both the oscillators. Thus, we analyze the phase as well as the amplitude response of two coupled thermoacoustic oscillators under the condition of asymmetric external forcing, and model the observations with a low-order model. This makes up the key objective of the present chapter, and is of general interest to the nonlinear dynamics community.

Biwa *et al.* (2015) were the first to experimentally demonstrate the control of LCO through AD in thermoacoustic engines coupled with each other using both the dissipative and time-delay couplings. The experimental results were qualitatively consistent with the results obtained from a linear stability analysis of hydrodynamic equations (Hyodo *et al.*, 2016). Thomas *et al.* (2018*b*) investigated amplitude death in a model of coupled Rijke tubes. They found that the simultaneous presence of dissipative and time-delay couplings was far more effective in attaining AD in the Rijke tubes than either of the two types of coupling applied separately. In a follow-up study with additive Gaussian white noise, Thomas *et al.* (2018*a*) observed that the presence of noise affects the coupled behavior of oscillators and mutual coupling leads to a suppression of only 80% in the amplitude of the uncoupled LCO as opposed to the state of AD observed in the absence of noise in the thermoacoustic oscillator. Hyodo and Biwa (2018*a*) used linear acoustic theory based on hydrodynamic equations to show that that a a smaller radius of coupling tubes is required to induce amplitude death if two tubes with different lengths are used for mutual coupling rather than one single tube of larger diameter. Later, Dange *et al.* (2019) performed detailed experimental characterisation of coupled Rijke tube oscillators and found that only time delay coupling is sufficient to achieve AD of low amplitude LCO. In oscillators undergoing high amplitude oscillations, frequency detuning is needed in addition to time delay coupling for attaining AD and PAD. They also reported the phenomenon of phase-flip bifurcation in the coupling of identical thermoacoustic oscillators. Frequency detuning also decreases the diameter of the coupling tube necessary to induce amplitude death (Hyodo and Biwa, 2019). Recently, Hyodo *et al.* (2020) used double-tube coupling method to significantly reduce the tube diameter necessary for demonstrating AD in a system of coupled identical Rijke tubes. Jegal *et al.* (2019) demonstrated the occurrence of AD in a practical turbulent system consisting of two lean-premixed model swirl combustors. Moon *et al.* (2020*a*) compared the characteristics of mutual synchronisation of these systems when the diameter & length of the coupling tube were changed. Jegal *et al.* (2019) also found that under different conditions, mutual synchronisation can also trigger the strong excitation of a new mode, even when the two combustors are individually stable in the absence of coupling.

On the other hand, Balusamy *et al.* (2015) experimentally studied the forced response of LCO in a swirl-stabilised combustor working in turbulent conditions using the framework of forced synchronisation and observed different states such as locking, trapping, and drifting of instantaneous phase. Kashinath *et al.* (2018) highlighted the route to forced synchronisation of limit cycle, quasiperiodic, and chaotic oscillations in a mathematical model of the premixed flame. These findings were verified in experiments on thermoacoustic engines (Penelet and Biwa, 2013; Hyodo *et al.*, 2015), Rijke tubes (Mondal *et al.*, 2019) and laminar combustors (Guan *et al.*, 2019*a*; Roy *et al.*, 2020; Guan *et al.*, 2019*b*). Mondal *et al.* (2019), Guan *et al.* (2019*a*) and Roy *et al.* (2020) further showed that forcing at frequencies away from the natural frequency of LCO lead to greater than 80% decrease in their amplitude through a phenomenon known as asynchronous quenching.

The aforementioned studies demonstrate the possibility of controlling TAI based on mutual or forced synchronisation. However, the scope of these studies is still limited as external forcing can quench TAI in a single system in a specific range of forcing parameters, whereas practical engines generally have multiple combustors working in tandem. Hence, the information on how the forcing of TAI in one combustor affects the TAI developed in another combustor is still unknown. Similarly, mutual coupling works for two coupled oscillators; however, the parametric regime for which amplitude death is observed is limited. Therefore, there is a need to combine both these methodologies to overcome their individual limitations. Essentially, in this chapter, we aim to implement a proof-of-concept capable of combining the best of both strategies – asynchronous quenching and mutual synchronisation – to control thermoacoustic oscillations. Towards this purpose, we couple two Rijke tubes during the state of TAI and subject one to external harmonic forcing (asymmetric forcing). We then measure the phase and amplitude response of the resultant acoustic pressure oscillations in the combustors at different conditions of coupling & forcing parameters. We perform asymmetric forcing experiments on identical and non-identical thermoacoustic oscillators to comprehensively assess the response to forcing. We find that through asymmetric forcing, we can expand the region of oscillation quenching of TAI in the system of coupled identical Rijke tubes by compounding the effect of asynchronous quenching and mutual synchronisation.

Finally, we develop a model where two Rijke tube oscillators are coupled through dissipative and time-delay coupling and are forced asymmetrically. We show that the model compares favourably with the experimental results, indicating the usefulness of reduced-order modelling of coupled oscillator models under forcing.

The rest of the chapter is organised as follows. In Section 6.1, we investigate the forced synchronisation characteristics of a single Rijke tube. We then demonstrate the presence of AD and PAD in mutually coupled Rijke tubes in Section 6.2. In Section 6.3, we characterise the response of coupled identical Rijke tubes to asymmetric forcing. We consider the response of non-identical oscillators in Section 6.4. In Section 6.5, we describe the model and numerically investigate the dynamics of coupled Rijke tube oscillators under forcing. Finally, we present the conclusions from this chapter in Section 6.6.

6.1 RESPONSE OF A THERMOACOUSTIC OSCILLATOR TO EXTERNAL FORCING

We begin by investigating the forced acoustic response of LCO in a single Rijke tube. Figure 6.1 shows a two-parameter bifurcation plot on an $\bar{A}_f - f_f$ plane illustrating the phase (Fig. 6.1a,c) and amplitude (Fig. 6.1b,d) response of LCO under external forcing. The natural frequency of LCO is $f_0 = 160 \pm 2$ Hz. The forced response is studied for two different amplitudes of unforced LCO: $p'_{0,\mathrm{rms}} = 120$ Pa corresponding to $p_0 = 26$ mV (Fig. 6.1a,b) and $p'_{0,\mathrm{rms}} = 200$ Pa corresponding to $p_0 = 43$ mV (Fig. 6.1c,d). Here, $p'_{0,\mathrm{rms}}$ refers to the amplitude of the unforced LCO in pascal (Pa), and p_0 refers to the equivalent reading obtained from the piezoelectric transducer in mV. The amplitude of the forcing signal A_f (in mV) is normalised with the amplitude of the LCO measured in the unforced state in mV such that $\bar{A}_f = A_f/p_0$.

In Fig. 6.1(a,c), we plot the distribution of phase locking value (PLV) between the forced LCO and the external forcing signal on the $\bar{A}_f - f_f$ plane. PLV quantifies the degree of

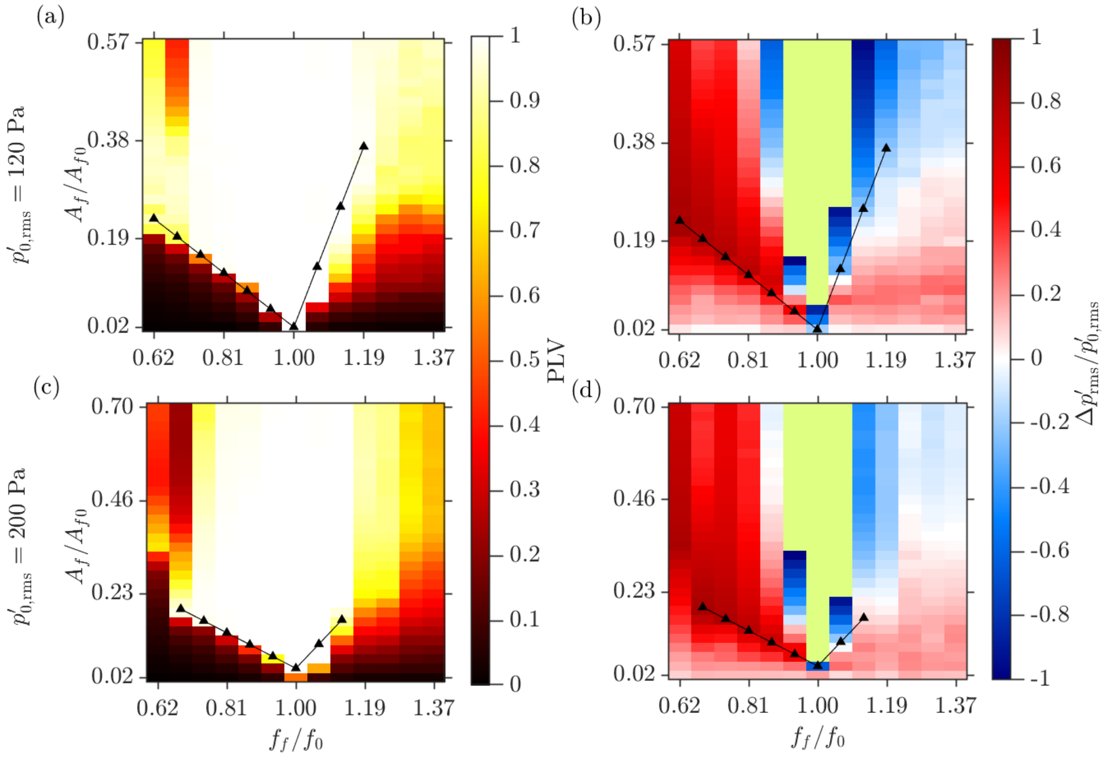

Figure 6.1: Forced response of a single Rijke tube. (a,c) The phase response shown in terms of PLV and (b,d) amplitude response in terms of fractional change in the amplitude of LCO in the Rijke tube for (a,b) $p'_{0,\mathrm{rms}} = 120$ Pa and (c,d) $p'_{0,\mathrm{rms}} = 200$ Pa for different values of $\bar{A}_f$ and f_f. The synchronisation boundaries in (a-d) are obtained through least-square-fit of points where $PLV = 0.98$. The R^2 values for the least-square fitting are given in Section I of the Supplemental Material. The region of forced synchronisation decreases with increase in $p'_{0,\mathrm{rms}}$ (a,c), while quenching of LCO is observed only for $f_f < f_0$ (b,d). Green region around $f_f/f_0 = 1$ in (b,d) indicates the amplification of LCO above twice the value of unforced amplitude.

synchronisation between a pair of oscillators at any given condition of forcing (A_f, f_f). It is defined as (Pikovsky *et al.*, 2003),

$$PLV = \frac{1}{N}\left|\sum_{n=1}^{N} \exp(i\Delta\phi)\right|, \tag{6.1}$$

where N is the length of the p' signal, and $\Delta\phi$ is the instantaneous phase difference between the p' and forcing signals. Here, forcing is assumed to be sinusoidal of the form $F(t) = A_f \sin(2\pi f_f t)$. The instantaneous phase of the signals is determined using the analytic signal approach utilising the Hilbert transform (Pikovsky *et al.*, 2003). A PLV of 1 indicates synchronisation of two oscillators, while a PLV of 0 indicates desynchronisation of the oscillators. In experimental situations, it is difficult to obtain $PLV = 1$; hence, we denote phase synchronisation boundaries of LCO through a least-square-fit of the points where $PLV = 0.98$. The R^2 values of the least-square-fit lines are presented in Appendix E. The V-shaped region, called the Arnold tongue, separates the region of forced synchronisation from the region of desynchronisation. The critical amplitude of forcing required for forced synchronisation of LCO, $A_f = A_{f,c}$, increases almost linearly with an increase in the frequency difference $\Delta f = |f_f - f_0|$.

From Fig. 6.1(a,c), we notice that for $p'_{0,\text{rms}} = 200$ Pa, the range of f_f for which forced synchronisation occurs in the system is smaller than that observed for $p'_{0,\text{rms}} = 120$ Pa, indicating the dependence of forced synchronisation of LCO on their amplitude in the unforced state. Further, at higher values of Δf, achieving forced synchronisation of both LCO becomes difficult. We also observe regions of desynchronised oscillations (indicated in red) in the range of $f_f/f_0 = 0.62 - 0.70$ at high values of $\bar{A}_f$ ($\bar{A}_f > 0.35$ in Fig. 6.1a,c). The reason for desynchrony in this region is a result of period-3 behavior in p', which leads to low values of PLV (see Section II of the Supplemental Material).

We also plot the normalised change in the amplitude of LCO due to external forcing, $\Delta\bar{p} = (p'_{0,\text{rms}} - p'_{\text{rms}})/p'_{0,\text{rms}}$ in Fig. 6.1(b,d). Here, $\Delta\bar{p} \sim 1$ corresponds to complete suppression of LCO in the Rijke tube due to forcing, whereas $\Delta\bar{p} < 0$ indicates increase in the amplitude of LCO above the unforced value due to forcing. The green region in Fig. 6.1(b,d) corresponds to an increase in the amplitude of LCO above twice of its unforced value (i.e., $\Delta\bar{p} < -1$) due to resonant amplification of the acoustic pressure signal as f_f is very close to f_0. $\Delta\bar{p} < -1$ implies that the resultant amplitude is more than twice the amplitude of LCO in unforced conditions. The simultaneous occurrence of forced synchronisation for $f_f \approx f_0$ along with the resonant amplification of the amplitude of LCO is referred to as synchronance (Mondal *et al.*, 2019). We further observe a large region with a reduction in amplitude greater than 80% of $p'_{0,\mathrm{rms}}$ only for $f_f < f_0$. A significant decrease in the amplitude of LCO at non-resonant conditions ($f_f \neq f_0$) of forcing is a result of asynchronous quenching (Mondal *et al.*, 2019; Guan *et al.*, 2019*a*). Asynchronous quenching of LCO is achieved through forced synchronisation, where the response p' signal oscillates at f_f, which can be seen from the coincidence of the boundaries of the Arnold tongue with region corresponding to $\Delta\bar{p} \approx 1$ (see Fig. 6.1b,d). The asymmetry in the characteristics of the Arnold tongue and asynchronous quenching of LCO arises due to the nonlinearity inherently present in the thermoacoustic system (Kashinath *et al.*, 2018).

6.2 RESPONSE OF THERMOACOUSTIC OSCILLATORS MUTUALLY COUPLED WITH EACH OTHER

We now examine the response of two mutually coupled Rijke tubes when the length of the coupling tube (L_c) and the frequency detuning Δf_0 $(= f_0^B - f_0^A)$ between them are varied independently, where f_0^a and f_0^B are natural frequencies of oscillators A and B in the uncoupled state, respectively. In this chapter, the diameter of the connecting tube is kept constant at 1 cm for all the experiments (see Section III of Supplemental Material).

An acoustic time delay in the coupling is induced through the connecting tube present between the two Rijke tubes, as a finite time is needed for the acoustic waves in the two oscillators to interact with one another (Dange *et al.*, 2019). A variation in the coupling tube's length changes the acoustic time-delay between the two mutually interacting Rijke tubes. A variation in the diameter of the coupling tube induces a change in the coupling strength between the two interacting Rijke tubes. The coupling strength comprises of two parts: time-delay coupling and dissipative coupling. Dissipative coupling is related to the interaction that is caused due to mass transfer between the two ducts (Bar-Eli, 1985). We notice both time delay and dissipative coupling in our system.

In Fig. 6.2, we plot the fractional change in the amplitude of LCO in these oscillators,

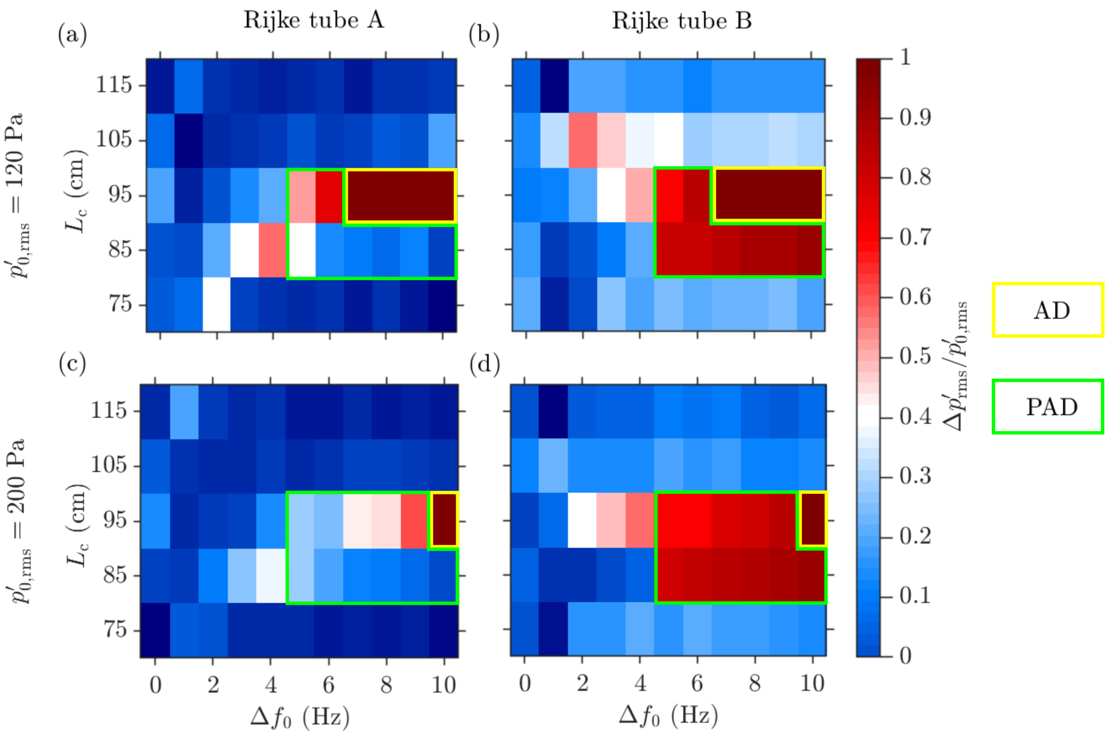

Figure 6.2: Coupled response of two Rijke tubes. Fractional change in the amplitude of LCO for Rijke tube A and B as functions of the frequency detuning ($\Delta f_0 = |f_0^A - f_0^B|$) and length of the connecting tube (L_c) for (a,b) $p'_{0,\mathrm{rms}} = 120$ Pa and (c,d) $p'_{0,\mathrm{rms}} = 200$ Pa in both the oscillators. The region of AD and PAD are indicated. At other regions in the plots, LCO is observed at reduced amplitude due to coupling. The parametric region exhibiting AD shrinks in size as $p'_{0,\mathrm{rms}}$ is increased from 120 Pa to 200 Pa.

$\Delta\bar{p}$, as a function of L_c and Δf_0 for two different values of $p'_0 = 120$ Pa (Fig. 6.2a,b) and 200 Pa (Fig. 6.2c,d). The colorbar illustrating $\Delta\bar{p}$ values range from 0 to 1. During mutual coupling of oscillators, we seldom observe any amplification of LCO.As a result, $\Delta\bar{p}$ is never negative. In contrast, during forcing experiments in Fig. 6.1(b,d), we observe resonant amplification of LCO.

In Fig. 6.2, for identical oscillators ($\Delta f_0 = 0$ Hz), we do not observe any perceivable reduction in the amplitude of LCO due to coupling for either values of $p'_{0,\mathrm{rms}}$. However, a significant reduction in the amplitude of LCO is observed when non-identical oscillators are coupled. We observe two states of oscillation quenching, i.e., amplitude death (AD) and partial amplitude death (PAD), in coupled Rijke tubes for a particular range of L_c.

For example, when $\Delta f_0 = 5 - 10$ Hz and $L_c = 85$ cm, we witness the presence of PAD in the system (see green box in Fig.6.2), while for $\Delta f_0 = 7 - 10$ Hz and $L_c = 95$ cm, we observe AD in the mutually coupled Rijke tubes (see yellow box Fig.6.2). During the state of PAD, LCO in Rijke tube B (unforced) undergoes suppression and that in Rijke tube A (forced) remains at the reduced amplitude. For the state of AD, we observe greater than 95% decrease in the amplitude of LCO in both the oscillators due to coupling. The range of Δf_0 for which AD is observed in the system is smaller for $p'_{0,\mathrm{rms}} = 200$ Pa (Fig.6.2c,d) when compared to that for $p'_{0,\mathrm{rms}} = 120$ Pa (Fig. 6.2a,b). Thus, the occurrence of AD in Rijke tube oscillators has a dependence on the amplitude of uncoupled LCOs. It is quite clear from Fig. 6.2 that the mutual coupling induced through the coupling tube is not capable of inducing AD in identical oscillators, and the occurrence of AD in high amplitude LCO is restricted to a small range of L_c and requires a finite value of Δf_0 in the system (Dange *et al.*, 2019).

6.3 RESPONSE OF COUPLED IDENTICAL THERMOACOUSTIC OSCILLATORS UNDER ASYMMETRIC FORCING

As observed in Fig.6.2, in the absence of frequency detuning, mutual coupling is ineffective in achieving mitigation of oscillations (i.e., PAD or AD) in the coupled system. Hence, we asymmetrically force the coupled thermoacoustic oscillators to enhance the quenching of LCOs. Figure 6.3 shows the representative time series of the acoustic pressure fluctuations in Rijke tube A (in blue) and B (in brown) under the effect of mutual coupling and external forcing when introduced sequentially. Both the oscillators are initially coupled through a single tube and then oscillator A is forced through loudspeakers. The time instant when coupling and forcing are switched on/off are marked as well. In some situations, we notice that coupling and forcing can marginally reduce the amplitude of LCO in the coupled system (Fig. 6.3a). While in others, forcing can completely quench LCO in one and reduce the amplitude of LCO in the other oscillator (Fig. 6.3b). This situation is akin to the state of PAD. Thus, forcing aids in

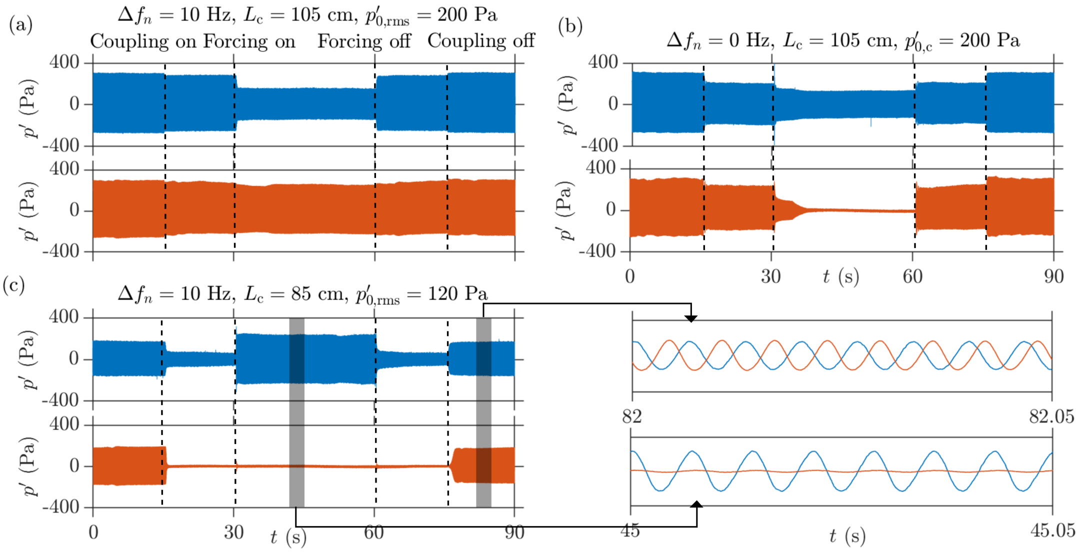

Figure 6.3: (a)-(c) Time series of p' in Rijke tubes A (blue) and B (brown) sequentially illustrating the effect of coupling and forcing on the amplitude of LCO in both the Rijke tubes for different coupling and forcing parameters. In (a,c), the Rijke tubes are non-identical and have a frequency difference of 10 Hz. (i,ii) The enlarged portions of the desynchronised LCO and the state of PAD in (c), respectively. The coupling of oscillators always leads reduction in the amplitude of LCO, while forcing of oscillators can have both reduction or amplification effects, depending on the values of coupling and forcing parameters. The common parameters in all plots are: $d_c = 10$ mm, $f_f = 140$ Hz, and $A_f = 30$ mV.

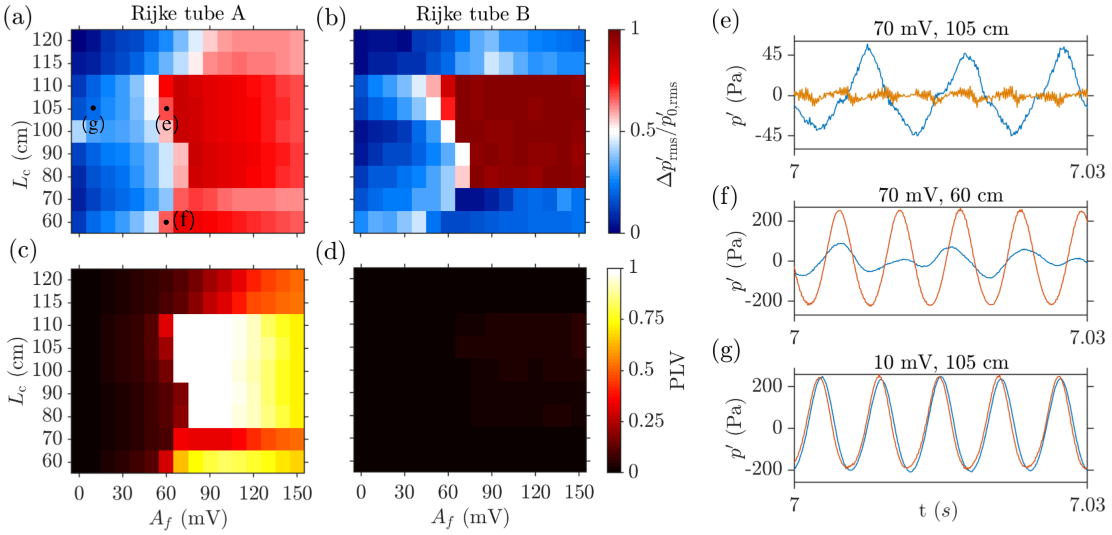

Figure 6.4: Response of coupled, identical oscillators to asymmetric forcing. (a,b) Amplitude and (c,d) phase response as functions of the forcing amplitude (A_f) and length of the coupling tube (L_c). (e-g) Representative time series of p' for the points indicated in (a) depicting difference in the response of Rijke tube A and B. Complementary forcing and coupling enhances the region of L_c over which the suppression of LCO is observed in both the oscillators. Forcing is ineffective in synchronisation of LCO in Rijke tube B (the black region in (d) denotes the complete desynchrony of LCO in Rijke tube B with the forcing signal), while the region of quenching of LCO in Rijke tube A nearly coincides with the region of forced synchronisation ($PLV \approx 1$). The common parameters in all the plots are: $p'_{0,\mathrm{rms}} = 200$ Pa, $f_f = 100$ Hz ($f_f/f_0 \approx 0.6$), $\Delta f_n = 0$ Hz, and $d_c = 1$ cm.

attaining PAD. On the flip side, in Fig. 6.3(c), we observe that forcing can also lead to an amplification of the acoustic pressure oscillations, as can be seen from the increased amplitude of these oscillations in Rijke tube A above the uncoupled value. In contrast, the acoustic pressure oscillations remain quenched in Rijke tube B. Thus, the effectiveness of coupling and forcing of thermoacoustic oscillators is restricted to a particular range of coupling and forcing parameters and hence, we focus on the identification of such regions in the subsequent discussion.

In Fig. 6.4, we plot the amplitude (Fig. 6.4a,b) and the phase (Fig. 6.4c,d) response of identical Rijke tubes as a function of the forcing amplitude (A_f) and the length of coupling tube (L_c). The phase response is determined from the PLV calculated between the external forcing signal and p' for either of the Rijke tubes. Only Rijke tube A is subjected to external forcing. The forcing frequency is chosen as $f_f = 100$ Hz ($f_f/f_0 \approx 0.6$) for which we observe asynchronous quenching in a single forced Rijke tube oscillator (Fig. 6.1d).

For $A_f = 0$, we observe that a change in L_c does not lead to any suppression of LCO in the oscillators (Fig. 6.4a,b). With an increase in A_f, we observe a slow decrease in the amplitude of LCO in both the oscillators with the effect on Rijke tube B (unforced) being more pronounced than Rijke tube A (forced). Complete suppression of LCO ($\Delta\bar{p} \approx 1$) is observed in a particular range of L_c in Rijke tube B (Fig. 6.4b), while a significant decrease in the amplitude of LCO (i.e., $\Delta\bar{p} \approx 0.8$) is observed over a wider range of L_c in Rijke tube A (Fig. 6.4a). For the coupled systems without forcing in Fig. 6.2, we did not observe AD or PAD when identical Rijke tubes were coupled for any L_c. However, the same coupled identical oscillators when asymmetrically forced exhibit the state of PAD for a range of L_c (see point (e) in Fig. 6.4a). Thus, we notice that a larger region over which suppression of high amplitude LCO can be achieved in coupled identical thermoacoustic oscillators when the oscillators are coupled in a particular range of L_c and asymmetric forcing is applied at non-resonant frequencies. We reiterate that we do not observe complete suppression of amplitude of LCO in Rijke tube A.

Further, we notice that the region of quenching of LCO in Rijke tube A (i.e. $\Delta\bar{p} > 0.8$ in Fig. 6.4a) nearly coincides with the region of forced synchronisation (i.e., $PLV \approx 1$ in Fig. 6.4c) while the other regions remain desynchronised with the forcing signal. However, the LCO in Rijke tube B always remains desynchronised with the forcing signal, which is observed from the value of $PLV \sim 0$ in Fig. 6.4(d). For the regions where we do not observe suppression of LCO in Rijke tube B, difference between f_f and f_0 is too large such that there is no phase locking between oscillations in Rijke tube B and the forcing signal, resulting in low PLV. For the regions where we notice complete suppression in Rijke tube B (Fig. 6.4e), the oscillations are noisy with very low amplitude, leading to low PLV.

The blue and red time series shown in Fig. 6.4(g) depict the acoustic pressure fluctuations in Rijke tubes A and B, respectively and the acoustic pressure time series correspond to data point (g) in Fig. 6.4(a,b). Although these signals appear mutual phase synchronised with each other in Fig. 6.4(g), they are desynchronised with the forcing signal due to a difference in the frequencies of their oscillations (i.e., $f_0 = 160$ Hz and $f_f = 100$ Hz). Therefore, the PLV distribution quantifying forced synchronisation in Fig. 6.4(c) and Fig 6.4(d) show zero values for data point (g).

Next, we measure the effect of forcing on the Arnold tongue and the amplitude quenching characteristics of the coupled identical Rijke tubes. The coupling tube parameters are fixed at $L_c = 105$ cm and $d_c = 1$ cm, respectively. Only Rijke tube A is forced externally. The natural frequency of both the oscillators is maintained at $f_0^A = f_0^B \approx 160$ Hz. In Fig. 6.5, we depict the fractional change in the amplitude of LCO for each oscillator overlapped with the Arnold tongue on the $\bar{A}_f - f_f$ plane for $p'_{0,\mathrm{rms}} = 120$ Pa (Fig. 6.5a,b) and $p'_{0,\mathrm{rms}} = 200$ Pa (Fig. 6.5c,d).

When the coupled Rijke tubes are asymmetrically forced, we notice forced synchronisation at a lower value of $\bar{A}_f$ for Rijke tube A than for Rijke tube B at any value of f_f. Therefore, the boundaries of the Arnold tongue are observed to be longer and the region of forced synchronisation is wider for Rijke tube A (Fig. 6.5a,c) than that for Rijke tube B (Fig. 6.5b,d). Furthermore, we notice that the boundaries of the Arnold tongue for $p'_{0,\mathrm{rms}} = 120$ Pa are less steeper than that for $p'_{0,\mathrm{rms}} = 200$ Pa. This means that a significantly larger value of forcing amplitude is required to synchronise and quench the large amplitude LCO in the coupled Rijke tube oscillators. As the external forcing is applied to Rijke tube A, the region of resonant amplification is larger than that for Rijke tube B. Moreover, as the forcing amplitude is increased, the oscillator which is subjected to external forcing (i.e., Rijke tube A) synchronises with the forcing signal first, followed by the forced

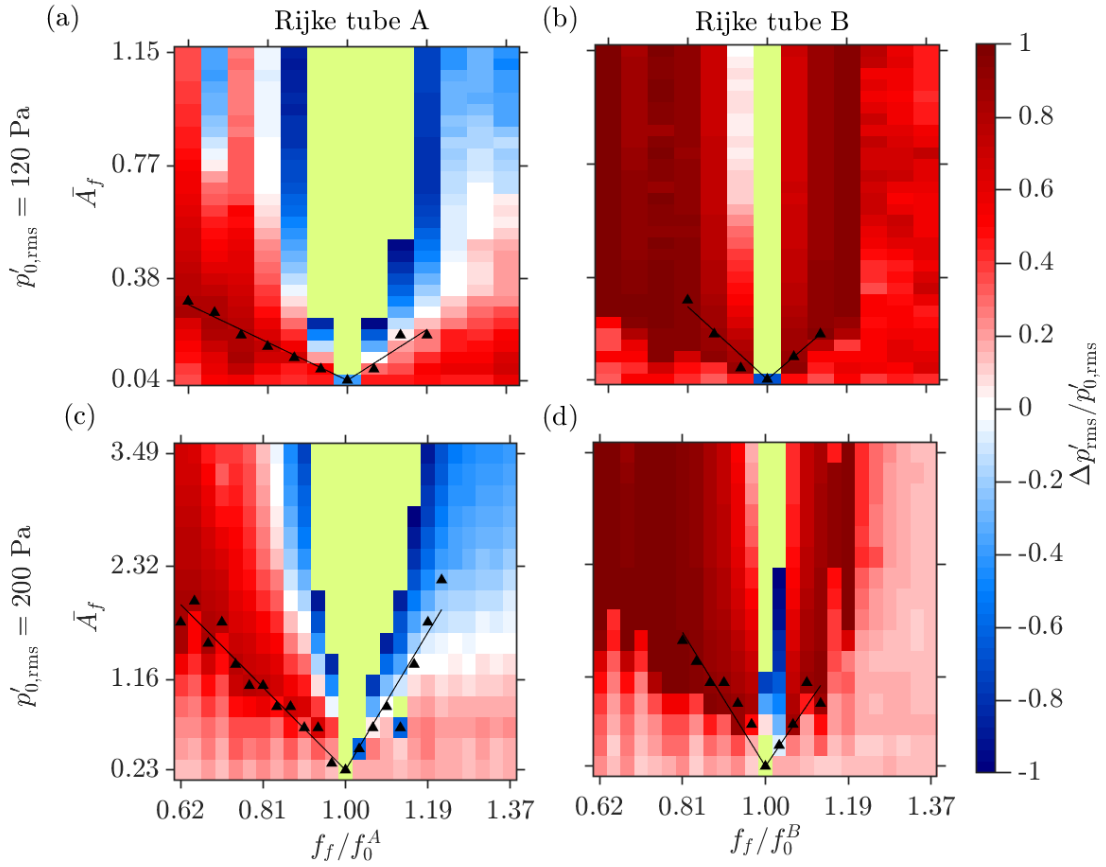

Figure 6.5: Amplitude and phase response (black lines) of Rijke tubes A and B when coupled identical oscillators are subjected to asymmetric forcing for (a,b) $p'_{0,\mathrm{rms}} = 120$ Pa and (c,d) $p'_{0,\mathrm{rms}} = 200$ Pa. The LCO in Rijke tube A is externally forced through the acoustic drivers. The region of forced synchronisation is wider for Rijke tube A than that observed for Rijke tube B, whereas a much larger magnitude of suppression of LCO is observed in Rijke tube B as compared to that in Rijke tube A. Green region around $f_f/f_0 = 1$ indicates the amplification of LCO above twice the value of LCO amplitude in the uncoupled-unforced Rijke tubes. Experimental conditions: $f_{n0}^A = f_{n0}^B \approx 160$ Hz, $L_c = 105$ cm, $d_c = 1$ cm.

synchronisation of the entire system, i.e., the coupled system of Rijke tubes A & B. Further, the transition from desynchronised to forced synchronisation for Rijke tubes A & B takes place through a sequence of bifurcations: (i) from desynchronised limit cycle at $f_0^{A,B}$ to two-frequency quasiperiodicity through torus-birth bifurcation ($f_0^{A,B}$, f_f); and (ii) from two-frequency quasiperiodicity to synchronised limit cycle (f_f) either through saddle-node bifurcation if $f_0^{A,B}$ is close to f_f or through torus-death bifurcation if $f_0^{A,B}$ is far from f_f. These two routes are quite well-known (Balanov *et al.*, 2008) and is observed for the identically coupled Rijke tubes under forcing. f_0 denotes the natural frequency of the Rijke tubes, and f_n denotes the frequency of the p' oscillations exhibited by the Rijke tubes after the ducts are coupled and asymmetrically forced.

Rijke tube A (Fig. 6.5a,c) shows a similar trend of quenching of different amplitude LCO as observed for the single oscillator (Fig. 6.1b,d). The similarities include an approximate coincidence of maximum amplitude suppression with the synchronisation boundary, significant amplitude suppression only for forcing frequencies of $f_f < f_0$, and the presence of region of resonant amplification around $f_f/f_0 \sim 1$ (shown in green). However, the $\bar{A}_f$ required for forced synchronisation at any f_f for the coupled identical oscillators (Fig. 6.5a,c) is higher than that for a single oscillator (Fig. 6.1b,d).

In contrast to the response of Rijke tube A, simultaneous effect of coupling and external forcing lead to a much greater suppression of limit cycle oscillations along the boundaries of forced synchronisation in Rijke tube B (Fig. 6.5b,d). Suppression of LCO in Rijke tube B is observed for both $f_f < f_0$ and $f_f > f_0$, unlike Rijke tube A where we notice a reduction only for $f_f < f_0$. Further, the range of f_f and $\bar{A}_f$ over which the suppression of LCO occurs in Rijke tube B is larger than that observed for Rijke tube A. Thus, we reassert that asymmetrically forced coupled system exhibits suppression of higher amplitude LCO for a larger range of forcing parameters than that observed when the oscillators are forced or coupled individually.

6.4 FORCED RESPONSE OF COUPLED NON-IDENTICAL LIMIT CYCLE OSCILLATORS

Now, we study the response of coupled non-identical Rijke tubes under asymmetric forcing. Only Rijke tube A is externally forced. In Fig. 6.6, we depict the Arnold tongue and the fractional change in the amplitude of LCO for $p'_{0,\mathrm{rms}}$ = 120 Pa (Fig. 6.6a,b) and $p'_{0,\mathrm{rms}}$ = 200 Pa (Fig. 6.6c,d). The oscillators are coupled through a tube of L_c = 105 cm and d_c = 1 cm. A frequency detuning between the uncoupled oscillators is fixed

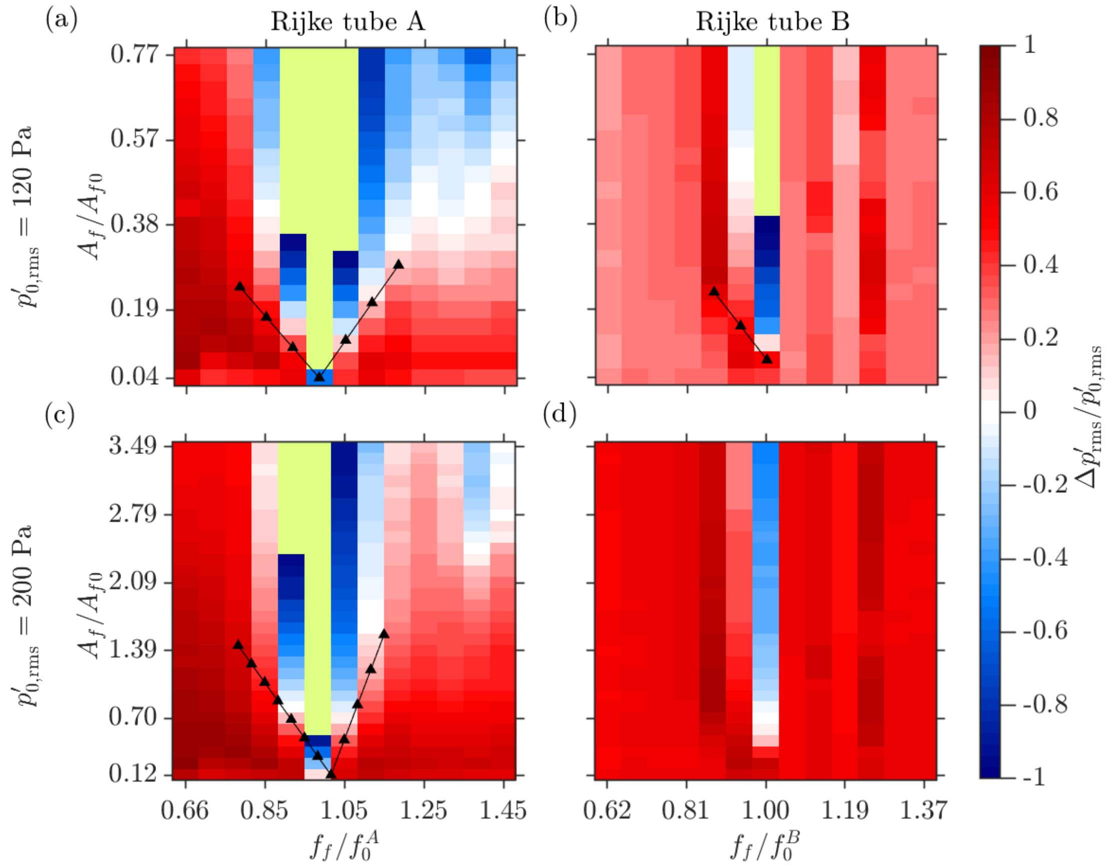

Figure 6.6: The amplitude and phase response (black lines) of Rijke tubes A and B when coupled non-identical oscillators are subjected to asymmetric forcing for (a,b) $p'_{0,\mathrm{rms}} = 120$ Pa and (c,d) $p'_{0,\mathrm{rms}} = 200$ Pa. The effect of forcing is less effective in synchronizing and quenching of LCO in Rijke tube B, while it shows regions of forced synchronisation and quenching of LCO in Rijke tube A. The common parameters in all the plots are: $\Delta f_0 = 10$ Hz, $L_c = 105$ cm, $d_c = 1$ cm.

at 10 Hz (i.e., $\Delta f_0 = f_0^B - f_0^A = 10$ Hz). We notice that the effect of forcing is quite insignificant for synchronisation of LCO in Rijke tube B. We observe a small range of f_f (i.e., $f_f < f_0^B$) over which Rijke tube B is synchronised to forcing for $p'_{0,\mathrm{rms}} = 120$ Pa (Fig. 6.6b). The region of forced synchronisation is completely absent when p'_0 is increased to 200 Pa (Fig. 6.6d). In contrast, as the external forcing is applied directly to Rijke tube A, it is easily synchronised with the forcing, as seen from the longer boundaries of the Arnold tongue for both $p'_{0,\mathrm{rms}} = 120$ and 200 Pa in Fig. 6.6(a,c), respectively.

Finally, the mechanism through which forced synchronisation is attained for $p'_{0,\mathrm{rms}} = 120$

Pa in the non-identical system is quite different from that of the coupled system. As the forcing amplitude is increased, the oscillator which is subjected to external forcing (i.e., Rijke tube A) synchronises with the forcing signal first, followed by the forced synchronisation of the entire system, i.e., the coupled system of Rijke tubes A & B. The entire system undergoes forced synchronisation only in $f_f/f_0^{A,B} < 1$ range. The transition from desynchronised to forced synchronisation for Rijke tube A takes place through the following sequence of bifurcations: (i) from desynchronised two-frequency quasiperiodicity (f_0^A, f_0^B) to three-frequency quasiperiodicity (f_0^A, f_0^B, f_f) as A_f is increased; and (ii) from three-frequency quasiperiodicity to synchronised limit cycle (f_f). This route was reported for coupled Van der Pol oscillators under asymmetric forcing (Anishchenko *et al.*, 2008, 2009*a*). However, Rijke tube B goes from two-frequency quasiperiodicity (f_0^A, f_0^B) to synchronised limit cycle (f_f) when $f_f/f_0 < 1$. For $p'_{0,\mathrm{rms}} = 200$ Pa, the acoustic pressure fluctuations in Rijke tube B remain desynchronised with the forcing signal throughout the $\bar{A}_f - f_f$ parameter plane.

The amplitude response of Rijke tube A and B shows that the significant suppression of LCO can still be achieved at non-resonant conditions of forcing. The region of resonant amplification observed around $f_f/f_0 \sim 1$ is very small for Rijke tube B as compared to Rijke tube A. Furthermore, the comparison of the forced response of the coupled oscillators with $p'_{0,\mathrm{rms}} = 120$ Pa (Fig. 6.6a,b) and $p'_{0,\mathrm{rms}} = 200$ Pa (Fig. 6.6c,d) shows that for the higher amplitude LCO, we need significantly larger values of $\bar{A}_f$ for synchronisation and quenching of oscillations in both the Rijke tubes. This is similar to the observations made for identical oscillators in Fig. 6.5. Note that the ordinate in Fig. 6.6(c,d) is much larger than that in Fig. 6.6(a,b). Thus, we re-emphasise that the effect of forcing is more significant in suppressing LCO in both coupled thermoacoustic oscillators if their natural frequencies are nearly the same as compared to that seen in the case of non-identical oscillators.

6.5 MATHEMATICAL MODEL

In this section, we will discuss a reduced-order model developed for the system of coupled horizontal Rijke tubes subjected to asymmetric forcing. The model of the uncoupled oscillator is based on Balasubramanian and Sujith (2008). We neglect the effects of mean flow and mean temperature gradient in the duct. The temporal evolution of a single Rijke tube is described by the following set of ODEs

$$\frac{d\eta_j}{dt} = \dot{\eta}_j, \tag{6.2}$$

$$\frac{d\dot{\eta}_j}{dt} + 2\xi_j \omega_j \dot{\eta}_j + k_j^2 \eta_j = -j\pi K \left[\sqrt{\left| \frac{1}{3} + u'_f(t - \tau_{\mathrm{h}}) \right|} - \sqrt{\frac{1}{3}} \right] \sin(j\pi x_f), \tag{6.3}$$

where $k_j = j\pi$ refers to the non-dimensional wave number and $\omega_j = j\pi$ refers to the non-dimensional angular frequency of the j^{th} mode. Other parameters are the non-dimensional heater power K, and non-dimensional velocity, u'_f at the non-dimensional heater location, xf. The thermal inertia of the heat transfer in the medium is captured by a parameter time lag τ. The coefficient ξ_j appearing in the second term of Eq. (6.3) represents the frequency-dependent damping (Matveev, 2003), and is given by the following ansatz (Sterling and Zukoski, 1991):

$$\xi_j = \frac{c_1 \dfrac{\omega_j}{\omega_1} + c_2 \sqrt{\dfrac{\omega_1}{\omega_j}}}{2\pi}, \tag{6.4}$$

where c_1 and c_2 are the damping coefficients. We choose the values $c_1 = 0.1$ and $c_2 = 0.06$ based on Sterling and Zukoski (1991) for all simulations. We also set $x_f = 0.25$ $(= L/4)$, as it is the most favorable location for the onset of TAI (Matveev, 2003). The non-dimensional velocity u' and non-dimensional pressure p' fluctuations in the model are written in terms of the Galerkin modes:

$$p'(x,t) = \sum_{j=1}^{N} -\frac{\gamma M}{j\pi}\dot{\eta}_j(t)\sin(j\pi x), \tag{6.5}$$

$$u'(x,t) = \sum_{j=1}^{N} \eta_j(t)\cos(j\pi x). \tag{6.6}$$

For Rijke tubes, Matveev (2003) and Sayadi *et al.* (2014) have shown that the first mode is the most unstable of all the other modes. Consequently, we consider only the first mode ($N = 1$) in our numerical analysis, to keep the model simple.

Let superscripts "a" and "b" denote Rijke tube A and B, respectively. We assume that the two Rijke tubes are coupled through time-delay and dissipative couplings. The governing equations for coupled non-identical Rijke tubes with asymmetric sinusoidal forcing can then be written as:

$$\frac{d\eta_j^{a,b}}{dt} = {\dot{\eta}_j}^{a,b}, \tag{6.7}$$

$$\begin{aligned}\frac{d{\dot{\eta}_j}^{a,b}}{dt} + 2\xi_j\left(\frac{\omega_j}{r^{a,b}}\right){\dot{\eta}_j}^{a,b} + \left(\frac{k_j}{r^{a,b}}\right)^2\eta_j^{a,b} = -\frac{j\pi}{{r^{a,b}}^2}K\left[\sqrt{\left|\frac{1}{3} + u_f'^{a,b}(t-\tau_{\text{h}})\right|} - \sqrt{\frac{1}{3}}\right] \times \\ \sin\left(\frac{j\pi x_f}{r^{a,b}}\right) + \underbrace{K_d({\dot{\eta}_j}^b - {\dot{\eta}_j}^a)}_{\text{Dissipative coupling}} + \underbrace{K_\tau({\dot{\eta}_j}^b(t-\tau) - {\dot{\eta}_j}^a(t))}_{\text{Time-delay coupling}} + \underbrace{[A_f\sin(2\pi f_f t)]^a}_{\text{Forcing term}},\end{aligned} \tag{6.8}$$

where, $r^{a,b}$ is defined as the ratio of the length of the duct to a reference length, $L_{a,b}/L_{ref}$. We consider L_a to be the reference length. For identical oscillators, $r^a = r^b = 1$. For non-identical oscillators, $r_a = 1$ and $r_b = L_b/L_a = \omega_a/\omega_b$. The detailed derivation of Eqs. 6.7 and 6.8 is provided in Appendix D.

Parameter	Value	Parameter	Value	Parameter	Value
N	1	τ_{h}	0.25	K	5
γ	1.4	M	0.005	x_f	0.25
c_1	0.1	c_2	0.06	ω_f	$j\pi$

Table 6.1: Model parameters kept constant throughout the numerical analysis of the reduced-order model.

The second and third terms on the right-hand side of Eq. (6.8) are the dissipative and time-delay coupling terms, respectively. Dissipative coupling encapsulates the interaction that arises from the mass transfer between the two ducts (Bar-Eli, 1985). Time-delay coupling quantifies the time taken by acoustic waves to propagate through the coupling tube connecting the two Rijke tubes (Biwa *et al.*, 2015; Thomas *et al.*, 2018*b*). Thus, τ denotes the time-delay in the response induced by one Rijke tube on the other, and is proportional to the length of the coupling tube, i.e., $\tau \propto L/c$, where c is the speed of sound inside the coupling tube. The fourth term is the sinusoidal forcing term with amplitude A_f and frequency f_f. The external forcing is applied only to Rijke tube A.

The effect of the source term is characterised by the time-delay τ, which captures the thermal inertia of the heat transfer in the medium. The ODEs given in Eqs. (6.7) and (6.8) are solved numerically using `dde23`, an inbuilt function for solving delay differential equations in MATLAB (Shampine and Thompson, 2001), and p' is calculated using Eq. (6.5). The parameters which are kept constant during the simulations are indicated in Table 6.1. These parameters have been chosen such that the both the oscillators exhibit LCO at a parametric location away from the bistable regime and also to quantitatively match the experimental results.

6.5.1 Model results for a single oscillator and mutually coupled oscillators

We begin by analysing the forced response of a single Rijke tube by adding the forcing term $A_f \sin(2\pi f_f t)$ to the right hand side Eq. (6.3). Considering only the first mode, we

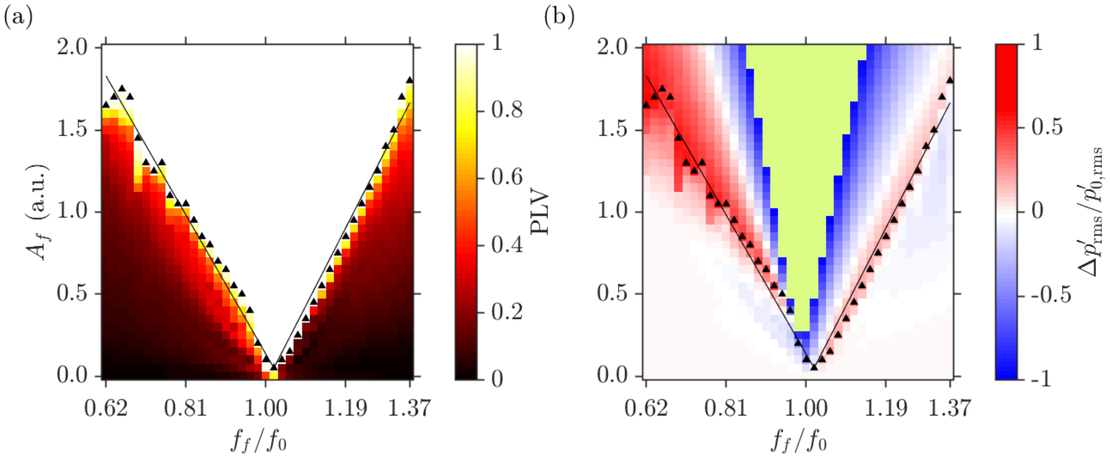

Figure 6.7: (a) The phase response and (b) the amplitude response obtained from the model of a single Rijke tube under external forcing. The synchronisation boundaries are obtained through a least-square-fit of points where $PLV = 0.98$. The Arnold tongue and extent of asynchronous quenching from the model show a qualitative match with the experimental results in Fig. 6.1.

get the following set of ODEs is:

$$\frac{d\eta_1}{dt} = \dot{\eta}_1, \tag{6.9}$$

$$\frac{d\dot{\eta}_1}{dt} + 2\xi_1\omega_1\dot{\eta}_1 + k_1^2\eta_1 = -\pi K \left[\sqrt{\left| \frac{1}{3} + u'_f(t-\tau) \right|} - \sqrt{\frac{1}{3}} \right] \sin(\pi x_f) + \underbrace{A_f \sin(2\pi f_f t)}_{\text{Forcing term}} . \tag{6.10}$$

Figure 6.7 shows the two-parameter bifurcation plot on the $A_f - f_f$ plane illustrating the amplitude & phase dynamics of LCO in a single Rijke tube, obtained from the mathematical model. We observe the existence of Arnold tongue in Fig. 6.7(a) along with the region of asynchronous quenching ($\Delta\bar{p} > 0.5$) in Fig. 6.7(b). We observe the qualitative match between experimental results shown in Fig. 6.1 and those obtained from the model in Fig. 6.7. However, there are a number of differences. First, the region of asynchronous quenching observed in the model is smaller than that observed in the experiments. Second, the region of resonant amplification is spread over a larger extent

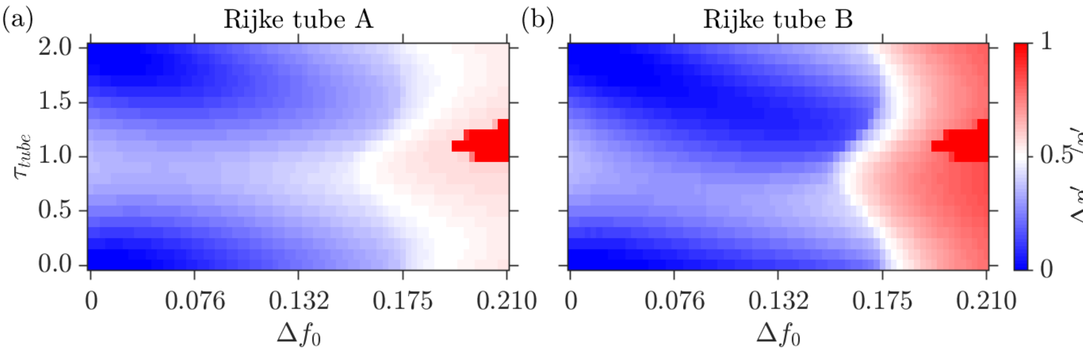

Figure 6.8: Bifurcation plots between frequency mismatch between the two Rijke tube model oscillators and τ. K_d and K_τ are kept constant at 1.0 and 0.2, respectively. The dark red region in both the plots represent regions of AD observed in the model oscillators. At other places, LCO is observed at reduced amplitude due to coupling.

of parameter values in the model. Finally, the Arnold tongue obtained from the model is symmetrical as opposed to left-skewed in the experiments. The skewness of the Arnold tongue increases as the model heater power K is increased to higher-values, indicating the nonlinear behavior of the overall systems. Figure 6.7 has been shown for a model heater power K for which we get the best match with the experimental results in Fig. 6.1.

In Fig. 6.2, we showed that the state of AD was attained in coupled Rijke tubes only when there was a frequency detuning present in the two oscillators, in addition to the dissipative and time-delay coupling due to the connecting tube. In Fig. 6.8, we show the effect of coupling and frequency detuning on the occurrence of the state of AD in the model. We fixed the value of $K_d = 1.0$ and $K_\tau = 0.2$, and varied τ and frequency detuning Δf_0. For identical oscillators ($\Delta f_0 = 0$), we did not observe any appreciable reduction in the amplitude of LCO. However, for finite value of detuning, we observe the state of AD in the model, consistent with our experimental observations in Fig. 6.2. Thus, the effect of change of the length of coupling tube is captured quite well by the time-delay τ.

The results summarised in Fig. 6.7 and 6.8 validate our model against experimental

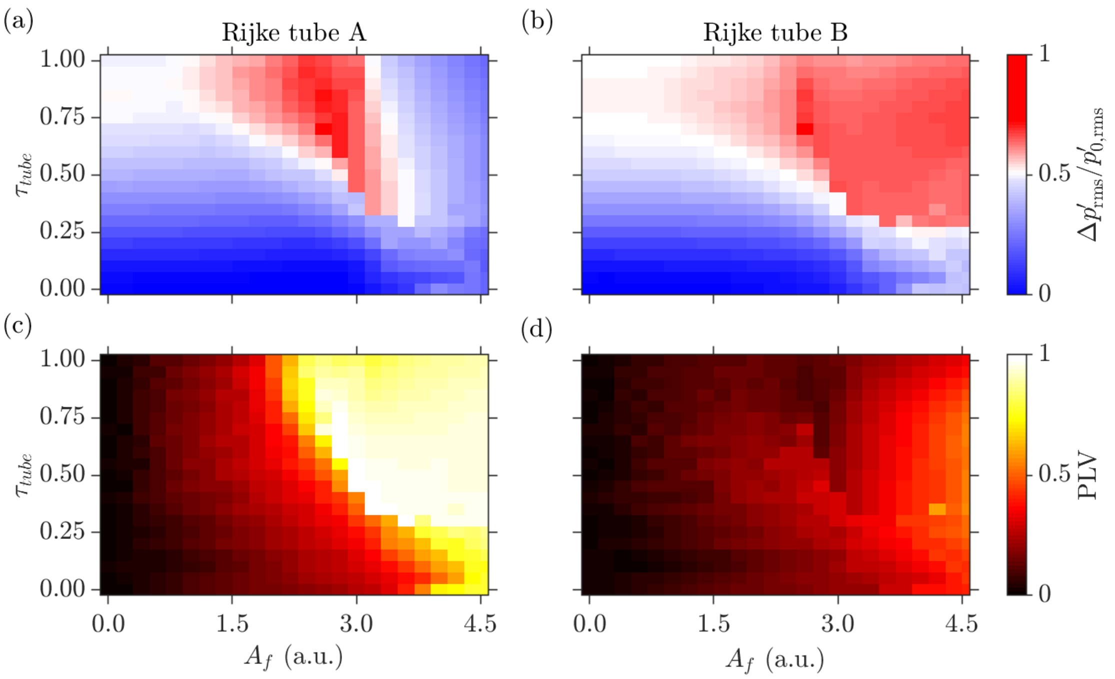

Figure 6.9: (a,b) Amplitude and (c,d) phase response of coupled, identical oscillators under asymmetric forcing for different values of τ and A_f. Amplitude response is indicated by the fractional change in the amplitude of LCO ($\Delta\bar{p}$) while phase response is quantified by the PLV between p' and forcing signal. For $\tau > 0.4$ and $A_f > 1.5$, large suppression in the amplitude of LCO is observed in the two Rijke tubes.

observations for a single and coupled Rijke tubes reported in the present chapter (Fig. 6.1 and 6.2), as well as those made in past studies (Thomas *et al.*, 2018*b*; Hyodo and Biwa, 2018*c*; Dange *et al.*, 2019). We now turn our attention towards modelling the effect of asymmetric forcing on the coupled Rijke tubes.

6.5.2 Model results for coupled behavior of thermoacoustic oscillators under asymmetric forcing

In Fig. 6.9, we plot the amplitude and the phase response of the coupled identical Rijke tubes under asymmetric forcing, i.e., only Rijke tube A is subjected to external forcing according to Eq. (6.8). The effect of coupling is parameterised by τ, while that of external forcing by A_f. The forcing frequency is fixed at $f_f/f_0 = 0.6$. K_d, K_τ & K values are fixed at 1.0, 0.2 and 5.0, respectively. Note that the heater power $K = 5.0$

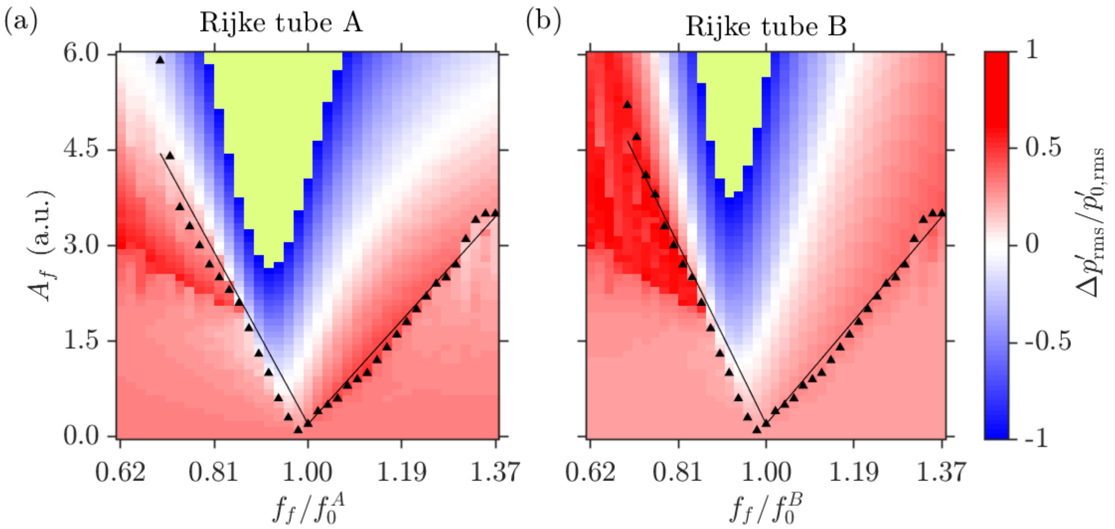

Figure 6.10: The amplitude response and overlapped Arnold tongue for identical, coupled Rijke tubes from the mathematical model. External forcing is applied to Rijke tube A. The synchronisation boundaries are obtained through least-square-fit of points where $PLV = 0.98$. The coupling parameters are: $K_d = 1.0$, $K_\tau = 0.2$ and $\tau = 0.4$.

leads to high amplitude LCO in the two Rijke tubes ($p_0'^{A,B} = 648$ Pa).

For $A_f = 0$, we notice that the change in τ leads to very low suppression in either of the oscillators ($\Delta\bar{p} < 0.5$). This is again a reflection of the fact that the region of AD is quite limited when identical oscillators are coupled. Our aim is to illustrate that external forcing can lead to significant quenching of LCO in the identical oscillators. When A_f is increased, we observe the amplitude of LCO decreasing in both the oscillators after a critical value of A_f. The effect of forcing is more pronounced in Rijke tube B as compared to that in Rijke tube A, which is evident from the larger “red" region in Fig. 6.9(b) compared to that in Fig. 6.9(a).

The results obtained from the model (Fig. 6.9) can be compared with the experimental results shown in Fig. 6.4. The ratio of forcing frequency to natural frequency is kept same for ease of comparison. Although the magnitude of amplitude suppression is not captured quantitatively by the model, the qualitative trends such as the extent of amplitude suppression in the two model oscillators along with the forced synchronisation characteristics are consistent between the experimental and numerical results. Compared to the pressure oscillations in Rijke tube B exhibiting complete suppression in the experimental study (for e.g., point (e) in Fig. 6.4a), we observe around 70% suppression in the amplitude of LCO in Rijke tube B.

Similar to experimental results, we also observe that the LCO in Rijke tube B remains desynchronised with the forcing signal through a large extent of the parameter plane. The region of quenching of LCO in Rijke tube A ($\Delta\bar{p} \sim 1$) nearly coincides with the onset of forced synchronisation ($PLV \sim 1$). The results shown in Fig. 6.9 are in qualitative agreement with the experimental results indicated in Fig. 6.4(a-d).

In Fig. 6.10, we depict the fractional change in the amplitude of LCO for each oscillator overlapped with the Arnold tongue on the $A_f - f_f$ plane, obtained from the numerical simulations for the case where identical oscillators are asymmetrically forced. The values of the coupling constants are fixed at $K_d = 1.0$, $K_\tau = 0.20$ and $\tau = 0.4$. The normalised natural frequency of both the oscillators is 0.5, and the normalised heater power are maintained at $K = 5.0$.

We see that the amplitude dynamics observed during the experiments, as depicted in Fig. 6.5, is well captured by the mathematical model in Fig. 6.10. From the results obtained from the mathematical model, we observe larger magnitude of suppression of LCO in Rijke tube B, as compared to that in Rijke tube A. Also, the high magnitude of suppression ($\Delta\bar{p} > 0.5$) in Rijke tube B nearly coincides with the boundary of Arnold tongue in Rijke tube A. The region of resonant synchronisation in Rijke tube B is smaller in size compared to that in Rijke tube A. The model does not adequately capture the phase dynamics as observed in the experiments. Although the Arnold tongue is similar for both the Rijke tubes, the PLV values observed prior to the forced synchronisation onset is lower in Rijke tube B than that in Rijke tube A. Also, the region of resonant amplification (shown in green) is skewed towards the left side of $f_f/f_0 = 1.00$ value.

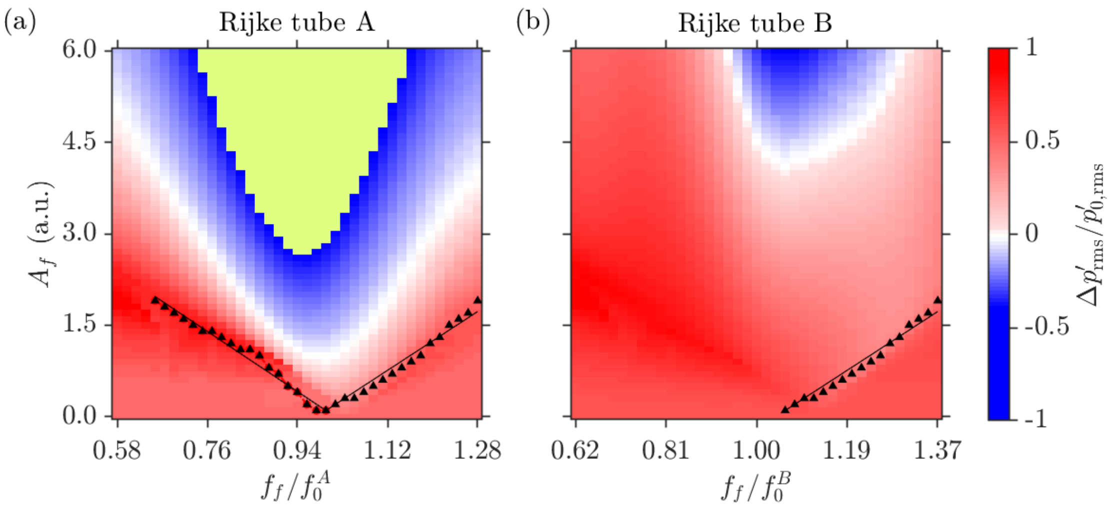

Figure 6.11: The amplitude response and overlapped Arnold tongue for non-identical, coupled Rijke tubes from the mathematical model. External forcing is applied to Rijke tube A. The synchronisation boundaries in are obtained through least-square-fit of points where $PLV = 0.98$. The coupling parameters are: $K_d = 1.0$, $K_\tau = 0.2$ and $\tau = 0.4$.

This is different from the experimental results (Fig. 6.5), where the region of resonant amplification was almost symmetrically located around the $f_f/f_0 = 1.00$ value.

Finally, we use our model to characterise the response of asymmetric forcing on the Arnold tongue and amplitude characteristics of coupled non-identical Rijke tubes (Fig.6.11). The coupling constants and non-dimensional heater power values are kept same as those used to get the results shown in Fig. 6.10, i.e., $K_d = 1.0$, $K_\tau = 0.2$, $\tau = 0.4$, and $K = 5$. This ensures the consistency of initial and boundary conditions, as was ensured in the experiments. In Section 6.4, to study the forced response of coupled non-identical Rijke tube oscillators, the natural frequencies of the LCO in Rijke tubes A and B were maintained at 150 Hz and 160 Hz, respectively, which equals a frequency ratio of $160/150 = 1.067$. Consistent with the experiments, the value of r is kept as 1.066 to analyze the reduced-order model given in Eqs. (6.7) and (6.8).

We observe that the effect of forcing is quite insignificant for forced synchronisation of LCO in Rijke tube B, consistent with the experimental results (Fig. 6.6). A significant suppression of the amplitude of LCO is observed at non-resonant conditions of forcing in Rijke tube A. The region of resonant amplification is absent for Rijke tube B, although we do observe amplification of the amplitude of LCO at higher values of A_f in Fig. 6.11(b). Some differences are present between the experimental (Fig. 6.6) and numerical results (Fig. 6.11). First, the forced synchronisation of Rijke tube B is observed for $f_f/f_0^B < 1$ values during experiments, whereas, the pressure oscillations in Rijke tube B model oscillator undergo forced synchronisation for $f_f/f_0^B > 1$ values. Second, the Arnold tongue is spread over a larger extent of parameter values for a coupled non-identical oscillators system as opposed to that in a coupled identical oscillator system (Fig. 6.11). During experiments, an opposite behavior was observed in Fig. 6.6(c), where the size of the Arnold tongue of Rijke tube A for a coupled non-identical system is less when compared to that in the coupled identical system (Fig. 6.5c). The qualitative differences between the results can be attributed to the various assumptions used while deriving the reduced-order model, such as absence of mean flow, zero temperature gradient, non-heat conducting gas, etc. A more detailed study is needed to examine the effects of such assumptions on the numerical results.

6.6 INTERIM SUMMARY

In this chapter, we investigated the amplitude & phase dynamics of coupled thermoacoustic oscillators under asymmetric forcing, and presented a model which satisfactorily captured the experimental results qualitatively. In particular, we discuss the viability of simultaneous coupling and forcing as a method for controlling TAI in a system of multiple combustors.

The forced response of limit cycle oscillations (LCO) in a single oscillator (Rijke tube) shows the presence of Arnold tongue along with the region of asynchronous quenching for the parametric range of $f_f < f_0$. The region of asynchronous quenching coincides with the boundary of forced synchronisation of the acoustic pressure fluctuations in the system (Mondal *et al.*, 2019). The presence of Arnold tongue and asynchronous quenching are consistent with the results observed in previous studies conducted on Rijke tubes (Mondal *et al.*, 2019) and laminar combustors (Guan *et al.*, 2019*a*; Roy *et al.*, 2020; Guan *et al.*, 2019*b*). We notice that the characteristics of forced synchronisation of LCO is dependent on the amplitude of LCO in the unforced state. In particular, the region of forced synchronisation (or Arnold tongue) of the oscillator gets narrower as the amplitude of LCO is increased. In addition, the coupled response of two Rijke tube oscillators (A and B) show the occurrence of two different states of oscillation quenching, i.e., amplitude death and partial amplitude death. These states occur only when a finite difference is present between the natural frequencies of the oscillators, and the length of the coupling tube lies within a specific range.

To expand the parametric range of oscillation quenching in two mutually coupled Rijke tube oscillators, we acoustically force Rijke tube A. We observe that the suppression of LCO in coupled identical Rijke tube oscillators is possible through the combined effect of mutual coupling and asynchronous quenching. A significantly larger value of forcing amplitude is required to synchronise and quench the large amplitude LCO in the coupled thermoacoustic oscillators. This behavior is depicted through the increase in the steepness of the boundaries of Arnold tongue as the amplitude of LCO is increased. Suppression of LCO is observed predominantly for $f_f < f_0$ in Rijke tube A, while it is observed on both sides of f_0 in Rijke tube B. We notice that external forcing widens the region of coupling and forcing parameters over which the oscillation quenching states are observed in both the oscillators than when only one of the two mechanisms of control are applied on its own. Most importantly, although Rijke tube A is forced, the suppression of LCO is more significant in Rijke tube B in comparison with that in Rijke tube A. We also studied the coupled behavior of two non-identical thermoacoustic oscillators under asymmetric forcing. We witness that because of direct influence of forcing, Rijke tube A exhibits the features of forced synchronisation, while Rijke tube B (not directly forced) remains desynchronised with the forcing signal. As a result, we observe a significant suppression of LCO in Rijke tube A and not in Rijke tube B, which is opposite to the behavior of forced response of coupled identical thermoacoustic oscillators. Finally, we qualitatively capture the experimental results through a reduced-order model of two coupled Rijke tubes. A good agreement is obtained between the experimental and numerical results.

Thus, periodic forcing aids the mitigation of TAI observed in coupled identical oscillators. We believe that the results on the asymmetrically forced prototypical coupled thermoacoustic oscillators would prove to be a benchmark specifically for the control of thermoacoustic oscillations observed in can combustors with multiple cans, and for coupled nonlinear oscillators subjected to external forcing in general nonlinear dynamics literature.

CHAPTER 7

CONCLUSION AND OUTLOOK

Thermoacoustic instability continues to be a significant impediment to the design of rockets and gas turbine engines. The periodic large amplitude acoustic pressure and heat release rate oscillations can cause substantial structural damage to the combustors, resulting in complete failure of the engines and, in worst cases, loss of lives. In the 1960s, NASA conducted around 2000 full-scale tests to understand the occurrence of thermoacoustic instability in F-1 rocket engines (Yang and Culick, 1990). Since then, our understanding of thermoacoustic instability has improved multi-fold, in addition to the enhanced computational facilities allowing researchers to incorporate the necessary changes required to mitigate thermoacoustic instability in the design stage itself. However, given the intricate dynamics that play an essential role in thermoacoustic instability arising due to a *complex* interaction between flame, flow, and the acoustic fields, a lot remains to be understood about the physics behind the phenomenon of thermoacoustic instability.

7.1 INTERPLAY BETWEEN HYDRODYNAMIC AND ACOUSTIC FIELDS

The present thesis focuses on understanding the interactions among different subsystems in a thermoacoustic system. In the first part of the thesis, we investigated the interplay between acoustic and hydrodynamic fields in a turbulent combustor. We identified regions of intense vortical interactions as vortical communities in the network space of weighted directed vortical networks constructed from two-dimensional velocity data. The network communities are obtained through an implementation of modularity maximisation technique implemented through the Louvain algorithm. Subsequently, we condensed the vortical interactions in the high-dimensional reactive flow into a low-dimensional network representation by leveraging inter-community strengths and weighted community centroids. We showed that the mean and maximum of all inter-community interactions exhibit a strong delayed correlation with the acoustic pressure oscillations during the state of thermoacoustic instability. The instances of maximum inter-community interactions match with the instances when a vortex is shed from the backwards-facing step of the combustor. Although this correspondence may seem trivial, our method considers the mutual proximity of all the vortical structures present in the reaction field of the combustor instead of simply looking at the single vortex present near the backwards-facing step. The spatiotemporal evolution of pairs of vortical communities with the maximum inter-community interactions provided insight into explaining the critical regions detected in the reaction field during the states of intermittency and thermoacoustic instability in previous studies. These critical regions are the optimal regions suited for open-loop control of thermoacoustic instability through targeted micro-jets of air. We further demonstrated that the high correlations between network measures and acoustic pressure oscillations during the state of thermoacoustic instability weakened when air microjets were introduced within the critical region to suppress the thermoacoustic oscillations.

The aforementioned subsystems of hydrodynamic and acoustic fields, along with the unsteady heat release rate from the flame, are present in the combustors of gas turbine engines. There are primarily three arrangements of combustors in gas turbine engines: can, annular, and can-annular. Can-annular combustors are predominantly used in land-based gas turbine engines for terrestrial power generation. In such a combustor arrangement, each can is a combustor, and the cans are arranged circumferentially. The adjacent cans can acoustically interact through the downstream transition gap between combustors and the first stage of the turbine or through the cross-fire tubes. Furthermore, a can combustor can also acoustically interact with itself through the downstream transition gap.

7.2 DELAYED ACOUSTIC SELF-FEEDBACK

Thus, in the second part of this thesis, we examined the implications of a thermoacoustic system interacting with itself through the concept of delayed acoustic self-feedback. Through experiments conducted in a bluff-body stabilised turbulent thermoacoustic system, we reported the occurrence of amplitude death (AD) by coupling the acoustic field of the combustor to itself through a single coupling tube attached near the anti-node position of the acoustic standing wave. Complete suppression (AD) of these oscillations was observed when the length of the coupling tube is nearly $3/8$ times the wavelength of the fundamental acoustic mode of the combustor. We showed that the dynamical behaviour of acoustic pressure changed from the state of limit cycle oscillations to low-amplitude chaotic oscillations via intermittency. We also studied the change in the nature of the coupling between the unsteady flame dynamics and the acoustic field as the length of the coupling tube is increased. We found that the temporal synchrony between these oscillations changed from the state of synchronised periodicity to desynchronised aperiodicity through intermittent synchronisation. Furthermore, we showed that applying delayed acoustic self-feedback with optimum feedback parameters completely disrupts the positive feedback loop between the flame, the flow, and the acoustic fields present in the combustor during thermoacoustic instability, thus mitigating instability.

Given the inherent challenges of conducting intricate experiments within a turbulent combustor environment, we directed our focus towards a horizontal laminar Rijke tube to further study delayed acoustic self-feedback in thermoacoustic systems. We examined the effect of both system and coupling parameters on the occurrence of amplitude death. We thereby showed that the parametric regions of amplitude death occur when the coupling tube length is close to an odd multiple of the length of the Rijke tube. Through experiments, we demonstrated that the optimal location to place the coupling tube for achieving amplitude death is near the antinode of the acoustic pressure standing wave in the Rijke tube. Furthermore, self-coupling mitigated thermoacoustic instability in a Rijke tube more effectively than the mutual coupling of two identical Rijke tubes.

7.3 ASYMMETRICALLY FORCED SYSTEM OF COUPLED THERMOACOUSTIC SYSTEMS

In the third and final part of the present thesis, we addressed the dynamical behaviour arising from two thermoacoustic systems interacting with each other. As mentioned, this scenario occurs when two adjacent combustors in a can-annular configuration gas turbine engine acoustically interact with each other via cross-fire tubes. With an emphasis on the mitigation of thermoacoustic instability in mutually coupled Rijke tubes, we studied the dynamics of two laminar horizontal Rijke tubes simultaneously subjected to mutual coupling and asymmetric external forcing through experiments and theoretical modelling. We investigated the forced response of identical and nonidentical Rijke tubes for two different amplitudes of thermoacoustic instability. Under mutual coupling alone, identical Rijke tubes displayed the occurrence of partial amplitude death and amplitude death.

In contrast, under forcing alone, asynchronous quenching of thermoacoustic instability was observed at nonresonant conditions. When the Rijke tubes were simultaneously subjected to mutual coupling and asymmetric forcing, we observed a larger parametric region of oscillation quenching than when the two mechanisms were utilised individually. This enhancement in the region of oscillation quenching is due to the complementary effect of amplitude death and asynchronous quenching. However, the forced response of coupled nonidentical Rijke tubes showed that the effect of forcing is insignificant in attaining synchronisation and quenching of oscillations in the Rijke tube that is not directly forced. Finally, we qualitatively captured the experimental results using a reduced-order theoretical model of two Rijke tubes coupled through dissipative and time-delay coupling and asymmetrically forced.

7.4 SUGGESTIONS FOR FUTURE WORK

This thesis aimed to understand the dynamics of interacting subsystems present in the reaction field of a turbulent thermoacoustic combustor and the implications of a thermoacoustic system acoustically interacting with itself and with an adjacent coupled themroacoustic system. This was achieved by performing a series of experimental campaigns on laminar and turbulent thermoacoustic systems and a computational investigation to understand the interactions between hydrodynamic and acoustic fields. As a follow-up to this research, the following points could be considered:

1. Acoustic characterisation can provide insights into the mitigation of thermoacoustic instability when combustors are coupled with specific lengths of the coupling tube. This can be done by employing a series of acoustic pressure transducers to measure the acoustic pressure fluctuations at different locations along the length of the coupling tube, and observing the acoustics when the coupling is switched on and off. The results from this study will have implications for understanding the occurrence of amplitude death in a diverse range of systems, such as electronic circuits (Ozden *et al.*, 2004), hair bundles present in auditory systems (Kim and Ahn, 2014), lasers (Wei and Lun, 2007), neuroscience (Cao and Liu, 2022), ecology (Eurich *et al.*, 2005), thermo-optical (Herrero *et al.*, 2000), aeroelastic (Raaj *et al.*, 2021; Raj *et al.*, 2021), and thermo-kinetic oscillators (Zeyer *et al.*, 2001). More specifically, it would be interesting to see a common thread connecting the phenomenon of AD in such diverse systems.

2. All the experiments in this thesis were performed under sea-level pressure conditions. This is reasonable since the focus was on interactions of different thermoacoustic systems in land-based gas turbine engines. However, aviation gas turbine engines work in conditions where the ambient pressure is significantly less than the sea-level pressure level. Investigating the interactions among the flame, flow, and the hydrodynamic subsystems in a turbulent combustor working in low pressure ambient conditions would be useful. The challenge lies in the fabrication of a suitable testing facility.

3. In continuation to the above point, the air flowing into the combustors is at a higher temperature than the ambient conditions in actual gas turbines. This preheating occurs due to an increase in pressure as the air passes through the compressor. A change in the pressure and temperature of the air changes the acoustic properties of the air. This will, in turn, change the amplitude death characteristics. It would be useful to study the implications of such changes toward amplitude death of thermoacoustic instability in coupled combustors.

APPENDIX A

VORTICAL COMMUNITIES

A.1 VORTICITY THRESHOLDING

We use vorticity thresholding to include only those fluid elements in vortical communities that have sufficiently high magnitude of vorticity. Here, we assess the effect of vorticity thresholding on the vortical communities detected through the Louvain algorithm (Newman, 2004). For each time instant, we calculate the range of vorticity values $\omega \in [\omega_-, \omega_+]$ that contribute to a lower range of 10% to 90% (in intervals of 10%) of the total circulation Γ present in the reaction field at that time instant (for instance, $\Gamma_{th} = 10\% = 0.1 \times \Gamma$). Finally, we take the average of all the vorticity thresholds calculated for each value of circulation threshold, i.e., $\overline{\omega}_- = \frac{1}{N}\sum \omega_-$ and, $\overline{\omega}_+ = \frac{1}{N}\sum \omega_+$, and plot it in Fig. A.1(a). Here, $N = 3796$ is the total number of snapshots of temporal vorticity fields available for each dynamical state.

The fluid elements with vorticity outside the aforementioned interval, i.e., the fluid elements with $\omega \notin [\omega_-, \omega_+]$, are subsequently used to calculate the vortical communities at each time step. The area occupied by all the vortical communities for a circulation threshold Γ_{th} is denoted by A_{th}. The average of A_{th} calculated at all the time instants, i.e., $\overline{A}_{th} = \frac{1}{N}\sum A_{th}$, is plotted in Fig. A.1(b) as a fraction of the total area of the spatial domain. The number of vortical communities is denoted by n(Ci). The average of n(Ci) calculated at all the time instants, i.e., $\overline{\mathrm{n(Ci)}} = \frac{1}{N}\sum \mathrm{n(Ci)}$, is plotted in Fig. A.1(c).

The vorticity values corresponding to lower range of 20% of the total circulation are used for vorticity thresholding in the current study. The threshold values are highlighted with green background in figure A.1(a), and are equal to $|\omega| = 456\ s^{-1}$, $380\ s^{-1}$, $843\ s^{-1}$, and $532\ s^{-1}$ during the states of combustion noise, intermittency, thermoacoustic instability, and microjet injection, respectively. The robustness of the thresholds is evaluated by noting that the qualitative results do not change significantly even if the threshold values are modified in ±50 s^{-1} range around the values considered in the current study. Approximately 40% of the area of the reaction field considered in the current study are occupied by the detected vortical communities during all the dynamical states.

A.2 THE LOUVAIN ALGORITHM AND ITS NON-DETERMINISTIC NATURE

Community detection algorithms are widely employed to bring out the underlying mesoscopic structure, thereby revealing the clustered nature of complex networks. While there is no formal definition for the concept of communities, the idea is to group nodes into distinct, densely connected parts, with the density between parts being low. Researchers continue to develop scalable methods to reveal densely connected groups due to the constant rise in data and dimensions. Due to the efficiency of their implementation, algorithms that maximise modularity have garnered considerable attention. Newman (2004) created modularity as a quality function to assess the quality of a partition as a community structure. It compares the existence of an edge within a community to the probability of having such an edge between corresponding vertices in a random network with the same degree distribution. While it is known that modularity has some limitations (Fortunato and Barthelemy, 2007; Lancichinetti and Fortunato, 2011), heuristic-based algorithms that maximise this measure remain the most effective on large networks to this day (Blondel *et al.*, 2008; Leicht and Newman, 2008). Louvain algorithm is one of the most popular algorithms used to maximise modularity (Blondel *et al.*, 2008).

The Louvain algorithm begins by creating communities of size one, where each node in the network forms a community. The algorithm then proceeds by executing two stages. The algorithm assigns a node i to a community of a neighbour j to increase the partition's modularity in the first stage. The first stage is repeated until the modularity cannot be

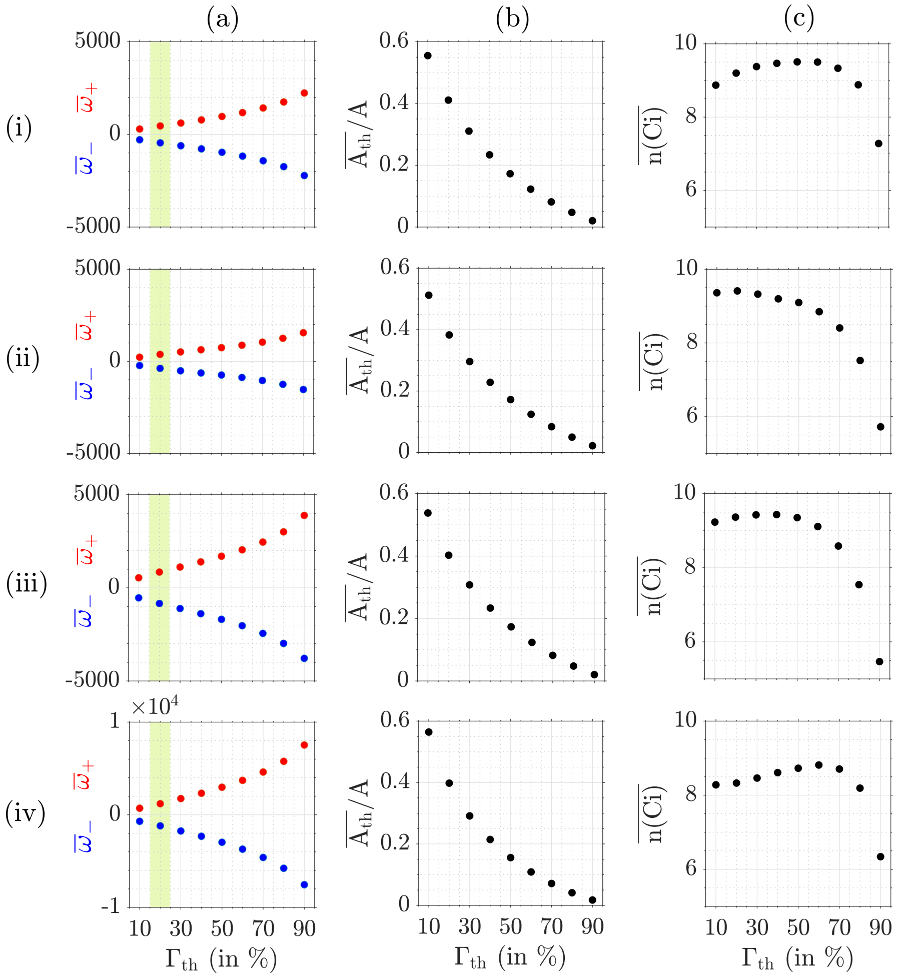

Figure A.1: (a) Variation of mean positive ($\overline{\omega}_+$) and mean negative ($\overline{\omega}_-$) vorticity threshold values with respect to the total circulation threshold (Γ_{th} in %) for the states of (i) combustion noise, (ii) intermittency, (iii) thermoacoustic instability, and (iv) suppression through air microjet injection. The fluid elements with vorticity $\omega \in [\overline{\omega}_-, \overline{\omega}_+]$ are disregarded to exclude the bottom Γ_{th} % of the total circulation present in the reaction field, thus capturing the influential regions of the flow. The $\overline{\omega}_+$ and $\overline{\omega}_-$ values present on the green band are subsequently used as thresholds while using the Louvain algorithm to detect vortical communities. (b) Variation of the mean of area percentage of the reaction field $\overline{A}_{\rm th}$ occupied by the vortical communities. We do not consider the area of the bluff-body mask while calculating the percentage w.r.t. the total area of the reaction field. (c) Variation of the average number of communities detected for each circulation threshold value. For all the cases, the resolution parameter γ used in the Louvain algorithm is kept consistent at 1 (Gopalakrishnan Meena *et al.*, 2018; Gopalakrishnan Meena and Taira, 2021).

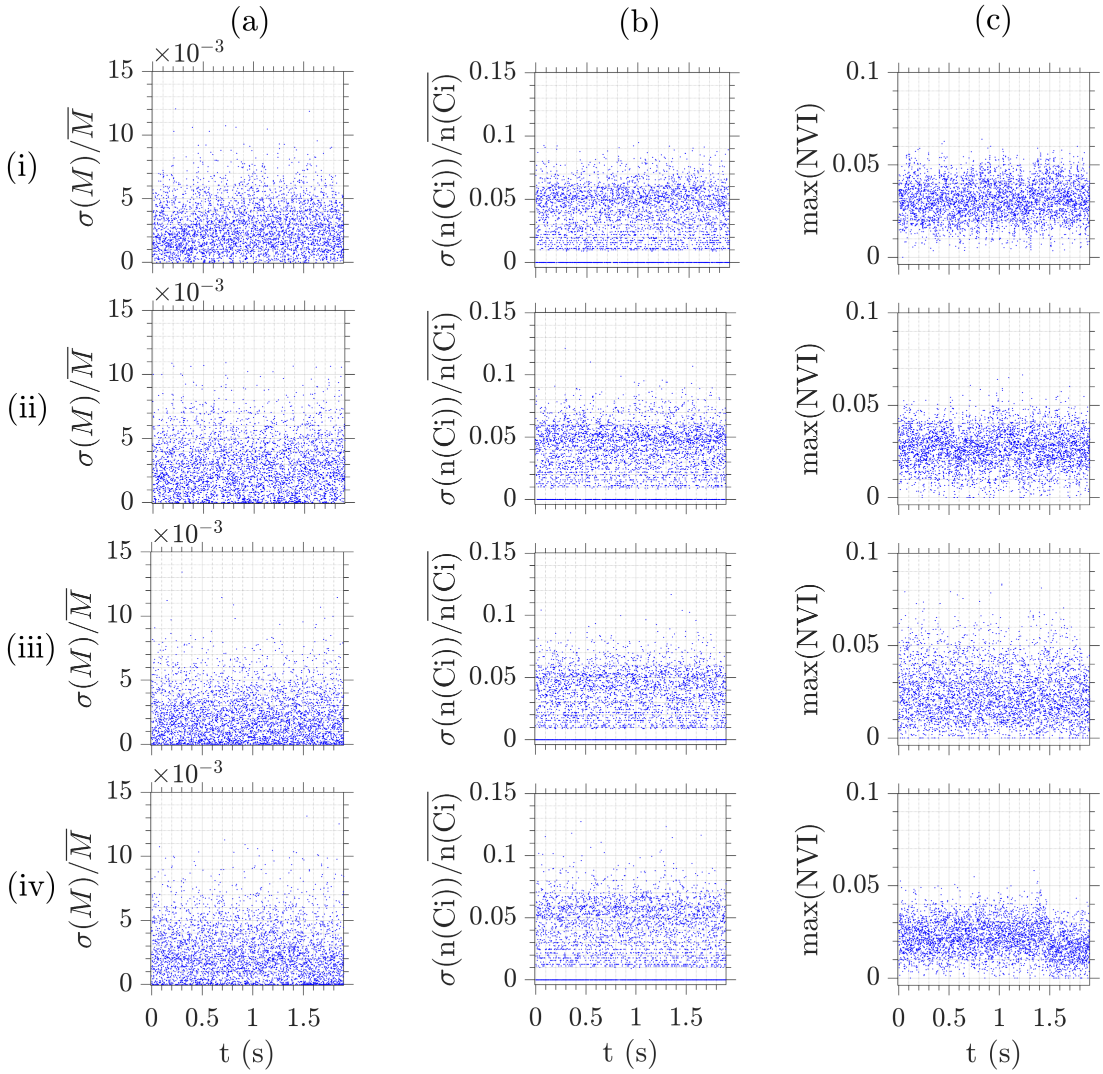

Figure A.2: (a) Plot of the standard deviation of modularity values, (b) coefficient of variation of the number of communities, and (c) maximum normalised variation of information calculated through 100 implementations of the Louvain algorithm at each time instant during the states of (i) combustion noise, (ii) intermittency, (iii) thermoacoustic instability, and (iv) suppression of thermoacoustic instability through air microjet injection.

increased. This procedure generates an initial network partition. In the second stage of the Louvain algorithm, each partition's community is considered a supernode. If at least one edge exists between nodes of each community that the supernode represents, then the supernodes are connected. After this second stage is completed, the algorithm iterates until the modularity can no longer increase.

The Louvain algorithm is non-deterministic due to the changes in the following two steps between different runs: (1) the order in which all the nodes are processed, and (2) the order in which two pairs of nodes are assigned to two different communities if the increase in modularity is equal for both the assignments (Cordeiro *et al.*, 2016). Thus, the community affiliations may vary between different implementations of the Louvain algorithm even when the exact same data set is used.

To evaluate the extent of consistency between community structures obtained from different implementations of the Louvain algorithm on the same vortical network, we implement the Louvain algorithm 100 times at each time instant and calculate the following quantities for all the vortical networks corresponding to all the time instants:

1. Coefficient of variation of modularity, $\sigma(M)/\overline{M}$, obtained from hundred different community affiliations at each time instant. The coefficient of variation is the ratio of the standard deviation to the mean of the modularity values obtained from different runs of the Louvain algorithm and shows the extent of variability with respect to the mean of the modularity values (Castagliola *et al.*, 2013). The higher the coefficient of variation is, the greater is the difference between the modularity values obtained between different implementations of the Louvain algorithm on the same vortical network.

2. Coefficient of variation of the number of communities obtained from 100 different community affiliations at each time instant.

3. Maximum of normalized variation of information (NVI) to indicate the maximum deviation between any two community affiliations out of 100 different implementations of the Louvain algorithm for each time instant (Meilă, 2007; Karrer *et al.*, 2008). NVI between two community affiliations X and Y is given by

$$NVI(X,Y) = -\sum_{ij} r_{ij} \left[\log\left(\frac{r_{ij}}{p_i}\right) + \log\left(\frac{r_{ij}}{q_j}\right) \right], \tag{A.1}$$

where,

$$p_i = |X_i|/n, q_j = |Y_j|/n, r_{ij} = |X_i \cap Y_j|/n, n = \sum_i |X_i| = \sum_j |Y_j|.$$

An NVI equal to one indicates the maximum difference between two clustering of the same complex network, which occurs when each node is assigned to its own community in one clustering, and the entire network is assigned to one single community in the other clustering.

In Fig. A.2, we observe that the three aforementioned quantities calculated are quite low for all four dynamical states, indicating that different implementations of the Louvain algorithm give us statistically similar community affiliations for a dataset.

A.3 SPATIAL COHERENCE OF VORTICAL COMMUNITIES

We observe that the communities detected during the state of combustion noise are highly fragmented in comparison to the communities detected during the other two dynamical states of intermittency and thermoacoustic instability. The highly fragmented communities present during the state of combustion noise are associated with the chaotic spatiotemporal dynamics observed in the reaction field. Furthermore, most of the pairs of communities with the maximum inter-community interactions are present on the top of the bluff-body and their spatial locations match with the coherent structures shed from the tip of the bluff-body. On the other hand, most of the highly interacting communities observed during the states of intermittency and thermoacoustic instability are match with the locations of coherent structures shed from the backward-facing step.

To quantify the extent of fragmentation of vortical communities during the three dynamical states, we adopt a measure used by Jadhav *et al.* (2022) that measures the size of the

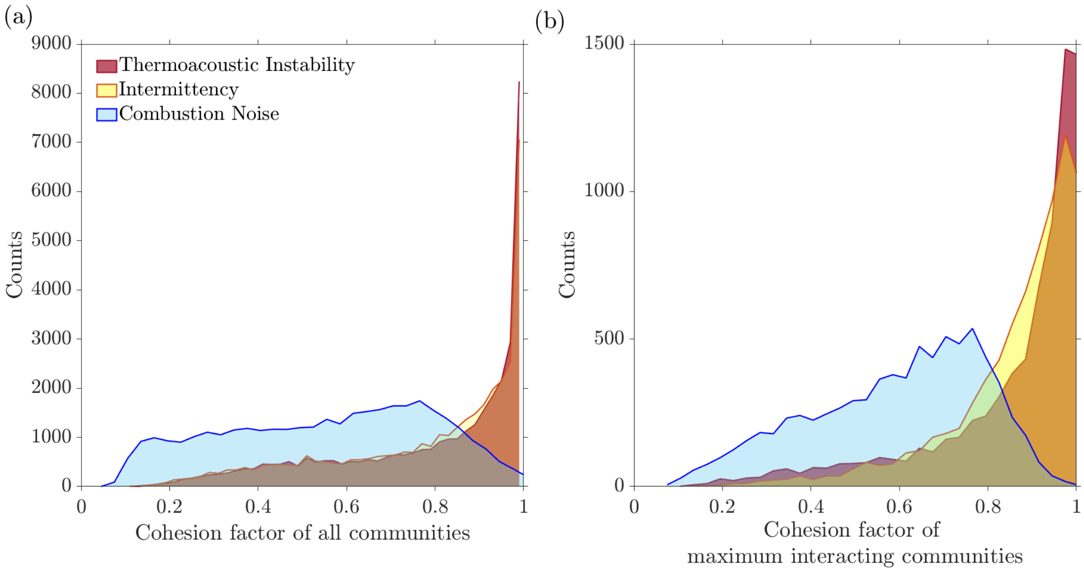

Figure A.3: Distributions of cohesion factor indicating the spatial coherence of (a) all vortical communities, and (b) vortical communities with maximum inter-community interactions during the three dynamical states.

largest 4-connected cluster in any detected community normalised by the total size of the community. This measure is named as cohesion factor. A cohesion factor equal to one implies that the communities are 4-connected everywhere, with no fragmentation at all. A cohesion factor of zero indicates an absence of any connected component.

In Fig. A.3, we plot the distributions of the cohesion factors of all the vortical communities and of the maximum interacting vortical communities during the three dynamical states. We notice that the cohesion factors of the communities during the state of combustion noise are comparatively low compared to the cohesion factors observed during the other dynamical states of intermittency and thermoacoustic instability. The highly fragmented nature of vortical communities detected during the state of combustion noise can be attributed to the presence of very few small vortices with high interaction strengths scattered throughout the spatial domain. Moreover, the fragmented nature of maximum interacting vortical communities is due to the small coherent structures primarily shed from the tip of the bluff-body during the state of combustion noise.

During the states of intermittency and thermoacoustic instability, most of the coherent structures are shed from the backward-facing step. Since these coherent structures are highly organised in the spatial domain, the vortical communities detected during these states are comparatively less fragmented that those present during the state of combustion noise. Thus, the cohesion factors of the vortical communities present during the states of intermittency and thermoacoustic instability are quite high and very close to 1.

APPENDIX B

KERNEL DENSITY ESTIMATION

Let's say we have some data with only one or two factors. How do we begin to look into them? One of the first things that people do is usually draw their histogram to see how they are spread out. One good thing about histograms is that they make it easy to see how the probabilities in our data are spread out quickly. But they are discrete, and it can be helpful to have a rough idea of the probability density function that they are based on.

There are two ways to obtain a smooth probability density function from the given discrete data:

1. Parametric probability density estimation - We choose a prototypical distribution, such as a normal distribution, and use the sample data to determine its parameters, such as its mean and standard deviation.

2. Nonparametric probability density estimation - We do not make any distributional assumptions. Instead, we utilise the available data to make inferences about the population. Kernel density estimation belongs to this category.

Kernel density estimation (KDE), sometimes referred to as Parzen's window (Parzen, 1962), is a widely recognised method for estimating the underlying probability density function of a given dataset. KDE is a statistical method for estimating the density of a random variable. Unlike parametric density estimators, KDE does not make any assumptions about the underlying density function belonging to a specific parametric family. The non-parametric aspect of KDE grants it a high degree of flexibility, rendering it a widely favoured method for analysing data that originates from complicated distributions.

Let $X_1, \cdots, X_n \in \mathbb{R}^d$ be an i.i.d. random sample from an unknown distribution P with a density function p. The kernel density estimator is the given by

$$\hat{p}_n(x, h) = \frac{1}{nh^d} \sum_{i=1}^{n} K\left(\frac{x - X_i}{h}\right), \tag{B.1}$$

where $K : \mathbb{R}^d \to \mathbb{R}$ is a smooth function called the kernel function. $h > 0$ controls the amount of smoothing, and is thus called the smoothing factor or the scaling factor. h controls how wide the probability mass is spread around a point, and the smoothness or roughness of a density estimate.

The kernel estimate $\hat{p}_n(x)$ is calculated by first centring a scaled kernel at X_i and then calculating the mean of the kernel ordinates at x. The estimate is positively correlated with the number of samples falling within a certain bandwidth, since regions with a greater number of observations yield higher estimates compared to regions with less observations. This method bears resemblance to the histogram method, as it involves the accumulation of kernel ordinates across the width of a window, rather than just tallying the number of observations within a bin.

Intuitively, KDE turns each data point into a smooth bump, and the kernel function $K(x)$ decides what shape the bump should have. Then, KDE adds up all of these bumps to get an estimate of the density. KDE will give a large value in places where there are a lot of data points because there will be a lot of bumps. But in places where there are less number of data points, the density value that comes from adding up the bumps is low, since only a few of them contribute to the density estimate.

The kernel function usually has three features:

$$K(x) \text{is symmteric} \tag{B.2}$$

$$\int K(x) = 1 \tag{B.3}$$

$$\lim_{x \to -\infty} K(x) = \lim_{x \to \infty} K(x) = 0 \tag{B.4}$$

Gaussian density is one common choice for kernel function:

$$K(x) = \frac{1}{\sqrt{2\pi\sigma^2}} \exp\left(\frac{-x^2}{2\sigma^2}\right) \tag{B.5}$$

B.1 UNIVARIATE KERNEL DENSITY ESTIMATION

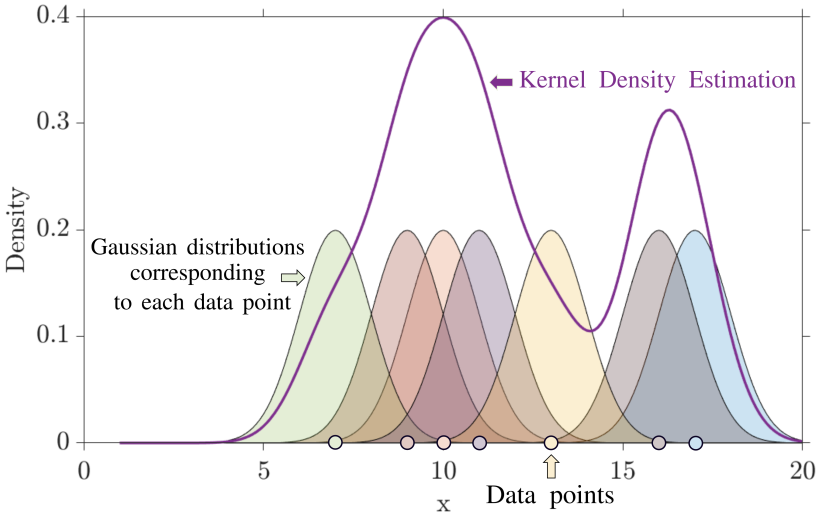

Figure B.1: Estimated kernel density for seven random data points selected from a normal distribution. The Gaussian kernels around each of the data points are shown with different colours.

Figure B.1 shows the kernel density estimate for seven data points. The data points are taken from range [120]. The kernel weight for each data point is calculated using $K(X_i - x)$. The kernel weights for different data points are plotted with different colours. The kernel density estimate (bold purple line) is the mean of the X_i ordinates at each x.

B.2 BIVARIATE KERNEL DENSITY ESTIMATION

The kernel density estimate for bivariate data is defined in a similar manner:

$$\hat{p}_n(\mathbf{x}, \mathbf{H}) = \frac{1}{N} \sum_{i=1}^{N} K_{\mathbf{H}}(\mathbf{x} - \mathbf{X_i}) \tag{B.6}$$

Since we are considering a two-dimensional dataset now, **x** are tuples of $(x, y$, and the

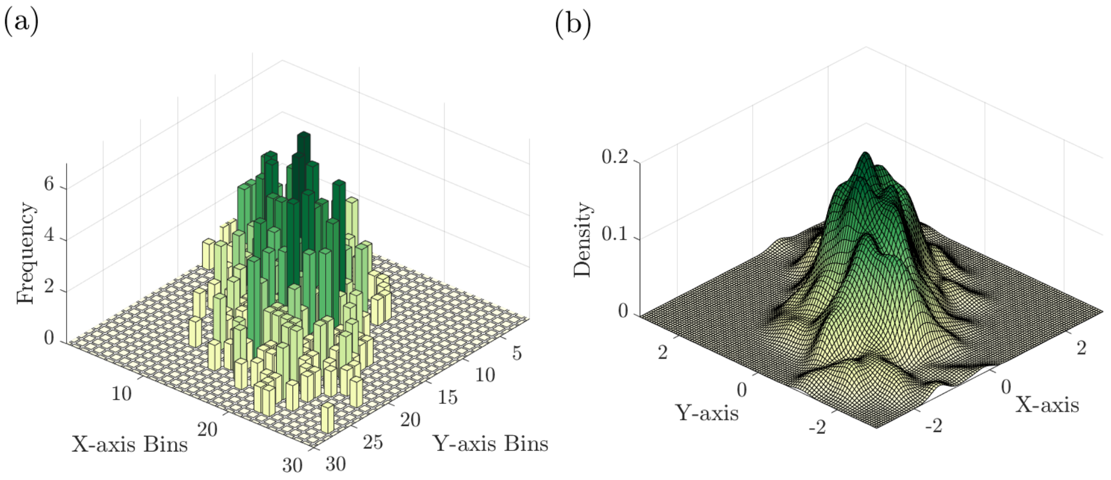

Figure B.2: (a) Two-dimensional histograms for fifty data points randomly selected from a bivariate normal distribution, and (b) the corresponding estimated kernel density distribution.

scaling factor $\mathbf{H}$ is a symmetric and positive definite matrix. The scaled version of the kernel is given by $K_{\mathbf{H}}(\mathbf{x}) = \det(\mathbf{H})^{-0.5} K(\mathbf{H}^{-0.5}\mathbf{x})$, where $\det(\mathbf{H})$ is the determinant of $\mathbf{H}$, and $K(\mathbf{x}) = \dfrac{1}{2\pi}\exp\left(-\dfrac{1}{2}\mathbf{x}^{\top}\mathbf{x}\right)$.

Figure B.2 shows the kernel density estimate for 500 data points plotted on a two-dimensional $x - y$ plane. The data points are taken from a bivariate normal distribution with mean $[0 \quad 0]$ and correlation coefficient $\rho = 0.6$.

APPENDIX C

MEASUREMENT OF ACOUSTIC DECAY RATE

To ensure repeatability of the experiments, we measure the acoustic damping of the thermoacoustic system and ensure that the experiments are conducted only when the damping is within a narrow range. The acoustic damping of the thermoacoustic system is represented by the decay rate. The following decay rates were maintained while conducting experiments:

1. Self-delayed acoustic feedback in turbulent combustor: 11 ± 1.5 s^{-1}
2. Self-delayed acoustic feedback in Rijke tube: 15.8 ± 2 s^{-1}
3. Asymmetrically forced system of coupled Rijke tubes - Rijke tube A: 16.5 ± 2 s^{-1}, Rijke tube B: 12.9 ± 1.8 s^{-1}

All the experimental setups mentioned above utilise compressed air stored in an external tank. A change in the ambient conditions, say due to heavy rainfall, might cause changes in the humidity and temperature of the air flow used in the experiments. This in turn affects the acoustic damping properties of the thermoacoustic system. The aforementioned ranges of decay rate were heuristically selected based on the ambient and experimental conditions.

We measure the decay rates by externally perturbing the thermoacoustic system at its natural frequency, and calculating the rate at which the acoustic pressure oscillations inside the system decay when the perturbation is switched off (Perry, 1970; Culick and Kuentzmann, 2006). We perturb the turbulent combustor and the Rijke tubes at 164 Hz and 160 Hz, respectively, under no-flow conditions. We use acoustic drivers (Minsound TD-200A), connected in parallel to a power amplifier (Ahuja UBA-500M), for the external acoustic forcing. The sinusoidal forcing signal used for external forcing is generated using a Tektronix function generator (Model No. AFG1022).

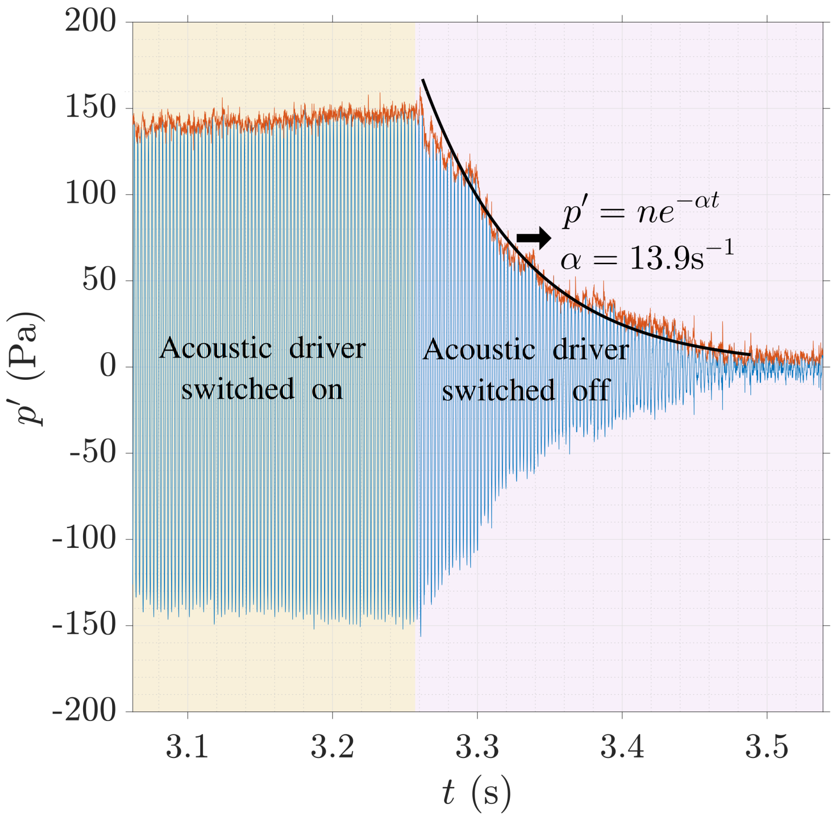

Figure C.1: Acoustic pressure oscillations before and after the acoustic driver is switched off abruptly under no-flow conditions. The brown line denotes the upper envelope of the decaying acoustic pressure oscillations, and is used to calculate the decay rate. The exponential curve fitted to the decaying portion is shown in black.

We abruptly switch off the acoustic drivers after the sinusoidal pressure perturbation is generated, and acquire the evolution of the acoustic pressure oscillations. Subsequently, we extract the envelope of the decaying acoustic pressure oscillations using Hilbert Transform. Finally, we fit a straight line to the semi-logarithmic plot of the envelope. The slope of the semi-logarithmic plot is the decay rate of the thermoacoustic system.

APPENDIX D

MATHEMATICAL MODEL OF COUPLED NON-IDENTICAL RIJKE TUBES WITH ASYMMETRIC EXTERNAL ACOUSTIC FORCING

Here, we derive a reduced-order model for the coupled horizontal Rijke tubes subjected to asymmetric forcing. The model is based on (Balasubramanian and Sujith, 2008). We neglect the effects of mean flow and mean temperature gradient in the duct. For two Rijke tubes A & B, the acoustic momentum and energy equations for a medium with a perfect, inviscid and non-heat conducting gas are then given as (Balasubramanian and Sujith, 2008):

$$\bar{\rho}\frac{\partial \tilde{u_a}'}{\partial \tilde{t}} + \frac{\partial \tilde{p_a}'}{\partial \tilde{x}} = 0, \tag{D.1}$$

$$\frac{\partial \tilde{p_a}'}{\partial \tilde{t}} + \gamma\bar{p}\frac{\partial \tilde{u_a}'}{\partial \tilde{x}} = (\gamma - 1)\dot{\tilde{Q}}'\delta(\tilde{x} - \tilde{x_f}), \tag{D.2}$$

$$\bar{\rho}\frac{\partial \tilde{u_b}'}{\partial \tilde{t}} + \frac{\partial \tilde{p_b}'}{\partial \tilde{x}} = 0, \tag{D.3}$$

$$\frac{\partial \tilde{p_b}'}{\partial \tilde{t}} + \gamma\bar{p}\frac{\partial \tilde{u_b}'}{\partial \tilde{x}} = (\gamma - 1)\dot{\tilde{Q}}'\delta(\tilde{x} - \tilde{x_f}). \tag{D.4}$$

where, $\tilde{p}'$ and $\tilde{u}'$ are the acoustic pressure and velocity fluctuations, respectively. γ is the ratio of specific heats of air at ambient conditions. $\tilde{x}$ is the distance along the axial direction in the duct, $\tilde{t}$ is the time, $\bar{\rho}$ and $\bar{p}$ are the ambient density and pressure, respectively. Subscripts a and b indicate the quantities corresponding to Rijke tube A & B, respectively. For a general system of non-identical oscillators, we define a quantity r

as:

$$r = \frac{L_b}{L_a} = \frac{\omega_b}{\omega_a}, \tag{D.5}$$

where, L_a and L_b are lengths of the Rijke tube ducts A & B, respectively. ω_a and ω_b are the natural frequencies of the Rijke tubes A and B, respectively.

We non-dimensionalise Eqs. (D.1) and (D.4) using the following transformations:

$$x = \frac{\tilde{x}}{L_a};\ \ t = \frac{c_0}{L_a}\tilde{t};\ \ u'_a = \frac{\tilde{u_a}'}{u_0};\ \ p'_a = \frac{\tilde{p_a}'}{\bar{p}};\ \ M = \frac{u_0}{c_0};\ \ u'_b = \frac{\tilde{u_b}'}{u_0};\ \ p'_b = \frac{\tilde{p_b}'}{\bar{p}};\ \ \dot{Q}' = \frac{\dot{\tilde{Q}}'}{c_0\bar{p}}. \tag{D.6}$$

Here, variables with tilde are dimensional and variables without tilde are non-dimensional. u_0 and $\bar{p}$ are the steady state velocity and pressure of the flow, respectively. c_0 is the speed of sound, and M is the Mach number of the mean flow. x and t are the non-dimensional axial distance and time, respectively. Using the above transformations, we obtain the following non-dimensionlised acoustic momentum and energy equations:

$$\gamma M \frac{\partial u'_a}{\partial t} + \frac{\partial p'_a}{\partial x} = 0, \tag{D.7}$$

$$\frac{\partial p'_a}{\partial t} + \gamma M \frac{\partial u'_a}{\partial x} = \frac{(\gamma - 1) L_a \dot{Q}'}{\bar{p} c_0} \delta[L_a(x - x_f)], \tag{D.8}$$

$$\gamma M \frac{\partial u'_b}{\partial t} + \frac{\partial p'_b}{\partial x} = 0, \tag{D.9}$$

$$\frac{\partial p'_b}{\partial t} + \gamma M \frac{\partial u'_b}{\partial x} = \frac{(\gamma - 1) L_a \dot{Q}'}{\bar{p} c_0} \delta[L_a(x - x_f)]. \tag{D.10}$$

The heat release rate $\dot{Q}'$ is modelled using a modified form of King's law (King and Barnes, 1914; Heckl, 1990) which correlates the quasi-steady heat transfer from a heated cylinder to the flow around it. The expression for normalised heat release rate fluctuations is written in terms of the acoustic velocity fluctuations, observed at the heater location

x_f after time delay τ_{h} as:

$$\dot{Q}' = \frac{2L_w(T_w - \bar{T})}{S\sqrt{3}}\sqrt{\pi\lambda C_v\bar{\rho}\frac{d_w}{2}}\left[\sqrt{\left|\frac{u_0}{3} + u'_f(t-\tau_{\mathrm{h}})\right|} - \sqrt{\frac{u_0}{3}}\right], \tag{D.11}$$

where, d_w, L_w and T_w are the diameter, length and temperature of the heater wire, respectively. $\bar{T}$ is the steady state temperature of the flow, S is the cross-sectional area of the duct, C_v & λ are the specific heat at constant volume and thermal conductivity, respectively, of the medium within the duct. τ_{h} quantifies the thermal inertia of the heat transfer from the heating element to the medium.

The non-dimensionalised set of PDEs in Eqs. (D.7)-(D.10) is reduced to a set of ordinary differential equations using the Galerkin technique (Lores and Zinn, 1973). To that end, the non-dimensional velocity u' and non-dimensional pressure p' fluctuations in the model are written in terms of the Galerkin modes:

$$p'_a(x,t) = \sum_{j=1}^{N} -\frac{\gamma M}{j\pi}\dot{\eta}_j^a(t)\sin(j\pi x), \tag{D.12}$$

$$u'_a(x,t) = \sum_{j=1}^{N} \eta_j^a(t)\cos(j\pi x), \tag{D.13}$$

$$p'_b(x,t) = \sum_{j=1}^{N} -\frac{\gamma M r}{j\pi}\dot{\eta}_j^b(t)\sin\left(\frac{j\pi x}{r}\right), \tag{D.14}$$

$$u'_b(x,t) = \sum_{j=1}^{N} \eta_j^b(t)\cos\left(\frac{j\pi x}{r}\right), \tag{D.15}$$

Here, η_j and $\dot{\eta}_j$ represent the time-varying coefficients of the jth mode of the acoustic velocity u' and acoustic pressure p', respectively. a and b correspond to the acoustic variables in Rijke tubes A and B, respectively. We can verify that the particular form of Galerkin modes satisfies the acoustically open-open boundary conditions:

$p'_a(x=0,t)=0$, $p'_a(x=1,t)=0$, $p'_b(x=0,t)=0$ and $p'_b(x=r,t)=0$. N represents the number of Galerkin modes considered. Substituting Eqs. (D.12)-(D.15) in Eqs. (D.7)-(D.10) with a damping term included (Matveev, 2003), and projecting the resultant equations along the basis functions, we obtain the following set of first-order ordinary differential equations:

$$\frac{d\eta_j^a}{dt} = \dot{\eta}_j^a, \tag{D.16}$$

$$\frac{d\dot{\eta}_j^a}{dt} + 2\xi_j\omega_j\dot{\eta}_j^a + k_j^2\eta_j^a = -2j\pi K\left[\sqrt{\left|\frac{1}{3} + u_f'^a(t-\tau_\mathrm{h})\right|} - \sqrt{\frac{1}{3}}\right]\sin(j\pi x_f), \tag{D.17}$$

$$\frac{d\eta_j^b}{dt} = \dot{\eta}_j^b, \tag{D.18}$$

$$\frac{d\dot{\eta}_j^b}{dt} + 2\xi_j\left(\frac{\omega_j}{r}\right)\dot{\eta}_j^b + \left(\frac{k_j}{r}\right)^2\eta_j^b = -\frac{2j\pi K}{r^2}\left[\sqrt{\left|\frac{1}{3} + u_f'^b(t-\tau_\mathrm{h})\right|} - \sqrt{\frac{1}{3}}\right]\sin\left(\frac{j\pi x_f}{r}\right), \tag{D.19}$$

where, $k_j = j\pi$ refers to the non-dimensional wave number and $\omega_j = j\pi$ refers to the non-dimensional angular frequency of the jth mode. The coefficient ξ_j appearing in the second term of Eqs. (D.17) & (D.19) represents the frequency-dependent damping (Matveev, 2003), and is given by the following ansatz (Sterling and Zukoski, 1991):

$$\xi_j = \frac{c_1\dfrac{\omega_j}{\omega_1} + c_2\sqrt{\dfrac{\omega_1}{\omega_j}}}{2\pi} \tag{D.20}$$

Here, c_1 and c_2 are the damping coefficients which determine the amount of damping. We choose the values $c_1 = 0.1$ and $c_2 = 0.06$ based on (Sterling and Zukoski, 1991) for all simulations.

To formulate a model for the coupled system, we assume that the two Rijke tubes are coupled through time-delay and dissipative couplings. Based on Eqs. (D.16)-(D.19), the governing equations for non-identical, coupled Rijke tubes with asymmetric sinusoidal forcing can be written as:

$$\frac{d\eta_j^{a,b}}{dt} = \dot{\eta}_j^{a,b}, \tag{D.21}$$

$$\frac{d\dot{\eta}_j^{a,b}}{dt} + 2\xi_j \left(\frac{\omega_j}{r^{a,b}}\right) \dot{\eta}_j^{a,b} + \left(\frac{k_j}{r^{a,b}}\right)^2 \eta_j^{a,b} = -\frac{2j\pi K}{r^{a,b^2}} \left[\sqrt{\left|\frac{1}{3} + u_f'^{a,b}(t-\tau_{\mathrm{h}})\right|} - \sqrt{\frac{1}{3}}\right] \times$$
$$\sin\left(\frac{j\pi x_f}{r^{a,b}}\right) + \underbrace{K_d(\dot{\eta}_j{}^b - \dot{\eta}_j{}^a)}_{\text{Dissipative coupling}} + \underbrace{K_\tau(\dot{\eta}_j{}^b(t-\tau) - \dot{\eta}_j{}^a(t))}_{\text{Time-delay coupling}} + \underbrace{[A_f \sin(2\pi f_f t)]^a}_{\text{Forcing term}}, \tag{D.22}$$

where, $r^{a,b}$ is defined as the ratio of the length of the duct to a reference length, $L_{a,b}/L_{ref}$. We consider L_a to be the reference length. For identical oscillators, $r^a = r^b = 1$. For non-identical oscillators, $r^a = 1$ and $r^b = L_b/L_a = \omega_a/\omega_b$.

The second and third terms on the right-hand side of Eq. (D.14) are the dissipative and time-delay coupling terms, respectively. Dissipative coupling encapsulates the interaction that arises from the mass transfer between the two ducts (Bar-Eli, 1985). Time-delay coupling quantifies the time taken by acoustic waves to propagate through the coupling tube connecting the two Rijke tubes. Thus, τ denotes the time-delay in the response induced by one Rijke tube on the other. The fourth term is the sinusoidal forcing term with amplitude A_f and frequency f_f. The external forcing is applied only to Rijke tube A.

APPENDIX E

EXTERNAL FORCING AND MUTUAL COUPLING

E.1 R^2 VALUES FOR SYNCHRONISATION BOUNDARIES

Table E.1: R^2 values of least-square-fitted boundaries of the Arnold tongue. The subscripts l, r denote the left and right boundaries, respectively.

		Rijke tube A		Rijke tube B	
Figures	p'_0	R_l^2	R_r^2	R_l^2	R_r^2
Fig. 5.1	120 Pa	0.98	0.96	-	-
	200 Pa	0.96	0.85	-	-
Fig. 5.5	120 Pa	0.99	0.88	0.96	1.00
	200 Pa	0.95	0.89	0.94	0.81
Fig. 5.6	120 Pa	0.98	0.93	0.94	-
	200 Pa	0.97	0.99	-	-
Fig. 5.7		0.98	0.98	-	-
Fig. 5.10		0.91	0.98	0.98	0.99
Fig. 5.11		0.98	0.98	-	0.98

Table E.1 shows the R^2 values obtained when a linear fit is applied to the data points on the forced synchronisation boundaries in the $\bar{A}_f - f_f$ plane. Figures 5.1, 5.5 and 5.6 refer to experimental results shown in the main manuscript, whereas Figs. 5.7, 5.10 and 5.11 refer to results obtained from the mathematical model. An $R^2 = 1$ indicates that the linear regression predictions perfectly fit the data.

E.2 PERIOD-3 OSCILLATIONS EXHIBIT BY A SINGLE RIJKE TUBE OSCILLATOR UNDER EXTERNAL FORCING

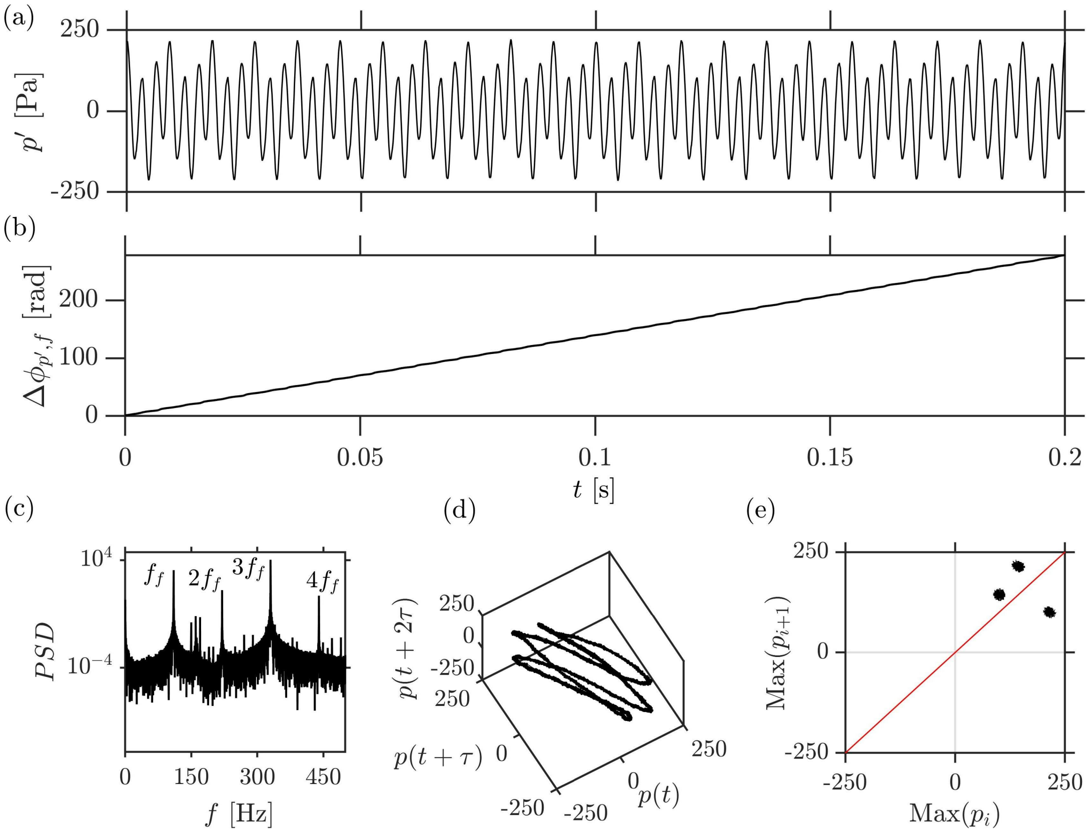

Figure E.1: Time series of (a) the acoustic pressure fluctuations and (b) instantaneous phase difference between the pressure and the forcing signal. (c) The power spectrum, (d) the reconstructed phase portrait, and (e) the first return map of the forced acoustic pressure oscillations in a single Rijke tube exhibiting LCO of amplitude $p'_{0,\mathrm{rms}}$ = 200 Pa. The forcing is applied at $f_f/f_{n0} = 0.69$ and $\bar{A}_f = 0.65$. As a result, the acoustic pressure fluctuations show period-3 oscillations and, hence, remain desynchronised with the forcing signal, causing a lower value of PLV. The period-3 oscillations are confirmed from the presence of three-looped attractor in the phase space and three fixed points in the return map.

During experiments in a single Rijke tube oscillator, we observe period-3 behavior in p' for high values of $\bar{A}_f$ in $f_f/f_{n0} = 0.62 - 0.70$ range, which leads to low PLV calculated between the p' and forcing signal. In Fig. E.1(a), we show the acoustic pressure fluctuations exhibited by the Rijke tube at $f_f/f_{n0} = 0.69$ and $\bar{A}_f = 0.65$. The unforced amplitude of the LCO exhibited by the Rijke tube is $p'_{0,\mathrm{rms}}$ = 200 Pa. The period-3 behavior can be observed from the time series in Fig. E.1(a), as well as the spectral peaks in Fig. E.1(c), where we notice the presence of spectral peaks of approximately same magnitude at $f_f, 2f_f$ and $3f_f$ locations. Correspondingly, in Fig. E.1(d), the structure representative of the system dynamics (referred to hereinafter as the attractor) is a triple-looped attractor, i.e., the trajectories need to loop thrice before coming back to the initial point. Because the orbit is periodic, we get three distinct dots in the single-sided return map for the acoustic pressure time series in Fig. E.1(e).

E.3 EFFECT OF VARYING COUPLING TUBE PARAMETERS ON THE AMPLITUDE DYNAMICS OF AN IDENTICAL RIJKE TUBES COUPLED SYSTEM

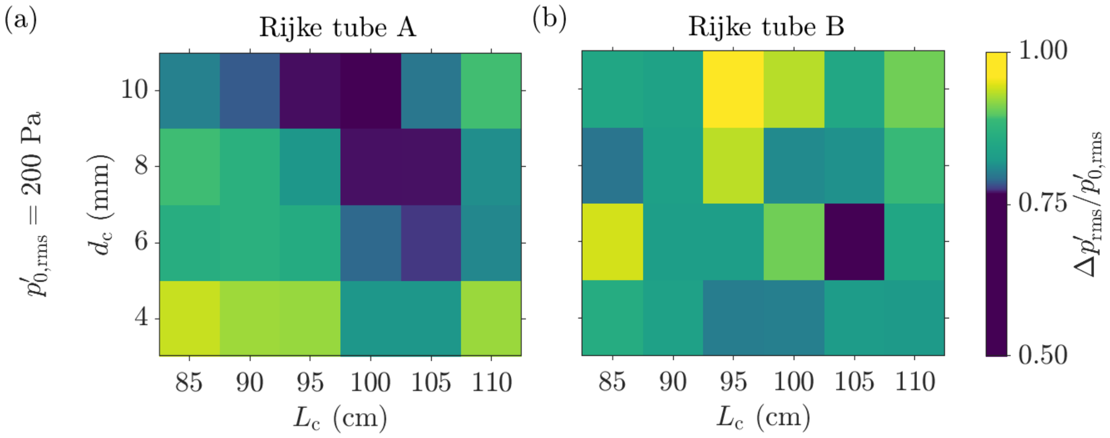

Figure E.2: Experimental two-parameter bifurcation plots showing the variation of $\Delta p'_{\mathrm{rms}}/p'_0$ for different values of coupling tube length L and internal diameter d in identical Rijke tubes ($\Delta f_0 = 0$ Hz). The maximum suppression obtained is around 50% in Rijke tube A for $L_\mathrm{c} = 100$ cm and $d_\mathrm{c} = 10$ mm.

Here, we explore experimentally the suppression of LCO in coupled Rijke tubes for connecting tubes of varying lengths and internal diameters. Figure E.2 shows the reduction in the amplitude of LCO for different combinations of L_c and d_c for identical Rijke tubes. We notice that for $d = 10$ mm, we obtain maximum suppression of about 50% in the acoustic pressure fluctuations for $L \sim 100$ cm, in Rijke tube A. Thus, we keep $d = 10$ mm for all our experiments. Large diameter connecting tubes may not be feasible for real-time combustors as it will require significant modification to engine hardware, whereas smaller diameters of connecting tube, such as the one used in the present study, can be very easily implemented.

REFERENCES

1. **Ahlborn, A.** and **U. Parlitz** (2005). Controlling dynamical systems using multiple delay feedback control. *Physical Review E*, **72**(1), 016206.

2. **Altay, H. M.**, **D. E. Hudgins**, **R. L. Speth**, **A. M. Annaswamy**, and **A. F. Ghoniem** (2010). Mitigation of thermoacoustic instability utilizing steady air injection near the flame anchoring zone. *Combustion and Flame*, **157**(4), 686–700.

3. **Altay, M.**, **R. Speth**, **D. Snarheim**, **D. Hudgins**, **A. Ghoniem**, and **A. Annaswamy**, Impact on microjet actuation on stability of a backward-facing step combustor. *In 45th AIAA Aerospace Sciences Meeting and Exhibit*. 2007.

4. **Anderson, W.**, **K. Miller**, **H. Ryan**, **S. Pal**, **R. Santoro**, and **J. Dressler** (1998). Effects of periodic atomization on combustion instability in liquid-fueled propulsion systems. *Journal of Propulsion and Power*, **14**(5), 818–825.

5. **Anderson, W. E.** and **V. Yang**, *Liquid Rocket Engine Combustion Instability*. AIAA, Reston, 2012.

6. **Anishchenko, V.**, **S. Astakhov**, and **T. Vadivasova** (2009*a*). Phase dynamics of two coupled oscillators under external periodic force. *EPL (Europhysics Letters)*, **86**(3), 30003.

7. **Anishchenko, V.**, **S. Nikolaev**, and **J. Kurths** (2008). Bifurcational mechanisms of synchronization of a resonant limit cycle on a two-dimensional torus. *Chaos: An Interdisciplinary Journal of Nonlinear Science*, **18**(3), 037123.

8. **Anishchenko, V. S.**, **S. V. Astakhov**, **T. E. Vadivasova**, and **A. V. Feoktistov** (2009*b*). Numerical and experimental study of external synchronization of two-frequency oscillations. *Nelineinaya Dinamika [Russian Journal of Nonlinear Dynamics]*, **5**(2), 237–252.

9. **Annaswamy, A. M.**, **M. Fleifil**, **J. W. Rumsey**, **R. Prasanth**, **J.-P. Hathout**, and **A. F. Ghoniem** (2000). Thermoacoustic instability: Model-based optimal control designs and experimental validation. *IEEE Transactions on Control Systems Technology*, **8**(6), 905–918.

10. **Annaswamy, A. M.** and **A. F. Ghoniem** (2002). Active control of combustion instability: Theory and practice. *IEEE Control Systems Magazine*, **22**(6), 37–54.

11. **Armstrong, R. R.**, **A. Michalke**, and **H. V. Fuchs** (1977). Coherent structures in jet turbulence and noise. *AIAA Journal*, **15**(7), 1011–1017.

12. **Atay, F. M.** (2003). Total and partial amplitude death in networks of diffusively coupled

oscillators. *Physica D: Nonlinear Phenomena*, **183**(1-2), 1–18.

13. **Baddeley, A.**, **E. Rubak**, and **R. Turner**, *Spatial point patterns: methodology and applications with R*. CRC Press, 2015.

14. **Balanov, A.**, **N. Janson**, **D. Postnov**, and **O. Sosnovtseva**, *Synchronization: From Simple to Complex*. Springer Science & Business Media, 2008.

15. **Balasubramanian, K.** and **R. Sujith** (2008). Thermoacoustic instability in a Rijke tube: Non-normality and nonlinearity. *Physics of Fluids*, **20**(4), 044103.

16. **Balusamy, S.**, **L. K. Li**, **Z. Han**, **M. P. Juniper**, and **S. Hochgreb** (2015). Nonlinear dynamics of a self-excited thermoacoustic system subjected to acoustic forcing. *Proceedings of the Combustion Institute*, **35**(3), 3229–3236.

17. **Banaszuk, A.**, **Y. Zhang**, and **C. A. Jacobson** (2001). Active control of combustion instabilities in gas turbine engines for low emissions. Part II: Adaptive control algorithm development, demonstration and performance limitations. Technical report, United Technologies Research Center, East Hartford CT.

18. **Bar-Eli, K.** (1985). On the stability of coupled chemical oscillators. *Physica D: Nonlinear Phenomena*, **14**(2), 242–252.

19. **Barabási, A.** (2012). The network takeover. *Nature Physics*, **8**(1), 14–16.

20. **Barabási, A.-L.** (2009). Scale-free networks: a decade and beyond. *Science*, **325**(5939), 412–413.

21. **Barabási, A.-L.** (2013). Network science. *Philosophical Transactions of the Royal Society A: Mathematical, Physical and Engineering Sciences*, **371**(1987), 20120375.

22. **Bassett, D. S.** and **E. Bullmore** (2006). Small-world brain networks. *The Neuroscientist*, **12**(6), 512–523.

23. **Basso, M.**, **R. Genesio**, **L. Giovanardi**, **A. Tesi**, and **G. Torrini** (1998). On optimal stabilization of periodic orbits via time delayed feedback control. *International Journal of Bifurcation and Chaos in Applied Sciences and Engineering*, **8**(08), 1699–1706.

24. **Battelino, P. M.** (1988). Persistence of three-frequency quasiperiodicity under large perturbations. *Physical Review A*, **38**(3), 1495.

25. **Bauer, H.-J.** (2004). New low emission strategies and combustor designs for civil aeroengine applications. *Progress in Computational Fluid Dynamics, An International Journal*, **4**(3-5), 130–142.

26. **Becker, B.**, **P. Berenbrink**, and **H. Brandner**, Premixing gas and air to reduce NO_x emissions with existing proven gas turbine combustion chambers. *In Turbo Expo: Power*

for Land, Sea, and Air, volume 79306. American Society of Mechanical Engineers, 1986.

27. **Bellows, B. D.**, **A. Hreiz**, and **T. Lieuwen** (2008). Nonlinear interactions between forced and self-excited acoustic oscillations in premixed combustor. *Journal of Propulsion and Power*, **24**(3), 628–631.

28. **Bellucci, V.**, **P. Flohr**, and **C. O. Paschereit** (2004*a*). Numerical and experimental study of acoustic damping generated by perforated screens. *AIAA Journal*, **42**(8), 1543–1549.

29. **Bellucci, V.**, **P. Flohr**, **C. O. Paschereit**, and **F. Magni** (2004*b*). On the use of Helmholtz resonators for damping acoustic pulsations in industrial gas turbines. *Journal of Engineering for Gas Turbines and Power*, **126**(2), 271–275.

30. **Benim, A. C.** and **K. J. Syed**, *Flashback mechanisms in lean premixed gas turbine combustion*. Academic Press, 2014.

31. **Benner, H.** and **W. Just** (2002). Control of chaos by time-delayed feedback in high-power ferromagnetic resonance experiments. *Journal of the Korean Physical Society*, **40**(6), 1046–1050.

32. **Benzi, R.**, **S. Ciliberto**, **R. Tripiccione**, **C. Baudet**, **F. Massaioli**, and **S. Succi** (1993). Extended self-similarity in turbulent flows. *Physical Review E*, **48**(1), R29.

33. **Bethke, S.**, **W. Krebs**, **P. Flohr**, and **B. Prade**, Thermoacoustic properties of can annular combustors. *In 8th AIAA/CEAS Aeroacoustics Conference & Exhibit*. 2002.

34. **Biggs, R.** (2009). Rocketdyne–F-1 Saturn first stage engine. *Remembering the Giants: Apollo Rocket Propulsion Development*, 15–26.

35. **Biwa, T.**, **Y. Sawada**, **H. Hyodo**, and **S. Kato** (2016). Suppression of Spontaneous Gas Oscillations by Acoustic Self-Feedback. *Physical Review Applied*, **6**(4), 044020.

36. **Biwa, T.**, **S. Tozuka**, and **T. Yazaki** (2015). Amplitude death in coupled thermoacoustic oscillators. *Physical Review Applied*, **3**(3), 034006.

37. **Blackman, A.** (1960). Effect of nonlinear losses on the design of absorbers for combustion instabilities. *ARS Journal*, **30**(11), 1022–1028.

38. **Blondel, V. D.**, **J.-L. Guillaume**, **R. Lambiotte**, and **E. Lefebvre** (2008). Fast unfolding of communities in large networks. *Journal of Statistical Mechanics: Theory and Experiment*, **2008**(10), P10008.

39. **Bloomfield, L. P.**, *Accidental encounters with history (and some lessons learned)*. Hot House Press, 2005.

40. **Bloxsidge, G.**, **A. Dowling**, **N. Hooper**, and **P. Langhorne** (1988). Active control of reheat buzz. *AIAA Journal*, **26**(7), 783–790.

41. **Bollobás, B.**, *Modern Graph Theory*, volume 184. Springer Science & Business Media, 1998.

42. **Bothien, M. R.**, **N. Noiray**, and **B. Schuermans** (2014). A novel damping device for broadband attenuation of low-frequency combustion pulsations in gas turbines. *Journal of Engineering for Gas Turbines and Power*, **136**(4).

43. **Boxx, I.**, **C. M. Arndt**, **C. D. Carter**, and **W. Meier** (2012). High-speed laser diagnostics for the study of flame dynamics in a lean premixed gas turbine model combustor. *Experiments in Fluids*, **52**, 555–567.

44. **Brasseur, G.**, **D. Hauglustaine**, **S. Walters**, **P. Rasch**, **J.-F. Müller**, **C. Granier**, and **X. Tie** (1998). MOZART, a global chemical transport model for ozone and related chemical tracers: 1. Model description. *Journal of Geophysical Research: Atmospheres*, **103**(D21), 28265–28289.

45. **Burnley, V.** and **F. Culick** (2000). Influence of random excitations on acoustic instabilities in combustion chambers. *AIAA Journal*, **38**(8), 1403–1410.

46. **Buschmann, P. E.**, **N. A. Worth**, and **J. P. Moeck** (2023). Thermoacoustic oscillations in a can-annular model combustor with asymmetries in the can-to-can coupling. *Proceedings of the Combustion Institute*, **39**(4), 5707–5715.

47. **Byrne, R.**, Longitudinal pressure oscillations in ramjet combustors. *In 19th Joint Propulsion Conference*. 1983.

48. **Candel, S.**, **D. Durox**, and **T. Schuller**, Flame interactions as a source of noise and combustion instabilities. *In 10th AIAA/CEAS Aeroacoustics Conference*. 2004.

49. **Cao, H.** and **Z. Liu** (2022). A novel synchronization transition and amplitude death in the local brain networks of cortical regions. *Nonlinear Dynamics*, **108**(4), 2861–2874.

50. **Castagliola, P.**, **A. Achouri**, **H. Taleb**, **G. Celano**, and **S. Psarakis** (2013). Monitoring the coefficient of variation using a variable sampling interval control chart. *Quality and Reliability Engineering International*, **29**(8), 1135–1149.

51. **Chaudhuri, S.**, **R. Gopakumar**, **S. Mondal**, **R. Paul**, and **S. Mahesh** (2018). Mitigating instability by actuating the swirler in a combustor. US Patent App. 15/753,117.

52. **Chen, L.**, **J. Li**, and **M. Ge** (2010). Drift study on cerium- tungsten/titiania catalyst for selective catalytic reduction of NO_3 with NH. *Environmental Science & Technology*, **44**(24), 9590–9596.

53. **Chishty, W. A.** (2005). *Effects of thermoacoustic oscillations on spray combustion dynamics with implications for lean direct injection systems*. Ph.D. thesis, Virginia Tech.

54. **Cho, J. H.** and **T. Lieuwen** (2005). Laminar premixed flame response to equivalence

ratio oscillations. *Combustion and flame*, **140**(1-2), 116–129.

55. **Clavin, P.**, **J. Kim**, and **F. Williams** (1994). Turbulence-induced noise effects on high-frequency combustion instabilities. *Combustion Science and Technology*, **96**(1-3), 61–84.

56. **Coats, C. M.** (1996). Coherent structures in combustion. *Progress in Energy and Combustion Science*, **22**(5), 427–509.

57. **Coderoni, M.**, **A. S. Lyrintzis**, and **G. A. Blaisdell** (2019). Large-eddy simulations analysis of supersonic heated jets with fluid injection for noise reduction. *AIAA Journal*, **57**(8), 3442–3455.

58. **Cohen, J.** and **T. Anderson**, Experimental investigation of near-blowout instabilities in a lean, premixed step combustor. *In 34th Aerospace Sciences Meeting and Exhibit*. 1996.

59. **Cohen, J. M.** and **A. Banaszuk** (2003). Factors affecting the control of unstable combustors. *Journal of Propulsion and Power*, **19**(5), 811–821.

60. **Cohen, R.** and **S. Havlin**, *Complex networks: structure, robustness and function*. Cambridge University Press, 2010.

61. **Cordeiro, M.**, **R. P. Sarmento**, and **J. Gama** (2016). Dynamic community detection in evolving networks using locality modularity optimization. *Social Network Analysis and Mining*, **6**, 1–20.

62. **Costa, L. d. F.**, **O. N. Oliveira Jr**, **G. Travieso**, **F. A. Rodrigues**, **P. R. Villas Boas**, **L. Antiqueira**, **M. P. Viana**, and **L. E. Correa Rocha** (2011). Analyzing and modeling real-world phenomena with complex networks: a survey of applications. *Advances in Physics*, **60**(3), 329–412.

63. **Crocco, L.** and **S.-I. Cheng** (1956). Theory of combustion instability in liquid propellant rocket motors. Technical report, Princeton University.

64. **Crow, S. C. J.** and **F. H. Champagne** (1971). Orderly structure in jet turbulence. *Journal of Fluid Mechanics*, **48**(3), 547–591.

65. **Crowell, R. H.** and **R. H. Fox**, *Introduction to knot theory*, volume 57. Springer Science & Business Media, 2012.

66. **Crump, J. E.**, **K. C. Schadow**, **V. Yang**, and **F. E. Culick** (1986). Longitudinal combustion instabilities in ramjet engines identification of acoustic modes. *Journal of Propulsion and Power*, **2**(2), 105–109.

67. **Crutzen, P. J.** (1974). Photochemical reactions initiated by and influencing ozone in unpolluted tropospheric air. *Tellus*, **26**(1-2), 47–57.

68. **Culick, F.** and **P. Kuentzmann** (2006). Unsteady motions in combustion chambers for propulsion systems. Technical report, NATO Research and Technology Organization, Neuilly-Sur-Seine (France).

69. **Culick, F. E.** and **V. Yang**, Overview of combustion instabilities in liquid-propellant rocket engines. *In* **V. Yang** and **W. Anderson** (eds.), *Liquid Rocket Engine Combustion Instability*, chapter 1. Oxford University Press, American Institute of Aeonautics and Astrophysics, 1995, 3–37.

70. **Cummings, A.** (1984). Acoustic nonlinearities and power losses at orifices. *AIAA Journal*, **22**(6), 786–792.

71. **Daggett, D.** (2004). Water misting and injection of commercial aircraft engines to reduce airport NO_x.

72. **Daggett, D. L.**, **R. C. Hendricks**, **L. Fucke**, and **D. J. Eames**, Water injection on commercial aircraft to reduce airport nitrogen oxides. *In 40th Joint Propulsion Conference and Exhibit*, AIAA Paper 2004-4198. 2010.

73. **Dai, H.**, **A. Abdelkefi**, **L. Wang**, and **W. Liu** (2015). Time-delay feedback controller for amplitude reduction in vortex-induced vibrations. *Nonlinear Dynamics*, **80**(1), 59–70.

74. **Dange, S.**, **K. Manoj**, **S. Banerjee**, **S. A. Pawar**, **S. Mondal**, and **R. I. Sujith** (2019). Oscillation quenching and phase-flip bifurcation in coupled thermoacoustic systems. *Chaos: An Interdisciplinary Journal of Nonlinear Science*, **29**(9), 093135.

75. **Davis, L. B.**, Dry low NO_x combustion systems for ge heavy-duty gas turbines. *In* **ASME** (ed.), *Turbo Expo: Power for Land, Sea, and Air*, volume 3: Coal, Biomass and Alternative Fuels; Combustion and Fuels; Oil and Gas Applications; Cycle Innovations. 1996.

76. **Deng, J.**, **T. Li**, **J. Wang**, and **C. Gao** (2022). Experimental study of suppressing the thermoacoustic instabilities in a Rijke tube using microsecond discharge plasma. *Aerospace*, **9**(12), 836.

77. **Desai, R.**, **S. Chakravarthy**, and **S. Ramgopal**, Effect of fuel injection location on combustion instability in a dump combustor. *In 48th AIAA Aerospace Sciences Meeting Including the New Horizons Forum and Aerospace Exposition*. 2010.

78. **Diestel, R.** (2000). Graduate texts in mathematics: Graph theory. *Heidelberg: SpringerVerlag*.

79. **Diggle, P.** (1985). A kernel method for smoothing point process data. *Journal of the Royal Statistical Society, Series C (Applied Statistics)*, **34**(2), 138–147.

80. **Dines, P. J.** (1984). *Active control of flame noise*. Ph.D. thesis, University of Cambridge.

81. **Donges, J. F.**, **Y. Zou**, **N. Marwan**, and **J. Kurths** (2009). Complex networks in climate dynamics. *European Physical Journal Special Topics*, **174**(1), 157–179.

82. **Doranehgard, M. H.**, **V. Gupta**, and **L. K. B. Li** (2022). Quenching and amplification of thermoacoustic oscillations in two nonidentical Rijke tubes interacting via time-delay and dissipative coupling. *Physical Review E*, **105**(6), 064206.

83. **Dorf, R. C.** and **R. H. Bishop**, *Modern Control Systems*. Pearson Prentice Hall, 2008.

84. **Dowd, C.** and **J. Meadows** (2022). Dynamics of thermoacoustic oscillations in swirl stabilized combustor without and with porous inert media. *Journal of Combustion*, **2022**.

85. **Dowling, A. P.** and **A. S. Morgans** (2005). Feedback Control of Combustion Oscillations. *Annual Review of Fluid Mechanics*, **37**, 151–182.

86. **Dranovsky, M. L.**, *Combustion instabilities in liquid rocket engines: testing and development practices in Russia*. American Institute of Aeronautics and Astronautics, 2007.

87. **Ducruix, S.**, **T. Schuller**, **D. Durox**, and **S. Candel** (2003). Combustion dynamics and instabilities: Elementary coupling and driving mechanisms. *Journal of Propulsion and Power*, **19**(5), 722–734.

88. **Duperé, I. D.** and **A. P. Dowling** (2005). The Use of Helmholtz Resonators in a Practical Combustor. *Journal of Engineering for Gas Turbines and Power*, **127**(2), 268–275.

89. **Dutta, A. K.**, **G. Ramachandran**, and **S. Chaudhuri** (2019). Investigating thermoacoustic instability mitigation dynamics with a Kuramoto model for flamelet oscillators. *Physical Review E*, **99**(3), 032215.

90. **Duvvur, A.**, **C. Chiang**, and **W. Sirignano** (1996). Oscillatory fuel droplet vaporization-driving mechanism for combustion instability. *Journal of Propulsion and Power*, **12**(2), 358–365.

91. **Eckart, C.** (1948). An analysis of the stirring and mixing processes in incompressible fluids. *Journal of Marine Research*, **7**(3-11), 265–275.

92. **Eldredge, J. D.** and **A. P. Dowling** (2003). The absorption of axial acoustic waves by a perforated liner with bias flow. *Journal of Fluid Mechanics*, **485**, 307–335.

93. **ElKady, A. M.**, **A. Evulet**, **A. Brand**, **T. P. Ursin**, and **A. Lynghjem**, Exhaust gas recirculation in DLN F-class gas turbines for post-combustion CO_2 capture. *In Turbo Expo: Power for Land, Sea, and Air*, volume 43130. 2008.

94. **ElKady, A. M.**, **A. Evulet**, **A. Brand**, **T. P. Ursin**, and **A. Lynghjem** (2009). Application of exhaust gas recirculation in a DLN F-class combustion system for postcombustion carbon capture. *Journal of Engineering for Gas Turbines and Power*, **131**(3).

95. **Etikyala, S.** and **R. Sujith** (2017). Change of criticality in a prototypical thermoacoustic system. *Chaos: An Interdisciplinary Journal of Nonlinear Science*, **27**(2), 023106.

96. **Euler, L.** (1741). Solutio problematis ad geometriam situs pertinentis. *Commentarii academiae scientiarum Petropolitanae*, 128–140.

97. **Eurich, C. W.**, **A. Thiel**, and **L. Fahse** (2005). Distributed delays stabilize ecological feedback systems. *Physical Review Letters*, **94**(15), 158104.

98. **Evesque, S.** and **A. Dowling**, Adaptive control of combustion oscillations. *In 4th AIAA/CEAS Aeroacoustics Conference*. 1998.

99. **Evulet, A. T.**, **A. M. ELKady**, **A. R. Branda**, and **D. Chinn** (2009). On the performance and operability of GE's dry low NO_x combustors utilizing exhaust gas recirculation for post combustion carbon capture. *Energy Procedia*, **1**(1), 3809–3816.

100. **Faloutsos, M.**, **P. Faloutsos**, and **C. Faloutsos** (1999). On power-law relationships of the internet topology. *ACM SIGCOMM Computer Communication Review*, **29**(4), 251–262.

101. **Fan, H.**, **L.-W. Kong**, **X. Wang**, **A. Hastings**, and **Y.-C. Lai** (2021). Synchronization within synchronization: transients and intermittency in ecological networks. *National Science Review*, **8**(10), nwaa269.

102. **Farisco, F.**, **L. Panek**, and **J. B. W. Kok** (2017). Thermo-acoustic cross-talk between cans in a can-annular combustor. *International Journal of Spray and Combustion Dynamics*, **9**(4), 452–469.

103. **Farsiani, Y.**, **Z. Saeed**, **B. Jayaraman**, and **B. R. Elbing** (2020). Modification of turbulent boundary layer coherent structures with drag reducing polymer solution. *Physics of Fluids*, **32**(1), 015107.

104. **Ffowcs Williams, J. E.** (1984). Review Lecture - Anti-sound. *Proceedings of the Royal Society of London. A. Mathematical and Physical Sciences*, **395**(1808), 63–88.

105. **Fiedler, H. E.** (1988). Coherent structures in turbulent flows. *Progress in Aerospace Sciences*, **25**(3), 231–269.

106. **Flandro, G.** (1986). Vortex driving mechanism in oscillatory rocket flows. *Journal of Propulsion and Power*, **2**(3), 206–214.

107. **Fleifil, M.**, **J. Hathout**, **A. Annaswamy**, and **A. Ghoniem** (1998). The origin of secondary peaks with active control of thermoacoustic instability. *Combustion Science and Technology*, **133**(4-6), 227–265.

108. **Flunkert, V.** and **E. Schöll** (2007). Suppressing noise-induced intensity pulsations in semiconductor lasers by means of time-delayed feedback. *Physical Review E*, **76**(6), 066202.

109. **Flynn, T.**, **T. Fuller**, **S. Rufener**, and **C. Daw**, Thermoacoustic Vibrations in Industrial Furnaces and Boilers. *In Proceedings of AFRC 2017 Industrial Combustion Symposium*. 2017.

110. **Fortunato, S.** (2010). Community detection in graphs. *Physics Reports*, **486**(3-5), 75–174.

111. **Fortunato, S.** and **M. Barthelemy** (2007). Resolution limit in community detection. *Proceedings of the National Academy of Sciences of the United States of America*, **104**(1), 36–41.

112. **Fournier, G. J.**, **M. Meindl**, **C. F. Silva**, **G. Ghirardo**, **M. R. Bothien**, and **W. Polifke** (2021). Low-order modeling of can-annular combustors. *Journal of Engineering for Gas Turbines and Power*, **143**(12).

113. **Franklin, G. F.**, **J. D. Powell**, **A. Emami-Naeini**, and **J. D. Powell**, *Feedback control of dynamic systems*, volume 4. Prentice hall Upper Saddle River, 2002.

114. **Fröhlich, J.**, **M. García-Villalba**, and **W. Rodi** (2008). Scalar mixing and large-scale coherent structures in a turbulent swirling jet. *Flow, Turbulence and Combustion*, **80**(1), 47–59.

115. **Fruchterman, T. M. J.** and **E. M. Reingold** (1991). Graph drawing by force-directed placement. *Software: Practice and Experience*, **21**(11), 1129–1164.

116. **Fuglestvedt, J. S.**, **T. K. Berntsen**, **I. S. Isaksen**, **H. Mao**, **X.-Z. Liang**, and **W.-C. Wang** (1999). Climatic forcing of nitrogen oxides through changes in tropospheric ozone and methane; global 3D model studies. *Atmospheric Environment*, **33**(6), 961–977.

117. **Gao, X.**, **Y. Jiang**, **Y. Zhong**, **Z. Luo**, and **K. Cen** (2010). The activity and characterization of CeO_2-TiO_2 catalysts prepared by the sol–gel method for selective catalytic reduction of NO with NH_3. *Journal of Hazardous Materials*, **174**(1-3), 734–739.

118. **Garrison, G.**, The role of acoustic absorbers in preventing combustion instability. *In 7th Propulsion Joint Specialist Conference*. 1971.

119. **George, N. B.**, **V. R. Unni**, **M. Raghunathan**, and **R. Sujith** (2018). Pattern formation during transition from combustion noise to thermoacoustic instability via intermittency. *Journal of Fluid Mechanics*, **849**, 615–644.

120. **Ghirardo, G.**, **C. Di Giovine**, **J. P. Moeck**, and **M. R. Bothien** (2019). Thermoacoustics of can-annular combustors. *Journal of Engineering for Gas Turbines and Power*, **141**(1), 011007.

121. **Ghirardo, G.**, **J. Moeck**, and **M. R. Bothien** (2020). Effect of noise and nonlinearities on thermoacoustics of can-annular combustors. *Journal of Engineering for Gas Turbines and Power*, **142**(4).

122. **Ghoniem, A. F.**, **A. Annaswamy**, **S. Park**, and **Z. C. Sobhani** (2005). Stability and emissions control using air injection and H_2 addition in premixed combustion. *Proceedings of the Combustion Institute*, **30**(2), 1765–1773.

123. **Ghosh, A.**, **S. Mondal**, and **R. I. Sujith** (2022). Occasional coupling enhances amplitude death in delay-coupled oscillators. *Chaos: An Interdisciplinary Journal of Nonlinear Science*, **32**(10), 101106.

124. **Godavarthi, V.**, **S. A. Pawar**, **V. R. Unni**, **R. Sujith**, **N. Marwan**, and **J. Kurths** (2018). Coupled interaction between unsteady flame dynamics and acoustic field in a turbulent combustor. *Chaos: An Interdisciplinary Journal of Nonlinear Science*, **28**(11), 113111.

125. **Godavarthi, V.**, **V. R. Unni**, **E. A. Gopalakrishnan**, and **R. I. Sujith** (2017). Recurrence networks to study dynamical transitions in a turbulent combustor. *Chaos: An Interdisciplinary Journal of Nonlinear Science*, **27**(6), 063113.

126. **Gomez del Campo, F.**, Plasma-assisted control of combustion instabilities in low-emissions combustors at realistic conditions. *In AIAA Propulsion and Energy 2019 Forum*. 2019.

127. **Gonzalez-Miranda, J. M.** (2002). Amplitude envelope synchronization in coupled chaotic oscillators. *Physical Review E*, **65**(3), 036232.

128. **Gopakumar, R.**, **R. Belur Vishwanath**, **J. Singh**, **A. Dutta**, and **S. Chaudhuri**, On the dynamics of instability mitigation by actuating swirler motion in a lean premixed turbulent combustor. *In Gas Turbine India Conference*, volume 58509. American Society of Mechanical Engineers, 2017.

129. **Gopakumar, R.**, **S. Mondal**, **R. Paul**, **S. Mahesh**, and **S. Chaudhuri** (2016). Mitigating instability by actuating the swirler in a combustor. *Combustion and Flame*, **165**, 361–363.

130. **Gopalakrishnan, E.** and **R. Sujith** (2014). Influence of system parameters on the hysteresis characteristics of a horizontal Rijke tube. *International Journal of Spray and Combustion Dynamics*, **6**(3), 293–316.

131. **Gopalakrishnan Meena, M.** (2020). *Network community-based analysis of complex vortical flows: laminar and turbulent flows*. Ph.D. thesis, UCLA.

132. **Gopalakrishnan Meena, M.**, **A. G. Nair**, and **K. Taira** (2018). Network community-based model reduction for vortical flows. *Physical Review E*, **97**(6), 063103.

133. **Gopalakrishnan Meena, M.** and **K. Taira** (2021). Identifying vortical network connectors for turbulent flow modification. *Journal of Fluid Mechanics*, **915**.

134. **Gotoda, H.**, **M. Amano**, **T. Miyano**, **T. Ikawa**, **K. Maki**, and **S. Tachibana** (2012). Characterization of complexities in combustion instability in a lean premixed gas-turbine model combustor. *Chaos: An Interdisciplinary Journal of Nonlinear Science*, **22**(4).

135. **Gotoda, H.**, **H. Kinugawa**, **R. Tsujimoto**, **S. Domen**, and **Y. Okuno** (2017). Characterization of combustion dynamics, detection, and prevention of an unstable combustion state based on a complex-network theory. *Physical Review Applied*, **7**(4), 044027.

136. **Govindarajan, R.** (2002). Universal behavior of entrainment due to coherent structures in turbulent shear flow. *Physical Review Letters*, **88**(13), 134503.

137. **Grewe, V.**, **M. Dameris**, **C. Fichter**, and **R. Sausen** (2002). Impact of aircraft NO_x emissions. Part 1: Interactively coupled climate-chemistry simulations and sensitivities to climate-chemistry feedback, lightning and model resolution. *Meteorologische Zeitschrift*, **11**(3), 177–186.

138. **Grinsted, A.**, **J. C. Moore**, and **S. Jevrejeva** (2004). Application of the cross wavelet transform and wavelet coherence to geophysical time series. *Nonlinear Processes in Geophysics*, **11**(5/6), 561–566.

139. **Gross, J. L.**, **J. Yellen**, and **M. Anderson**, *Graph theory and its applications*. Chapman and Hall/CRC, 2018.

140. **Guan, Y.**, **V. Gupta**, **K. Kashinath**, and **L. K. Li** (2019*a*). Open-loop control of periodic thermoacoustic oscillations: experiments and low-order modelling in a synchronization framework. *Proceedings of the Combustion Institute*, **37**(4), 5315–5323.

141. **Guan, Y.**, **V. Gupta**, and **L. K. Li** (2020). Intermittency route to self-excited chaotic thermoacoustic oscillations. *Journal of Fluid Mechanics*, **894**, R3.

142. **Guan, Y.**, **V. Gupta**, **M. Wan**, and **L. K. Li** (2019*b*). Forced synchronization of quasiperiodic oscillations in a thermoacoustic system. *Journal of Fluid Mechanics*, **879**, 390–421.

143. **Guan, Y.**, **L. K. Li**, **B. Ahn**, and **K. T. Kim** (2019*c*). Chaos, synchronization, and desynchronization in a liquid-fueled diffusion-flame combustor with an intrinsic hydrodynamic mode. *Chaos: An Interdisciplinary Journal of Nonlinear Science*, **29**(5), 053124.

144. **Guan, Y.**, **K. Moon**, **K. T. Kim**, and **L. K. Li** (2022). Synchronization and chimeras in a network of four ring-coupled thermoacoustic oscillators. *Journal of Fluid Mechanics*, **938**.

145. **Guan, Y.**, **K. Moon**, **K. T. Kim**, and **L. K. B. Li** (2021). Low-order modeling of the mutual synchronization between two turbulent thermoacoustic oscillators. *Physical Review E*, **104**(2), 024216.

146. **Guan, Y.**, **M. Murugesan**, and **L. K. B. Li** (2018). Strange nonchaotic and chaotic attractors in a self-excited thermoacoustic oscillator subjected to external periodic forcing. *Chaos: An Interdisciplinary Journal of Nonlinear Science*, **28**(9), 093109.

147. **Guimera, R.** and **L. A. N. Amaral** (2005). Functional cartography of complex metabolic networks. *Nature*, **433**(7028), 895–900.

148. **Gullaud, E.** and **F. Nicoud** (2012). Effect of perforated plates on the acoustics of annular combustors. *AIAA Journal*, **50**(12), 2629–2642.

149. **Gürcan, Ö. D.** (2017). Nested polyhedra model of turbulence. *Physical Review E*, **95**(6), 063102.

150. **Gürcan, Ö. D.** (2018). Nested polyhedra model of isotropic magnetohydrodynamic turbulence. *Physical Review E*, **97**(6), 063111.

151. **Gysling, D.**, **G. Copeland**, **D. McCormick**, and **W. Proscia** (2000). Combustion system damping augmentation with Helmholtz resonators. *Journal of Engineering for Gas Turbines and Power*, **122**(2), 269–274.

152. **Hadjighasem, A.**, **D. Karrasch**, **H. Teramoto**, and **G. Haller** (2016). Spectral-clustering approach to Lagrangian vortex detection. *Physical Review E*, **93**(6), 063107.

153. **Hardalupas, Y. L.** and **M. Orain** (2004). Local measurements of the time-dependent heat release rate and equivalence ratio using chemiluminescent emission from a flame. *Combustion and Flame*, **139**(3), 188–207.

154. **Harp, J. L.**, **W. W. Velie**, and **L. Bryant**, *Investigation of Combustion Screech and a Method of its Control*. National Advisory Committee for Aeronautics, 1954.

155. **Harrje, D. T.** and **F. H. Reardon**, *Liquid propellant rocket combustion instability*, volume 1. Scientific and Technical Information Office, National Aeronautics and Space Administration, 1972.

156. **Hashimoto, T.**, **H. Shibuya**, **H. Gotoda**, **Y. Ohmichi**, and **S. Matsuyama** (2019). Spatiotemporal dynamics and early detection of thermoacoustic combustion instability in a model rocket combustor. *Physical Review E*, **99**(3), 032208.

157. **Hassa, C.** (2013). Partially premixed and premixed aero engine combustors. *Gas Turbine Emissions*, **38**, 237.

158. **Heckl, M. A.** (1985). *Heat sources in acoustic resonators*. Ph. d. thesis, University of Cambridge, Cambridge, UK. Available at `https://www.repository.cam.ac.uk/items/b0d5adbc-f97b-4250-b86f-1f2aa08e8598`.

159. **Heckl, M. A.** (1988). Active control of the noise from a Rijke tube. *Journal of Sound and Vibration*, **124**(1), 117–133.

160. **Heckl, M. A.** (1990). Non-linear acoustic effects in the Rijke tube. *Acta Acustica united with Acustica*, **72**(1), 63–71.

161. **Hegde, U.**, **D. Reuter**, **B. Daniel**, and **B. Zinn** (1987). Flame driving of longitudinal instabilities in dump type ramjet combustors. *Combustion Science and Technology*, **55**(4-6), 125–138.

162. **Hermann, J.**, **A. Orthmann**, **S. Hoffmann**, and **P. Berenbrink** (2001). Combination of active instability control and passive measures to prevent combustion instabilities in a 260 MW heavy duty gas turbine. Technical report, Ingenieurbuero Fuer Thermoakustik Gmbhgroebenzell (Germany).

163. **Hermeth, S.**, **G. Staffelbach**, **L. Y. Gicquel**, and **T. Poinsot** (2013). LES evaluation of the effects of equivalence ratio fluctuations on the dynamic flame response in a real gas turbine combustion chamber. *Proceedings of the Combustion Institute*, **34**(2), 3165–3173.

164. **Herndon, S. C.**, **E. C. Wood**, **M. J. Northway**, **R. Miake-Lye**, **L. Thornhill**, **A. Beyersdorf**, **B. E. Anderson**, **R. Dowlin**, **W. Dodds**, and **W. B. Knighton** (2009). Aircraft hydrocarbon emissions at Oakland International Airport. *Environmental Science & Technology*, **43**(6), 1730–1736.

165. **Herrero, R.**, **M. Figueras**, **J. Rius**, **F. Pi**, and **G. Orriols** (2000). Experimental observation of the amplitude death effect in two coupled nonlinear oscillators. *Physical Review Letters*, **84**(23), 5312.

166. **Hidalgo, H.** and **P. Crutzen** (1977). The tropospheric and stratospheric composition perturbed by NO_x emissions of high-altitude aircraft. *Journal of Geophysical Research*, **82**(37), 5833–5866.

167. **Hill, S.** and **L. D. Smoot** (2000). Modeling of nitrogen oxides formation and destruction in combustion systems. *Progress in Energy and Combustion Science*, **26**(4-6), 417–458.

168. **Hitimana, E.**, **R. O. Fox**, **J. C. Hill**, and **M. G. Olsen** (2021). Coherent structure characteristics of the swirling flow during turbulent mixing in a multi-inlet vortex reactor. *Physics of Fluids*, **33**(6), 065119.

169. **Ho, C. M.** and **L. S. Huang** (1982). Subharmonics and vortex merging in mixing layers. *Journal of Fluid Mechanics*, **119**, 443–473.

170. **Ho, C. M.** and **P. Huerre** (1984). Perturbed free shear layers. *Annual Review of Fluid Mechanics*, **16**, 365–424.

171. **Ho, C. M.** and **N. S. Nosseir** (1981). Dynamics of an impinging jet. Part 1. the feedback phenomenon. *Journal of Fluid Mechanics*, **105**, 119–142.

172. **Hodnebrog, Ø.**, **T. Berntsen**, **O. Dessens**, **M. Gauss**, **V. Grewe**, **I. Isaksen**, **B. Koffi**, **G. Myhre**, **D. Olivié**, **M. Prather**, *et al.* (2011). Future impact of non-land based traffic emissions on atmospheric ozone and OH–an optimistic scenario and a possible mitigation strategy. *Atmospheric Chemistry and Physics*, **11**(21), 11293–11317.

173. **Honerkamp, J.** (1983). The heart as a system of coupled nonlinear oscillators. *Journal of Mathematical Biology*, **18**(1), 69–88.

174. **Hong, S.**, **R. L. Speth**, **S. J. Shanbhogue**, and **A. F. Ghoniem** (2013). Examining flow-flame interaction and the characteristic stretch rate in vortex-driven combustion dynamics using piv and numerical simulation. *Combustion and Flame*, **160**(8), 1381–1397.

175. **Howe, M.** (1979). On the theory of unsteady high Reynolds number flow through a circular aperture. *Proceedings of the Royal Society of London. A. Mathematical and Physical Sciences*, **366**(1725), 205–223.

176. **Howe, M. S.** (1980). The dissipation of sound at an edge. *Journal of Sound and Vibration*, **70**(3), 407–411.

177. **Huang, Y.** and **V. Yang** (2009). Dynamics and stability of lean-premixed swirl-stabilized combustion. *Progress in Energy and Combustion Science*, **35**(4), 293–364.

178. **Huddy, S. R.** and **J. D. Skufca** (2012). Amplitude death solutions for stabilization of dc microgrids with instantaneous constant-power loads. *IEEE Transactions on Power Electronics*, **28**(1), 247–253.

179. **Hughes, I.** and **A. Dowling** (1990). The absorption of sound by perforated linings. *Journal of Fluid Mechanics*, **218**, 299–335.

180. **Hung, W.** (1974). Accurate method of predicting the effect of humidity or injected water on NO_x emissions from industrial gas turbines. *ASME Paper*.

181. **Hussain, A. K. M. F.** (1983). Coherent structures—reality and myth. *Physics of Fluids*, **26**(10), 2816–2850.

182. **Hussain, A. K. M. F.** (1986). Coherent structures and turbulence. *Journal of Fluid Mechanics*, **173**, 303–356.

183. **Hussain, M.**, **S. Jamshed**, and **M. Ozair**, Simulations and analysis of vortex driven combustion instability. *In 2022 19th International Bhurban Conference on Applied Sciences and Technology (IBCAST)*. IEEE, 2022.

184. **Huygens, C.** (1665). Letter to his father, dated 26 February 1665. *Oeuvres complets de Christian Huygens*, **5**, 243.

185. **Hyodo, H.** and **T. Biwa** (2018*a*). Derivation of coupling conditions of amplitude death in delay-coupled thermoacoustic oscillators. *Proceedings of Meetings on Acoustics*, **34**(1), 030004.

186. **Hyodo, H.** and **T. Biwa** (2018*b*). Phase-locking and suppression states observed in forced synchronization of thermoacoustic oscillator. *Journal of the Physical Society of Japan*, **87**(3), 034402.

187. **Hyodo, H.** and **T. Biwa** (2018*c*). Stabilization of thermoacoustic oscillators by delay coupling. *Physical Review E*, **98**(5), 052223.

188. **Hyodo, H.** and **T. Biwa**, *Amplitude death in coupled thermoacoustic oscillators with frequency detuning*. Universitätsbibliothek der RWTH Aachen, 2019.

189. **Hyodo, H.**, **M. Iwasaki**, and **T. Biwa** (2020). Suppression of Rijke tube oscillations by delay coupling. *Journal of Applied Physics*, **128**(9), 094902.

190. **Hyodo, H.**, **I. Shinkai**, and **T. Biwa** (2016). Amplitude death in delay-coupled thermoacoustic oscillators. *The Journal of the Acoustical Society of America*, **140**, 2955.

191. **Hyodo, H.**, **Y. Tanizaki**, and **T. Biwa**, Dynamics of forced synchronization in thermoacoustic system. *In Third International Workshop on Thermoacoustics*. University of Twente, Enschede, 2015.

192. **Iacobello, G.**, **M. Marro**, **L. Ridolfi**, **P. Salizzoni**, and **S. Scarsoglio** (2019*a*). Experimental investigation of vertical turbulent transport of a passive scalar in a boundary layer: Statistics and visibility graph analysis. *Physical Review Fluids*, **4**(10), 104501.

193. **Iacobello, G.**, **L. Ridolfi**, and **S. Scarsoglio** (2021). A review on turbulent and vortical flow analyses via complex networks. *Physica A: Statistical Mechanics and its Applications*, **563**, 125476.

194. **Iacobello, G.**, **S. Scarsoglio**, **J. G. M. Kuerten**, and **L. Ridolfi** (2018*a*). Spatial characterization of turbulent channel flow via complex networks. *Physical Review E*, **98**(1), 013107.

195. **Iacobello, G.**, **S. Scarsoglio**, **J. G. M. Kuerten**, and **L. Ridolfi** (2019*b*). Lagrangian network analysis of turbulent mixing. *Journal of Fluid Mechanics*, **865**, 546–562.

196. **Iacobello, G.**, **S. Scarsoglio**, and **L. Ridolfi** (2018*b*). Visibility graph analysis of wall turbulence time-series. *Physical Letters A*, **382**(1), 1–11.

197. **ICAO** (2022). ICAO Future of Aviation. `https://www.icao.int/Meetings-/FutureOfAviation/Pages/default.aspx`. Accessed: 13-12-2022.

198. **Ingard, U.** and **V. K. Singhal** (1975). Effect of flow on the acoustic resonances of an open-ended duct. *The Journal of the Acoustical Society of America*, **58**(4), 788–793.

199. **IPCC, E.** (1999). Aviation and the global atmosphere. *Intergovernmental Panel on Global Change–Cambridge University Press: Cambridge*.

200. **Isella, G.**, **C. Seywert**, **F. Culick**, and **E. Zukoski** (1997). A further note no active cpmtrol of combustion instabilities besed on hyeteresis. *Combustion Science and Technology*, **126**(1-6), 381–388.

201. **Jadhav, V.**, **V. Guttal**, and **D. R. Masila** (2022). Randomness in the choice of neighbours promotes cohesion in mobile animal groups. *Royal Society Open Science*, **9**(3), 220124.

202. **Jahnke, C. C.** and **F. E. C. Culick** (1994). Application of dynamical systems theory to nonlinear combustion instabilities. *Journal of Propulsion and Power*, **10**(4), 508–517.

203. **Jegal, H.**, **K. Moon**, **J. Gu**, **L. K. B. Li**, and **K. T. Kim** (2019). Mutual synchronization of two lean-premixed gas turbine combustors: Phase locking and amplitude death. *Combustion and Flame*, **206**, 424–437.

204. **Jenkins, A.** (2013). Self-oscillation. *Physics Reports*, **525**(2), 167–222.

205. **Jiménez, A.**, **Y. Lu**, **A. Jambhekar**, and **G. Lahav** (2022). Principles, mechanisms and functions of entrainment in biological oscillators. *Interface Focus*, **12**(3), 20210088.

206. **Johnson, N.**, *Simply complexity: A clear guide to complexity theory*. Simon and Schuster, 2009.

207. **Juniper, M. P.** and **R. I. Sujith** (2018). Sensitivity and nonlinearity of thermoacoustic oscillations. *Annual Review of Fluid Mechanics*, **50**, 661–689.

208. **Junker, B. H.** and **F. Schreiber**, *Analysis of biological networks*, volume 2. Wiley Online Library, 2008.

209. **Kabiraj, L.**, **A. Saurabh**, **P. Wahi**, and **R. Sujith** (2012*a*). Route to chaos for combustion instability in ducted laminar premixed flames. *Chaos: An Interdisciplinary Journal of Nonlinear Science*, **22**(2).

210. **Kabiraj, L.**, **R. Sujith**, and **P. Wahi** (2012*b*). Bifurcations of self-excited ducted laminar premixed flames. *Journal of Engineering for Gas Turbines and Power*, **134**(3).

211. **Karrer, B.**, **E. Levina**, and **M. E. Newman** (2008). Robustness of community structure in networks. *Physical Review E*, **77**(4), 046119.

212. **Kashinath, K.**, **L. K. Li**, and **M. P. Juniper** (2018). Forced synchronization of periodic and aperiodic thermoacoustic oscillations: lock-in, bifurcations and open-loop control. *Journal of Fluid Mechanics*, **838**, 690–714.

213. **Kashinath, K.**, **I. C. Waugh**, and **M. P. Juniper** (2014). Nonlinear self-excited thermoacoustic oscillations of a ducted premixed flame: bifurcations and routes to chaos. *Journal of Fluid Mechanics*, **761**, 399–430.

214. **Kasthuri, P.**, **I. Pavithran**, **A. Krishnan**, **S. A. Pawar**, **R. I. Sujith**, **R. Gejji**, **W. Anderson**, **N. Marwan**, and **J. Kurths** (2020). Recurrence analysis of slow–fast systems. *Chaos: An Interdisciplinary Journal of Nonlinear Science*, **30**(6), 063152.

215. **Kasthuri, P.**, **S. A. Pawar**, **R. Gejji**, **W. Anderson**, and **R. I. Sujith** (2022). Coupled

interaction between acoustics and unsteady flame dynamics during the transition to thermoacoustic instability in a multi-element rocket combustor. *Combustion and Flame*, **240**, 112047.

216. **Kaufmann, P.**, **W. Krebs**, **R. Valdes**, and **U. Wever**, 3D thermoacoustic properties of single can and multi can combustor configurations. *In Turbo Expo: Power for Land, Sea, and Air*, volume 43130. 2008.

217. **Kawano, K.**, **H. Gotoda**, **Y. Nabae**, **Y. Ohmichi**, and **S. Matsuyama** (2023). Complex-network analysis of high-frequency combustion instability in a model single-element rocket engine combustor. *Journal of Fluid Mechanics*, **959**, A1.

218. **Keanini, R.**, **K. Yu**, and **J. Daily**, Evidence of a strange attractor in ramjet combustion. *In 27th Aerospace Sciences Meeting*. 1989.

219. **Keen, B. E.** and **W. H. W. Fletcher** (1970). Suppression of a plasma instability by the method of "asynchronous quenching". *Physical Review Letters*, **24**(4), 130.

220. **Keller, J.**, **L. Vaneveld**, **D. Korschelt**, **G. Hubbard**, **A. Ghoniem**, **J. Daily**, and **A. Oppenheim** (1982). Mechanism of instabilities in turbulent combustion leading to flashback. *AIAA Journal*, **20**(2), 254–262.

221. **Kellerer, H.**, **H. Bauer**, and **S. Wittig**, Soot formation from rich hydrocarbon oxidation under elevated pressure conditions. *In Proceedings of the 20th International Symposium on Shock Waves, Pasadena, CA*. 1995.

222. **Ken, H. Y.**, **A. Trouvé**, and **J. W. Daily** (1991). Low-frequency pressure oscillations in a model ramjet combustor. *Journal of Fluid Mechanics*, **232**, 47–72.

223. **Kendrick, D. W.**, **T. J. Anderson**, **W. A. Sowa**, and **T. S. Snyder** (1999). Acoustic sensitivities of lean-premixed fuel injectors in a single nozzle rig. *Journal of Engineering for Gas Turbines and Power*, **121**(3), 429–436. ISSN 0742-4795.

224. **Kenett, D. Y.** and **S. Havlin** (2015). Network science: a useful tool in economics and finance. *Mind & Society*, **14**(2), 155–167.

225. **Kernighan, B. W.** and **S. Lin** (1970). An efficient heuristic procedure for partitioning graphs. *The Bell System Technical Journal*, **49**(2), 291–307.

226. **Khodayari, A.**, **S. Tilmes**, **S. Olsen**, **D. Phoenix**, **D. Wuebbles**, **J.-F. Lamarque**, and **C.-C. Chen** (2014). Aviation 2006 NO_x-induced effects on atmospheric ozone and HOx in Community Earth System Model (CESM). *Atmospheric Chemistry and Physics*, **14**(18), 9925–9939.

227. **Kim, K.**, **J. Lee**, **J. Stenzler**, and **D. A. Santavicca**, Optimization of active control systems for suppressing combustion dynamics. *In NATO RTO/AVT Symposium on Active Control Technology for Enhanced Performance in Land, Air, and Sea Vehicles*. 2000.

228. **Kim, K.-J.** and **K.-H. Ahn** (2014). Amplitude death of coupled hair bundles with stochastic channel noise. *Physical Review E*, **89**(4), 042703.

229. **King, L. V.** and **H. T. Barnes** (1914). On the convection of heat from small cylinders in a stream of fluid: Determination of the convection constants of small platinum wires, with applications to hot-wire anemometry. *Proceedings of the Royal Society of London. Series A, Containing Papers of a Mathematical and Physical Character*, **90**(622), 563–570.

230. **Kobayashi, W.**, **H. Gotoda**, **S. Kandani**, **Y. Ohmichi**, and **S. Matsuyama** (2019). Spatiotemporal dynamics of turbulent coaxial jet analyzed by symbolic information-theory quantifiers and complex-network approach. *Chaos: An Interdisciplinary Journal of Nonlinear Science*, **29**(12), 123110.

231. **Köhler, M. O.**, **G. Rädel**, **O. Dessens**, **K. P. Shine**, **H. L. Rogers**, **O. Wild**, and **J. A. Pyle** (2008). Impact of perturbations to nitrogen oxide emissions from global aviation. *Journal of Geophysical Research: Atmospheres*, **113**(D11).

232. **Koo, J.** (2011). *Adjoint sensitivity analysis of the intercontinental impacts of aviation emissions on air quality and health*. Ph.D. thesis, Massachusetts Institute of Technology.

233. **Kopasakis, G.**, **J. C. DeLaat**, and **C. T. Chang** (2009). Adaptive instability suppression controls method for aircraft gas turbine engine combustors. *Journal of Propulsion and Power*, **25**(3), 618–627.

234. **Krebs, W.**, **S. Bethke**, **J. Lepers**, **P. Flohr**, **B. Prade**, **C. Johnson**, and **S. Sattinger** (2005). Thermoacoustic design tools and passive control: Siemens power generation approaches. *Progress in Astronautics and Aeronautics*, **210**, 89.

235. **Krishnan, A.**, **R. Manikandan**, **P. R. Midhun**, **K. V. Reeja**, **V. R. Unni**, **R. I. Sujith**, **N. Marwan**, and **J. Kurths** (2019*a*). Mitigation of oscillatory instability in turbulent reactive flows: A novel approach using complex networks. *EPL (Europhysics Letters)*, **128**(1), 14003.

236. **Krishnan, A.**, **R. Sujith**, **N. Marwan**, and **J. Kurths** (2021). Suppression of thermoacoustic instability by targeting the hubs of the turbulent networks in a bluff body stabilized combustor. *Journal of Fluid Mechanics*, **916**, A20.

237. **Krishnan, A.**, **R. I. Sujith**, **N. Marwan**, and **J. Kurths** (2019*b*). On the emergence of large clusters of acoustic power sources at the onset of thermoacoustic instability in a turbulent combustor. *Journal of Fluid Mechanics*, **874**, 455–482.

238. **Krueger, P. S.**, **M. Hahsler**, **E. V. Olinick**, **S. H. Williams**, and **M. Zharfa** (2019). Quantitative classification of vortical flows based on topological features using graph matching. *Proceedings of the Royal Society A: Mathematical, Physical and Engineering Sciences*, **475**(2228), 20180897.

239. **Kumar, A.**, **S. Cardanobile**, **S. Rotter**, and **A. Aertsen** (2011). The role of inhibition in

generating and controlling Parkinson's disease oscillations in the basal ganglia. *Frontiers in Systems Neuroscience*, **5**, 86.

240. **Kurosaka, T.**, **S. Masuda**, and **H. Gotoda** (2021). Attenuation of thermoacoustic combustion oscillations in a swirl-stabilized turbulent combustor. *Chaos: An Interdisciplinary Journal of Nonlinear Science*, **31**(7).

241. **Lakshmanan, M.** and **K. Murali**, *Chaos in nonlinear oscillators: controlling and synchronization*, volume 13. World Scientific, 1996.

242. **Lakshmanan, M.** and **D. V. Senthilkumar**, *Dynamics of nonlinear time-delay systems*. Springer Science & Business Media, 2011.

243. **Lancichinetti, A.** and **S. Fortunato** (2011). Limits of modularity maximization in community detection. *Physical Review E*, **84**(6), 066122.

244. **Lancichinetti, A.**, **S. Fortunato**, and **F. Radicchi** (2008). Benchmark graphs for testing community detection algorithms. *Physical Review E*, **78**(4), 046110.

245. **Lang, W.**, **T. Poinsot**, and **S. Candel** (1987). Active control of combustion instability. *Combustion and Flame*, **70**(3), 281–289.

246. **Langhorne, P.**, **A. Dowling**, and **N. Hooper** (1990). Practical active control system for combustion oscillations. *Journal of Propulsion and Power*, **6**(3), 324–333.

247. **Lato, T.**, **A. Mohany**, and **M. Hassan** (2019). A passive damping device for suppressing acoustic pressure pulsations: The infinity tube. *The Journal of the Acoustical Society of America*, **146**(6), 4534–4544.

248. **Latora, V.**, **V. Nicosia**, and **G. Russo**, *Complex networks: principles, methods and applications*. Cambridge University Press, 2017.

249. **Laudien, E.**, **R. Pongratz**, **R. Pierro**, and **D. Preclik** (1995*a*). Experimental Procedures Aiding the Design of Acoustic Cavities. *Progress in Astronautics and Aeronautics*, **169**, 377–402.

250. **Laudien, E.**, **R. Pongratz**, **R. Pierro**, and **D. Preclik** (1995*b*). Experimental procedures aiding the design of acoustic cavities. *Progress in Astronautics and Aeronautics*, **169**, 377–402.

251. **Lee, J.**, **S. Lukachko**, and **I. Waitz** (2004). Aircraft and energy use. *Encyclopedia of Energy*, **1**, 29–38.

252. **Lee, J. G.**, **K. Kim**, and **D. Santavicca** (2000). Measurement of equivalence ratio fluctuation and its effect on heat release during unstable combustion. *Proceedings of the Combustion Institute*, **28**(1), 415–421.

253. **Lefebvre, A. H.**, Lean premixed/prevaporized combustion. *In Workshop*, NASA-CP-2016. 1977.

254. **Lefebvre, A. H.** and **D. R. Ballal**, *Gas turbine combustion: alternative fuels and emissions*. CRC press, 2010.

255. **Lei, L.**, **G. Zhihui**, **Z. Chengyu**, and **S. Xiaofeng** (2010). A passive method to control combustion instabilities with perforated liner. *Chinese Journal of Aeronautics*, **23**(6), 623–630.

256. **Lei, S.** and **A. Turan** (2009). Nonlinear/chaotic behaviour in thermo-acoustic instability. *Combustion Theory and Modelling*, **13**(3), 541–557.

257. **Leicht, E. A.** and **M. E. J. Newman** (2008). Community structure in directed networks. *Physical Review Letters*, **100**(11), 118703.

258. **Lewis, N. S.** (2007). Powering the planet. *MRS bulletin*, **32**(10), 808–820.

259. **Li, H.**, **A. ElKady**, and **A. Evulet**, Effect of exhaust gas recirculation on NO_x formation in premixed combustion system. *In 47th AIAA Aerospace Sciences Meeting Including The New Horizons Forum and Aerospace Exposition*. 2009.

260. **Li, H.**, **G. Haugen**, **M. Ditaranto**, **D. Berstad**, and **K. Jordal** (2011). Impacts of exhaust gas recirculation (EGR) on the natural gas combined cycle integrated with chemical absorption CO_2 capture technology. *Energy Procedia*, **4**, 1411–1418.

261. **Li, Q.**, **Y. Hou**, **N. Xiang**, **Y. Liu**, and **Z. Huang** (2020). A new insight into the promotional effect of nitrogen-doping in activated carbon for selective catalytic reduction of NO_x with NH_3. *Science of The Total Environment*, **740**, 140158.

262. **Li, W.**, **D. Zhao**, **X. Chen**, **Y. Sun**, **S. Ni**, **D. Guan**, and **B. Wang** (2021). Numerical investigations on solid-fueled ramjet inlet thermodynamic properties effects on generating self-sustained combustion instability. *Aerospace Science and Technology*, **119**, 107097.

263. **Lieuwen, T.** and **A. Banaszuk** (2005). Background noise effects on combustor stability. *Journal of Propulsion and Power*, **21**(1), 25–31.

264. **Lieuwen, T.**, **V. McDonell**, **E. Petersen**, and **D. Santavicca** (2008). Fuel flexibility influences on premixed combustor blowout, flashback, autoignition, and stability. *Journal of Engineering for Gas Turbines and Power*, **130**(1).

265. **Lieuwen, T.** and **K. McManus** (2003). Introduction: Combustion dynamics in lean-premixed prevaporized (LPP) gas turbines. *Journal of Propulsion and Power*, **19**(5), 721–721.

266. **Lieuwen, T.** and **Y. Neumeier** (2002). Nonlinear pressure-heat release transfer function measurements in a premixed combustor. *Proceedings of the Combustion Institute*, **29**(1),

99–105.

267. **Lieuwen, T.**, **Y. Neumeier**, and **B. T. Zinn** (1998). The role of unmixedness and chemical kinetics in driving combustion instabilities in lean premixed combustors. *Combustion Science and Technology*, **135**(1-6), 193–211.

268. **Lieuwen, T. C.** (2002). Experimental investigation of limit-cycle oscillations in an unstable gas turbine combustor. *Journal of Propulsion and Power*, **18**(1), 61–67.

269. **Lieuwen, T. C.**, *Unsteady combustor physics*. Cambridge University Press, 2012.

270. **Lieuwen, T. C.** and **V. Yang**, *Combustion Instabilities in Gas Turbine Engines: Operational Experience, Fundamental Mechanisms, and Modeling*. American Institute of Aeronautics and Astronautics, 2005.

271. **Lin, J.** and **Y. Ban** (2013). Complex network topology of transportation systems. *Transport Reviews*, **33**(6), 658–685.

272. **Liu, Y.**, **J. Li**, **Z. Tian**, **T. Zhang**, and **Y. Yan** (2022). Experimental Studies on Suppression of Combustion Instability with the Addition of Helium. *Journal of Applied Fluid Mechanics*, **15**(6), 1703–1715.

273. **Liu, Z.**, **H. Zhou**, **D. Wei**, and **H. Fang** (2021). Experimental research on using CO_2-Ar microjets to control liquid fuel combustion instability and pollutant emission. *Journal of the Energy Institute*, **98**, 346–353.

274. **Lores, M. E.** and **B. T. Zinn** (1973). Nonlinear Longitudinal Combustion Instability in Rocket Motors. *Combustion Science and Technology*, **7**(6), 245–256.

275. **Lořstad, D.**, **J. Pettersson**, and **A. Lindholm**, Emission reduction and cooling improvements due to the introduction of passive acoustic damping in an existing sgt-800 combustor. *In Turbo Expo: Power for Land, Sea, and Air*, volume 48845. 2009.

276. **Lubarsky, E.**, **D. Shcherbik**, **A. Bibik**, and **B. Zinn**, Open loop control of severe combustion instabilities by fuel flow modulation at non resonant frequencies. *In 42nd AIAA Aerospace Sciences Meeting and Exhibit*. 2004.

277. **Luque, S.**, **V. Kanjirakkad**, **I. Aslanidou**, **R. Lubbock**, **B. Rosic**, and **S. Uchida** (2015). A new experimental facility to investigate combustor–turbine interactions in gas turbines with multiple can combustors. *Journal of Engineering for Gas Turbines and Power*, **137**(5), 051503.

278. **Lüthje, O.**, **S. Wolff**, and **G. Pfister** (2001). Control of chaotic Taylor-Couette flow with time-delayed feedback. *Physical Review Letters*, **86**(9), 1745.

279. **Lynn, C. W.** and **D. S. Bassett** (2019). The physics of brain network structure, function and control. *Nature Reviews Physics*, **1**(5), 318–332.

280. **Lyon, R. K.** (1987). Thermal DeNO$_x$ controlling nitrogen oxides emissions by a noncatalytic process. *Environmental Science & Technology*, **21**(3), 231–236.

281. **Ma, F.**, **J. Li**, **V. Yang**, **K.-C. Lin**, and **T. Jackson**, Thermoacoustic flow instability in a scramjet combustor. *In 41st AIAA/ASME/SAE/ASEE Joint Propulsion Conference & Exhibit*. 2005.

282. **Magri, L.** and **M. P. Juniper** (2013). Sensitivity analysis of a time-delayed thermoacoustic system via an adjoint-based approach. *Journal of Fluid Mechanics*, **719**, 183–202.

283. **Mahesh, S.**, **R. Gopakumar**, **B. Rahul**, **A. Dutta**, **S. Mondal**, and **S. Chaudhuri** (2018). Instability control by actuating the swirler in a lean premixed combustor. *Journal of Propulsion and Power*, **34**(3), 708–719.

284. **Mankbadi, R.** and **J. T. C. Liu** (1984). Sound generated aerodynamically revisited: large-scale structures in a turbulent jet as a source of sound. *Philosophical Transactions of the Royal Society of London. Series A, Mathematical and Physical Sciences*, **311**(1516), 183–217.

285. **Manoj, K.**, **S. A. Pawar**, **J. Kurths**, and **R. I. Sujith** (2022). Rijke tube: A nonlinear oscillator. *Chaos: An Interdisciplinary Journal of Nonlinear Science*, **32**(7), 072101. ISSN 1054-1500.

286. **Manoj, K.**, **S. A. Pawar**, and **R. I. Sujith** (2018). Experimental evidence of amplitude death and phase-flip bifurcation between in-phase and anti-phase synchronization. *Scientific Reports*, **8**(1), 1–7.

287. **Marbán, G.**, **R. Antuña**, and **A. B. Fuertes** (2003). Low-temperature SCR of NO$_x$ with NH$_3$ over activated carbon fiber composite-supported metal oxides. *Applied Catalysis B: Environmental*, **41**(3), 323–338.

288. **Marble, F. E.** and **D. W. Cox Jr** (1953). Servo-stabilization of low-frequency oscillations in a liquid bipropellant rocket motor. *Journal of the American Rocket Society*, **23**(2), 63–74.

289. **Mariappan, S.** and **R. Sujith** (2011). Modelling nonlinear thermoacoustic instability in an electrically heated Rijke tube. *Journal of Fluid Mechanics*, **680**, 511–533.

290. **Masson-Delmotte, V.**, **P. Zhai**, **A. Pirani**, **S. Connors**, **C. Péan**, **S. Berger**, **N. Caud**, **Y. Chen**, **L. Goldfarb**, **M. Gomis**, **M. Huang**, **K. Leitzell**, **E. Lonnoy**, **J. Matthews**, **T. Maycock**, **T. Waterfield**, **O. Yelekçi**, **R. Yu**, and **B. Zhou** (eds.), *Climate Change 2021: The Physical Science Basis. Contribution of Working Group I to the Sixth Assessment Report of the Intergovernmental Panel on Climate Change*. Cambridge University Press, 2021.

291. **Matveev, K. I.**, *Thermoacoustic instabilities in the Rijke tube: Experiments and modeling*.

California Institute of Technology, 2003.

292. **Matveev, K. I.** and **F. Culick** (2003). A model for combustion instability involving vortex shedding. *Combustion Science and Technology*, **175**(6), 1059–1083.

293. **McManus, K.**, **F. Han**, **W. Dunstan**, **C. Barbu**, and **M. Shah**, Modeling and control of combustion dynamics in industrial gas turbines. *In Turbo Expo: Power for Land, Sea, and Air*, volume 41669. 2004.

294. **McSherry, F.**, Spectral partitioning of random graphs. *In Proceedings 42nd IEEE Symposium on Foundations of Computer Science*. IEEE, 2001.

295. **Meilă, M.** (2007). Comparing clusterings—an information based distance. *Journal of Multivariate Analysis*, **98**(5), 873–895.

296. **Mirollo, R. E.** and **S. H. Strogatz** (1990). Amplitude death in an array of limit-cycle oscillators. *Journal of Statistical Physics*, **60**(1), 245–262.

297. **Mok, Y. S.** and **H.-J. Lee** (2006). Removal of sulfur dioxide and nitrogen oxides by using ozone injection and absorption–reduction technique. *Fuel Processing Technology*, **87**(7), 591–597.

298. **Mondal, S.**, **S. A. Pawar**, and **R. I. Sujith** (2019). Forced synchronization and asynchronous quenching of periodic oscillations in a thermoacoustic system. *Journal of Fluid Mechanics*, **864**, 73–96.

299. **Mondal, S.**, **V. R. Unni**, and **R. I. Sujith** (2017). Onset of thermoacoustic instability in turbulent combustors: an emergence of synchronized periodicity through formation of chimera-like states. *Journal of Fluid Mechanics*, **811**, 659–681.

300. **Mongia, H. C.**, **T. Held**, **G. Hsiao**, and **R. Pandalai** (2003). Challenges and progress in controlling dynamics in gas turbine combustors. *Journal of Propulsion and Power*, **19**(5), 822–829.

301. **Montoya, J. M.**, **S. L. Pimm**, and **R. V. Solé** (2006). Ecological networks and their fragility. *Nature*, **442**(7100), 259–264.

302. **Moon, K.**, **Y. Guan**, **L. K. B. Li**, and **K. T. Kim** (2020*a*). Mutual synchronization of two flame-driven thermoacoustic oscillators: Dissipative and time-delayed coupling effects. *Chaos: An Interdisciplinary Journal of Nonlinear Science*, **30**(2), 023110.

303. **Moon, K.**, **H. Jegal**, **C. Yoon**, and **K. T. Kim** (2020*b*). Cross-talk-interaction-induced combustion instabilities in a can-annular lean-premixed combustor configuration. *Combustion and Flame*, **220**, 178–188.

304. **Moon, K.**, **C. Yoon**, and **K. T. Kim** (2021). Influence of rotational asymmetry on thermoacoustic instabilities in a can-annular lean-premixed combustor. *Combustion and*

Flame, **223**, 295–306.

305. **Morgan, C.** and **B. Phillips** (1967). Mechanical absorption of acoustic oscillations in simulated rocket combustion chambers. Technical report, National Aeronautics and Space Administration.

306. **Murayama, S.** and **H. Gotoda** (2019). Attenuation behavior of thermoacoustic combustion instability analyzed by a complex-network-and synchronization-based approach. *Physical Review E*, **99**(5), 052222.

307. **Murayama, S.**, **H. Kinugawa**, **I. T. Tokuda**, and **H. Gotoda** (2018). Characterization and detection of thermoacoustic combustion oscillations based on statistical complexity and complex-network theory. *Physical Review E*, **97**(2), 022223.

308. **Murcio, R.**, **A. P. Masucci**, **E. Arcaute**, and **M. Batty** (2015). Multifractal to monofractal evolution of the London street network. *Physical Review E*, **92**(6), 062130.

309. **Murugappan, S.**, **S. Acharya**, **D. Allgood**, **S. Park**, **A. Annaswamy**, and **A. Ghoniem** (2003). Optimal control of a swirl-stabilized spray combustor using system identification approach. *Combustion Science and Technology*, **175**(1), 55–81.

310. **Murugappan, S.**, **E. Gutmark**, and **S. Acharya**, Application of extremum seeking controller for suppression of combustion instabilities in spray combustion. *In 38th Aerospace Sciences Meeting and Exhibit*. 2000.

311. **Murugesan, M.** and **R. I. Sujith** (2015). Combustion noise is scale-free: transition from scale-free to order at the onset of thermoacoustic instability. *Journal of Fluid Mechanics*, **772**, 225–245.

312. **Musielak, Z. E.** and **D. Musielak** (2009). High-dimensional chaos in dissipative and driven dynamical systems. *International Journal of Bifurcation and Chaos*, **19**(09), 2823–2869.

313. **Myerson, A. L.**, The reduction of nitric oxide in simulated combustion effluents by hydrocarbon-oxygen mixtures. *In Symposium (International) on Combustion*, volume 15. Elsevier, 1975.

314. **Nair, A. G.**, **S. L. Brunton**, and **K. Taira** (2018). Networked-oscillator-based modeling and control of unsteady wake flows. *Physical Review E*, **97**(6), 063107.

315. **Nair, A. G.** and **K. Taira** (2015). Network-theoretic approach to sparsified discrete vortex dynamics. *Journal of Fluid Mechanics*, **768**, 549–571.

316. **Nair, V.** and **R. Sujith** (2014). Multifractality in combustion noise: predicting an impending combustion instability. *Journal of Fluid Mechanics*, **747**, 635–655.

317. **Nair, V.**, **G. Thampi**, and **R. Sujith** (2014). Intermittency route to thermoacoustic

instability in turbulent combustors. *Journal of Fluid Mechanics*, **756**, 470–487.

318. **Natanzon, M. S.**, *Combustion instability*. American Institute of Aeronautics and Astronautics, 2008.

319. **Naumann, N. L.**, **S. M. Hein**, **A. Knorr**, and **J. Kabuss** (2014). Steady-state control in an unstable optomechanical system. *Physical Review A*, **90**(4), 043835.

320. **Neamtu-Halic, M. M.**, **D. Krug**, **G. Haller**, and **M. Holzner** (2019). Lagrangian coherent structures and entrainment near the turbulent/non-turbulent interface of a gravity current. *Journal of Fluid Mechanics*, **877**, 824–843.

321. **Newman, M.** (2008). The physics of networks. *Physics Today*, **61**(11), 33–38.

322. **Newman, M.**, *Networks*. Oxford University Press, 2018.

323. **Newman, M. E.** (2003). The structure and function of complex networks. *SIAM Review*, **45**(2), 167–256.

324. **Newman, M. E.** (2006). Modularity and community structure in networks. *Proceedings of the National Academy of Sciences of the United States of America*, **103**(23), 8577–8582.

325. **Newman, M. E. J.** (2004). Fast algorithm for detecting community structure in networks. *Physical Review E*, **69**(6), 066133.

326. **Newman, M. E. J.** and **M. Girvan** (2004). Finding and evaluating community structure in networks. *Physical Review E*, **69**(2), 026113.

327. **Noiray, N.**, **D. Durox**, **T. Schuller**, and **S. Candel** (2007). Passive control of combustion instabilities involving premixed flames anchored on perforated plates. *Proceedings of the Combustion Institute*, **31**(1), 1283–1290.

328. **O'Connor, J.**, **V. Acharya**, and **T. Lieuwen** (2015). Transverse combustion instabilities: Acoustic, fluid mechanic, and flame processes. *Progress in Energy and Combustion Science*, **49**, 1–39.

329. **O'Connor, J.**, **S. Hemchandra**, and **T. Lieuwen**, Combustion instabilities in lean premixed systems. *In Lean Combustion*. Elsevier, 2016, 231–259.

330. **Okuno, Y.**, **M. Small**, and **H. Gotoda** (2015). Dynamics of self-excited thermoacoustic instability in a combustion system: Pseudo-periodic and high-dimensional nature. *Chaos: An Interdisciplinary Journal of Nonlinear Science*, **25**(4), 043107.

331. **Orchini, A.**, **T. Pedergnana**, **P. E. Buschmann**, **J. P. Moeck**, and **N. Noiray** (2022). Reduced-order modelling of thermoacoustic instabilities in can-annular combustors. *Journal of Sound and Vibration*, **526**, 116808.

332. **Otte, E.** and **R. Rousseau** (2002). Social network analysis: a powerful strategy, also for the information sciences. *Journal of information Science*, **28**(6), 441–453.

333. **Ouyang, H.**, **W. Liu**, and **M. Sun** (2015). The large-amplitude combustion oscillation in a single-side expansion scramjet combustor. *Acta Astronautica*, **117**, 90–98.

334. **Ouyang, H.**, **W. Liu**, and **M. Sun** (2016). Parametric study of combustion oscillation in a single-side expansion scramjet combustor. *Acta Astronautica*, **127**, 603–613.

335. **Ouyang, H.**, **W. Liu**, and **M. Sun** (2017). The influence of cavity parameters on the combustion oscillation in a single-side expansion scramjet combustor. *Acta Astronautica*, **137**, 52–59.

336. **Ozden, I.**, **S. Venkataramani**, **M. Long**, **B. Connors**, and **A. Nurmikko** (2004). Strong coupling of nonlinear electronic and biological oscillators: Reaching the "amplitude death" regime. *Physical Review Letters*, **93**(15), 158102.

337. **Pandalai, R.** and **H. Mongia**, Combustion instability characteristics of industrial engine dry low emission combustion systems. *In 34th AIAA/ASME/SAE/ASEE Joint Propulsion Conference and Exhibit*. 1998.

338. **Park, I.-S.** and **C. H. Sohn** (2010). Nonlinear acoustic damping induced by a half-wave resonator in an acoustic chamber. *Aerospace Science and Technology*, **14**(6), 442–450.

339. **Park, J. H.**, **Y. T. Guahk**, and **H. D. Shin**, Thermo-acoustic Instability in a Combustor with Branch Tube. *In 7th; JSME & KSME ME-Conference Papers*. JSME-KSME, 2008.

340. **Park, J.-H.**, **D.-K. Lee**, and **H.-D. Shin** (2009). Experimental Study on the Characteristics of Pressure Fluctuation in the Combustion Chamber with Branch Tube. *Transactions of the Korean Society of Mechanical Engineers, B*, **33**(7), 552–558.

341. **Park, J. H.** and **C. H. Sohn** (2009). On optimal design of half-wave resonators for acoustic damping in an enclosure. *Journal of Sound and Vibration*, **319**(3-5), 807–821.

342. **Parker, L.**, **R. Sawyer**, and **A. Ganji** (1979). Measurement of vortex frequencies in a lean, premixed prevaporized combustor. *Combust. Science and Technology*, **20**(5-6), 235–241.

343. **Parmananda, P.**, **R. Madrigal**, **M. Rivera**, **L. Nyikos**, **I. Z. Kiss**, and **V. Gáspár** (1999). Stabilization of unstable steady states and periodic orbits in an electrochemical system using delayed-feedback control. *Physical Review E*, **59**(5), 5266.

344. **Parzen, E.** (1962). On estimation of a probability density function and mode. *The Annals of Mathematical Statistics*, **33**(3), 1065–1076.

345. **Paschereit, C. O.** and **E. Gutmark** (2008). Combustion Instability and Emission Control by Pulsating Fuel Injection. *Journal of Turbomachinery*, **130**(1), 011012. ISSN

0889-504X.

346. **Paschereit, C. O.**, **E. Gutmark**, and **W. Weisenstein** (1999). Coherent structures in swirling flows and their role in acoustic combustion control. *Physics of Fluids*, **11**(9), 2667–2678.

347. **Passarelli, M. L.**, **A. Kazbekov**, **V. Salazar**, **K. Venkatesan**, and **A. M. Steinberg** (2023). Experimental study of forced synchronization and cross-coupling in a liquid-fuelled gas turbine combustor at elevated pressure. *Proceedings of the Combustion Institute*, **39**(4), 4751–4759. ISSN 1540-7489.

348. **Pavan, C. A.**, **C. Guerra-Garcia**, **D. Weibel**, **M. Nishihara**, **F. del Campo**, **S. Shanbhogue**, and **A. Ghoniem**, Nanosecond pulsed discharge dynamics in a swirl-stabilized combustor with an unstable flame. *In AIAA Aviation 2022 forum*. 2022.

349. **Pavithran, I.**, **V. R. Unni**, **A. J. Varghese**, **D. Premraj**, **R. Sujith**, **C. Vijayan**, **A. Saha**, **N. Marwan**, and **J. Kurths** (2020). Universality in spectral condensation. *Scientific Reports*, **10**(1), 1–8.

350. **Pawar, S. A.**, **S. Mondal**, **N. B. George**, and **R. I. Sujith** (2019). Temporal and Spatiotemporal Analyses of Synchronization Transition in a Swirl-Stabilized Combustor. *AIAA Journal*, **57**(2), 836–847.

351. **Pawar, S. A.**, **A. Seshadri**, **V. R. Unni**, and **R. I. Sujith** (2017). Thermoacoustic instability as mutual synchronization between the acoustic field of the confinement and turbulent reactive flow. *Journal of Fluid Mechanics*, **827**, 664–693.

352. **Pedergnana, T.** and **N. Noiray** (2022*a*). Coupling-induced instability in a ring of thermoacoustic oscillators. *Proceedings of the Royal Society A*, **478**(2259), 20210851.

353. **Pedergnana, T.** and **N. Noiray** (2022*b*). Steady-state statistics, emergent patterns and intermittent energy transfer in a ring of oscillators. *Nonlinear Dynamics*, **108**(2), 1133–1163.

354. **Penelet, G.** and **T. Biwa** (2013). Synchronization of a thermoacoustic oscillator by an external sound source. *American Journal of Physics*, **81**(4), 290–297.

355. **Peracchio, A. A.** and **W. M. Proscia** (1999). Nonlinear Heat-Release/Acoustic Model for Thermoacoustic Instability in Lean Premixed Combustors. *Journal of Engineering for Gas Turbines and Power*, **121**(3), 415–421. ISSN 0742-4795.

356. **Perry, E. H.**, *Investigations of the T-burner and its Role in Combustion Instability Studies*. California Institute of Technology, 1970.

357. **Phillips, B.**, *On the Design of Acoustic Liners for Rocket Engines: Helmholtz Resonators Evaluated with a Rocket Combustor*. National Aeronautics and Space Administration, 1969.

358. **Pierce, A. D.** (1983). Sound and Sources of Sound by Ann P. Dowling and John E. Ffowcs Williams. *The Journal of the Acoustical Society of America*, **74**(5), 1660–1661. ISSN 0001-4966.

359. **Pierre, T.**, **G. Bonhomme**, and **A. Atipo** (1996). Controlling the chaotic regime of nonlinear ionization waves using the time-delay autosynchronization method. *Physical Review Letters*, **76**(13), 2290.

360. **Pikovsky, A.**, **M. Rosenblum**, and **J. Kurths**, *Synchronization: A Universal Concept in Nonlinear Sciences*. 12. Cambridge University Press, 2003.

361. **Pitz, R.** and **J. Daily**, Experimental study of combustion in a turbulent free shear layer formed at a rearward facing step. *In 19th Aerospace Sciences Meeting*. 1981.

362. **Poinsot, T.** (2017). Prediction and control of combustion instabilities in real engines. *Proceedings of the Combustion Institute*, **36**(1), 1–28.

363. **Poinsot, T.**, **F. Bourienne**, **S. Candel**, **E. Esposito**, and **W. Lang** (1989). Suppression of combustion instabilities by active control. *Journal of Propulsion and Power*, **5**(1), 14–20.

364. **Poinsot, T. J.**, **A. C. Trouve**, **D. P. Veynante**, **S. M. Candel**, and **E. J. Esposito** (1987). Vortex-driven acoustically coupled combustion instabilities. *Journal of Fluid Mechanics*, **177**, 265–292.

365. **Prasad, C.** and **P. Morris** (2019). Effect of fluid injection on turbulence and noise reduction of a supersonic jet. *Philosophical Transactions of the Royal Society of London. Series A, Mathematical and Physical Sciences*, **377**(2159), 20190082.

366. **Prasanth, R.**, **A. Annaswamy**, **J. Hathout**, and **A. Ghoniem** (2002). When do open-loop strategies for combustion control work? *Journal of Propulsion and Power*, **18**(3), 658–668.

367. **Prell, C.**, **K. Hubacek**, and **M. Reed** (2009). Stakeholder analysis and social network analysis in natural resource management. *Society & Natural Resources*, **22**(6), 501–518.

368. **Premchand, C. P.**, **A. Krishnan**, **M. Raghunathan**, **M. Raghunath**, **R. I. Sujith**, **V. Nair**, *et al.* (2023). Control of thermoacoustic instability through lagrangian saddle point analysis. *arXiv preprint arXiv:2308.14261*.

369. **Premraj, D.**, **S. A. Pawar**, **L. Kabiraj**, and **R. Sujith** (2020). Strange nonchaos in self-excited singing flames. *EPL (Europhysics Letters)*, **128**(5), 54005.

370. **Putnam, A. A.**, *Combustion-driven oscillations in industry*. Elsevier Publishing Company, 1971.

371. **Pyragas, K.**, **F. Lange**, **T. Letz**, **J. Parisi**, and **A. Kittel** (2000). Stabilization of an

unstable steady state in intracavity frequency-doubled lasers. *Physical Review E*, **61**(4), 3721.

372. **Qin, L.**, **X. Wang**, **G. Zhang**, and **X. Sun** (2021). Effect of nonlinear flame response on the design of perforated liners in suppression of combustion instability. *Journal of Sound and Vibration*, **511**, 116314.

373. **Raaj, A.**, **S. Mondal**, and **V. Jagdish** (2021). Investigating amplitude death in a coupled nonlinear aeroelastic system. *International Journal of Non-Linear Mechanics*, **129**, 103659.

374. **Raffel, M.**, **C. E. Willert**, **J. Kompenhans**, *et al.*, *Particle image velocimetry: a practical guide*, volume 2. Springer, 1998.

375. **Raghunathan, M.**, **N. B. George**, **V. R. Unni**, **P. R. Midhun**, **K. V. Reeja**, and **R. I. Sujith** (2020). Multifractal analysis of flame dynamics during transition to thermoacoustic instability in a turbulent combustor. *Journal of Fluid Mechanics*, **888**.

376. **Raj, A.**, **A. Raaj**, **J. Venkatramani**, and **S. Mondal** (2021). Effect of parameter mismatch and dissipative coupling on amplitude death regime in a coupled nonlinear aeroelastic system. *Chaos: An Interdisciplinary Journal of Nonlinear Science*, **31**(12).

377. **Rajaram, R.** and **D. M. Ritland** (2012). Attenuation of combustion dynamics using a Herschel-Quincke filter. US Patent 8,336,312.

378. **Ralph, M.**, **P. Kuentzmann**, **L. Maurice**, and **J. Tilston** (2009). Report of the independent experts to CAEP/8 on the second NO_x review & long term technology goals. *London, March.*

379. **Raun, R. L.**, **M. W. Beckstead**, **J. C. Finlinson**, and **K. P. Brooks** (1993). A review of Rijke tubes, Rijke burners and related devices. *Progress in Energy and Combustion Science*, **19**(4), 313–364.

380. **Rawlins, D. C.**, Dry Low Emissions: Improvements to the SoLoN0x Combustion System. *In Eleventh Symposium on Industrial Applications of Gas Turbines Canadian Gas Association, Banff, Alberta, Canada, October*. 1995.

381. **Rayleigh, J. W. S.**, *The Theory of Sound*, volume 2. Dover, 1945.

382. **Rayleigh, L.** (1878). The explanation of certain acoustical phenomena. *Nature*, **8**, 536–542.

383. **Reddy, D. V. R.**, **A. Sen**, and **G. L. Johnston** (2000). Dynamics of a Limit Cycle Oscillator under Time Delayed Linear and Nonlinear Feedbacks. *Physica D: Nonlinear Phenomena*, **144**(3-4), 335–357.

384. **Reichardt, J.** and **S. Bornholdt** (2006). Statistical mechanics of community detection.

Physical Review E, **74**(1), 016110.

385. **Reichel, T. G.** and **C. O. Paschereit** (2017). Interaction mechanisms of fuel momentum with flashback limits in lean-premixed combustion of hydrogen. *International Journal of Hydrogen Energy*, **42**(7), 4518–4529.

386. **Renard, P.-H.**, **D. Thevenin**, **J.-C. Rolon**, and **S. Candel** (2000). Dynamics of flame/vortex interactions. *Progress in Energy and Combustion Science*, **26**(3), 225–282.

387. **Ressler, S.** (2006). Social network analysis as an approach to combat terrorism: Past, present, and future research. *Homeland Security Affairs*, **2**(2).

388. **Richards, G. A.** and **M. C. Janus** (1998). Characterization of Oscillations During Premix Gas Turbine Combustion. *Journal of Engineering for Gas Turbines and Power*, **120**(2), 294–302. ISSN 0742-4795.

389. **Richards, G. A.**, **D. L. Straub**, and **E. H. Robey** (2003). Passive control of combustion dynamics in stationary gas turbines. *Journal of Propulsion and Power*, **19**(5), 795–810.

390. **Richards, G. A.**, **J. D. Thornton**, **E. H. Robey**, and **L. Arellano** (2006). Open-loop active control of combustion dynamics on a gas turbine engine. *Journal of Engineering for Gas Turbines and Power*, **129**(1), 38–48.

391. **Richardson, L. F.**, *Weather prediction by numerical process*. University Press, 1922.

392. **Rijke, P. L.** (1859). On the Vibration of the Air in a Rijke Tube Open at Both Ends. *Philosophical Magazine*, **17**(116), 419–422.

393. **Ritchie, H.**, **M. Roser**, and **P. Rosado** (2020). CO_2 and Greenhouse Gas Emissions. *Our World in Data*. Https://ourworldindata.org/co2-and-greenhouse-gas-emissions.

394. **Rizk, N.** and **H. Mongia**, *Low* NO_x *rich-lean combustion concept application*. AIAA Paper 91-1962. AIAA, Sacramento, California, USA, 1991.

395. **Rogers, D. E.** and **F. E. Marble** (1956). A mechanism for high-frequency oscillation in ramjet combustors and afterburners. *Journal of Jet Propulsion*, **26**(6), 456–462.

396. **Røkke, P.** and **J. Hustad** (2005). Exhaust gas recirculation in gas turbines for reduction of CO_2 emissions; combustion testing with focus on stability and emissions. *International Journal of Thermodynamics*, **8**(4), 167–173.

397. **Roongthumskul, Y.**, **J. Faber**, and **D. Bozovic** (2021). Dynamics of mechanically coupled hair-cell bundles of the inner ear. *Biophysical Journal*, **120**(2), 205–216. ISSN 0006-3495.

398. **Rosic, B.**, **J. D. Denton**, **J. H. Horlock**, and **S. Uchida** (2011). Integrated Combustor and Vane Concept in Gas Turbines. *Journal of Turbomachinery*, **134**(3), 031005. ISSN

0889-504X.

399. **Roy, A.**, **S. Mondal**, **S. A. Pawar**, and **R. I. Sujith** (2020). On the mechanism of open-loop control of thermoacoustic instability in a laminar premixed combustor. *Journal of Fluid Mechanics*, **884**.

400. **Roy, A.**, **C. P. Premchand**, **M. Raghunathan**, **A. Krishnan**, **V. Nair**, and **R. I. Sujith** (2021). Critical region in the spatiotemporal dynamics of a turbulent thermoacoustic system and smart passive control. *Combustion and Flame*, **226**, 274–284.

401. **Samojeden, B.** and **T. Grzybek** (2016). The influence of the promotion of N-modified activated carbon with iron on NO removal by NH_3-SCR (Selective Catalytic Reduction). *Energy*, **116**, 1484–1491.

402. **Sattinger, S. S.**, **Y. Neumeier**, **A. Nabi**, **B. T. Zinn**, **D. J. Amos**, and **D. D. Darling** (2000). Sub-scale demonstration of the active feedback control of gas-turbine combustion instabilities. *Journal of Engineering for Gas Turbines and Power*, **122**(2), 262–268.

403. **Sawyer, R. F.** (2009). Science based policy for addressing energy and environmental problems. *Proceedings of the Combustion Institute*, **32**(1), 45–56.

404. **Sayadi, T.**, **V. Le Chenadec**, **P. J. Schmid**, **F. Richecoeur**, and **M. Massot** (2014). Thermoacoustic instability–a dynamical system and time domain analysis. *Journal of Fluid Mechanics*, **753**, 448–471.

405. **Schadow, K.** and **E. Gutmark** (1992). Combustion instability related to vortex shedding in dump combustors and their passive control. *Progress in Energy and Combustion Science*, **18**(2), 117–132.

406. **Schadow, K.**, **E. Gutmark**, **T. Parr**, **D. Parr**, **K. Wilson**, and **J. Crump** (1989). Large-scale coherent structures as drivers of combustion instability. *Combustion Science and Technology*, **64**(4-6), 167–186.

407. **Schlueter-Kuck, K. L.** and **J. O. Dabiri** (2017). Coherent structure colouring: identification of coherent structures from sparse data using graph theory. *Journal of Fluid Mechanics*, **811**, 468–486.

408. **Schneide, C.**, **A. Pandey**, **K. Padberg-Gehle**, and **J. Schumacher** (2018). Probing turbulent superstructures in Rayleigh-Bénard convection by Lagrangian trajectory clusters. *Physical Review Fluids*, **3**(11), 113501.

409. **Schöll, E.**, **P. Hövel**, **V. Flunkert**, and **M. A. Dahlem**, Time-delayed feedback control: from simple models to lasers and neural systems. *In Complex time-delay systems*. Springer, 2009, 85–150.

410. **Schuermans, B.**, **M. Bothien**, **M. Maurer**, and **B. Bunkute**, Combined acoustic damping-cooling system for operational flexibility of GT26/GT24 reheat combustors.

In Turbo Expo: Power for Land, Sea, and Air, volume 56680. American Society of Mechanical Engineers, 2015.

411. **Ser-Giacomi, E.**, **V. Rossi**, **C. López**, and **E. Hernandez-Garcia** (2015). Flow networks: A characterization of geophysical fluid transport. *Chaos: An Interdisciplinary Journal of Nonlinear Science*, **25**(3), 036404.

412. **Seshadri, A.** and **R. Sujith** (2016). A bifurcation giving birth to order in an impulsively driven complex system. *Chaos: An Interdisciplinary Journal of Nonlinear Science*, **26**(8), 083103.

413. **Seume, J. R.**, **N. Vortmeyer**, **W. Krause**, **J. Hermann**, **C.-C. Hantschk**, **P. Zangl**, **S. Gleis**, **D. Vortmeyer**, and **A. Orthmann** (1998). Application of Active Combustion Instability Control to a Heavy Duty Gas Turbine. *Journal of Engineering for Gas Turbines and Power*, **120**(4), 721–726. ISSN 0742-4795.

414. **Shampine, L. F.** and **S. Thompson** (2001). Solving DDEs in Matlab. *Applied Numerical Mathematics*, **37**(4), 441–458.

415. **Shanbogue, S.**, **D. Weibel**, **F. Gomez del Campo**, **C. Guerra-Garcia**, and **A. Ghoniem**, Active control of large amplitude combustion oscillations using nanosecond repetitively pulsed plasmas. *In AIAA Scitech 2022 Forum*. 2022.

416. **Shima, S.**, **K. Nakamura**, **H. Gotoda**, **Y. Ohmichi**, and **S. Matsuyama** (2021). Formation mechanism of high-frequency combustion oscillations in a model rocket engine combustor. *Physics of Fluids*, **33**(6), 064108.

417. **Shreekrishna, S. H.** and **T. Lieuwen** (2010). Premixed flame response to equivalence ratio perturbations. *Combustion Theory and Modelling*, **14**(5), 681–714.

418. **Singh, J.**, **R. Belur Vishwanath**, **S. Chaudhuri**, and **R. I. Sujith** (2017). Network structure of turbulent premixed flames. *Chaos: An Interdisciplinary Journal of Nonlinear Science*, **27**(4), 043107.

419. **Sirovich, L.** and **S. Karlsson** (1997). Turbulent drag reduction by passive mechanisms. *Nature*, **388**(6644), 753–755.

420. **Sivakumar, R.** and **S. Chakravarthy** (2008). Experimental investigation of the acoustic field in a bluff-body combustor. *International Journal of Aeroacoustics*, **7**(3-4), 267–299.

421. **Skalska, K.**, **J. Miller**, and **S. Ledakowicz** (2010). Kinetics of nitric oxide oxidation. *Chemical Papers*, **64**(2), 269–272.

422. **Skene, C. S.** and **K. Taira** (2022). Phase-reduction analysis of periodic thermoacoustic oscillations in a Rijke tube. *Journal of Fluid Mechanics*, **933**.

423. **Smith, K.**, **H. Brighton**, and **S. Kirby** (2003). Complex systems in language evolution:

the cultural emergence of compositional structure. *Advances in complex systems*, **6**(04), 537–558.

424. **Smith, K. O.** (2005). Combustion instabilities in industrial gas turbines: solar turbines' experience. *Progress in Astronautics and Aeronautics*, **210**, 29–41.

425. **Smoot, L.**, **S. Hill**, and **H. Xu** (1998). NOx control through reburning. *Progress in Energy and Combustion Science*, **24**(5), 385–408.

426. **Smoot, L. D.**, *Fundamentals of coal combustion for clean and efficient use*. Elsevier Science Ltd., 1993.

427. **Sohn, C. H.**, **I.-S. Park**, **S.-K. Kim**, and **H. J. Kim** (2007). Acoustic tuning of gas–liquid scheme injectors for acoustic damping in a combustion chamber of a liquid rocket engine. *Journal of Sound and Vibration*, **304**(3-5), 793–810.

428. **Sohn, C. H.** and **J. H. Park** (2011). A comparative study on acoustic damping induced by half-wave, quarter-wave, and Helmholtz resonators. *Aerospace Science and Technology*, **15**(8), 606–614.

429. **Sowa, J. F.** *et al.* (1992). Semantic networks. *Encyclopedia of artificial intelligence*, **2**, 1493–1511.

430. **Speth, R.**, **H. Altay**, **D. Hudgins**, **A. Annaswamy**, and **A. Ghoniem**, Vortex-driven combustion instabilities in step and swirl-stabilized combustors. *In 46th AIAA Aerospace Sciences Meeting and Exhibit*. 2008.

431. **Spicer, C.**, **M. Holdren**, **R. Riggin**, and **T. Lyon**, Chemical composition and photochemical reactivity of exhaust from aircraft turbine engines. *In Annales Geophysicae*, volume 12. Copernicus GmbH, 1994.

432. **Sporns, O.**, *Networks of the Brain*. MIT press, 2016.

433. **Sreenivasan, K.** and **C. Meneveau** (1986). The fractal facets of turbulence. *Journal of Fluid Mechanics*, **173**, 357–386.

434. **Srikanth, S.** (2022). *Dynamics Of Coupled Thermoacoustic Oscillators*. Bachelor's thesis, Indian Institute Of Technology Madras.

435. **Srikanth, S.**, **S. A. Pawar**, **K. Manoj**, and **R. I. Sujith** (2022). Dynamical states and bifurcations in coupled thermoacoustic oscillators. *Chaos: An Interdisciplinary Journal of Nonlinear Science*, **32**(7), 073129. ISSN 1054-1500.

436. **Steele, R. C.**, **L. H. Cowell**, **S. M. Cannon**, and **C. E. Smith** (2000). Passive control of combustion instability in lean premixed combustors. *Journal of Engineering for Gas Turbines and Power*, **122**(3), 412–419.

437. **Steinberg, A. M.**, **I. Boxx**, **M. Stöhr**, **C. D. Carter**, and **W. Meier** (2010). Flow–flame interactions causing acoustically coupled heat release fluctuations in a thermo-acoustically unstable gas turbine model combustor. *Combustion and Flame*, **157**(12), 2250–2266.

438. **Steinfurth, B.** and **F. Haucke** (2018). Coherent structures in the actively controlled wake of a high-lift configuration. *AIAA Journal*, **56**(10), 3848–3856.

439. **Sterling, J. D.** (1993). Nonlinear analysis and modelling of combustion instabilities in a laboratory combustor. *Combustion Science and Technology*, **89**(1-4), 167–179.

440. **Sterling, J. D.** and **E. E. Zukoski** (1991). Nonlinear dynamics of laboratory combustor pressure oscillations. *Combustion Science and Technology*, **77**(4-6), 225–238.

441. **Stöhr, M.**, **I. Boxx**, **C. Carter**, and **W. Meier** (2011). Dynamics of lean blowout of a swirl-stabilized flame in a gas turbine model combustor. *Proceedings of the Combustion Institute*, **33**(2), 2953–2960.

442. **Strogatz, S.**, *Sync: The emerging science of spontaneous order*. Penguin UK, 2004.

443. **Strogatz, S. H.**, **D. M. Abrams**, **A. McRobie**, **B. Eckhardt**, and **E. Ott** (2005). Crowd synchrony on the Millennium Bridge. *Nature*, **438**(7064), 43–44.

444. **Suchorsky, M. K.**, **S. M. Sah**, and **R. H. Rand** (2010). Using delay to quench undesirable vibrations. *Nonlinear Dynamics*, **62**(1), 407–416.

445. **Sujith, R. I.** and **S. A. Pawar**, *Thermoacoustic Instability - A Complex Systems Perspective*. Springer Nature, 2021.

446. **Summerfield, M.**, **E. W. Price**, and **L. D. Price**, *Nonsteady Burning and Combustion Stability of Solid Propellants*. AIAA, Reston, 1992.

447. **Sun, Y.** and **J. Han** (2013). Mining heterogeneous information networks: a structural analysis approach. *Acm Sigkdd Explorations Newsletter*, **14**(2), 20–28.

448. **Sutton, G. P.** (2003). History of liquid-propellant rocket engines in Russia, formerly the Soviet Union. *Journal of Propulsion and Power*, **19**(6), 1008–1037.

449. **Tachibana, S.**, **L. Zimmer**, **Y. Kurosawa**, and **K. Suzuki** (2007). Active control of combustion oscillations in a lean premixed combustor by secondary fuel injection coupling with chemiluminescence imaging technique. *Proccedings of the Combustion Institute*, **31**(2), 3225–3233.

450. **Taira, K.**, **S. L. Brunton**, **S. T. M. Dawson**, **C. W. Rowley**, **T. Colonius**, **B. J. McKeon**, **O. T. Schmidt**, **S. Gordeyev**, **V. Theofilis**, and **L. S. Ukeiley** (2017). Modal analysis of fluid flows: An overview. *AIAA Journal*, **55**(12), 4013–4041.

451. **Taira, K.** and **A. G. Nair** (2022). Network-based analysis of fluid flows: Progress and

outlook. *Progress in Aerospace Sciences*, **131**, 100823.

452. **Taira, K.**, **A. G. Nair**, and **S. L. Brunton** (2016). Network structure of two-dimensional decaying isotropic turbulence. *Journal of Fluid Mechanics*, **795**.

453. **Tandon, S.** and **R. I. Sujith** (2023). Multilayer network analysis to study complex inter-subsystem interactions in a turbulent thermoacoustic system. *Journal of Fluid Mechanics*, **966**, A9.

454. **Tao, C.** and **H. Zhou** (2020). Effects of different preheated CO_2/O_2 jet in cross-flow on combustion instability and emissions in a lean-premixed combustor. *Journal of the Energy Institute*, **93**(6), 2334–2343.

455. **Tao, C.** and **H. Zhou** (2021*a*). Dilution effects of CO_2, ar, n_2 and he microjets on the combustion dynamic and emission characteristics of unsteady premixed flame. *Aerospace Science and Technology*, **111**, 106537.

456. **Tao, C.** and **H. Zhou** (2021*b*). Effects of superheated steam on combustion instability and NO_x emissions in a model lean premixed gas turbine combustor. *Fuel*, **288**, 119646.

457. **Tetteh, J. N.**, **E. A. Hernandez-Vargas**, *et al.* (2021). Network models to evaluate vaccine strategies towards herd immunity in COVID-19. *Journal of Theoretical Biology*, **531**, 110894.

458. **Thomas, N.**, **S. Mondal**, **S. A. Pawar**, and **R. I. Sujith** (2018*a*). Effect of noise amplification during the transition to amplitude death in coupled thermoacoustic oscillators. *Chaos: An Interdisciplinary Journal of Nonlinear Science*, **28**(9), 093116.

459. **Thomas, N.**, **S. Mondal**, **S. A. Pawar**, and **R. I. Sujith** (2018*b*). Effect of time-delay and dissipative coupling on amplitude death in coupled thermoacoustic oscillators. *Chaos: An Interdisciplinary Journal of Nonlinear Science*, **28**(3), 033119.

460. **Tierno, J. E.** and **J. C. Doyle**, Multimode active stabilization of a Rijke tube. *In ASME Winter Annual Meeting*, volume 38. 1992.

461. **Tony, J.**, **E. A. Gopalakrishnan**, **E. Sreelekha**, and **R. I. Sujith** (2015). Detecting deterministic nature of pressure measurements from a turbulent combustor. *Physical Review E*, **92**(6), 062902.

462. **Tsien, H.** (1952). Servo-stabilization of combustion in rocket motors. *Journal of the American Rocket Society*, **22**(5), 256–262.

463. **Uhm, J. H.** and **S. Acharya** (2004). Control of combustion instability with a high-momentum air-jet. *Combustion and Flame*, **139**(1-2), 106–125.

464. **Uhm, J. H.** and **S. Acharya** (2005). Low-bandwidth open-loop control of combustion instability. *Combustion and Flame*, **142**(4), 348–363.

465. **Unni, V. R.**, **A. Krishnan**, **R. Manikandan**, **N. B. George**, **N. Sujith, R. I.and Marwan**, and **J. Kurths** (2018). On the emergence of critical regions at the onset of thermoacoustic instability in a turbulent combustor. *Chaos: An Interdisciplinary Journal of Nonlinear Science*, **28**(6), 063125.

466. **Unni, V. R.** and **R. Sujith** (2015). Multifractal characteristics of combustor dynamics close to lean blowout. *Journal of Fluid Mechanics*, **784**, 30–50.

467. **Unni, V. R.** and **R. Sujith** (2017). Flame dynamics during intermittency in a turbulent combustor. *Proceedings of the Combustion Institute*, **36**(3), 3791–3798.

468. **Unni, V. R.**, **R. I. Sujith**, and **P. Aghalayam** (2015). Role of flame dynamics on the bifurcation characteristics of a ducted v-flame. *Combustion Science and Technology*, **187**(6), 894–905.

469. **Utvik, D.**, **H. Ford**, and **A. Blackman** (1966). Evaluation of absorption liners for suppression of combustion instability in rocket engines. *Journal of Spacecraft and Rockets*, **3**(7), 1039–1045.

470. **Varun, A. V.**, **K. Balasubramanian**, and **R. I. Sujith** (2008). An automated vortex detection scheme using the wavelet transform of the d_2 field. *Experiments in Fluids*, **45**(5), 857–868.

471. **Venkatesan, K.**, **A. Cross**, **C. Yoon**, **F. Han**, and **S. Bethke**, Heavy duty gas turbine combustion dynamics study using a two-can combustion system. *In Turbo Expo: Power for Land, Sea, and Air*, volume 58615. American Society of Mechanical Engineers, 2019.

472. **Victor Gaigbe-Togbe, V.**, **L. Bassarsky**, **D. Gu**, **T. Spoorenberg**, and **L. Zeifman** (2022). United Nations Department of Economic and Social Affairs, Population Division (2022). World Population Prospects 2022: Summary of Results UN DESA/POP/2022/TR/NO. 3. Technical report, United Nations.

473. **Vincent, D. W.**, *Experimental investigation of acoustic liners to suppress screech in storable propellant rocket motors*. National Aeronautics and Space Administration, 1968.

474. **Vuillot, F.** (1995). Vortex-shedding phenomena in solid rocket motors. *Journal of Propulsion and Power*, **11**(4), 626–639.

475. **Wayson, R. L.**, **G. G. Fleming**, and **R. Iovinelli** (2009). Methodology to estimate particulate matter emissions from certified commercial aircraft engines. *Journal of the Air & Waste Management Association*, **59**(1), 91–100.

476. **Wei, M.-D.** and **J.-C. Lun** (2007). Amplitude death in coupled chaotic solid-state lasers with cavity-configuration-dependent instabilities. *Applied Physics Letters*, **91**(6).

477. **Wei, X.**, **M. Randrianandrasana**, **M. Ward**, and **D. Lowe** (2011). Nonlinear dynamics of a periodically driven duffing resonator coupled to a Van der Pol oscillator. *Mathematical*

Problems in Engineering, **2011**.

478. **Weng, Y.**, **V. R. Unni**, **R. Sujith**, and **A. Saha** (2020). Synchronization framework for modeling transition to thermoacoustic instability in laminar combustors. *Nonlinear Dynamics*, **100**, 3295–3306.

479. **Wesocky, H.** and **M. Prather**, Atmospheric Effects of Stratospheric Aircraft: A Status Report from NASA's High Speed Research Program. *In Proceedings Of Tenth International Symposium On Air Breathing Engines*. 1991.

480. **Williams, L. J.**, **J. Meadows**, and **A. K. Agrawal** (2016). Passive control of thermoacoustic instabilities in swirl-stabilized combustion at elevated pressures. *International Journal of Spray and Combustion Dynamics*, **8**(3), 173–182.

481. **Wu, W.-J.** and **L.-C. Kung** (2000). Determination of triggering condition of vortex-driven acoustic combustion instability in rocket motors. *Journal of Propulsion and Power*, **16**(6), 1022–1029.

482. **Xiong, M.**, **C. Xu**, **X. Gao**, **D. Li**, **D. Qu**, **Z. Wang**, and **X. Deng** (2018). Improved grid partitioning algorithms for load-balancing high-order structured aerodynamics simulations. *Computers & Electrical Engineering*, **67**, 70–84.

483. **Xu, D.-l.**, **H.-c. Zhang**, **S.-y. Xia**, **C. Lu**, **E.-r. Qi**, **C. Tian**, and **Y.-s. Wu** (2018). Nonlinear dynamic characteristics of a multi-module floating airport with rigid-flexible connections. *Journal of Hydrodynamics*, **30**, 815–827.

484. **Yang, V.** and **F. E. C. Culick** (1990). On the existence and stability of limit cycles for transverse acoustic oscillations in a cylindrical combustion chamber. Part I: Standing modes. *Combustion Science and Technology*, **72**(1-3), 37–65.

485. **Yeh, C. A.**, **M. Gopalakrishnan Meena**, and **K. Taira** (2021). Network broadcast analysis and control of turbulent flows. *Journal of Fluid Mechanics*, **910**.

486. **Yi, T.** and **D. A. Santavicca** (2009). Forced flame response of turbulent liquid-fueled lean-direct-injection combustion to fuel modulations. *Journal of Propulsion and Power*, **25**(6), 1259–1271.

487. **Yu, K. H.** and **K. C. Schadow** (1997). Role of large coherent structures in turbulent compressible mixing. *Experimental Thermal and Fluid Science*, **14**(1), 75–84.

488. **Yu, K. H.**, **A. Trouvé**, and **J. W. Daily** (1991). Low-frequency pressure oscillations in a model ramjet combustor. *Journal of Fluid Mechanics*, **232**, 47–72.

489. **Yu, K. H.** and **K. J. Wilson** (2002). Scale-up experiments on liquid-fueled active combustion control. *Journal of Propulsion and Power*, **18**(1), 53–60.

490. **Zeyer, K.-P.**, **M. Mangold**, and **E. Gilles** (2001). Experimentally coupled thermokinetic

oscillators: Phase death and rhythmogenesis. *The Journal of Physical Chemistry A*, **105**(30), 7216–7224.

491. **Zhang, G.**, **X. Wang**, **L. Li**, and **X. Sun** (2020). Effects of perforated liners on controlling combustion instabilities in annular combustors. *AIAA Journal*, **58**(7), 3100–3114.

492. **Zhang, S.**, **C. Wang**, **H. Zhang**, **P. Ma**, and **X. Li** (2022). Dynamic analysis and bursting oscillation control of fractional-order permanent magnet synchronous motor system. *Chaos, Solitons & Fractals*, **156**, 111809.

493. **Zhao, D.**, **E. Gutmark**, and **A. Reinecke** (2019). Mitigating self-excited flame pulsating and thermoacoustic oscillations using perforated liners. *Science Bulletin*, **64**(13), 941–952.

494. **Zhao, D.** and **X. Li** (2015). A review of acoustic dampers applied to combustion chambers in aerospace industry. *Progress in Aerospace Sciences*, **74**, 114–130.

495. **Zhao, D.**, **A. S. Morgans**, and **A. P. Dowling** (2011). Tuned passive control of acoustic damping of perforated liners. *AIAA journal*, **49**(4), 725–734.

496. **Zhong, Z.** and **D. Zhao** (2012). Time-domain characterization of the acoustic damping of a perforated liner with bias flow. *The Journal of the Acoustical Society of America*, **132**(1), 271–281.

497. **Zhou, H.** and **L. Hu** (2023). Mitigation of combustion instability and NO_x emissions by microjets in lean premixed flames with different swirl numbers. *Journal of Thermal Science*, 1–13.

498. **Zhou, H.** and **C. Tao** (2020). Effects of annular N_2/O_2 and CO_2/O_2 jets on combustion instabilities and NO_x emissions in lean-premixed methane flames. *Fuel*, **263**, 116709.

499. **Zhou, S.**, **W. Nie**, and **Y. Tian** (2021). High frequency combustion instability control by discharge plasma in a model rocket engine combustor. *Acta Astronautica*, **179**, 391–406.

500. **Zilitinkevich, S.** (1970). Non-local turbulent transport: pollution dispersion aspects of coherent structure of connective flows. *WIT Transactions on Ecology and the Environment*, **9**, 53–60.

501. **Zinn, B. T.** and **T. C. Lieuwen** (2005). Combustion instabilities: basic concepts. *Progress in Astronautics and Aeronautics*, **210**, 3.

502. **Zou, W.**, **D. V. Senthilkumar**, **M. Zhan**, and **J. Kurths** (2021). Quenching, aging, and reviving in coupled dynamical networks. *Physics Reports*, **931**, 1–72.

503. **Zou, Y.**, **R. V. Donner**, **N. Marwan**, **J. F. Donges**, and **J. Kurths** (2019). Complex network approaches to nonlinear time series analysis. *Physics Reports*, **787**, 1–97.

504. **Zukoski, E.**, Combustion instability sustained by unsteady vortex combustion. *In 21st Joint Propulsion Conference*. 1985.

505. **Zukowski, E. E.**, *Afterburners*, chapter 21. Air Force Aero Propulsion Laboratory, Air Force Wright Aeronautical Laboratories, 1978, 21–16.

CURRICULUM VITAE

NAME	Ankit Sahay
DATE OF BIRTH	02 March 1993

EDUCATION QUALIFICATIONS

2016 **Bachelor of Engineering (B. E.)**

Institution	Birla Institute of Technology
Specialization	Mechanical Engineering

2024 **M. Tech. and Ph. D. Dual Degree**

Institution	Indian Institute of Technology Madras
Specialization	Aerospace Engineering
Registration Date	23rd July 2018

DOCTORAL COMMITTEE

Chairperson	Dr. H. S. N. Murthy Professor and Head Department of Aerospace Engineering
Guide	Dr. R. I. Sujith Institute Professor and D. Srinivasan Institute Chair Professor Department of Aerospace Engineering
Members	Dr. Sunetra Sarkar Professor Department of Aerospace Engineering
	Dr. Nandan Kumar Sinha Professor Department of Aerospace Engineering
	Dr. Arul Lakshminarayan Professor and Head Department of Physics